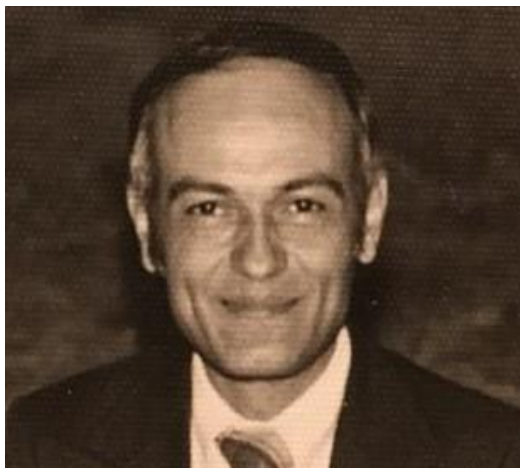


IN MEMORIAM

Prof. Eng. Lubomir A. Boyadzhiev. PhD, DSc, Corresponding Member of the Bulgarian Academy of Sciences (1934-2019)



On May 14, 2019 the Corresponding Member of the Bulgarian Academy of Sciences, Prof. DSc Lubomir Boyadzhiev passed away. He was an eminent scientist and international authority in the field of chemical engineering.

Prof. Boyadzhiev was born on November 16th 1934 in Sofia, Bulgaria. He graduated from the Institute of Chemical Technology in Sofia (now: University of Chemical Technology and Metallurgy) in 1958, and worked for a couple of years as an engineer in the industry. Then, he was appointed at the Chemical Institute at the Bulgarian Academy of Sciences (BAS). Prof. Boyadzhiev defended his PhD thesis in 1968 and was promoted to associate professor the next year. During the period 1977/87 he was lecturing at the Faculty of Chemistry of the Sofia University „St. Climent Ohridski“. He specialized at the Institut du Genie Chimique (Toulouse, France, 1965) and at Washington University (Seattle, USA, 1975). After defending his „Doctor of Sciences“ (DSc) thesis in 1982 he was promoted to full professor in 1984, and in 1995 was elected as corresponding member of BAS.

Prof. L. Boyadzhiev was a scientific secretary of BAS (1979/82) and at this position he introduced the practice of planning the scientific research in BAS on the basis of research projects. Later this practice was adopted by all scientific institutions and Universities in Bulgaria. He has been a deputy-director of the United Centre for Chemistry at BAS (1985/88) and for the period 1990/92 was the Director of the Institute of Chemical Engineering at BAS.

Prof. Boyadzhiev was a member of different editorial boards of Bulgarian and foreign scientific journals. He was co-founder and president of the Bulgarian Society of Chemical Engineering (1993/99), a consultant of UNESCO for education and research on chemical engineering (1978/80), of the 12th Commission of the European Union in Brussels, of a number of foreign companies and Bulgarian enterprises. The scientific and research activities of Prof. Boyadzhiev were in the field of process engineering and, in particular, on separation and transfer processes in multiphase systems. He has published over 150 scientific papers in high impact journals, which were cited till present more than 2000 times. An evidence for the international respect to him is his inclusion in *Who's Who in the Science* (Longman Publ. London) and *Current Bibliographic Directory: Art & Science* (ISI Publ., Philadelphia).

He has delivered over 150 scientific presentations and lectures at various scientific events in Bulgaria and abroad (Europe, Asia and America). As a visiting professor he has delivered lectures at the Polytechnique in Toulouse (France, 1973, 1993/94); Ecole Polytechnique (Montreal, Canada, 1983), Université de Paris-3 and Rouen (1992 and 1998), as well as at Tokyo University (1995).

Corr. Mem. L. Boyadzhiev was a supervisor of over 50 applied projects and a co-author of over 20 inventions and two patents abroad, one of them sold to the big chemical corporation Henkel Corp. (USA).

Corr. Mem. L. Boyadzhiev had perceptive scientific intuition. Because of it, his research was in pioneering areas and consonant with the new world trends. In the first years of his career he worked in the then modern direction of intensifying the processes in chemical technology for their enhanced operation. He is a co-author of a monograph „Intensification of absorption and extraction“, published in Bulgaria (Technika, Sofia, 1968).

He was one of the first researchers in the world to begin working on liquid membrane processes and he had world-wide renowned contributions in it.

An innovative approach in this area is the development of new integrated processes for recovery of valuable products of better quality at

lower expenses. An example of this approach is the solid-liquid extraction integrated with isolation and enrichment of target compounds by the liquid membrane technique. In this process a concentration difference is continuously maintained to provoke continuous mass transfer until the complete exhaustion of the source takes place. This application is appropriate for cases of low solubility in the solvent, thus enabling the use of non-specific and harmless solvents, e.g. water. This integrated approach makes it possible to replace numerous classical operations, like multiple extraction, filtration, evaporation, etc.

The competence of Prof. L. Boyadzhiev in this field is confirmed by the authorship of two monographs, ordered and published by eminent international publishing houses for scientific literature: „Technology of Membrane Separation. Principles and Applications“, in: Handbook of Membrane Technologies (Elsevier, Amsterdam, 1995), “Liquid membranes”, in: Encyclopedia of Separation Science (Ed. I. Wilson), Academic Press, London. 2000.

Later he developed and supervised the research group for recovery of natural biologically active substances from renewable natural resources. This subject became recently very popular because of the growing interest in the pharmaceutical industry for replacement of the synthetic medicines by natural ones.

There are some industrial processes for extraction and separation of valuable or toxic substances developed by him (e.g. Aromex, Phytex, Rotex, etc.). They were applied in Bulgarian enterprises.

Prof. L. Boyadzhiev was initiator of long lasting and fruitful collaboration with the Institut du Genie

Chimique (Toulouse, France), starting from 1965. Within the framework of the cooperation many long-time research visits of young Bulgarian scientists, as well as many bi-lateral research projects supported by BAS and CNRS have been accomplished. These contacts were the background for founding a francophone courses on chemical engineering in the University of Chemical Technology and Metallurgy together with joint MSc and PhD theses.

Prof. L. Boyadzhiev was the main person also for the contacts of the Institute of Chemical Engineering (BAS) with the Institute of Chemical Process Fundamentals at the Czechoslovak Academy of Sciences in Prague (former Czechoslovakia) where many young scientists passed short scientific visits on joint research projects.

Corr. Mem. L. Boyadzhiev was awarded twice with the Sign of Honour of BAS „Prof. M. Drinov“ (1969 and 2004), as well as by numerous state rewards, including the order „Sts Cyrill and Methodius“

We and his colleagues from the Bulgarian and the international scientific community remember him as a radiant and charming personality with big erudition, profound scientific competence and a comprehensive common culture. He was an honest and polite person with a wonderful sense of humor, with open and predisposed way of contacts and equal treatment of younger colleagues.

That is why he enjoyed universal respect among the colleagues of many generations, due to his personal human qualities and his naturally developed scientific authority.

Prof. George Angelov, DSc

Voltammetric detection of hydrochlorothiazide at molybdenum oxide modified screen-printed electrodes

M.F. Khanfar¹, E. S. M. Abu-Nameh²*, A. T. Afaneh², M. M. Saket¹, A. Ahmad², W. Faraj¹, M. Khalil¹, H. Al Khotaba², M. Al Bujog²

¹ Pharmaceutical and Chemical Engineering Department, School of Applied Medical Sciences, German Jordanian University, P.O.Box 35247 Amman 11180, Jordan

² Department of Chemistry, Faculty of Science, Al-Balqa Applied University, Al-Salt 19117, Jordan

Received February 15, 2018; Accepted March 21, 2019

Electrochemical oxidation of hydrochlorothiazide (HCT) was investigated both experimentally and theoretically to explore the connection between thermodynamics and the oxidation potential. In this work, screen printed carbon electrodes were modified with molybdenum oxide by means of voltammetry. The modified surfaces demonstrated significant sensitivity toward hydrochlorothiazide detection in pH 2.00–buffered aqueous solutions. The employed method was validated and used for hydrochlorothiazide quantification in commercial drug products. In this work, we presented results of density functional calculations for the standard reduction potential of the HCT (H)₂/HCT couple in aqueous solution. After consideration of 20 density functionals with 4 different basis sets, it was found that the hybrid meta functionals provide the most accurate prediction of the reduction potential in comparison with the available experimental data. The reported reduction potential is underestimated with GGA and MGGA and is overestimated with hybrid and meta hybrid functionals. Our results highlighted the importance of including solute-solvent hydrogen bonding effects in the theoretical modeling of redox processes.

Keywords: Molybdenum oxide, Hydrochlorothiazide, Screen-printed electrodes, Electrochemical deposition, Density functional theory (DFT).

INTRODUCTION

Hydrochlorothiazide is chemically 6-chloro-1,1-dioxo-3,4-dihydro-2H-1,2,4-benzothiazine-7-sulfonamide. Hydrochlorothiazide is a diuretic drug used for treatment of high blood pressure. For high blood pressure, it is often recommended as a first line treatment. HCT is taken orally and may be combined with other blood pressure medications as a single pill to increase the effectiveness, and decrease the accumulation of fluid (edema). It works by blocking salt and fluid reabsorption from the urine in the kidneys, causing increased urine output (diuresis). Hydrochlorothiazide is used to treat excessive fluid accumulation and swelling (edema) of the body caused by heart failure, cirrhosis, chronic kidney failure, corticosteroid medications, and nephrotic syndrome [1,2]. In Jordan, pharmaceutical analysis is mainly carried out by means of photometry and chromatography, a little attention is usually paid to electrochemistry. Therefore, in this work, we focused on the electrochemical analysis of HCT.[3-5]

EXPERIMENTAL

The EN AW-6060 alloy was chosen for the experimental investigation. The alloy was delivered by “AlCu metali d.o.o.” company, in peak-aged

state (T6 temper). The chemical composition was determined by using an optical emission spectrometer “Belec Compact Port” and is presented in Table 1. Peak-aged state was removed and O-temper achieved by annealing at 550 °C for 6 h in the electric resistance furnace Heraeus K-1150/2.

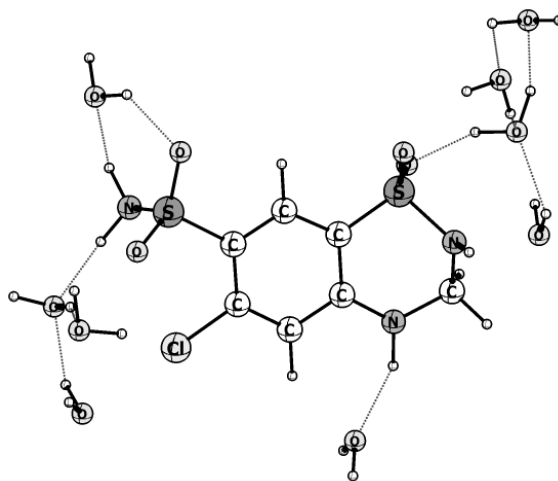


Figure 1. Structure of hydrochlorothiazide (HCT) with 9 water molecules.

Hydrochlorothiazide (HCT), Figure 1, is an active pharmaceutical of unique structural properties. It is electroactive (could be oxidized to its imine analogue), chromophore, due to the

* To whom all correspondence should be sent:
E-mail: abunameh@bau.edu.jo

presence of a noticeable conjugated system, and as most of the active ingredients, it has an organic skeleton. With these properties, it could be quantified by a wide range of analytical methods such as electrochemistry, spectroscopy, and chromatography [6-11].

Electrochemical methods are considered as the most convenient tools that could be used for HCT analysis, especially if the target analyte exists in the form of pharmaceutical dosage that is mainly blended with inactive, non-interfering species that may alter the detected signal attributed to HCT. These methods are simple, cheap, quick, and could be performed with portable hand-held equipment. By means of electrochemical methods, HCT has been analyzed using voltammetry (cyclic, differential pulse, square wave) and impedance spectroscopy, where the sensor is modified with a material which conductivity is affected by the quantity of HCT present in the analyte solution [12-15].

Most of the sensors utilized for HCT are carbon-based materials. HCT has been analyzed on glassy carbon, multi-wall carbon nano tubes, graphite, graphene, and carbon paste electrodes. These carbon materials could be classified as unmodified, so that they are composed from carbonaceous material, or modified ones. Usually, carbon is blended with a modifier that elevates its conductivity so that the charge transfer rate across the electrode-electrolyte increases, or enhances the sensitivity so that the electrode becomes more responsive to the target analyte, especially at the low concentration levels. In the case of HCT, the carbon portion of the sensor has been mixed with conductivity enhancers such as ferrocene and its derivatives, or with sensitivity amplifiers such as metalloporphyrin [16-22].

One of the goals of modern quantum chemical simulations is to recognize and expect chemical reactivity, and another is to study the mechanisms of condensed-phase catalytic, photochemical and electrochemical reactions. Many reactions involve electron-transfer steps, sometimes combined with the breaking or formation of chemical bonds. Such reactions are significant in environmental chemistry, biochemistry, fuel cells, and electro-analytical field devices. The reduction potential is the key thermodynamic variable that describes the tendency of a chemical species to gain or lose electrons, which may be measured, for example, by cyclic voltammetry or spectrophotometric techniques combined with pulse radiolysis [23].

In this work, we report the experimental and theoretical studies of the oxidation of HCT compound. The experimental part combines both

simplicity and detection sensitivity. Screen-printed carbon electrode (SPE) was utilized as the carbon foundation while molybdenum oxide was added as an electrochemical reaction catalyst. The SPE is an almost 1 cm² area sensor that confines the three electrodes needed for the voltammetric measurements, namely the working, the reference, and the counter electrode. With that configuration, aliquots of less than 500 μL of the HCT solution could be analyzed for the active ingredient concentration. Molybdenum oxide has been electrochemically deposited on the carbon surface where molybdenum exists in the tetravalent oxidation state and hence acts as an electron-deficient center positive enough to oxidize the HCT to its imine counterpart.

The computational chemistry has evolved to the point that it is sometimes competitive to experiment to obtain precise values for certain molecular properties, density functional theory (DFT) [24-26]. In this study, the redox potential of hydrochlorothiazide was calculated with the employment of the density functional theory (DFT) molecular orbital calculations at a different level of theories (will be mentioned in detail in the computational methods section). The details of the calculation will be explained in the theoretical section of the present work.

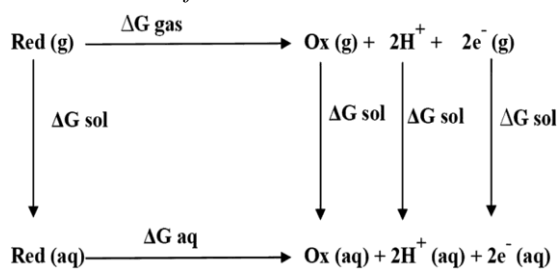
THEORETICAL CALCULATIONS

The general procedure for computation of standard reduction potential E° is given here. E° is related to the standard reduction free energy in solution given by

$$E^\circ = -\frac{\Delta G_{sol}^\circ}{nF} \quad (i)$$

where n is the number of transferred electrons in the reaction which is equal to 2 for the reaction under investigation, F is the Faraday constant and ΔG_{sol}° is the free energy change associated with reduction at standard conditions. To calculate ΔG_{sol}° , it is necessary to use the following thermodynamic cycle (Born-Haber), which is used for transferring all of the species involved in the reaction from the gas to solution phase, Scheme 1.

The free energy change in the gas phase equals the adiabatic ionization potential, ΔG_I° , of the reduced species. Consequently, the aqueous standard-state reduction potential to the modified



Scheme 1. Presentation of the 2-electron, 2-proton thermodynamic cycle

electrode, ΔG_{ME}° can then be estimated from equation (ii):

$$E^{\circ} = \frac{\Delta G_{I}^{\circ} + \Delta \Delta G_{S}^{\circ} + \Delta G_{ME}^{\circ}}{nF} \quad (ii)$$

Finally, $\Delta \Delta G_{S}^{\circ}$ is the difference of solvation free energies of products and reactants, $\Delta \Delta G_{S}^{\circ} = \Delta G_{S}^{\circ}(O) - \Delta G_{S}^{\circ}(R)$.

EXPERIMENTAL PART

Chemicals and Reagents

Britton-Robinson buffer (B-R buffer) with pH = 2.00 was prepared using 0.04 M H_3PO_4 , 0.04 M H_3BO_3 (Honywell, U.S.A.), and 0.04 M CH_3COOH (S-D Fine Chem. India). The desired pH value was obtained by the addition of the needed amounts of aqueous 0.2 M NaOH (VWR, U.K.) solution. Hydrochlorothiazide was a kind gift from the Jordanian Pharmaceutical Manufacturing Company. The pure hydrochlorothiazide (HCT) powder was used to prepare 2.22×10^{-4} M standard solution in the previously prepared B-R buffer pH = 2 solution. Standard solutions of HCT were prepared by serial dilution using the same buffer. Sodium molybdate (provided by Gainland Chemical Company, U.K.) and sodium sulfate (AZ Chemicals, China) were prepared as aqueous solutions with concentrations equal to 88.2 μ M and 3.22 mM, respectively.

Instrumentation

All of the voltammetric measurements were performed using PGSTAT 101 (Autolab, Metrohm, The Netherlands). Screen-printed electrodes (DRP-C110) provided by Dropsense, Asturias, Spain, were used for the measurements. The electrodes have carbon working and counter electrodes and a silver reference electrode. Except for the molybdenum oxide deposition, unless otherwise stated, all of the voltammetric measurements are differential pulse with scan rate = 50 mV/s, step potential = 5 mV, modulation amplitude = 25 mV, modulation time = 20Hz, interval time = 0.5 s. The

data were collected using the NOVA 2.0 software provided by Metrohm.

Preparation of the Modified Electrodes

The molybdenum oxide modified surface was prepared by the addition of Na_2MoO_4/Na_2SO_4 on the SPE and cycling potential of the working electrode between +0.20 to -0.80 V at 50 mV/s for 10 cycles.

Sample preparation

The HCT content of two different commercial diuretic drugs was analyzed. Of each, ten tablets were weighed and powdered. A portion of the powder equivalent to the average weight of one tablet was transferred into a 25 ml volumetric flask using about 15 ml of 0.02 M NaOH. The mixture was sonicated for 5 min, then completed to volume with the same solvent. The resulted suspension was allowed to settle and 0.100 ml from the supernatant was diluted to 25 ml using the prepared B-R buffer of pH 2.00. 1.00 ml of the diluted solution was then diluted with 5.00 ml of the buffer and 500 μ L of the solution was used for the voltammetric measurements.

Computational Methods

The structure of HCT was optimized at different DFT/Basis sets level of theories in the gas phase. All the stationary points were characterized by frequency calculations at the same levels. The DFT we used in this study can be classified into four categories, specifically generalized gradient approximation (GGA), hybrid-GGA (H), meta-GGA (MGGA), and hybrid meta-GGA (HM). Both GGA and MGGA exchange functionals depend on the electron spin density and its gradient; MGGA functionals also depend on the spin kinetic energy density. Both H and HM functionals depend on Hartree-Fock exchange, electron spin-density, and its gradient; HM functionals also depend on spin kinetic energy density. The GGA functionals considered here are BLYP, BP86, BPW91, BPBE and PBE. The hybrid functionals that we used are B3LYP, B3P86, B3PW91, BH&HLYP and PBEh. The MGGA functionals tested in the present work are BB95, mPWB95, PBEKCIS, TPSS and TPSSKCIS. The hybrid meta functionals that we considered here are B1B95, BB1K, MPW1B95, TPSS1KCIS and TPSSh [27,28].

The calculations were carried out with the Northwest Computational Chemistry Package (MWChem), version 6.3 [29]. The choice of basis sets was made to be consistent with the valence basis set used for HCT compound: LANL2DZ,

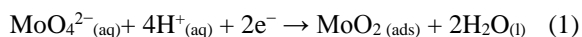
DZP (Dunning), cc-pVTZ and aug-cc-PVTZ [30,31].

The gas-phase calculations were followed with single points at the same level of theories in the aqueous environment. COSMO calculations at DFT/Basis sets levels were carried out on the stationary points to address solvation effects using the dielectric constant of water (78.39) in order to simulate the aqueous environment. In this study, we used the cluster model for the calculations of the solvation free energy for HCT. Put different, a hybrid solvation model was used in this study, implicit/explicit hybrid solvation model for the calculations.

RESULTS AND DISCUSSION

Modification of SPE by Molybdenum Oxide

The deposition of molybdate ion on the SPE surface was accomplished by using a cycling potential of the working electrode between 200 and -800 mV *versus* reference electrode. The deposition process (shown in Figure 2) is an irreversible reduction of molybdate to molybdenum dioxide due to the absence of anodic features in the voltammogram. The reduction reaction is:



The pH dependence of the reduction process is beyond the scope of the current study. The described cycling was repeated 10 times until a steady and stable voltammogram (not shown) was obtained.

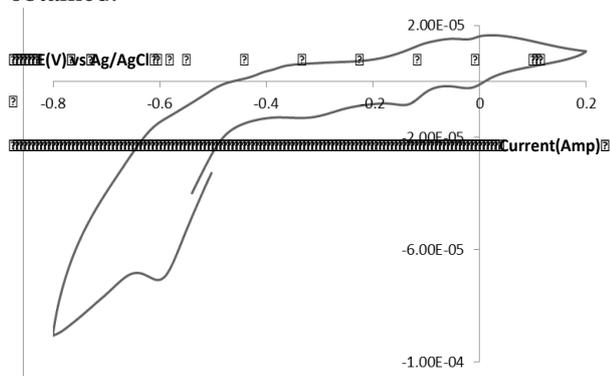


Figure 2. Deposition of molybdenum oxide on the SPE electrode. Cyclic voltammetry with scan rate = 50 mV/s

Oxidation of HCT

The molybdenum-modified electrode was used for the oxidation of hydrochlorothiazide as shown in Figure 3. The modified surface demonstrates improved performance toward the oxidation reaction, when compared to its unmodified counterpart, appearing as enhancement of the oxidation current at +0.950 V.

Further research and investigation are needed to improve the reported catalytic activity that usually appears as a combination of the shift of the oxidation toward less positive potentials and enhancement in the oxidation to an extent higher than that reported in this work.

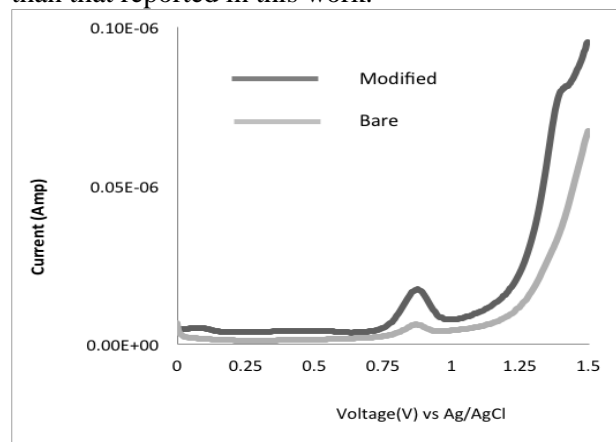
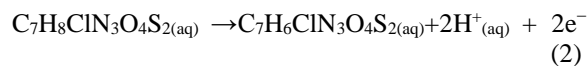
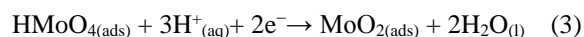


Figure 3. Effect of modification by molybdate on the oxidation of HCT.

The oxidation of HCT is described in reaction (2) that shows how HCT undergoes two-electron, two-proton oxidation reaction and is converted to its imine counterpart:



At potentials close to the value where the HCT oxidation occurs, molybdenum exists in the form of hydrogen molybdate that is reduced back to molybdenum dioxide previously deposited on the SPE surface [32]. The molybdenum oxide is generated as shown in reaction (3):



Diffusion of the target analyte toward the electrode surface was studied by tracking the scan rate dependence of the oxidation peak current as shown in Figure 4.

According to Randless–Sevcik equation for diffusion-controlled electrochemical reactions, the peak electrolysis current depends on the square root of the employed scan. In this work, that dependence was examined over the 1-160 mVs⁻¹ scan range and linear adherence with R² = 0.9919 was reported as shown in Figure 5 which confirms electrolysis of HCT at the modified surface.

Validation of the Analytical Method

In order to check the validity of the investigated method toward HCT in commercial tablets, four key analytical parameters were estimated for the employed method, namely, linearity, limit of detection, limit of quantitation, and recovery. By

serial dilutions, the response of the modified electrode toward the oxidation of HCT was studied in the 1.42-29.77 ppm concentration range.

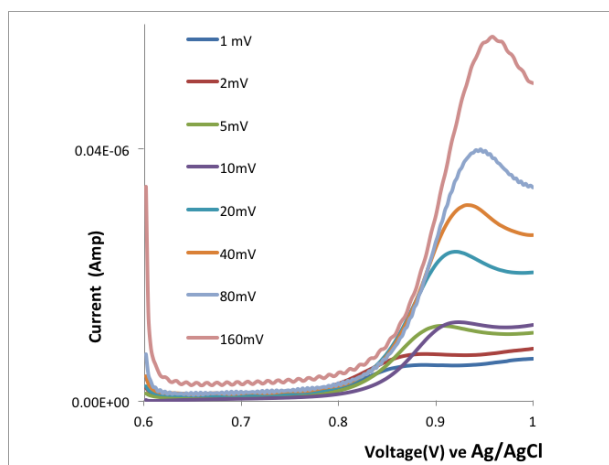


Figure 4. Dependence of the oxidation potential on the scan rate as obtained by linear sweep voltammetry.

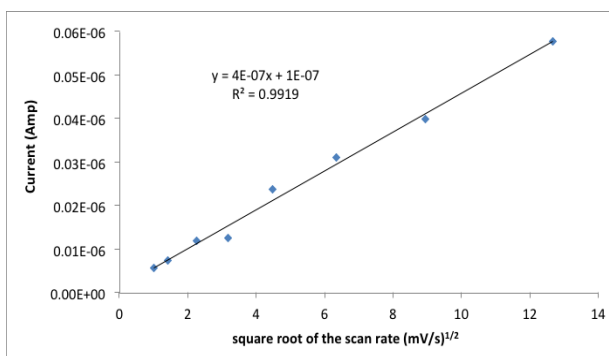


Figure 5. Dependence of the peak oxidation current on the scan rate.

The measurements were performed in sets of six trials per concentration in the mentioned range and the linear response of the modified SPE to elevation in the HCT concentration is shown in Figure 6. From the graph, the R^2 value was found to be 0.9942 while the limits of detection and quantitation were calculated to be equal to 6.991 and 21.185 ppm, respectively.

Recovery was checked for two commercial drugs, namely monozone (12.5 mg) and amuretic (25 mg) and the corresponding recovery values were reported as 81.2 and 96.3%, respectively. The relatively low recovery value reported for monozone could be attributed to the presence of species that may cause interference or masking.

Standard Reduction Potential in DFT Model

The resulting values of $E_{\text{HCT}(\text{H})_2|\text{HCT}}^{\circ}$ are given in Table 1 for the calculations with 9 explicit water molecules with implicit solvation model, ISM, (hybrid model).

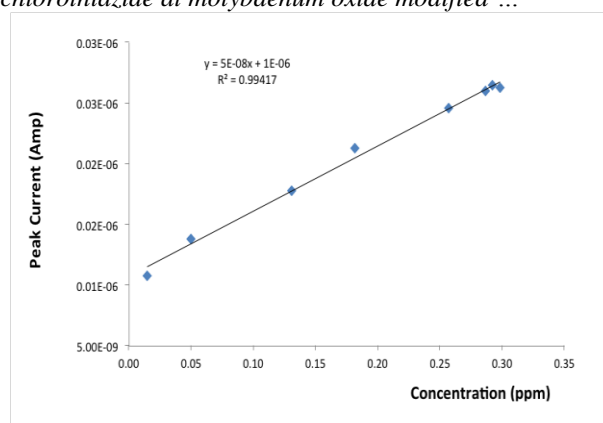


Figure 6. Calibration curve for the oxidation of HCT at the molybdenum-modified surface.

We also show the average values of E° and standard deviations of each combination of basis set and type of density functional. The values in Table 1 significantly differ from the values calculated with ISM. The corresponding values overestimated E° by over 1.62V with all types of density functionals. The significant difference between standard reduction potentials computed using ISM and hybrid model stems from the different physical descriptions of the solvent. The hybrid model description contains many physical effects that are absent in the ISM, including solute flexibility, solute-solvent interaction, and hydrogen bonding. Furthermore, there is a probability that the errors in ISM are a consequence of incorrect parameterization of the atomic radii. Generally, the HM methods combined with aug-cc-pVTZ predict the experimental value of $E_{\text{HCT}(\text{H})_2|\text{HCT}}^{\circ} = 0.95\text{V}$ better than the other methods. The GGA and MGGA predictions are underestimated with respect to the experiment, whereas the H and HM overestimate the corresponding values except for B3PW91/cc-pVTZ, PBEh/cc-pVTZ and PBEh/aug-cc-pVTZ hybrid GGA and MPW1B95/cc-pVTZ, TPSS1KCIS and TPSSh with all basis sets we used, Table 1.

Finally, using ΔG_1° (MP2/aug-cc-pVTZ) along with the values of $\Delta\Delta G_5^{\circ} = -10.7$ and -7.1 eV, respectively, for the 9 water molecules averaged over all the DFT results at the aug-cc-pVTZ basis level, we predict the following $E_{\text{HCT}(\text{H})_2|\text{HCT}}^{\circ}$ magnitude: 0.96V. Again, the inclusion of the explicit solvation shell in the treatment significantly improves the agreement of theory and experiment (0.95V).

Table 1. Standard reduction potential $E_{\text{HCT(H)}_2|\text{HCT}}^{\circ}$ using ISM with hydration shell explicitly included.

Method	LANL2DZ	DZP (Dunning)	cc- pVTZ	aug-cc- pVTZ	Method	LANL2DZ	DZP (Dunning)	cc- pVTZ	aug- cc- pVTZ
GGA					H				
BLYP	0.81	0.86	0.70	0.83	B3LYP	1.17	1.22	1.00	1.10
BP86	0.89	0.90	0.75	0.88	B3P86	1.61	1.63	1.45	1.52
BPW91	0.82	0.85	0.67	0.79	B3PW91	1.07	1.09	0.87	1.00
BPBE	0.79	0.82	0.64	0.75	BH&HLYP	1.34	1.39	1.14	1.20
PBE	0.79	0.81	0.63	0.74	PBEh	1.01	1.05	0.82	0.89
Average	0.82	0.85	0.68	0.80	Average	1.24	1.28	1.06	1.14
SD	0.04	0.04	0.05	0.06	SD	0.24	0.24	0.25	0.24
MGGA					HM				
BB95	0.79	0.84	0.67	0.80	B1B95	1.11	1.15	0.87	0.90
mPWB95	0.82	0.87	0.71	0.81	BB1K	1.23	1.27	1.04	1.08
PBEKCIS	0.85	0.87	0.69	0.80	MPW1B95	1.15	1.18	0.89	1.02
TPSSKCIS	0.75	0.80	0.62	0.72	TPSS1KCIS	0.88	0.90	0.72	0.82
TPSS	0.70	0.77	0.59	0.67	TPSSh	0.84	0.85	0.67	0.75
Average	0.78	0.83	0.66	0.76	Average	1.05	1.07	0.84	0.91
SD	0.06	0.04	0.05	0.06	SD	0.17	0.18	0.15	0.14

CONCLUSIONS

The analysis performed in this work shows that the modification of carbon electrodes with species that exist in different oxidation states enhances the voltammetric detection of target pharmaceuticals like HCT. The modified surface demonstrated promising performance toward the oxidation reaction; further studies could involve imaging of the modified surface and correlating topography of the modified surface to its activity.

Enhancement of the oxidation current in the presence of the adsorbed molybdates points to their catalytic activity; further effort in that direction may include modification of the screen printed electrodes with a binary adsorbate besides the molybdenum oxide.

We have presented the computational study of the aqueous reduction potential of the $E_{\text{HCT(H)}_2|\text{HCT}}^{\circ}$ redox reaction. We used exchange–correlation functionals classified into four categories: GGA, MGGA, HGGGA and HMGGGA combined with four basis sets. The computational procedure is based on a thermodynamic cycle where the electrochemical parameters are determined by the ionization free energy, and the solvation free energy of the species. The reduction potential $E_{\text{HCT(H)}_2|\text{HCT}}^{\circ}$ is overestimated when ISM is treated only whereas it

is in good agreement with the experimental value when the explicit shell is included in the ISM.

The correlation between the experimentally reported reduction potential and that calculated theoretically is of significant importance, especially for the selection of the working electrode and the materials added to it.

REFERENCES

- 1 S.S. Badawy, B. AbdelAzeem, *ChemXpress*, **6**, 14 (2014).
- 2 A.F. Alghamdi, *J. Food Drug Analysis*, **22**, 363 (2014).
- 3 M.I.H. Helaleh, T. Korenaga, E.S.M. Abu-Nameh, R.M.A.Q. Jamhour, *Pharmaceutica Acta Helvetiae*, **73**, 255 (1999).
- 4 M.I.H. Helaleh, ESM Abu-Nameh, *Anales de Quimica*, **94**, 160 (1998).
- 5 M.I.H. Helaleh, E.S.M. Abu-Nameh, R. Jamhour, *Acta Poloniae Pharmaceutica*, **55**, 93 (1998).
- 6 S. S. Abd El-Hay, H. Hashem, A. A. Gouda, *Acta Pharm.*, **66**, 109 (2016).
- 7 H.W. Darwish, A. H. Bakheit, A.S. Abdelhameed, *Acta Pharm.* **66**, 83 (2016).
- 8 K. Deventer, O.J. Pozo, P. Van Eenoo, F.T. Delbeke, *J. Chromatogr. A*, **1216**, 2466 (2009).
- 9 L. Fei, X. Yu, S. Gaob, J. Zhang, Q. Guo, *J. Pharm. Biomed. Analysis*, **44**, 1187 (2007).
- 10 R. Onnainty, E.M. Schenfeld, M.R. Longhi, M.A. Quevedo, G.E. Granero, *Biomed. Chromatography*, **31**, 1 (2017).

- 11 M.L. Jadhav, M.V. Girase, S.K. Tidme, M.S. Junagade, *Int. J. Spectroscopy*, **1** (2014).
- 12 A. Chmielewska, L. Konieczna, A. Plenis, H. Lamparczyk, *J. Chromatogr. B*, **839**, 102 (2006).
- 13 M. Cristina, G. Santosa, C. Ricardo, T. Tarleya, L.H. Dall'Antonia, E.R. Sartoria, *Sensors and Actuators B*, **188**, 263 (2013).
- 14 M.B. Gholivand, M. Khodadadian, *Electroanalysis*, **25**, 51263 (2013).
- 15 N. Kumar, R.N. Goyalz, Melamine/Fe₃O₄ Nanoparticles Based Molecular Imprinted Highly Sensitive Sensor for Determination of Hydrochlorothiazide: An Antihypertensive Drug, *J. Electrochem. Soc.*, **164**, B240 (2017).
- 16 B. Rezaei, S. Damiri, *IEEE Sensors Journal*, **8**, 9, 1523 (2008).
- 17 B.S. Wesley, D. N. Machini, M. David-Parra, F.S. Teixeira, *Materials Sci. Eng. C*, **57**, 344 (2015).
- 18 H. Beitollahi, F. Ghorbani, *Ionics*, **19**, 1673 (2013).
- 19 E. Er, H. Çelikkan, M. L. Aksuc, N. Erka, *Anal. Methods*, **7**, 9254 (2015).
- 20 O. Abdel Razak, *J. Pharm. Biomed. Analysis*, **34**, 433 (2004).
- 21 H. Beitollahi, M. Hamzavi, M. Torzkadeh-Mahani, *Materials Sci. Eng. C*, **52**, 297 (2015).
- 22 B. Uslu, S.I.A. Ozkan, *Analytical Letters*, **40**, 817 (2007).
- 23 P. Wardman, Reduction *J. Phys. Chem. Ref. Data*, **18**, 1637 (1989).
- 24 P. Hohenberg, W. Kohn, *Phys. Rev. B*, **136**, 864 (1964).
- 25 M. Koch, C. Holthausen, *A Chemists Guide to Density Functional Theory*, Wiley-VCH, Weinheim, 2000.
- 26 R. G. Parr, W. Yang, *Density Functional Theory of Atoms and Molecules*, Oxford University Press, Oxford, 1989.
- 27 K. Burke, *J. Chem. Phys.* **136** (15), 150901 (2012).
- 28 A. D. Becke, *J. Chem. Phys.*, **140** (18), 18A301 (2014).
- 29 M. Valiev, E. J. Bylaska, N. Govind, K. Kowalski, T. P. Straatsma, H. J. J. van Dam, D. Wang, J. Nieplocha, E. Apra, T. L. Windus, W. A. de Jong, *Comput. Phys. Commun.* **181**, 1477 (2010).
- 30 D. Feller, *J. Comp. Chem.*, **17**, 1571 (1996).
- 31 K. L. Schuchardt, B. T. Didier, T. Elsethagen, L. Sun, V. Gurumoorthi, J. Chase, J. Li, T. L. Windus, Basis Set Exchange: A Community Database for Computational Sciences, *J. Chem. Inf. Model.*, **47**(3), 1045 (2007).
- 32 S. S. Viswanathan, L. Chi-Woo, *ChemSusChem*, **5**, 1146 (2012).

The effect of plastic waste and elemental sulfur additives on chemical and physical properties of bitumen

M. Ashjari, S. Masoud Kandomal*

Chemical Engineering Department, Faculty of Engineering, University of Kashan, P.O. Box 87317-51167, Kashan, Islamic Republic of Iran

Received April 22, 2018; Revised March 8, 2019

In this study we describe the modification of bitumen for obtaining better chemical and physical properties. For this goal, we added sulfur or plastic waste in different percentages to the bitumen matrix. The effect of sulfur ratio in the range of 20-40% (w/w) and plastic waste ratio in the range of 2-5% (w/w) was investigated on the softening point, penetration, tensile factor and loss of weight of bitumen. The obtained data confirmed the improvement in chemical and physical properties of bitumen in the presence of plastic waste and sulfur additives. The results showed that tensile factor of bitumen decreases from 1020 mm to 820 mm and 980 mm after addition of 30% of sulfur and 3% of plastic waste, respectively. On the other hand, the best penetration was obtained in the presence of 30% sulfur and 3% plastic waste, respectively. Finally, we suggest the application of sulfur and plastic waste as two important additives for bitumen modification.

Keywords: Bitumen, Sulfur, Plastic waste, Chemical and physical properties

INTRODUCTION

Removal of plastic waste is a major and important subject in developed and developing countries. The high volume of plastic waste is now one of the most important environmental problems due to the lack of recovery [1-5]. Therefore, suggesting a new application for this type of materials can be useful for improving quality of life.

Sulfur is a useful and important additive in asphalt mixtures with good properties [6]. Some of the studies showed that sulfur can improve the stiffness of compacted asphalt mixtures [7]. On the other hand, sulfur is a harmful and toxic element obtained from natural gas resources and petroleum. So, application of surplus generated sulfur in a new field can be helpful to environmental health.

Bitumen used for paving (85%), roofing (10%) and other uses (5%) is a black or dark-colored, amorphous, cementitious material that can be found in different forms. New additives can improve the quality and durability of bitumen [8].

In this research, we tried to investigate the effect of elemental sulfur and plastic waste on the chemical and physical properties of bitumen. The study will follow two general purposes, 1) improving the quality of bitumen for application in roads and 2) suggesting a new way for consumption of sulfur and waste plastics as major environmental pollutants. Our results showed that sulfur and waste plastics can improve the chemical and physical

properties of bitumen and the optimum conditions for preparation of modified bitumen are described in this work.

EXPERIMENTAL

Materials

Bitumen of 60/70 penetration grade was chosen as unmodified bitumen for all investigations. Elemental sulfur with purity of 99% was used in all experiments. All of the other compounds were purchased from Sigma-Aldrich Company.

Methods

Process for addition of plastic waste: 500 g of bitumen 60/70 was put in a metal container and heated at 190 °C for 30 min. After melting of bitumen, the obtained sample was homogenized with a stirrer for 10 min. Then we added the plastic waste at different ratios (1%; 2%; 3%; 4% and 5% w/w) and the speed of stirring was increased to 850 rpm for 20 min.

Process for addition of elemental sulfur: 500 g of bitumen 60/70 was put in a metal container and heated at 190 °C for 30 min. After melting of bitumen, the obtained sample was homogenized with a stirrer for 10 min. Then, we added the elemental sulfur at different ratios (0%; 20%; 25.0%; 30% and 40% w/w) and the speed of stirring was increased to 850 rpm for 20 min.

Softening point determination: For determination of softening point we used the standard test ASTM D36 for unmodified and modified bitumen.

* To whom all correspondence should be sent:
E-mail: masoudkandomal@gmail.com

Loss of weight test: For investigation of the loss of weight for bitumen, we used the standard test ASTM D6 and the results of this test were reported according to the weight ratio for total samples with the equation below:

$$\text{Loss of weight} = (W_a - W_b/W_a) \times 100 \quad (1)$$

where, W_a is the weight of sample before input of sample in an air furnace and W_b is the weight of sample after leaving the furnace.

Tensile test: For study of tensile factor we used the standard test ASTM D113 for unmodified and modified bitumen.

Penetration test: For study of penetration we used the standard test ASTM D5 for unmodified and modified bitumen.

RESULTS AND DISCUSSION

The effect of plastic waste and elemental sulfur on softening point

As we know, the softening point is a very important factor for bitumen. The softening point for unmodified bitumen is ~ 49 °C.

Figures 1 and 2 show the changes in softening point of bitumen after addition of plastic waste and elemental sulfur, respectively.

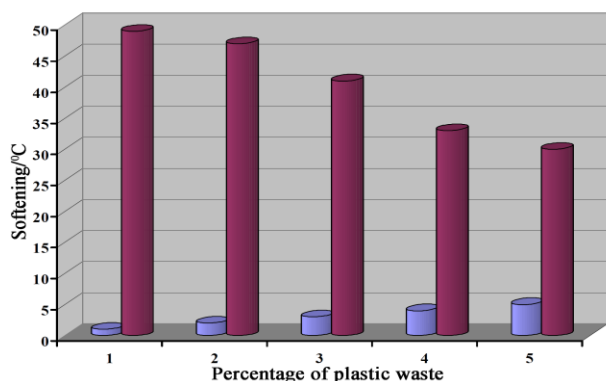


Figure 1. Softening point diagram of bitumen after addition of plastic waste.

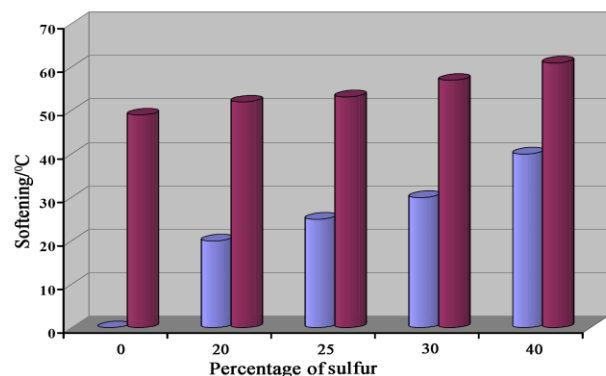


Figure 2. Softening point diagram of bitumen after addition of sulfur.

The obtained results confirmed that the conversion of unmodified bitumen to bitumen

modified with 3% of plastic waste improves the quality of bitumen, but after modification we found a high degree of softening of bitumen that is not a good condition for application of bitumen in industrial materials. The same results were observed after addition of elemental sulfur to bitumen. According to figure 2, we found the best modification of bitumen in the presence of 25-30% of elemental sulfur.

The effect of plastic waste and elemental sulfur on loss of weight

For investigation of the effect of plastic waste and elemental sulfur on the loss of weight, we checked the weight of bitumen in the presence of different percentages of plastic waste or elemental sulfur before and after input of bitumen in the furnace. As we know, the best condition is when the weight of bitumen is the same before and after input in furnace.

The same weight of bitumen before and after input of bitumen in the furnace confirmed the stability of additives in the modified bitumen. Tables 1 and 2 show the obtained results for the weight loss of bitumen after addition of plastic waste and elemental sulfur, respectively. The best conditions were obtained in the presence of 3% of plastic waste and 25-30% of elemental sulfur.

Table 1. The obtained data for addition of plastic waste on the loss of weight of bitumen

Percentage of waste plastic (w/w)	Weight (g) of bitumen before furnace	Weight (g) of bitumen after furnace
1	70	68.7±0.4
2	70	66.3±0.5
3	70	69.2±0.7
4	70	68.0±0.4

Table 2. The obtained data for addition of sulfur on the loss of weight of bitumen

Percentage of sulfur (w/w)	Weight (g) of bitumen before furnace	Weight (g) of bitumen after furnace
10	70	66.4±0.6
20	70	67.2±0.5
30	70	68.1±0.3
40	70	69.4±0.6

Tensile factor investigation

The tensile factor of bitumen after addition of plastic waste and of elemental sulfur is presented in figures 3 and 4. As can be seen the value of tensile

M. Ashjari, S. Masoud Kandomal: The effect of plastic waste and elemental sulfur additives on chemical and physical... factor in the presence of 3% of plastic waste and 25-30% of elemental sulfur showed the best stability and good responses. unmodified bitumen in the presence of 3% w/w of plastic waste and 25-30% w/w of elemental sulfur.

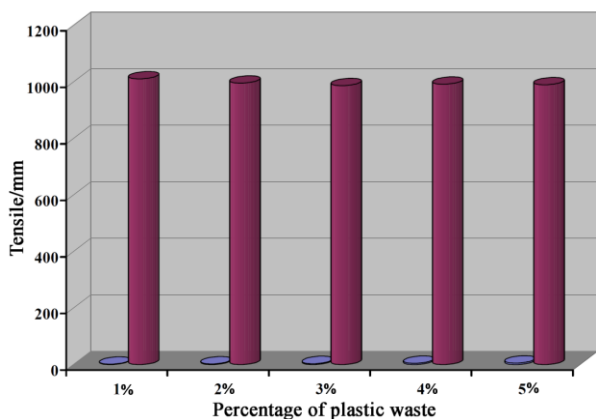


Figure 3. Tensile diagram of bitumen after addition of plastic waste.

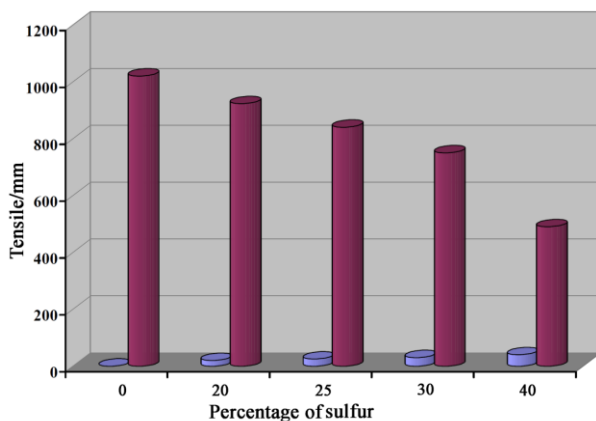


Figure 4. Tensile diagram of bitumen after addition of sulfur.

Penetration investigation

In the final step, we investigated the effect of the two additives on the penetration properties of bitumen. As we know, the addition of additives can reduce the penetration of bitumen due to binding of sulfur with bitumen functional groups. According to figures 5 and 6 we found the best penetration properties in the presence of 3% of plastic waste and 25-30% of elemental sulfur.

CONCLUSION

In this paper we describe a new strategy for application of two important environmental pollutants in industrial products. As we know, plastic waste and elemental sulfur are two major non-recyclable compounds. The present study describes the application of plastic waste and elemental sulfur for improving the quality of bitumen. We optimized the values of the two additives in the bitumen matrix and we found that bitumen showed the best properties compared to

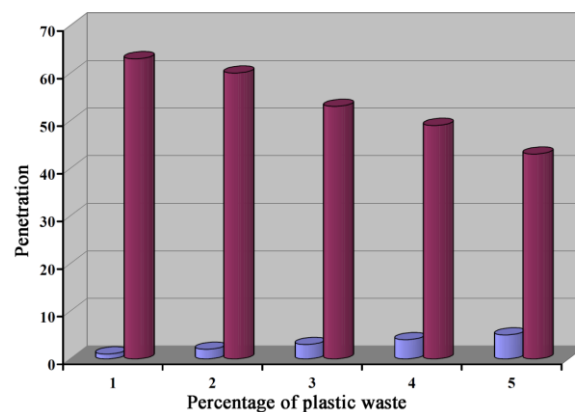


Figure 5. Penetration diagram of bitumen after addition of plastic waste.

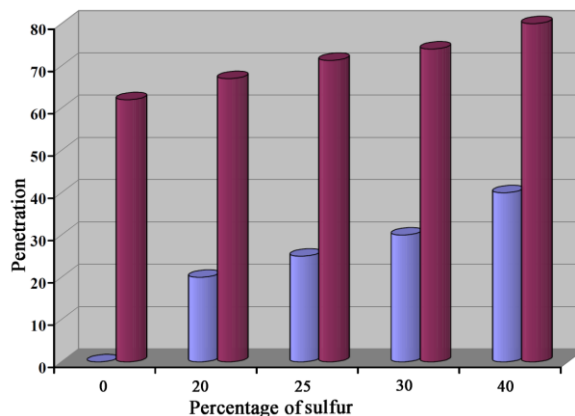


Figure 6. Penetration diagram of bitumen after addition of sulfur.

REFERENCES

1. J.R. Jambeck, R. Geyer, C. Wilcox, T.R. Siegler, M. Perryman, A. Andrady, R. Narayan, K. Lavender Law, *Science*, **347**, 768 (2015).
2. C.M. Rochman, M.A. Browne, B.S. Halpern, B.T. Hentschel, E. Hoh, H.K. Karapanagioti, L.M. Rios-Mendoza, H. Takada, S. The, R.C. Thompson, *Nature*, **494**, 169 (2013).
3. Y. Zheng, E.K. Yanful, A.S. Bassi, *Critical Reviews in Biotechnology*, **25**, 243 (2005).
4. E.A. Williams, P.T. Williams, *J. Analytical Appl. Pyrolysis*, **40-41**, 347 (1997).
5. N. Miskolczi, L. Bartha, G. Deák, B. Jöver, *Polymer Degrad. Stability*, **86**, 357 (2004).
6. D. D'Melo, S. Raju, S. Bhattacharya, S. Subramani, *Construction and Building Materials*, **126**, 976 (2016).
7. W.C. McBee, P.A. Romans, T.A. Sullivan, R.R. Uhde, Role of sulfur in SEA pavements, *Sulphur Res. Dev.*, **4**, 5 (1981).
8. J. Colange, D. Strickland, G. McCabe, K. Gilbert, R. May, S. Banbury, *Road Mater. Pavement*, **11**, 459 (2010).

Comparative removal of naphthalene by adsorption on different sand/bentonite mixtures

S. Rennane^{1*}, N. Bendjaballah-Lalaoui¹, M. Trari²

¹Laboratory of Catalytic Materials and Catalysis in Organic Chemistry, Faculty of Chemistry (USTHB) BP 32 El-Alia 16111, Algiers, Algeria

²Laboratory of Storage and Valorization of Renewable Energies, Faculty of Chemistry (USTHB), BP 32, 16111, Algiers, Algeria

Received June 26, 2018, Revised March 12, 2019

The purpose of this study was to advance the understanding of naphthalene (polycyclic aromatic hydrocarbon) adsorption on sand/bentonite mixtures in the context of their use in the lining of waste disposal facilities. Batch adsorption studies were carried out to estimate the adsorption capacities of sand/bentonite mixtures. Different percentages of the bentonite (0% to 12%) in sand/bentonite mixtures were tested. These mixtures were characterized by X-ray diffraction (XRD), scanning electron microscopy (SEM), and Fourier transform infrared spectroscopy (FTIR). It was found that the mixture with 2% of bentonite adsorbs the highest amount of naphthalene over the whole range of initial naphthalene concentrations studied (C_0 : 2.5–22 mg L⁻¹); this optimal fraction was therefore selected. The effect of the initial naphthalene concentration, percentage of the bentonite in the sand/bentonite mixture and temperature on the adsorption was investigated. The adsorption isotherms, established for every percentage of bentonite, revealed that the naphthalene adsorption follows a linear Freundlich isotherm for the optimal fraction of bentonite (2%). The kinetic study showed that the process obeys a pseudo-second-order equation model. The thermodynamic parameters (ΔG° , ΔH° , and ΔS°) indicated an endothermic and spontaneous nature of the naphthalene adsorption. The adsorption of naphthalene is more favorable at high temperatures and activation energy (8.263 kJ mol⁻¹) suggests a physical adsorption.

Keywords: Adsorption; Naphthalene; Bentonite; Sand/bentonite mixture.

INTRODUCTION

As the world population grows, the industrialization increases, thus generating more wastes and pollutants. Polycyclic aromatic hydrocarbons (PAHs), such as naphthalene, are among the most widespread organic pollutants and occur both naturally (in volcanic eruptions and forest fires) and by anthropogenic activities. Most PAHs emissions result from incomplete combustion of fossil fuels, and vehicle exhaust [1, 2]. The sources of naphthalene discarded in aquatic environment include industrial and domestic wastewaters, leakage of PAHs-containing materials, like petroleum fractions, creosote and pharmaceutical waste [3]. The US Environmental Protection Agency (U.S.E.P.A) has classified naphthalene as a hazardous pollutant for its carcinogenic and mutagenic effects for humans [4]. Hence, various methods for removing naphthalene from aqueous solutions including photocatalytic oxidation [5], biodegradation using surfactants [6], electron beam irradiation [7], ozonation [8], adsorption using zeolites [9] and activated carbon [10–12] have been reported. The adsorption process is known for its simplicity, low-cost and insensitivity to toxic substances [11]; it is also applied in active barriers in the soil remediation.

The most common forms of groundwater remediation are physical containment and pump-and-treat methods and both methods are expensive [13]. The natural materials widely used in liner applications are clays and sand/bentonite mixtures. Soil liners are preferred because of their low cost, large leachate attenuation capacity and resistance to damage and perforations [15]. The use of clays as liner materials has been applied over the last few decades [16, 17]. Recently Lamichhane *et al.* [18] published a review gathering several adsorbents such as modified clay minerals used to remove PAHs from aqueous solutions and documented in ~ 150 papers.

Bentonite (mainly montmorillonite) is the most preferable clay mineral for barrier applications due to its high surface area, cation-exchange capacity, large swelling potential, and low hydraulic conductivity to water [19]. Bentonite is 2:1 mineral with one alumina octahedral sheet and two silica sheets, which form layers held together by Van der Waals forces [20]. Most studies have shown that natural or modified bentonite is an effective adsorbent for heavy metals [21, 22] and toxic compounds such as phenol and related compounds [23, 24], as well as naphthalene [25, 26].

* To whom all correspondence should be sent:
E-mail: samira_rennane@yahoo.fr

Sand/bentonite mixtures represent efficient barriers for removing contaminants. It is possible to vary their proportions in order to combine the advantages of both materials: the waterproofing capacity of bentonite associated with the relatively high shear strength typical of sand [27].

Kenney *et al.* [28] proposed the sand/bentonite mixture as an alternative material to the clay liners. Staninska *et al.* [29] have studied the sorption of phenanthrene onto sand/bentonite mixtures. The amount of bentonite is varied in the range (1.25%–5%). The authors have demonstrated that the increase in sorption efficiency is less pronounced at high bentonite percentages. Also, the compacted bentonite (3%) could achieve a hydraulic conductivity of $10^{-7} \text{ cm s}^{-1}$ which is a regular recommended value for the construction of hydraulic barriers [19]. Large clay deposits exist in the Northwest of Algeria (Mostaganem and Maghnia) with significant recoverable reserves of bentonite. The choice of the bentonite percentage range (0–12%) is based on previous works [30] since lower percentages do not have real applications in the construction of barriers.

The effects of bentonite fractions and initial concentration of naphthalene on the adsorption were analyzed to optimize the percentage of bentonite which better removes naphthalene. The Langmuir and Freundlich isotherms, kinetic models (pseudo-first-order, pseudo-second-order, Elovich and intraparticle diffusion models) were adopted to investigate the mechanism of naphthalene adsorption on the mixture sand/bentonite (2%); the thermodynamic parameters were also calculated.

MATERIALS AND METHODS

Preparation of naphthalene solution

Due to the low water solubility (26.54 mg L^{-1} at $20 \pm 2^\circ\text{C}$) of naphthalene (Sigma Aldrich, USA, 99% purity), a water-methanol (Sigma Aldrich, 99.7% purity) solution was used. Methanol is a good solvent to enhance the adsorption of non-polar compounds, such as naphthalene. A stock solution (30 mg L^{-1}) was prepared by dissolving 30 mg of naphthalene in 20 mL of methanol, diluted to 1 L with distilled water and stored in airtight glass bottles in the dark at room temperature. The various solutions of naphthalene ($2.5\text{--}22 \text{ mg L}^{-1}$) were prepared by diluting the stock solution with water-methanol solution (2% vol. methanol). Low amounts of methanol (up to 5% vol.) do not modify the sorption properties of both naphthalene and phenanthrene [31].

Preparation of the adsorbent

The adsorbent used in this study was the mixture sand/bentonite. Sand comes from a petroleum region (Hassi Messaoud, Southern Algeria) (Table 1); while bentonite comes from Western Algeria (Maghnia). It is natural clay marketed by the National Company of Non-Ferrous Mineral Products BENTAL Factory, located in Maghnia (Table 2). The sand was previously washed to eliminate all impurities, and then dried at 105°C for 24 h.

The bentonite was dried at 50°C for 48 h and used at ratios of 0%, 2%, 6%, 8% and 12%.

Experimental characterization techniques

The sand/bentonite mixtures were characterized by various techniques. X-ray diffraction (XRD) was performed to confirm the phases obtained after mixing. A PANalytical diffractometer equipped with a Cu anticathode ($\lambda \text{ K}\alpha = 1.541874 \text{ \AA}$) at a working voltage of 40 kV and a current intensity of 30 mA was used. The interaction between sand and bentonite was investigated by scanning electron microscope (SEM) using the JEOL JSM 6830 system equipped with an energy-dispersive spectrometer (EDS). The FTIR spectra of sand/bentonite mixtures were determined on a JASCO FT/IR-4600 model. All standards and various sand/bentonite mixture samples were prepared using KBr technique.

Batch sorption experiments

Batch experiments were carried out in 250 mL Erlenmeyer flasks, 1 g of adsorbent (sand/bentonite mixture) was immersed in 100 mL of naphthalene solutions ($2.5\text{--}22 \text{ mg L}^{-1}$). The flasks were shaken at 500 rpm, allowing sufficient time (30 min) for the adsorption equilibrium. The effect of temperature was studied at 10, 20 and 30°C at natural pH. The residual naphthalene concentration was determined by UV-visible spectrophotometry (Shimadzu, UV 1800) at the maximum wavelength ($\lambda_{\text{max}} = 277 \text{ nm}$). The amount of adsorbed naphthalene q_t (mg g^{-1}) at a given time t , was calculated as follows:

$$q_t = \frac{(C_0 - C_t)}{W} V \quad (1)$$

where C_0 and C_t are the initial and residual concentrations of naphthalene (mg L^{-1}) in solution, respectively; V the volume of solution (L) and W the mass of dry adsorbent (g).

RESULTS AND DISCUSSION

Characterization of the adsorbent

The properties of sand and bentonite are reported in Tables 1 and 2. The results show that the Hassi Messaoud sand contains a low percentage of organic carbon and a high percentage of sand, indicating that it is very clean and hence can be used as reference (Table 1).

Table 1. Hassi Messaoud sand properties.

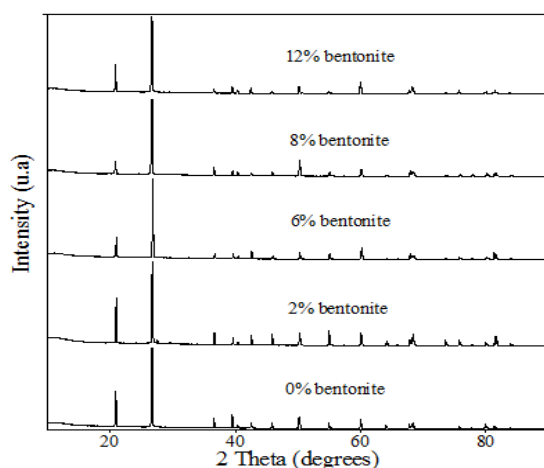
Particles <80 μm (%)	Sand particles (1–0.2 mm) (%)	Sand particles (0.2–0.8 mm) (%)	Specific density (g L^{-1})	Total organic C (%)	Equivalent of sand (%)	pH
1.72	94	4.28	2640	0.014	93	7.64

Table 2. Maghnia bentonite properties [30].

Parti- cles <80 μm (%)	Parti- cles <2 μm (%)	Speci- fic area (m^2g^{-1})	Water content (%)	pH	SiO ₂ (%)	Al ₂ O ₃ (%)	CaO (%)	Na ₂ O (%)	Fe ₂ O ₃ (%)	K ₂ O (%)	TiO ₂ (%)	MgO (%)
100	42.5	394	8.5	10.5	64.98	16.08	0.61	3.88	2.93	2.02	0.20	3.51

XRD results

As expected, the powder XRD patterns of the sand/bentonite mixtures (Fig. 1) show the presence of silica SiO₂ as the main phase of the sand and alumina Al₂O₃ as a minor phase coming from the bentonite present at low percentages (< 12%). All peaks are indexed according to the JCPDS Cards N° 46-1045 and N° 17-3014. Such result agrees with the nominal composition of the system sand/bentonite.

**Fig. 1.** XRD diffraction pattern of the various sand/bentonite mixtures.

SEM/EDS results

Firstly, we noted that the grain sizes of the sand in the range (50–200 μm) are not homogeneous (Fig. 2a) and the bentonite content increases in the mechanical mixture (sand/bentonite). The sand

The SiO₂/Al₂O₃ ratio is 4.04 and the percentage of sodium is higher than that of calcium. It reveals that Maghnia bentonite is sodic montmorillonite [32]. The high value of the specific surface area of Maghnia bentonite (Table 2) indicates that the naphthalene adsorption on sand/bentonite mixtures is mainly controlled by bentonite. Details concerning the characteristics of bentonite were reported by Debieche and Kaoua [30].

grains are covered with the bentonite whose size averages 1 μm . However, a part of the bentonite with a large diameter ($\sim 50 \mu\text{m}$) is also present in the intergranular space of the sand (Fig. 2b, c). The bentonite located both on the sand grains and in the interstitial space is identified *via* EDS analysis (Fig. 3 and Table 3).

In summary, the structural analysis reveals a large covering of sand grains with a high percentage of bentonite. This could lead to a decrease in the adsorption efficiency due to the agglomeration of bentonite grains, thus reducing the accessibility to the adsorption sites.

FTIR results

The spectral analysis for the sand/bentonite mixtures (0%, 2%, 6%, and 12%), illustrated in Figure 4 and Table 4, permits to distinguish three main regions: the elongation bands of OH groups of water are visible in the region (3800–3300 cm^{-1}) while the deformation bands related to O-H elongation of water absorbed onto the bentonite are in the region (1730–1340 cm^{-1}). However, the intensity of bands is very low due to negligible absorption of humidity by the various sand/bentonite mixtures, attributed to the high content of sand in these mixtures.

The region (1340–840 cm^{-1}) corresponds to the Si-O valence vibration in a tetrahedral site while the region (840–610 cm^{-1}) is assigned to the deformation vibration of Al-OH bond groups. The bands (610–400 cm^{-1}) are attributed to the angular deformation of the Si-O-Al unit.

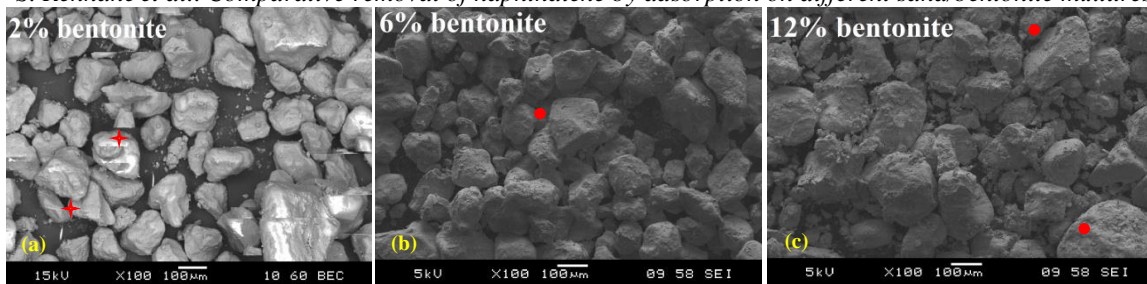


Fig. 2. SEM micrographs showing the dispersion of the bentonite in the mixture sand/bentonite.

✦ Bentonite aggregate ● Upholstering sand grains by bentonite

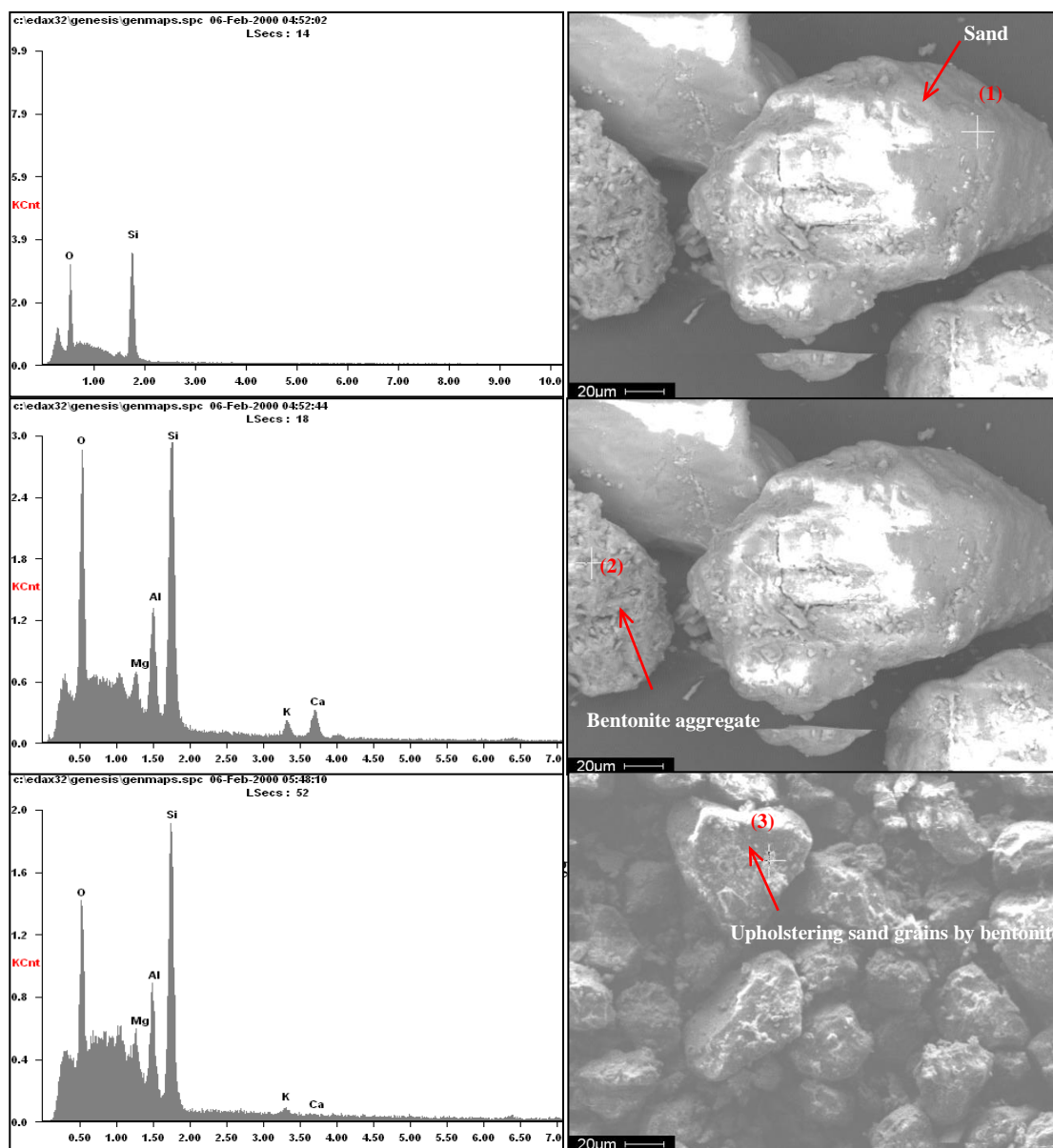


Fig. 3. EDS results and SEM micrographs for sand and bentonite.

Table 3. EDS analysis results obtained for the three positions depicted in Figure 3.

Zone	Wt.%					
	O	Mg	Al	Si	K	Ca
1	59.44	-	-	40.56	-	-
2	54.36	01.82	08.45	29.14	02.07	4.16
3	44.54	08.95	12.78	32.48	00.99	00.26

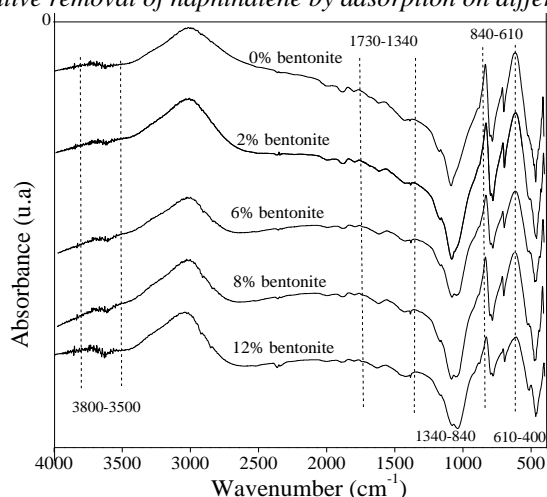


Fig. 4. FTIR spectra of the sand/bentonite mixtures.

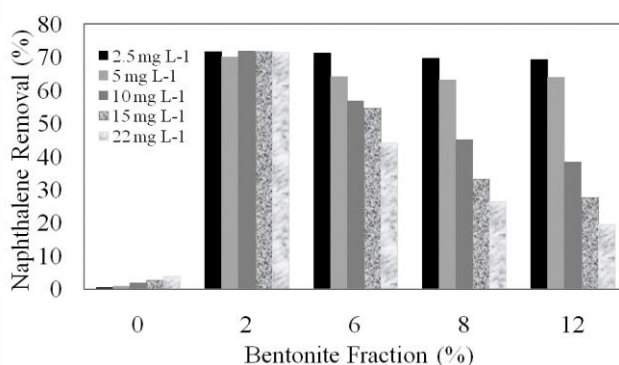


Fig. 5. Optimal fraction of bentonite at different initial concentrations of naphthalene.

Table 4. FTIR analysis results obtained for the various sand/bentonite mixtures.

Frequency	OH	Si-O-Si	Al-OH	Si-O-Al
Sand	3625/1617-1420	1082	782-690	458
2%	3627/1612-1425	1081	775-687	452
6%	3631/1622-1427	1078	777-692	461
8%	3630/1613-1429	1080	778-694	460
12%	3650/1630-1425	1073	780-696	463

Optimal fraction of bentonite

To evaluate the optimal fraction of the bentonite (0%, 2%, 6%, 8% and 12%) in the sand, experiments were carried out under the above conditions. The adsorption efficiency of naphthalene (E) on the sand/bentonite mixtures was calculated as follows:

$$E = \frac{C_0 - C_e}{C_0} \times 100 \quad (2)$$

where: C_0 (mg L^{-1}) and C_e (mg L^{-1}) are the initial and equilibrium liquid-phase concentrations of naphthalene, respectively.

Figure 5 shows that the naphthalene removal efficiency on pure sand (0% of bentonite) is negligible (maximum value 3.84%). The optimal naphthalene adsorption (71%) is obtained at low initial naphthalene concentration C_0 (2.5 mg L^{-1})

for all bentonite percentages. This result can be attributed to the mobility of the reaction medium, which is amplified at low concentrations, thereby promoting the adsorption. At 2% bentonite, the optimum adsorption efficiency is conserved independently of the concentration C_0 . This is due to the good dispersion of the bentonite particles on the external sand surface, allowing a great accessibility to active sites. By contrast, at 6%, 8% and 12% of bentonite, the adsorption efficiency decreases with increasing the concentrations C_0 . This is due to the increase in resistance to the transfer of solute molecules from the solution toward the external surface of the adsorbent, generated by the large concentrations of naphthalene C_0 . On the other hand, the reduction of active sites is caused by the agglomeration of bentonite particles related to the texture of the

latter. Ge *et al.* [33] have studied the adsorption of naphthalene on activated carbon modified with nitric acid using microwave radiation and obtained a removal efficiency of 92% while Agarry *et al.* [3] found that the removal efficiency of naphthalene onto spent tea leaves reached 96%.

Effect of initial concentration and percentage of bentonite on the sand/bentonite mixtures

The initial concentration of the adsorbate C_0 is an important factor which significantly affects the adsorption. The adsorbed amount of naphthalene onto the sand/bentonite mixtures at different concentrations C_0 (2–22 mg L⁻¹) is shown in Figure 6. The sorption is rapid in the initial stage and gradually decreases with the progress of sorption until equilibrium is reached. At 2% and 6% of bentonite, the equilibrium is very fast (6 min) for concentrations above 10 mg L⁻¹, while above and below this concentration, the equilibrium time lies between 12 and 20 min. At 8 and 12% of bentonite, the equilibrium is rapidly reached (3 to 6 min) over the whole concentrations range. The longer

equilibrium time obtained with 2% bentonite (optimal fraction) revealed that the adsorption process is long due to the probable existence of an intraparticle transfer of naphthalene molecules. This result will be verified subsequently in the kinetic study of the adsorption process.

The adsorbed amount of naphthalene on the sand/bentonite mixtures increases with increasing the concentration C_0 (Fig. 6) and decreases with the bentonite percentage. The maximum adsorbed amounts of naphthalene, at C_0 of 22 mg L⁻¹, are 1.57, 0.97, 0.58, and 0.43 mg g⁻¹ for bentonite percentages of 2%, 6%, 8% and 12%, respectively.

The positive effect of the concentration C_0 on the adsorbed amount by using other adsorbents has been reported in the literature. Agarry *et al.* [3] indicated an increase in the naphthalene adsorption onto spent tea leaves with raising the initial concentrations while Sener and Ozyilmaz [34] found the same trend for the adsorption of naphthalene on sonicated talc.

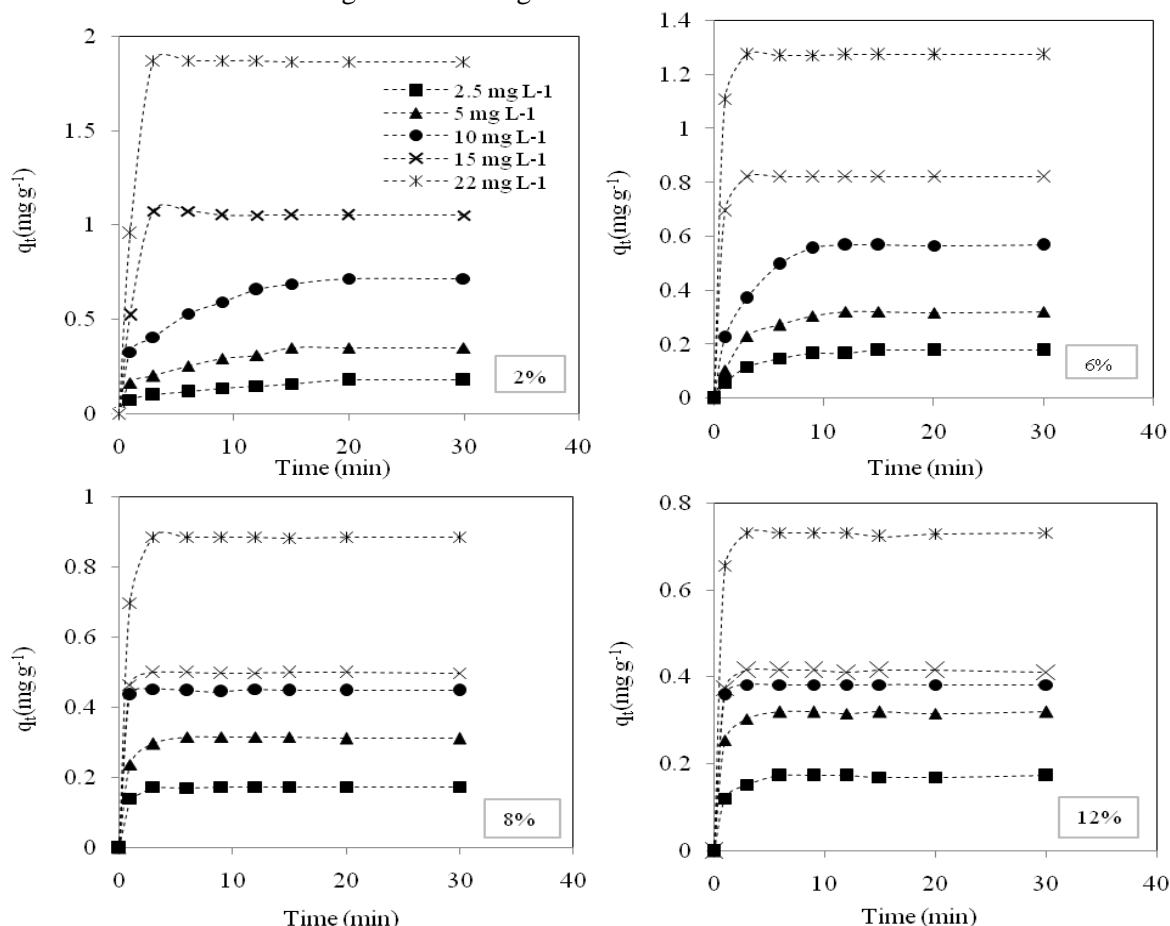


Fig. 6. Effect of the initial concentration on naphthalene adsorption onto sand/bentonite mixtures.

Table 5. Isotherm model parameters for adsorption of naphthalene onto sand/bentonite mixtures.

Model isotherm	Bentonite percentages onto sand/bentonite mixtures				
	0%	2 %	6%	8%	12%
<i>Langmuir</i>					
$q_m(\text{mg g}^{-1})$	-5.7×10^{-3}	38.462	1.164	0.628	0.482
$b (\text{L mg}^{-1})$	-0.067	6.5×10^{-3}	0.245	0.510	0.766
R^2	0.970	0.998	0.989	0.996	0.970
ERRSQ	0.117	5.52×10^{-3}	2.09×10^{-2}	1.60×10^{-3}	2.37×10^{-3}
<i>Freundlich</i>					
$1/n$	2.050	1.009	0.623	0.376	0.266
$K_F(\text{mg g}^{-1}/(\text{mg L}^{-1})^{1/n})$	1.64×10^{-4}	0.247	0.224	0.218	0.223
R^2	0.998	0.998	0.989	0.949	0.844
ERRSQ	2.98×10^{-6}	8.54×10^{-4}	1.56×10^{-2}	5.33×10^{-3}	7.17×10^{-3}

Adsorption isotherms

The adsorption isotherms were obtained by considering the same conditions as above. The concentration C_o was in the range of (2.5–22 mg L⁻¹) while the bentonite ratios in the sand/bentonite mixtures were 2%, 6%, 8% and 12%. The adsorbed amount at equilibrium q_e (mg g⁻¹) was calculated from the following equation:

$$q_e = \frac{(C_o - C_e)V}{W} \quad (3)$$

where: C_e is the equilibrium concentration of naphthalene (mg L⁻¹).

The isotherm results were analyzed using the Langmuir and Freundlich models [35, 36] mathematically expressed as:

$$q_e = \frac{q_m b C_e}{(1 + b C_e)} \quad (4)$$

$$q_e = K_F C_e^{1/n} \quad (5)$$

The Langmuir constants $q_m(\text{mg g}^{-1})$ and $b (\text{L mg}^{-1})$, are the maximum amount of adsorbed naphthalene and the sorption equilibrium constant, respectively. $K_F(\text{mg g}^{-1}/(\text{mg L}^{-1})^{1/n})$ and n are the constants of Freundlich related to the adsorption capacity and adsorption intensity, respectively. The linearized forms of both equations are:

$$\frac{1}{q_e} = \frac{1}{q_m b C_e} + \frac{1}{q_m} \quad (6)$$

$$\ln(q_e) = \ln(K_F) + \left(\frac{1}{n}\right) \ln(C_e) \quad (7)$$

The correlation coefficient (R^2) and the sum of square errors (ERRSQ) were used for testing the isotherm models. ERRSQ is represented by the following equation [37]:

$$\text{ERRSQ} = \sum_{i=1}^P (q_{(e,m)} - q_{(e,meas)})_i^2 \quad (8)$$

where: P is the number of experimental data points, $q_{e,m}$ and $q_{e,meas}$ the equilibrium amounts of adsorption obtained from isotherm model and experiments data, respectively.

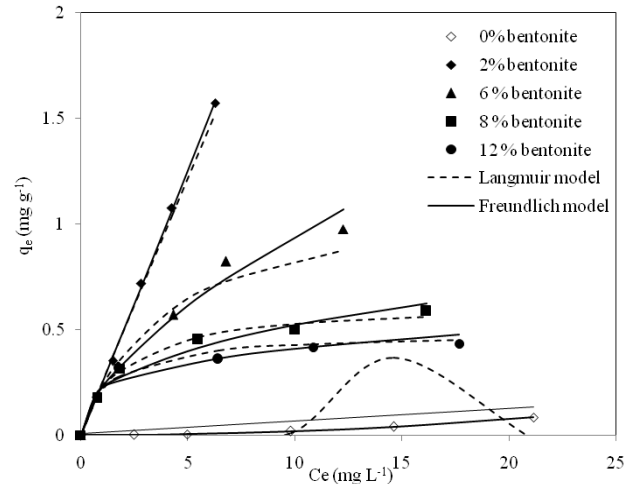


Fig. 7. Adsorption isotherms of naphthalene onto sand/bentonite mixtures.

The Langmuir and Freundlich coefficients are summarized in Table 5. The obtained isotherms at different percentages of bentonite in the sand/bentonite mixtures are illustrated in Fig. 7. According to R^2 and ERRSQ values (Table 5), it appears that the most appropriate isotherm depends on the bentonite ratio. For the pure sand, $1/n > 1$ indicates an unfavorable adsorption. The aberrant values of the Langmuir parameters ($q_m = -5.7 \times 10^{-3} \text{ mg g}^{-1}$ and $b = -0.067 \text{ L mg}^{-1}$) clearly show that these data cannot be described by the Langmuir equation.

As illustrated in Fig. 7 and Table 5, the addition of 2% of bentonite (optimal fraction) in the sand/bentonite mixture greatly increases the

naphthalene adsorption. Both the Freundlich and Langmuir models show high coefficients R^2 . The lower ERRSQ value obtained by the Freundlich model (linear isotherm $n \approx 1$), reveals a slight predominance of this model with a distribution coefficient (K_d). The results obtained for 6% of bentonite (Table 5), indicate that the adsorption data fit well the Freundlich model. For 2% and 6% bentonite, the distribution coefficients practically indicate that the adsorption phenomenon is governed by the adsorption intensity. The maximum amounts of adsorbed naphthalene obtained from Eq. 7 are 1.58 mg g^{-1} (2% bentonite) and 1.07 mg g^{-1} (6%).

The Langmuir monolayer model (Fig. 7) appears to be the most appropriate for the highest percentages of bentonite (8% to 12%). This is due to the rapid formation of the boundary layer which stops the transfer of adsorbate molecules to the solid surface and consequently prevents multilayer formation (characteristic of Freundlich model). Table 5 shows that the maximum amount of naphthalene decreases with increasing the percentage of bentonite (0.628 mg g^{-1} for 8% and 0.428 mg g^{-1} for 12%). Several works on the naphthalene adsorption onto different clays and adsorbents, involved linear and non-linear models such as: linear model [38–40], Freundlich model [21, 34, 41] and Langmuir model [42, 43].

Adsorption kinetics

The adsorption kinetics is useful for elucidating the adsorption mechanism. In this study, four kinetic models, including pseudo-first order, pseudo-second order, Elovich and intraparticle diffusion were used to investigate the adsorption of naphthalene on sand/bentonite mixture.

The pseudo-first-order equation is given by Lagergren [44]:

$$\ln(q_e - q_t) = \ln(q_e) - k_1 t \quad (9)$$

where q_e and q_t (mg g^{-1}) are the amounts of naphthalene adsorbed onto the mixture sand/bentonite at equilibrium and at time t , respectively and k_1 the rate constant (min^{-1}).

The pseudo-second-order model is expressed by the following equation [45]:

$$\frac{t}{q_t} = \frac{1}{k_2 q_e^2} + \frac{1}{q_e} t \quad (10)$$

where k_2 is the rate constant ($\text{g mg}^{-1} \text{min}^{-1}$).

The Elovich equation is generally expressed as follows [46, 47]:

$$\frac{dq_t}{dt} = \alpha \exp(-\beta q_t) \quad (11)$$

To simplify the Elovich equation, Chien and Clayton [48] assumed $\alpha \beta t \gg 1$. By applying the boundary conditions ($q_t = 0$ at $t = 0$ and $q_t = q_t$ at $t = t$), equation (11) becomes [49]:

$$q_t = \frac{1}{\beta} \ln(\alpha \beta) + \frac{1}{\beta} \ln(t) \quad (12)$$

where α is the initial adsorption rate ($\text{mg g}^{-1} \text{min}^{-1}$) and β the desorption constant (g mg^{-1}) for the Elovich model.

The straight-lines $\ln(q_e - q_t)$ vs. t for the pseudo-first-order model, t/q_t vs. t for the pseudo-second-order model, and the plots q_t vs. $\ln(t)$ for the Elovich model were plotted to obtain the kinetic parameters of the naphthalene adsorption onto sand/bentonite mixtures.

According to the high R^2 values [0.977–1] (Table 6), the kinetics of naphthalene adsorption onto the sand/bentonite mixtures are well described by the pseudo-second-order model. Similar results of the retention of naphthalene have been reported using other adsorbents, namely the bentonite clay mineral [26], organo-sepiolite [50], natural and chemically modified bentonite [51] and activated carbons modified by microwave [12].

To determine the diffusibility of naphthalene molecules into the adsorbent pores, the Weber-Morris intraparticle diffusion model was used (Eq. 13) [52]:

$$q_t = k_p t^{1/2} + C \quad (13)$$

where k_p is the intraparticle diffusion rate ($\text{mg g min}^{-1/2}$) and C the intercept (mg g^{-1}) which is proportional to the boundary layer thickness. The intraparticle diffusion is the rate-controlling step if the plot of q_t versus $t^{1/2}$ gives a straight line passing by the origin. However, if the plot deviates from linearity, then the boundary layer diffusion (film diffusion) controls the sorption process.

The intraparticle diffusion plot for the naphthalene adsorption onto sand/bentonite mixtures at different initial concentrations (Fig. 8a, b) can be divided into different stages. The first linear stage is attributed to the values of K_p and C are calculated from the slope and intercept of plots (q_t versus $t^{1/2}$) of the second linear stage (Table 6). Transfer of naphthalene molecules from the solution toward the external surface of adsorbent; the second portion is the gradual adsorption stage, where the intraparticle diffusion is the rate controlling step. The third stage is attributed to the establishment of adsorption equilibrium.

Table 6. Kinetic model parameters for the adsorption of naphthalene onto sand/bentonite mixtures.

Kinetic model	2.5 mg L ⁻¹		5 mg L ⁻¹			10 mg L ⁻¹
	2%	2%	6%	8%	12%	2%
<i>Pseudo-first-order</i>						
$k_1(\text{min}^{-1})$	0.125	0.165	0.328	0.908	0.976	0.195
$q_e(\text{mg g}^{-1})$	0.136	0.267	0.297	0.261	0.248	0.594
R^2	0.957	0.956	0.986	0.967	0.952	0.981
<i>Pseudo-second-order</i>						
$k_2(\text{gmg}^{-1}\text{min}^{-1})$	1.705	1.094	1.066	6.973	9.443	0.516
$q_e(\text{mg g}^{-1})$	0.194	0.384	0.387	0.338	0.336	0.792
R^2	0.977	0.979	0.996	1	1	0.993
<i>Elovich</i>						
$\alpha(\text{mg g}^{-1}\text{min}^{-1})$	0.251	0.601	0.331	9.115	46.638	1.187
$\beta(\text{gmg}^{-1})$	30.303	14.925	11.628	22.222	27.777	7.246
R^2	0.953	0.945	0.978	0.973	0.972	0.972
<i>Intraparticle diffusion</i>						
$k_p(\text{mg g}^{-1}\text{min}^{-1/2})$	0.029	0.064	0.053	0.054	0.044	0.130
$C(\text{mg g}^{-1})$	0.047	0.095	0.141	0.189	0.216	0.196
R^2	0.996	0.991	0.988	0.919	0.917	0.992

The values of K_p and C are calculated from the slope and intercept of plots (q_t versus $t^{1/2}$) of the second linear stage (Table 6). The values of C ($\neq 0$) can be attributed to the difference in the mass transfer rate between the initial and final stages of adsorption [53], demonstrating that the intraparticle diffusion is not the only rate-controlling step during the naphthalene adsorption; this result was supported by several authors [12, 41].

The time elapsed during the intraparticle diffusion decreases with increasing the bentonite amount (Fig. 8a). It is evaluated at 14 min for 2% and 9 min for 6% and decreases for 12% bentonite. These results indicate that the time required for intraparticle diffusion is large compared with the global time.

The obtained values of K_p increase in the following order: k_p (12%) < K_p (8%) < K_p (6%) < K_p (2%) for the effect of bentonite percentage (Table 6) and in the order of: K_p (2.5 mg L⁻¹) < K_p (5 mg L⁻¹) < K_p (10 mg L⁻¹) for the effect of naphthalene concentration C_0 . On the other hand, the intercept increases with both the percentage of bentonite and naphthalene concentration C_0 . The lowest values are obtained for 2% bentonite (optimal fraction) and low initial concentration of naphthalene (2.5 mg L⁻¹), indicating a small film resistance to the mass transfer surrounding the adsorbent particle. The R^2 values indicate that the intraparticle diffusion model is more suitable for the low bentonite percentages (R^2 (2%) = 0.999 and R^2 (6%) = 0.988) in comparison with other percentages (R^2 (8%) = 0.91 and R^2 (12%) = 0.91).

Effect of temperature and thermodynamic study

The effect of temperature on the naphthalene adsorption onto the sand/bentonite mixture at optimal fraction (2% of bentonite) was investigated at 10, 20 and 30 °C (Table 7). The thermodynamic parameters for the adsorption process; free energy change (ΔG°), enthalpy change (ΔH°), and entropy change (ΔS°), were calculated using the following equations:

$$\Delta G^\circ = -RT \ln K_d \quad (14)$$

$$\ln K_d = \frac{\Delta S^\circ}{R} - \frac{\Delta H^\circ}{RT} \quad (15)$$

K_d , R , and T are: the distribution coefficient of the adsorbate (q_e/C_e), the universal gas constant (8.314 J K⁻¹mol⁻¹) and the absolute temperature (K), respectively.

Table 7 shows that the amount of adsorbed naphthalene increases with increasing temperature. The ΔH° and ΔS° values were computed from the slope and intercept of the plot $\ln K_d$ versus $1/T$, while ΔG° was calculated at different temperatures and is shown in Table 7. The positive values of ΔH° and ΔS° suggest an endothermic reaction and increase in randomness at the solid-liquid interface during the adsorption. The negative value of ΔG° indicates a spontaneous nature of adsorption process. The decrease in ΔG° with increasing temperature (-28.72 to -30.751 kJ mol⁻¹) indicates that the adsorption of naphthalene on the sand/bentonite mixture is more favorable at higher temperature (30 °C).

The activation energy (E_a , kJ mol⁻¹) of adsorption is determined from the Arrhenius law in the studied temperature range:

$$\ln k_2 = \ln A - \frac{E_a}{RT} \quad (16)$$

where A is the pre-exponential factor, and k_2 the value of the pseudo-second-order. The activation energy (E_a) is deduced from the straight line $\ln k_2$

against reciprocal temperature (Table 7). The low energy E_a is in the range (5-40 kJ mol⁻¹), indicating that naphthalene is physisorbed [54]. Therefore, the affinity of bentonite for naphthalene molecules may be ascribed to Van der Waals forces and electrostatic attractions with the clay surface.

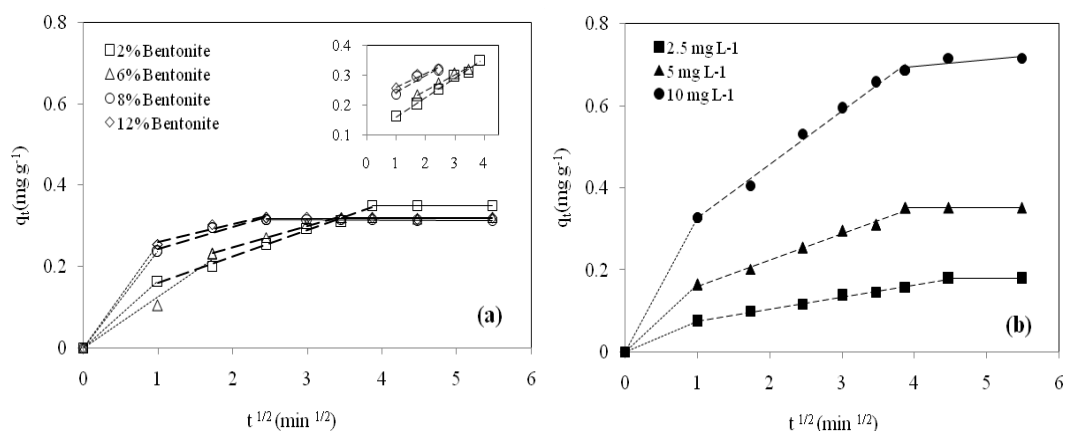


Fig. 8. Intraparticle diffusion plots for naphthalene adsorption: (a) at different bentonite ratios, (b) at different initial concentrations.

Table 7. Thermodynamic parameters for adsorption of naphthalene onto the sand/bentonite mixture.

T (°C)	q _e (mg g ⁻¹)	K _d (L g ⁻¹)	k ₂ (gmg ⁻¹ min ⁻¹)	ΔH° (kJ mol ⁻¹)	ΔS° (J K ⁻¹ mol ⁻¹)	ΔG° (kJ mol ⁻¹)	E _a (kJ mol ⁻¹)
10	0.272	0.165	0.930	-	-	-28.720	-
20	0.350	0.247	1.094	32.95	101.597	-29.735	8.263
30	0.447	0.482	1.171	-	-	-30.751	-

CONCLUSION

Based on detailed studies carried on the naphthalene adsorption at different initial concentrations and on different sand/bentonite mixtures, it was found that the adsorbed amount of naphthalene increased with increasing the initial concentration and decreasing the bentonite percentage. The maximum yield of adsorption (71%) was found by adding 2% of bentonite to the sand/bentonite mixture. This result was consolidated by SEM analysis that showed the remarkable effect of the very low bentonite content on the sand structure. The isotherm model describing the naphthalene adsorption on bentonite mixtures was presented.

The optimal ratio of bentonite (2%) was well fitted by the Freundlich model with a constant K_d of 0.247 L g⁻¹. The kinetic data were well represented by the pseudo-second-order model. The intraparticle diffusion plays an important role, but cannot be considered as the sole limiting step during the adsorption process. The thermodynamic parameters indicated a spontaneous and endothermic nature of the naphthalene adsorption. The low activation energy E_a is characteristic of a

physical adsorption of naphthalene. All these results show that the sand/bentonite mixture can be a promising adsorbent for the removal of naphthalene from wastewaters.

REFERENCES

1. C. J. Halsall, P. J. Coleman, B. J. Davis, V. Burnett, K. S. Waterhouse, P. Harding-Jones, K. C. Jones, *Environ. Sci. Technol.* **28**, 2380 (1994).
2. S. M. Bamforth, I. Singleton, *Chem. Technol. Biotechnol.*, **80**, 723 (2005).
3. S. E. Agarry, O. O. Ogunleye, O. A. Aworanti, *Environ. Technol.*, **34**, 825 (2013).
4. U.S. Environmental Protection Agency, Health effects assessment for naphthalene, EPA/540/1D86/014. Cincinnati, OH: Environmental Criteria and Assessment Office, Office of Health and Environmental Assessment, Office of Research and Development, 1986.
5. T. Ohno, K. Tokieda, S. Higashida, M. Matsumura, *Appl. Catal. A. General*, **244**, 383 (2003).
6. Z. Liu, A. M. Jacobson, R. G. Luthy, *Appl. Environ. Microbiol.*, **61**, 145 (1995).
7. W. J. Cooper, M. G. Nickelsen, R. V. Green, S. P. Mezyk, *Rad. Phys. Chem.*, **65**, 571 (2002).
8. B. Legube, S. Guyon, H. Sugimitsu, M. Dore, Ozonation of naphthalene in aqueous solution-I:

- ozone consumption and ozonation products, *Water Res.*, **20**, 197 (1986).
9. C. F. Chang, C.Y. Chang, K. H. Chen, W.T. Tsai, J. L. Shie, H. Chen, *J. Colloid Interface Sci.*, **277**, 29 (2004).
 10. C. O. Ania, B. Cabal, C. Pevida, A. Arenillas, J. B. Parra, F. Rubiera, J. J. Pis, *Water Res.*, **41**, 333 (2007).
 11. X. Y. Ge, F. Tian, Z. L.Wu, Y. J. Yan, G. Cravotto, Z. S. Wu, *Chem. Eng. Process.*, **91**, 67 (2015).
 12. D. Liu, Z. S. Wu, X.Y. Ge, G. Cravotto, Z. Wu, Y. Yan, *J Taiwan Inst. Chem. Eng.*, **59**, 563 (2016).
 13. C. Valderrama, X. Gamisans, X. de las Heras, A. Farran, J. L Cortina, *J. Hazard. Mater.*, **157**, 386 (2008).
 14. S.A.S. Mohammed, M. Naik, *Int. J. Ecol. Dev.*, **19**, 15 (2011).
 15. D. E. Daniel, *J. Geotech. Eng.*, **110**, 285 (1984).
 16. K. S. King, R. M. Quigley, F. Fernandez, D. W. Reades, A. Bacopoulos, *Canad. Geotech. J.*, **30**, 124 (1993).
 17. J. H. Kleppe, R. E. Olson, *Hydraulic Barriers in Soil and Rock ASTM STP*, **874**, 263 (1985).
 18. S. Lamichhane, K.C. Bal Krishna, R. Sarukkalgige, *Chemosphere*, **148**, 336 (2016).
 19. T. Chalermyanont, S. Arrykul, *J. Sci. Technol.*, **27**, 313 (2005).
 20. J. K. Mitchell, *Fundamentals of Soil Behaviour*, second edn., John Wiley, New York, 1993.
 21. A. Kapoor, T. Viraraghavan, *J. Environ. Eng.*, **124**, 1020 (1998).
 22. F. Barbier, G. Duc, M. Petit-Ramel, *Colloids Surf. A.*, **166**, 153 (2000).
 23. S. Al-Asheh, F. Banat, L. Abu-Aitah, *Sep. Purif. Technol.*, **33**, 1 (2003).
 24. A. Kaya, *J. Environ. Eng.*, **130**, 918 (2004).
 25. L. Zhu, R. Zhu, *Fresenius Environ. Bull.*, **20**, 521 (2011).
 26. C. Obi, I.P. Okoye, *J. Appl. Sci. Environ. Manage.*, **18**, 143 (2014).
 27. R. Proia, P. Croce, G. Modoni, *Procedia Engineering*, **158**, 51 (2016).
 28. T. C. Kenney, W. A. Van Veen, M. A. Swallow, M. A. Sungalia, *Canad. Geotech. J.*, **29**, 364 (1992).
 29. S. Justyna, S. Zuzanna, C. Paweł, P. Agnieszka, *J. Res. Appl. Agric.*, **60**, 98 (2015).
 30. M. Debieche, F. Kaoua, *Mater. Sci. Appl.*, **5**, 347 (2014).
 31. J. C. Appert-Collin, S. Dridi-Dhaouadi, M. O. Simonno, M. Sardin, *Phys. Chem. Earth*, **24**, 543 (1999).
 32. L.C. Lin, C.H. Benson, *J. Geotech. Geoenviron. Eng.*, **123**, 402 (2000).
 33. X. Y. Ge, X. Ma, Z. S. Wu, X. Xiao, Y. Yan, *Res. Chem. Intermed.*, **41**, 7327 (2015).
 34. S. Sener, A. Ozyilmaz, *Ultrasonics Sonochem.*, **17**, 932 (2010).
 35. I. Langmuir, *J. Am. Chem. Soc.*, **40**, 1361 (1918).
 36. H. Freundlich, *Z. Phys. Chem.*, **57A**, 384 (1906).
 37. K.V. Kumar, S. Sivanesan, *Hazard. Mater.*, **36**, 721 (2006).
 38. Y. El-Nahhal, J. Safi, *J. Food Agri. Environ.*, **3**, 295 (2005).
 39. B. Chen, W. Huang, J. Mao, Lv. Shaofang, *J. Hazard. Mater.*, **158**, 116 (2008).
 40. S. Changchaivong, S. Khaodhiar, *Appl. Clay Sci.*, **43**, 317 (2009).
 41. R. Abu-Ellella, M. E. Ossman, M. Abd-Elfatah, A. Elgendi, *Desalin. Water Treat.*, **51**, 3472 (2013).
 42. S. E. Moradi, *Chem. Biochem. Eng.*, **27**, 365 (2013).
 43. A. Balati, A. Shahbazi, M. Amini, S. H. Hashemi, K. Jadidi, *Eur. J. Environ. Sci.*, **4**, 69 (2014).
 44. S. Lagergren, *Kungliga Svenska Vetenskapsakademiens, Handlingar*, **24**, 1 (1898).
 45. Y.S. Ho, G. McKay, *Process. Saf. Environ. Protect.*, **76**, 183 (1998).
 46. S. J. Elovich, in: *Proceedings of the Second International Congress of Surface Activity*, Butterworths Scientific Publications, London, 1957, p. 252.
 47. M.J.D. Low, *Chem. Rev.*, **60**, 267 (1960).
 48. S. H. Chien, W. R. Clayton, *Soil Sci. Soc. Am. J.*, **44**, 265 (1980).
 49. D. L. Sparks, *Kinetics and mechanisms of chemical reactions at the soil mineral/water interface*, Soil Phys. Chem., D.L. Sparks (ed.), 2nd edn., CRC Press, Boca Raton, 1999, p. 135.
 50. Ö. Gök, A. S. Özcan, A. Özcan, *Desalination*, **220**, 96 (2008).
 51. E. M. Ö. Kaya, A. S. Özcan, Ö. Gök, A. Özcan, *Adsorption*, **19**, 879 (2013).
 52. W. J. Jr. Weber, J. C. Morris, *J. Sanit. Eng. Div. Proceed. Am. Soc. Civil Eng.*, **89**, 31 (1963).
 53. H. Koyuncu, *Appl. Clay. Sci.*, **38**, 279 (2008).
 54. M. E. Argun, *J. Hazard. Mater.*, **1(50)**, 587 (2008).

Ibuprofen/ β -CD complexation by controlled annealing of their mechanical mixture

St. Pereva¹, Ts. Sarafska¹, V. Petrov², M. Spassova¹, S. Bogdanova¹, T. Spassov^{1*}

¹University of Sofia "St. Kl. Ohridski", Faculty of Chemistry and Pharmacy, Department of Applied Inorganic Chemistry, 1, J. Bourchier str., 1164 Sofia, Bulgaria

²University of Sofia "St. Kl. Ohridski", Faculty of Chemistry and Pharmacy, Department of Physicochemistry, 1, J. Bourchier str., 1164 Sofia, Bulgaria

Received July 12, 2018, Accepted March 7, 2019

Ibuprofen/ β -cyclodextrin complex was formed applying a modified melting method, consisting in melting only the drug in the mechanical mixture of ibuprofen and β -cyclodextrin. The ibuprofen inclusion into β -CD was monitored by differential scanning calorimetry after initial release of the water molecules from the CD cavity and was proved by X-ray diffraction and FTIR analyses.

Keywords: β -cyclodextrin, ibuprofen, inclusion complex, melting method

INTRODUCTION

Cyclodextrins are natural cyclic oligosachharides consisting of (α -1,4)-linked α -D-glucopyranose units with a cavity able to host foreign molecules. In pharmacy, cyclodextrins are mainly used as complexing agents to increase the aqueous solubility of poorly water-soluble drugs, and to increase their bioavailability and stability [1-6]. The main and most studied cyclodextrins are α -, β - and γ -cyclodextrin, which differ from one another by the number of repeating glucose units. From the three natural cyclodextrins, β -CD is the most used in the pharmaceutical industry due to the cavity size, availability and low cost [7].

Ibuprofen ((RS)-2-(4-(2-methylpropyl)phenyl)propanoic acid) is a nonsteroidal anti-inflammatory drug (NSAID), commonly administered for treatment of fever, pain and inflammation. The drug is pH-dependent and practically insoluble in water. Throughout the years, a variety of ibuprofen (IBU) complexes with β -cyclodextrin and its derivatives were synthesized and studied, aiming to increase ibuprofen water solubility [8-10]. Inclusion compounds with ibuprofen and β -cyclodextrin have been studied using different synthetic methods – kneading [11], solid dispersion [11-15], freeze/spray drying [11-16], super-critical CO₂ [17, 18], microwave treatment [18, 19], ball milling [20-23], sealed heating [16, 18, 20], etc. Solid dispersion (SD) method is one of the most applied methods for preparation of inclusion compounds. The advantages that the solid dispersion method provides are high purity of the inclusion compound, particle size reduction, high crystallinity. Although, the method is long, it needs large quantities of solvent and energy and there is a risk of

cyclodextrin-solvent reaction.

Melting and solvent evaporation methods are other techniques of preparing inclusion compounds [16, 18]. Sekiguchi and Obi proposed in 1961 the melting technique, aiming to achieve reduction of particle size and to increase the dissolution rate and absorption [24, 25]. In this technique, the physical mixture of a drug and a water-soluble carrier is heated directly to melting. The melting point of a binary system depends on the selection of the carrier and the weight fraction of the drug in the system. The melted mixture is then cooled and rapidly solidified in an ice bath under rigorous stirring. The final solid mass is crushed, pulverized, sieved, and then compressed into tablets. For the complex formation by the hot melt method the miscibility of the drug and carrier in the molten form and their thermostability are important. The molecular mobility of the carrier also plays an important role, because it can change the drug's incorporation. To reduce the process temperature, a commonly used adaptation is applied to the melting phase, which consists of suspending the active drug in a previously melted carrier, instead of using both drug and carrier in the melted state. The main advantage of this technique is its simplicity and economy. For enhancing this method, a few modifications have been introduced over the years like hot-stage extrusion [26-28], MeltrexTM [29] and melt agglomeration [30, 31]. In the hot-stage extrusion the drug and carrier, previously mixed, extruded at high rotational speed, at melting temperature for a short period. The product is then collected after cooling at room temperature and milled. MeltrexTM is another manufacturing process. The new element in this technology is the use of a special twin extruder and the presence of two independent hoppers, which control the

* To whom all correspondence should be sent:
E-mail: tpassov@chem.uni-sofia.bg

temperature range and expand it. The process permits a reduced residence of the drug in the extruder, thus allowing a continuous mass flow and avoiding thermal stress to the drug. Another positive side of this technique is the possibility of protecting the drugs to oxidation and hydrolysis by complete elimination of oxygen and moisture from the mixture [29].

Melt agglomeration allows the preparation of complexes in conventional high-shear mixers. This method also allows production in a rotary processor. There are three techniques for production by melt agglomeration – by adding the molten carrier containing the drug to the heated excipients; by adding the molten carrier to a heated mixture of drug and excipients; or by heating a mixture of the drug, carrier and excipients to a temperature within or above the melting range of the carrier [30, 31].

A variation of the melting method consists in heating the mechanical mixture to the melting of the drug only, as the CD is solid. Thus, the complex is formed due to facilitated diffusion of the molten component of the mixture. To the best of our knowledge, this method has only been applied for naproxen (NP)/ β -CD complex formation [32]. Grandelli *et al.* used a wide range of NP: β -CD molar ratios (0.5:1 to 5:1) and their results showed that the complexation *via* the physical mixture is influenced by transport limitations and also β -CD:NP ratios. According to them, ratios greater than 2:1 lead to higher efficiency of complexation.

The goal of this work was to examine the formation of inclusion complex between ibuprofen and β -cyclodextrin by annealing their mechanical mixture at a temperature above the melting temperature of ibuprofen and far enough from the decomposition temperature of β -CD and ibuprofen.

MATERIALS AND METHODS

β -cyclodextrin was purchased from Wacker Chemie AG, Germany and ibuprofen was purchased from Teva Pharmaceuticals. Both reagents are of analytical grade with purity of 99.9 %.

Preparation of ibuprofen- β -cyclodextrin mechanical mixture

Ibuprofen and β -cyclodextrin were mixed in a molar ratio of 1:1 in dry conditions at room temperature. This mixture was further used for all thermal annealing experiments (DSC at scanning and isothermal conditions) aiming to form inclusion complexes.

Characterization of the mechanical mixture and the ibuprofen/ β -cyclodextrin complex

The thermal behavior of ibuprofen/ β -cyclodextrin mechanical mixture, as well as of the pure substances was characterized with Perkin-Elmer DSC-7 differential scanning calorimeter under pure Ar atmosphere. The heating/cooling experiments were carried out with a rate of 5 and 10 °C /min, respectively. The structure and microstructure of cyclodextrin, ibuprofen and their complex were studied by X-ray diffraction with Cu-K α radiation (Bruker D8 Advance diffractometer).

The Attenuated Total Reflectance Fourier Transform InfraRed (ATR-FTIR) spectra of β -CD, ibuprofen and the melting complex were recorded on Bruker Tensor 27 FT spectrometer by direct deposition on a diamond ATR crystal, with 64 scans at a resolution of 2 cm⁻¹ in the middle IR region (600-4000 cm⁻¹).

RESULTS AND DISCUSSION

The thermal behavior of pure ibuprofen and β -CD in the temperature range of 40 °C to 140 °C is presented in Figure 1a. The sharp endothermic peak of the pure drug at 78 °C indicates its melting, while β -CD shows a broad endothermic effect in the range of 80-140 °C, associated with water release from the inner cavity of the cyclodextrin molecule. The melting enthalpy of ibuprofen (ΔH^m) was determined to be 127 J/g, corresponding to that of racemic ibuprofen [33].

It was already shown that the DSC melting peak of the drug (in this case ibuprofen) can be used to determine if a drug/CD host-guest complex is formed, as well as to obtain the degree of complexation at various conditions of the drug inclusion [32, 34]. The distinct melting peaks in the DSC scans do not appear if the entire drug is included in the cyclodextrin cavity, while reduction of the drug melting enthalpy, measured by DSC, is an indication for partial complex formation [34]. As already argued, in order to form the desired inclusion complex we started from a mechanical mixture of ibuprofen and β -CD in molar ratio of 1:1 [34]. The thermal analysis for the mechanical mixture is presented in Figure 1b and shows two endothermic peaks. The first one indicates the melting of drug, and the second one is associated with water release from β -CD. The shift with 6 °C to lower temperatures (from 78 °C to 72 °C) of the ibuprofen melting peak can only be explained with the presence of solid particles of β -CD in the ibuprofen/ β -CD mixture.

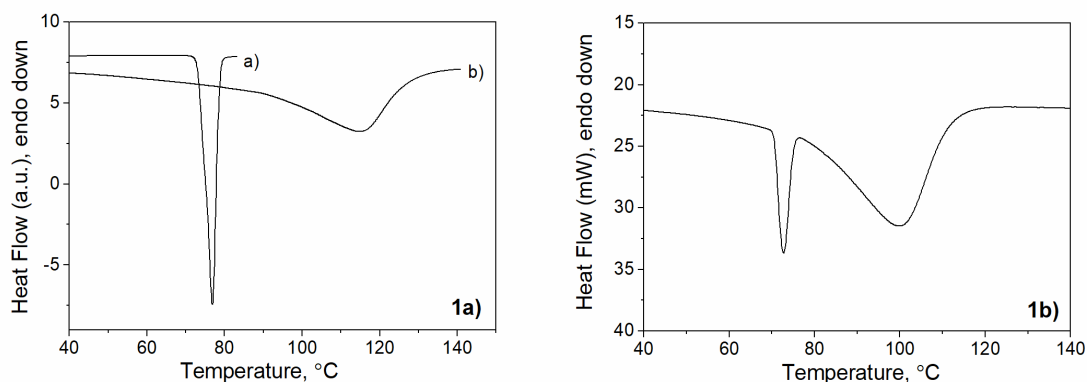


Figure 1. (a) DSC curves of pure (a) ibuprofen and (b) β -cyclodextrin; (b) DSC curve of ibuprofen/ β -CD mechanical mixture.

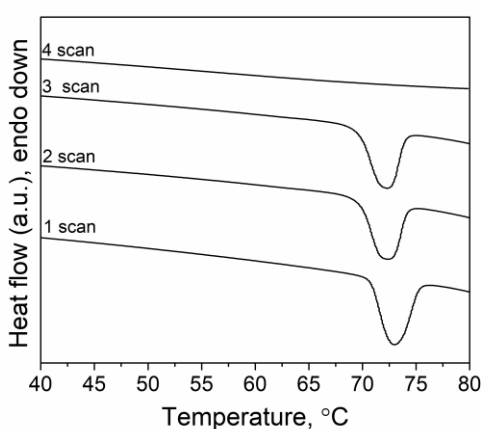


Figure 2. DSC scans of ibuprofen/ β -CD mechanical mixture (1:1 molar ratio).

Figure 2 reveals successive DSC scans of ibuprofen/ β -CD mechanical mixture in the temperature range 40-80 °C. In the first three heating/cooling runs (with heating/cooling rate of 10 K/min) the ibuprofen melting peak is clearly observed. The melting enthalpies of ibuprofen in the first three runs decrease in the following order: 116 J/g, 106 J/g and 105 J/g, respectively, for the first, second and third heating run, giving in this way an indication for a very small degree of complex formation reached at these annealing conditions. Only when the mixture was preliminary annealed at 80 °C for 30 min and then heated up with a constant rate to 80°C the endothermic melting peak was not detected (4th scan). This result is an obvious indication that the sample already contains no free ibuprofen due to its interaction in a molten state with the solid cyclodextrin.

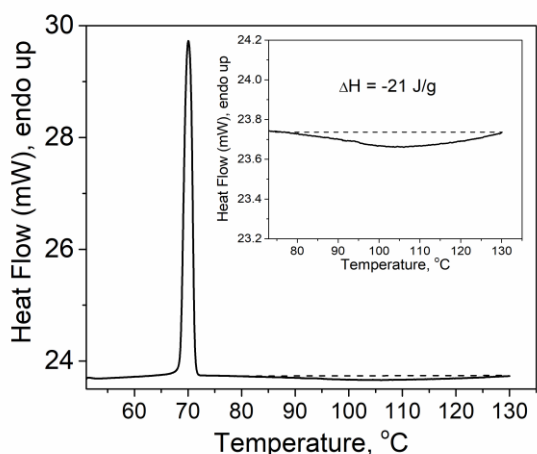
In contrast to the inclusion of naproxen into β -CD, realized applying the above described thermal regime of heating [32], annealing the ibuprofen/ β -CD mechanical mixture at a scanning regime to a

temperature above the melting temperature of ibuprofen does not result in complexation, Figure 2. Annealing naproxen/ β -CD mixture in DSC to a temperature above the endothermic melting peak (at $T > T^m$ of naproxen) results in naproxen/ β -CD complex formation (inclusion of the drug into the β -CD cavities) [32]. The reason why ibuprofen/ β -CD mechanical mixture does not form a complex at these annealing conditions should be sought in the lower rate of ibuprofen inclusion into β -CD compared to naproxen/ β -CD. Apparently, for the ibuprofen/ β -CD complex formation longer annealing time or higher temperature of annealing are required to overcome the diffusion difficulties of the drug insertion.

With the aim to register by DSC the interaction between ibuprofen and β -CD, the following experiment was carried out: the mechanical mixture at a molar ratio of 1:1 was initially annealed in DSC under isothermal conditions at 65 °C for 1 hour. The temperature and the annealing time were selected/optimized so as to allow the complete release of the water molecules from the cyclodextrin without melting the ibuprofen. The idea of this heat treatment is releasing of the pores of β -CD from the water to ease the incorporation of ibuprofen molecules into the already hollow pores. Then, immediately, without removing the sample from the DSC, subsequent annealing was carried out from room temperature to 130 °C at a scanning rate of 5 K/min, Figure 3. The final temperature (130 °C) was adjusted so, as to avoid ibuprofen decomposition. At first look, the observed DSC curve contains only an endothermic ibuprofen's melting peak with a melting enthalpy corresponding to pure ibuprofen, 116 kJ/mole. When changing the scale of the DSC signal in the temperature range 100-130°C, a broad exothermic effect (peak) with enthalpy change of around 21 kJ/mole was observed (Figure 3, inset), which can

only be associated with the reaction between the two components of the mechanical mixture. Due to the low speed of ibuprofen inclusion into the β -CD and relatively weak interaction between them, the effect is bare and with low enthalpy change. It is important to note that without the prior release of the β -CD cavities from the water molecules, the ibuprofen inclusion reaction could not be monitored by DSC. The enthalpy of ibuprofen inclusion appears to be comparable to that determined by Grandelli [32] for naproxen/ β -CD complexation.

Figure 3. DSC curve of the mechanical mixture of ibuprofen/ β -CD (1:1) after initial isothermal annealing at



65°C for 1 h.

To verify if ibuprofen has reacted completely during the above described annealing of the mechanical mixture FT-IR analysis was performed. The FT-IR spectra of the host, the complex obtained by the melting method and the guest are presented in Figure 4. In order to estimate the differences between the complex and the possible mechanical mixture, a spectral subtraction based on Excel Solver optimization was performed according to eq. (1):

$$A_{Difference} = [A_{complex} - \alpha A_{\beta-CD} - \beta A_{IBU}]^2 \rightarrow \min \quad (1)$$

where A_x is the absorbance of the respective substance and α , β are optimized scaling coefficients. The inset of Figure 4 indicates peaks that suffered shape modifications or shifts. As expected, the maximum displacement can be observed at the hydroxyl group band of the host located around 3265 cm^{-1} and the carbonyl group band of the guest, located around 1705 cm^{-1} , groups where possible hydrogen bonds are typically formed. Observed shifts and changes of the spectral shape are good evidences for complex formation. Lack of changes of the methyl groups bands suggests that this groups most probably are located outside of the host cavity.

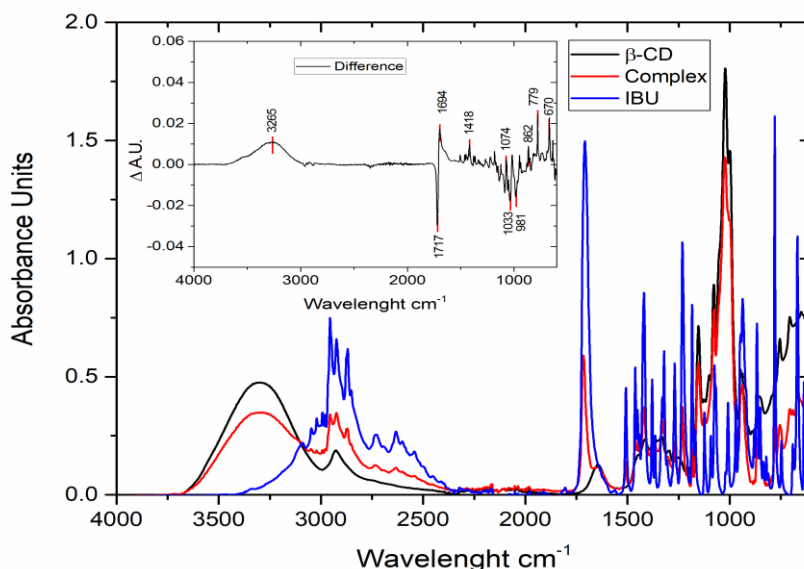
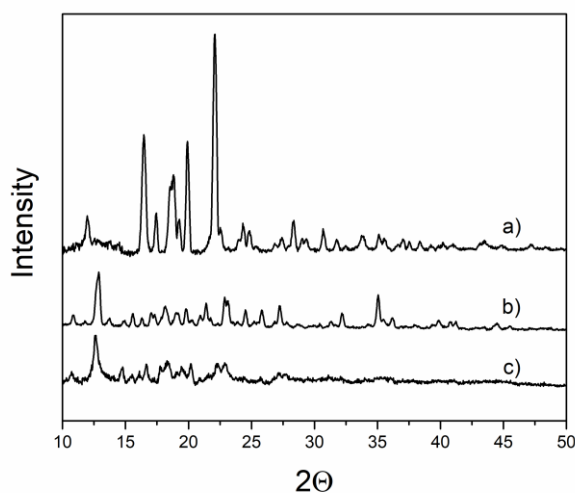


Figure 4. FT-IR spectra of β -CD, ibuprofen and ibuprofen/ β -CD complex. Inset: The difference between simulated mixture of β -CD and ibuprofen and the complex spectra.

Additional proof for the formation of the inclusion complex was obtained by X-ray diffraction analysis. Figure 5 shows the XRD patterns of ibuprofen, β -CD, and the inclusion complex formed by the “melting” method. Qualitatively different is the X-ray diffraction pattern of the inclusion complex showing the presence of new crystalline peaks and the disappearance of these of ibuprofen. The new diffraction peaks are broader and with



reduced intensity, revealing a nanocrystalline nature of the complex formed.

Figure 5. XRD of (a) ibuprofen, (b) β -CD and (c) inclusion complex obtained by the “melting” method.

CONCLUSIONS

To form ibuprofen/ β -cyclodextrin inclusion complex, a mechanical mixture of the two components was isothermally annealed at a temperature below the melting point of ibuprofen, but high enough to release the water molecules from β -CD. At these heat treatment conditions (1 h at 65 °C) no interaction between ibuprofen and β -CD molecules takes place. However, in subsequent annealing in DSC at a constant rate, the reaction proceeds and is observed as a broad exothermic peak in the range 80-130°C. The enthalpy of the drug inclusion (-21 J/g) was determined to be comparable to that of the naproxen inclusion in β -CD [32]. In addition, it was found that applying the melting method complete complex formation was achieved even at 1:1 ibuprofen/ β -CD molar ratio. The modified melting method applied in this work allows quantitative investigation of the drug inclusion kinetics, which is a subject of a current study.

REFERENCES

1. S. Vaidya, *Resonance*, **9**, 18 (2004).
2. E. Bilensoy, D. Duchene, A. Ahuja, S. Baboota, J. Ali, G. Mustafa, F. Acartürk, N. Celebi, Part 1, Ch. 1 & Ch. 3, *Cyclodextrins in pharmaceuticals, cosmetics and biomedicine*, John Wiley & Sons, Inc., Hoboken, New Jersey, 2011, p. 3.
3. T. Loftsson, D. Duchene, *Int. J. Pharm.*, **329**, 1 (2007).
4. L. Liu, Q. X. J. Guo, *Inclusion Phenom. Macrocyclic Chem.*, **42**, 1 (2002).
5. M. E. Brewster, T. Loftsson, *Adv. Drug Delivery Rev.*, **59**, 645 (2007).
6. K. Uekama, Design and evaluation of cyclodextrin-based drug formulation, *Chem. Pharm. Bull.*, **52**, 900 (2004).
7. F. Trotta, R. Cavalli, K. Martina, M. Biasizzo, J. Vitillo, S. Bordiga, P. Vavia, K. Ansari, *J. Incl. Phenom. Macrocycl. Chem.*, **71**, 189 (2011).
8. P. J. Salústio, G. Feio, *Eur. J. Pharm. Biopharm.*, **71**, 377 (2009).
9. P. Mura, A. Bettinetti, *Int. J. Pharm.*, **166**, 189 (1998).
10. G. M. Khan, Jia-Bi Zhu, *J. Chinese Pharm. Sci.*, **7**, 72 (1998).
11. T. Vasconcelos, B. Sarmiento, P. Costa, *Drug Discovery Today*, **12**, 1068 (2007).
12. W.L. Chiou, S. Riegelman, *J. Pharm. Sci.*, **60**, 9 (1971).
13. T. Vilhelmsen, H. Eliassen, T. Schaefer, *Int. J. Pharm.*, **303**, 132 (2005).
14. V.B. Pokharkar, L.P. Mandpe, M.N. Padamwar, A.A. Ambike, K.R. Paradka, *Powder Technol.*, **167**, 20 (2006).
15. D-H. Won, M-S. Kim, J-S. Park, S-J. Hwang, *Int. J. Pharm.*, **301**, 199 (2005).
16. A.H. Al-Marzouqi, H.M. Elwy, I. Shehadi, A. Adem, *J. Pharm. Biomed. Anal.*, **49**, 227 (2009).
17. P. York, *Pharm. Sci. Technol. Today*, **2**, 430 (1999).
18. M. Cirri, F. Maestrelli, N. Mennini, P. Mura, *J. Pharm. Biomed. Anal.*, **50**, 690 (2009).
19. X.H. Wen, F. Tan, Z.J. Jing, Z.Y. Liu, *J. Pharm. Biomed. Anal.*, **34**, 517 (2004).
20. A. Al-Marzouqi, B. Jobe, G. Corti, M. Cirri, P. Mura, *J. Incl. Phenom. Macrocycl. Chem.*, **57**, 2233 (2007).
21. J.S. Patil, D.V. Kadam, S.C. Marapur, M.V. Kamalapur, *Int. J. Pharm. Sci. Review Res.*, **2**, 29 (2010).
22. Q. L. Sanming, X. Che, X. Fan, C. Lib, *Asian J. Pharm. Sci.*, **5**, 188 (2010).
23. I. Colombo, G. Grassi, M. Grassi, *J. Pharm. Sci.*, **98**, 3961 (2009).
24. K. Sekiguchi, N. Obi, *Chem. Pharm. Bull.*, **9**, 866 (1961).
25. K. Sekiguchi, N. Obi, *Chem. Pharm. Bull. (Tokyo)*, **12**, 134 (1964).
26. C.W. Pouton, *Eur. J. Pharm. Sci.*, **29**, 278 (2006).
27. G. Verreck, A. Decorte, K. Heymans, J. Adriaensen, D. Cleeren, A. Jacobs, D. Liu, D. Tomasko, A.

- Arien, J. Peeters, P. Rombaut, G. Van den Mooter, ME. Brewster, *Eur. J. Pharm. Sci.*, **26**, 349 (2005).
28. G. Van den Mooter, I. Weuts, T. De Ridder, N. Blaton, *Int. J. Pharm.*, **316**, 1 (2006).
29. J. Breitenbach, J. Lewis, Two concepts, one technology: controlled release and solid dispersion with meltrex, in: *Modified-Release Drug Delivery Technology* (M.J. Rathbone et al., eds.), Marcel Dekker, 2003, p. 125.
30. M.K. Gupta, Y-C. Tseng, D. Goldman, R.H. Bogner, *Pharm. Res.*, **19**, 1663 (2002).
31. A. Seo, P. Holm, H. G. Kristensen, T. Schaefer, *Int. J. Pharm.*, **259**, 161 (2003).
32. H. E. Grandelli, B. Stickle, A. Whittington, E. Kiran, *J. Inclusion Phenomena*, **77**, 269 (2013).
33. S. Lerdkanchanaporn, D. Dollimore, A Thermal Analysis Study of Ibuprofen, *J. Thermal Analysis*, **49**, 879 (1997).
34. St. Pereva, Tzv. Sarafska, Sv. Bogdanova, T. Spassov, *J. Drug Delivery Sci. Technol.*, **35**, 34 (2016).

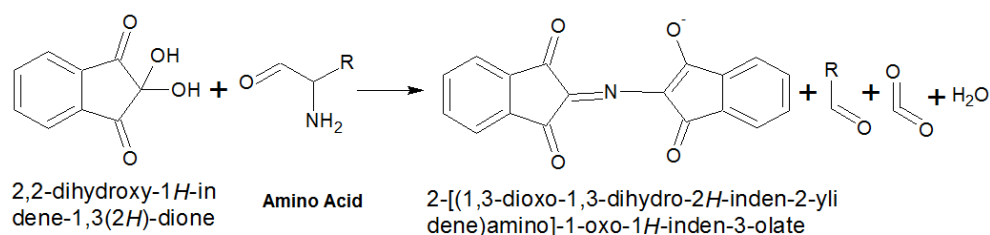
A novel approach to analyze total amino acids contents of food samples by computational image scanning densitometry

W. Uz-Zaman, R. Rehman*, J. Zafar

Institute of Chemistry, University of the Punjab, Lahore-54590, Pakistan

Received November 17, 2015; Accepted February 27, 2019

In the current work, computational image scanning densitometry technique was used instead of conventional and traditional instruments like IC, HPLC, GC and UV/visible spectroscopy for quantification of micro samples of amino acids (lysine hydrochloride, β -alanine, asparagine monohydrate, glutamic acid). The general reaction between locating reagent and amino acid is:



This technique has accuracy at the parts per billion level and precision as indicated from percent recovery from sample analysis, which is quite good. Due to certain limits associated with conventional techniques, this technique may be presented as a progressive and important event in the history of evaluation at micro level.

Keywords: amino acids, densitometry, micro level.

INTRODUCTION

Absorption spectroscopy is a sort of estimation of an interaction by the relation between electromagnetic radiation and content of atoms of a chemical substance. Pharmaceutical analysis usually involves atomic absorption, ultraviolet/visible and infrared spectroscopy. Colorimetry is basically a spectrophotometric measurement in the visible region which is apt to be called "colorimetry" only when taking into consideration human perception of color. There are several techniques which employed and developed AAS and ICP, but in developing countries most of the analytical labs cannot afford such costly techniques. As a result, the only novel technique which is left is spectrophotometry which is used around the world for estimation at micro level. Despite the fact, there are several benefits along with few disadvantages. For instance, the expected results in respect of accuracy and precision are not achieved in the case of micro samples. Likewise, spectrophotometric technique cannot be laid off directly [1], as is the matter of coagulation just like Ni^{2+} with DMG. Similarly, atomic absorption spectrometry (AAS) is a well accepted and useful technique for the estimation of metals in minute

amounts, but still the method has to require many developmental series concerning getting more in accuracy and ease of operation and, predominantly, it requires a lot of improvement for estimation up to a certain limit [2]. In the laboratory practice of protein purification a comparatively quick and discriminating procedure to quantify (estimation of LOD) the polymers of amino acids is frequently needed, this protocol eliminates the requirement of this kind of estimation [3]. To overcome the limitation of spectrophotometry, researchers around the world are keenly working and trying to elaborate particular methods for the accurate and precise analysis of micro quantities of samples [4]. Teasdale *et al.* advanced this approach for sulfur containing compound evaluation [5].

A quality-level scanner and imaging software was utilized to make the densitometric calculations. Abraham *et al.* used this protocol for the separation of allantoin on the thin layer chromatogram and dimethylaminobenzaldehyde was sprinkled on the spot [6]. Densitometer was used to read the yellow colored spot. As the matter of bottom value for quantification was 0.1 mg (0.5 mg = 100 ml) for every spot. Quantization of allantoin in urine, serum and lymph can be done through this method which is an advantage. The practice of scanning densitometry for the examination of dyes in food products was probed by Ueno *et al.* [7].

* To whom all correspondence should be sent:
E-mail: grinorganic@yahoo.com

Pharmacologically active curcuminoids were isolated by Paramasivam *et al.* from the rhizome of *curcuma longa* [8]. By using extraction (Soxhlet extraction) the curcuminoids were separated from the rhizomes of turmeric. Crystallization and column chromatography were used for the separation and spectroscopic analysis for identification. TLC aluminum plates with silica gel spread on the plate were used in this method. Curcuminoids were analyzed using the densitometric method in assimilation-deliberation mode at 425 nm. To examine the percentage of these three curcuminoids, 7 different kinds of germplasm of turmeric were detected. Mohammad and Zehra have developed a chromatographic system containing a mobile phase of borate-phosphate buffer with pH 2.3 and a silica layer saturated with an anionic surfactant as a stationary phase [9]. It was shown as the most apt system for the mutual separation of *dl*-tryptophan and *l*-histidine. Stability, lowest detectable amount, reproducibility and retardation factor values of these two amino acids were estimated. Silica TLC plates and silica gel 60F254HPTLC plates were used for the evaluation and comparison of chromatographic parameters including separation factor and dissolution factor for the separation of *l*-histidine and *dl*-tryptophan.

Amino acids are carbon compounds containing both nitrogenous compounds and carboxylic groups. Apart from glycine, every other amino acid has chirality and is optically active [10]. In the present years it is found that amino acids not only exist as single molecules inside the cell but they are also considered as a circulator of the protein phosphorylation cascade and of gene expression. Moreover, amino acids act as forerunners for preparation of steroidal compounds and least atomic mass nitrogen containing compounds, both have huge biological significance. The body-required level of amino acids and their related end products (e.g., nitric oxide, polyamines, uric acid, glutathione, steroidal chemical messenger) are needed for many functions in the body. Inflated concentrations of amino acids and their resulting compounds (e.g., NH_3 , asymmetric dimethyl arginine and homocysteine) are fatal and responsible for abnormalities related to neurons, higher potential of oxidation, and diseases associated to heart. Hence, an optimal, apt and suitable balance among amino acids in the diet taken is critical and crucial for the body homeostasis [11]. Relative examination of amino acids at α -position is done by treating with ninhydrin (2,2-dihydroxy-1,3-indandione). The product is dehydrogenated alcohol which contains

an atom of carbon less than the amino acid having α -position along with CO_2 in stoichiometric ratio, also formed different values of hydrindantin, NH_3 and a color imparting compound called Ruhemann's Purple (diketohydrindylidenediketohydrindamine). Ruhemann's Purple pigment tends to serve as a basis of quantitative analysis along with estimation of α -amino acids [12]. In amino acid sample analysis, total amino acid contents were determined by various methods like chromatography, HPLC, spectroscopy, etc., instead of reporting individual amino acid contents. This is the main limitation in their analysis.

In the current work, instead of the use of conventional and traditional instrumentation like IC, HPLC, GC and UV/visible spectroscopy, a technique was used for quantification of micro samples of amino acids (lysine hydrochloride, β -alanine, asparagine monohydrate, glutamic acid). Particular media (silica plate and TLC) were used to shift the measured volume (0.5 μL) of sample and standard. The medium may contain a reagent (Ninhydrin reagent) impregnated, succeeding deposit the reagent, after enough drying, digital scan of developed spot is transferred inside the computer by using a high-quality scanner at 300 dpi, RGB mode of 24 bit. By using appropriately and specially developed software the image is quantified by making the spot well inside the selection marquee. The GBR, (green, blue, red) component of every visual display (a mixed area of illumination) from the periphery and added amounts up to ultimate color innermost quantity are measured by the software illustrated below. A model for subtractive color presentation is the RGB color space, each of RGB components is at its maximum value shown by pure white color (eight bit per component $\frac{1}{4}255$), similarly $\text{R}\frac{1}{4}\text{G}\frac{1}{4}\text{B}\frac{1}{4}128$ indicated grey color, $\text{R}\frac{1}{4}\text{B}\frac{1}{4}\text{G}\frac{1}{4}0$ showed pure black color. The issue we are concerned with is density measurement; it only required a simple difference from the highest value (two hundred and twenty five) that will provide you with one fourth of RGB for White, one twenty eighth for Grey, and one two hundred and fifty fifth for Black. This technique is fundamentally applied for some other colors. A dusky color or, in other words, a higher intensification of component under examination, will cause a high intensity of color. Moreover, there are more than thousand visual units within the image of a mark (a 1 mL blot on TLC encloses a circle of point two'' diameter, which forms a three dpi image enclosing almost twenty eight hundred visual units), the ultimate accruing color intensity of the complete blot consequence into six numerals [13].

Concentration of analyte in the sample is calculated by plotting the calibration curve. It is noteworthy that the selectivity depends not on the instrumental methodology but on the reagent; therefore be careful when selecting the developing reagents. Extremely small sample volume is used; colored and black precipitation can be quantified in contrary to spectrophotometry; for measurement no costly instrument is required; by using a laptop and a digital camera this technique can be portably used; all these are few advantages of this technique.

EXPERIMENTAL

Apparatus and instrumentation

For development of the spots, a μL pipette and TLC foil (Merck, TLC aluminum membrane, $(20 \times 20 \text{ cm})$, silicon dioxide gel 60f254) was utilized. For transcribing into the digital form of the image of the mode, HP thirty six hundred and seventy CCD contemplative smooth level color scanner was used.

Quantification of amino acids

Amounts of 0.938 g, 1.877 g, 2.283 g and 1.114 g of glycine, asparagine monohydrate, lysine monohydrochloride and β -alanine, respectively, were taken to make 25 mL of 0.5M solution of each one. Ninhydrin reagent was prepared by mixing 1.0 g of the reacting compound in 10 mL of pure ethanol. By making different concentrations of the standard solution mentioned, standards (0.5M-0.1M) were prepared.

Spot development

By using the micro pipette 0.5 μL of ninhydrin reagent followed by each standard was applied on TLC plates (35 cm) at suitable distances. The plates were placed inside an oven at 80°C for 10 min to develop the brownish red spot after short drying, as shown in Fig. 1. The general reaction is shown in Fig. 2.

To measure the color density of each spot, the TLC sheet was scanned on a high-resolving scanner and the consequent image was estimated in software. Between the concentration and color consistency, the gauging line was dragged, and then to measure the intensity of the amino acids inside the sample, the calibration data were used. Moreover, for comparison of optical densitometric technique with visible spectrophotometry, 2 mL from each solution in the range from 0.1-0.5M of each amino acid were taken in separate test tubes and 3 mL of ninhydrin reagent were added. These solutions were heated in an oven at 80°C for 10 min and the absorbance was read at 624 nm.

While mentioning the application of densitometry using ninhydrin as a reagent for detection and estimation of amino acids, samples of wheat flour, jatropha seed cake (seed cake left after the extraction of oil from it) and grinded rice were taken, their sample preparation involves the lysis and extraction of proteins by treatment with 6M HCl followed by incubation in a microwave for about 10 min. Afterwards the sample was neutralized (to $\text{pH} = 8.03$) with liquid ammonia.

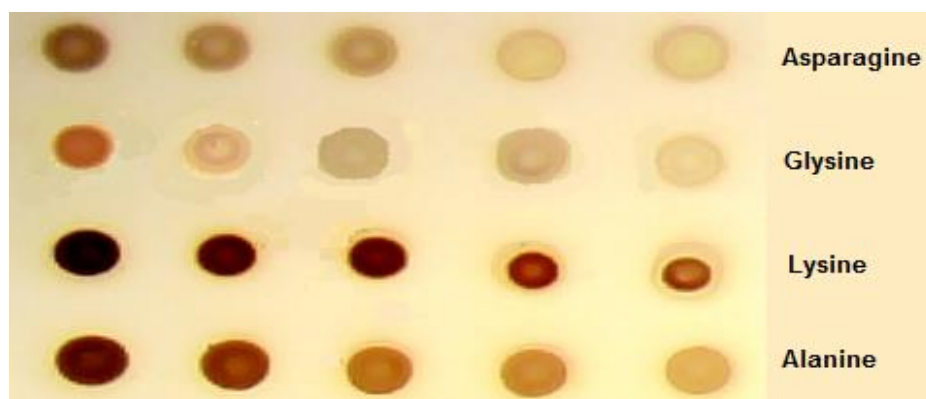


Fig. 1. Developed spots of amino acids with ninhydrin for densitometric analysis.

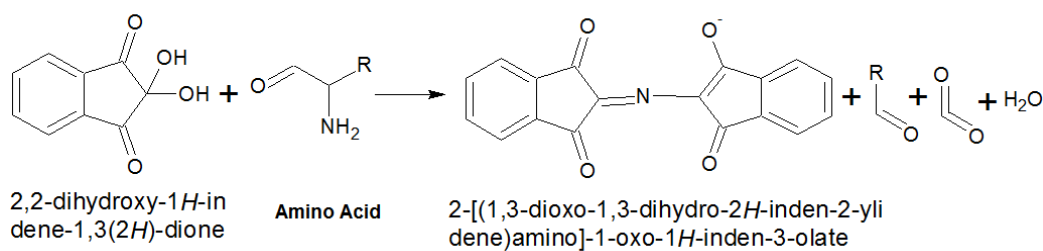


Fig. 2. Schematic reaction of amino acid with reagent.

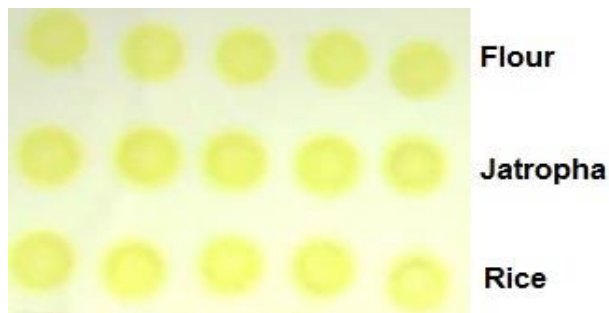


Fig. 3. Developed replicate spots of amino acids contents of samples.

Each sample was diluted by taking 1 mL, 2 mL, 3 mL, 4 mL and 5 mL from the stock solution and made up to a total volume of 5 mL with distilled water. Each sample was then placed on a TLC plate. After adding ninhydrin reagent and by following the same procedure as marked out before, the brownish red color spots were developed and then quantified with the algorithm designed for it.

RESULTS AND DISCUSSION

The estimation of total amino acid can be carried out by various methods - the classical method and the spectrophotometric method. Due to their low precision at micro level, difficult handling and cost these methods are not appropriate. Quantification is a very sensitive issue at micro level in food samples. All over the earth efforts are being made to find out a reasonable inexpensive and authentic methodology for the estimation of metal content at micro level in the sample.

In this study, an approach was advanced at micro level for absolute consideration of amino acids similar to β -alanine, lysine monohydrochloride, asparagine monohydrate and glutamic acid. The fascination of this protocol is its being easy to handle and not needing formal

apparatus. It can be used with great precision at very low levels for the quantification of toxic metals. Other advantages include: use of minor amount; quantification of the color coagulation; intensified delicacy; perfection.

The gauging equalization for β -alanine, lysine monohydrochloride, asparagine monohydrate and glutamic acid reveal an impressive correlation coefficient ($R^2 > 0.9$). The calibration data for determination of amino acids are shown in Table 1. It indicates that calibration line can be made with any of the selected amino acids giving similar results with total amino acid contents of samples being analyzed, as shown in Table 2. For checking the applicability of this method, total amino acid contents of wheat flour, jatropha and rice were determined using calibration line of β -alanine and spiking its standard solution in these samples for estimating percent recovery as shown in Fig.3. This method was also compared to standard visible spectrophotometry using standard solutions ranging from 0.1 to 0.5M of β -alanine. From each solution 2 mL were taken in separate test tubes and 3 mL of ninhydrin reagent were added. The solutions were heated in the oven at 80°C for 10 min and then the absorbance was read at 624 nm. Same was done with wheat flour, jatropha and rice samples for analysis comparison.

Table 2 indicates that more than 98.5 % have been recovered. So it is safely concluded that this method can be applied on industrial scale for continuous monitoring of staples samples for their total amino acid contents. The results indicated that the computational image scanning densitometry method is comparable in accuracy with the standard method.

Table 1. Calibration data for determination of amino acids.

Concentration (ng/mL)	Color density			
	β -Alanine	Lysine monohydrochloride	Asparagine monohydrate	Glutamic acid
1	31418	61418	44180	69418
2	94517	124517	67517	142517
3	142107	162107	115107	190107
4	190110	200110	163110	238110
5	218985	238985	191985	256985
6	259193	279193	232193	297193
Calibration equation	$y = 44579x + 26.8$	$y = 42008x + 30693$	$y = 38899x - 465.2$	$y = 43722x + 46027$
Correlation coefficient (R^2)	0.986	0.9913	0.9925	0.967

Table 2. Concentration of total amino acids in food samples.

Sample No	Sample name	Average concentration mg/100 g		Standard deviation \pm	Percent recovery	Percent error
		Found by spectroscopy	Found by densitometry			
1.	Wheat flour	71.231	71.536	0.005508	99.2	0.7
2.	Jatropha	77.962	78.723	0.000577	99.3	0.9
3.	Rice	77.581	77.357	0.00026	98.6	1.3

CONCLUSION

This work has exhibited that blot test utilizing scanning is more appropriate for computational quantification in many aspects like time, handling and cost as compared to the conventional techniques. This technique has parts per billion level accuracy and precision as indicated by percent recovery from sample analysis, which is quite good. Due to certain limits associated with conventional techniques, this technique may be presented as a progressive and important event in the history of evaluation at micro level.

REFERENCES

1. P. Nagaraja, H. S. Yathirajan, H. R. Arunkumar, R. A. Vasantha, *J. Pharmaceut. Biomed.*, **29**(1–2), 277 (2002).
2. S. Olsen, L. C. R. Pessenda, J. Ruizicka, E. H. Hansen, *Analyst*, **108**, 1289 (1983).
3. M. Bradford, *Anal. Biochem.*, **72**, 248 (1976).
4. S. Kundu, M. Mundal, A. Pal, *Talanta*, **58**(5), 935 (2002).
5. P.R. Teasdale, S. Hayward, W. Davison, *Anal. Chem.*, **71**(11), 2186 (1999).
6. J. Abraham, F. A. Simeone, R. W. Hopkins, *Anal. Biochem.*, **70**(2), 377 (1976).
7. E. Ueno, T. Ohno, H. Oshima, *Shokuhin Eiseigaku Zasshi*, **39**(4), 286 (1998).
8. M. Paramasivam, R. Poi, H. Banerjee, A. Bandyopadhyay, *Food Chem.*, **113**(2), 640 (2009).
9. A. Mohammad, A. Zehra, *Colloid. Surfaces A*, **301**(1–3), 404 (2007).
10. F. Galli, *Amino Acids*, **32**, 497 (2007).
11. G. Wu, *Amino Acids*, **37**, 1 (2009).
12. C. B. Bottom, S.S. Hanna, D. J. Siehr, *Biol. Chem.*, **176**, 367 (1948).
13. J. Anwar, W. Uz-Zaman, U. Shafique, M. Salman, *Anal. Lett.*, **43**(2), 367 (2010).

Rapid photocatalytic degradation of methylene blue, tartrazine and brilliant green dyes by high-flux UV irradiation photolysis reactor

R. Rehman^{1*}, W. Uz-Zaman¹, A. Abbas¹, L. Mitu²

¹Institute of Chemistry, University of the Punjab, Lahore-54590, Pakistan

²Department of Chemistry, University of Pitesti, Pitesti-110040, Romania

Received October 24, 2017; Revised December 11, 2017

The aim of this work was to investigate the removal of dyes from wastewater by photocatalytic degradation using a modified assembly of photolysis reactor. It was more efficient and dye degradation occurred very fast. UV/Visible spectrophotometry was used to monitor the reaction. The degradation of dyes with different catalysts was compared and found to follow first-order kinetics. The optimal result for Methylene Blue was $t_{(1/2)}=4$ min, $k = 0.4471 \text{ min}^{-1}$, $R^2 = 0.9650$, for Tartrazine - $t_{(1/2)} = 1.2$ min, $k = 0.9723 \text{ min}^{-1}$, $R^2 = 0.9980$ and for Brilliant Green - $t_{(1/2)} = 0.8$ min, $k = 0.9716 \text{ min}^{-1}$, $R^2 = 0.9938$. So, it can be efficiently employed on a larger scale.

Keywords: Methylene Blue, Tartrazine, Brilliant Green, Photolysis, Degradation.

INTRODUCTION

Water contamination by coloring materials is a serious life threat. These coloring materials are known as dyes. They can originate from natural plant sources or synthetic ones. Synthetic dyes are usually better coloring materials, but their biodegradation is difficult. They can be classified into acidic (like Tartrazine or Congo Red) or basic (like: Methylene Blue, Brilliant Green) on the basis of pH, or on the basis of functional groups like sulphonic, azo, naphtholic dyes, etc. They are commonly used in textile, leather, paper, paint and pharmaceutical industries for coloring various materials [1-8]. Their discharge in waste streams leads to depletion in light penetration into deeper layers of water. This leads to death of aquatic plant and animal species, disturbing food chain and ecosystem in a brutal way. So, their continuous removal from waste streams in an economical and

efficient way is very crucial for saving life on this planet [9-16].

There are various physico-chemical and biological methods for removing these dyes. The adsorption on synthetic or agricultural waste derived activated material is the most common method of removal of dyes [16-21]. Dyes can be degraded biologically, chemically or using photolysis [22-25]. Natural methods of degradation are microbial and photolytic [26-32].

Some weaknesses of these practices are: long time is required and resulting byproducts are more harmful for the ecosystem. For example: using ZnO and UV light, 64.90 % degradation of Methylene Blue, Methyl Orange and Reactive Orange 16 occurred in 2 hours. Using CaIn_2O_4 , degradation of $47.8 \mu\text{mol/L}$ of Methylene Blue was achieved in neutral medium within 2 hours. Design of a simple reactor formerly commonly used for photolysis is shown in Fig. 1 [16-18].

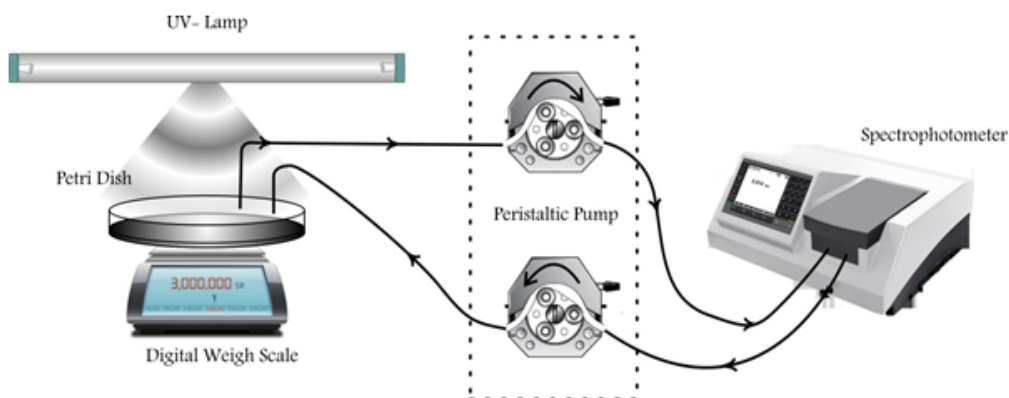


Fig. 1. The UV degradation setup for dyes.

* To whom all correspondence should be sent:
E-mail: grinorganic@yahoo.com

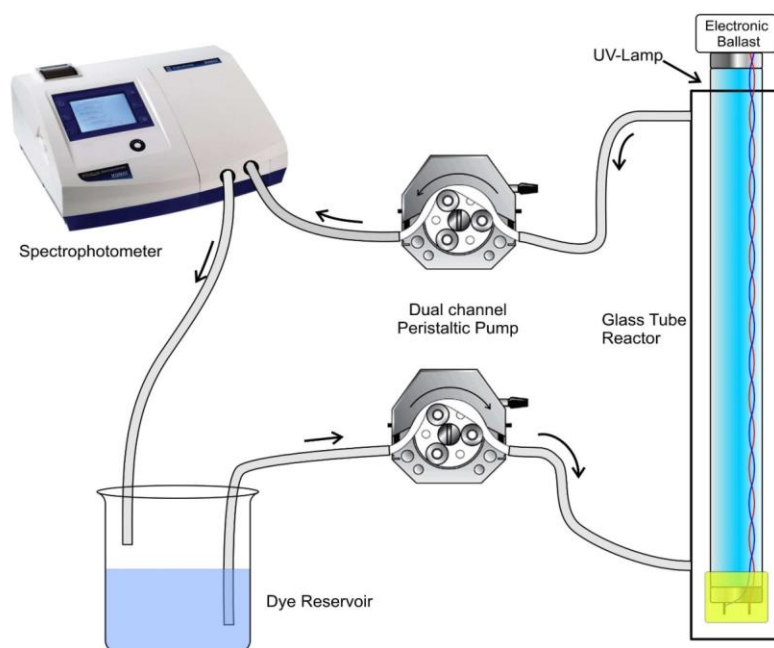


Fig. 2. Systematic diagram of the newly designed photolysis reactor.

The problems faced in this setup are:

(i) Distance between light source and dye solution is large, resulting in wastage of UV light intensity along with decrease in efficiency of process.

(ii) UV light converts O_2 present in ambient air into O_3 (ozone).

(iii) Ozone production lowers the efficiency of the process and moreover, it is toxic for the environment.

(iv) Ozone delays the photodegradation of dye.

So, there is need to develop an efficient assembly for degradation of dyes. In this work, that design was presented and applied for degradation of Methylene Blue, Tartrazine and Brilliant Green dyes.

EXPERIMENTAL

The assembly shown in Fig. 2 was used in this work for addressing the above mentioned issues in an effective and economical way using indigenous sources.

It consists of UV lamp put inside a hollow cylindrical glass rod with two openings, one on the upper side and a second one on the lower side. They are joined through peristaltic pumps to dye solution container and UV/Vis spectrometer.

Since the UV light source and dye solution are in close contact, maximum light is used for photodegradation of the dye in a short interval of time. Along with this, it has the following advantages:

(i) No light intensity and energy is wasted.

(ii) As there is no air in-between UV light and dye solution, no ozone production takes place.

(iii) Less time is required for photodegradation; and last, but not least, this process is in continuous mode which is superior to batch process for removal of dyes for adopting on industrial scale.

Methodology for photocatalytic degradation

Chemicals: Methylene Blue, Brilliant Green, Tartrazine, H_2O_2 , TiO_2 , all obtained from Merck (Germany).

Equipment used: Tubular UV lamp (15 Watts, length 43 cm, ϕ 27 mm), Electrical balance, pH meter, UV/VIS spectrophotometer, quartz flow cell (10 mm), dual channel peristaltic pump, magnetic stirrer.

Preparation of stock solutions: 1M stock solution of each dye was used. Further dilutions required for each dye were accordingly prepared.

Setup used for photodegradation investigations: For this, a UV lamp, dual channel peristaltic pump with 150 mL/min flow rate and UV-Vis spectrometer were used. Spectrometer was attached to PC for data monitoring. Dye solution was loaded in a beaker with magnetic stirrer and placed on a hot plate. The peristaltic pump takes this solution to the glass tube reactor from the bottom side, where it is exposed to UV radiation. Then the dye solution goes to the spectrometer flow cell from the upper side through the peristaltic pump. After this, it is mixed again with the initial solution container. As degradation proceeded, the concentration of dye solution was continuously monitored at 655 nm for Methylene Blue, 425 nm for Tartrazine and 625 nm

R. Rehman et al.: Rapid photocatalytic degradation of Methylene Blue, Tartrazine and Brilliant Green dyes by ... for Brilliant Green dye, through a PC based data logging system [13-17].

(i) Degradation of dyes without catalyst

Dye solutions (0.06 mM of Methylene Blue, 0.018 mM of Tartrazine and 0.08 mM of Brilliant Green) were run through this assembly one by one and came in contact with the UV light and the absorption of the solution was noted after regular time intervals.

(ii) Degradation of dyes with catalyst TiO_2

Solutions of Methylene Blue (0.03 mM), Tartrazine (0.036 mM) and Brilliant Green (0.08 mM) were prepared. To each 5 mg of TiO_2 catalyst was added. Then the solution was passed through the assembly and the light absorption was registered.

(iii) Degradation of dyes with H_2O_2

Solutions of Methylene Blue (0.03 mM), Tartrazine (0.036 mM) and Brilliant Green (0.08 mM) were prepared. Then 0.5 mL of H_2O_2 was added to each. The solutions were placed on the stirrer and passed through the reactor. Then the light absorption was registered.

(iv) Degradation of dyes with TiO_2 and H_2O_2

Solutions of Methylene Blue (0.03 mM), Tartrazine (0.036 mM) and Brilliant Green (0.08 mM) were prepared and 5 mg of TiO_2 and 0.5 mL of H_2O_2 were added in all of them. Then they were passed through the reactor and degradation of dyes was monitored.

RESULTS AND DISCUSSION

The degradation of dyes was performed using UV light and catalysts. The absorption of dye solutions was monitored and graphically represented below. It was shown that degradation of dyes followed first-order kinetics (eq. 1):

$$\ln(A_0/A_t) = kt \quad (1)$$

Here A_0 is the initial dye solution absorbance and A_t is the absorbance after time t , k is rate constant [18-27]. All experiments were performed in triplicate and average values were used for graphical representation and statistical validation using paired t-test.

Case 1: Photolytic degradation of Methylene Blue

(a) Without catalyst: The results are shown in Fig. 3. The statistical analysis indicated that 1st order kinetic model was followed. Complete removal of dye occurred within 110 min. $t_{(1/2)} = 110$ min, $K = 0.006302 \text{ min}^{-1}$, $R^2 = 0.996091$.

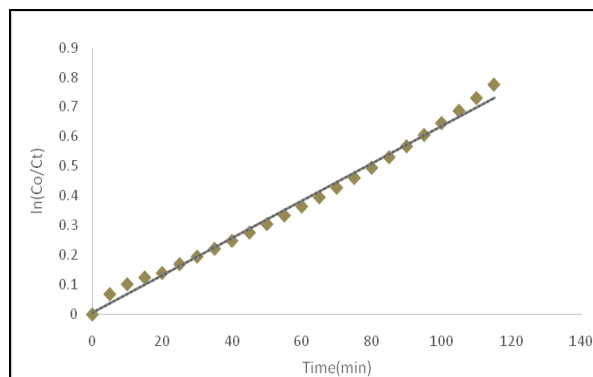


Fig. 3. Photolysis kinetics of Methylene Blue without catalyst.

(b) With catalysts TiO_2 , H_2O_2 applied separately and simultaneously: The results are graphically presented in Fig. 4. Statistical analysis indicated that 1st order kinetic model was followed. Statistical results are as follows:

with TiO_2 : $t_{(1/2)} = 29$ min, $K = 0.022984 \text{ min}^{-1}$, $R^2 = 0.99560$

with H_2O_2 : $t_{(1/2)} = 4$ min, $K = 0.447125 \text{ min}^{-1}$, $R^2 = 0.965032$

with $TiO_2 + H_2O_2$: $t_{(1/2)} = 2.5$ min, $K = 0.162375 \text{ min}^{-1}$, $R^2 = 0.954916$.

Complete removal of dye occurred within 2.5 min using both catalysts at the same time. So, it can be effectively employed on larger scale Methylene Blue removal in an economical way like adsorptive removal of methylene blue or using other catalytic methods for removal of dyes [28-33].

Case 2. Photolytic degradation of Tartrazine

(a) Without catalyst: The results are shown in Fig. 5. The statistical analysis revealed that it followed the same 1st order kinetic model with $t_{(1/2)} = 2.75$ min, $K = 0.498606 \text{ min}^{-1}$, $R^2 = 0.982249$.

(b) With catalysts TiO_2 , H_2O_2 applied separately and simultaneously: The results are presented in Fig. 6. Their statistical validation indicated that 1st order kinetic model was followed in all cases:

with TiO_2 : $t_{(1/2)} = 2.2$ min, $K = 0.115235 \text{ min}^{-1}$, $R^2 = 0.978703$

with H_2O_2 : $t_{(1/2)} = 1.2$ min, $K = 0.972361 \text{ min}^{-1}$, $R^2 = 0.998037$

with $TiO_2 + H_2O_2$: $t_{(1/2)} = 1.3$ min, $K = 0.057659 \text{ min}^{-1}$, $R^2 = 0.99270$.

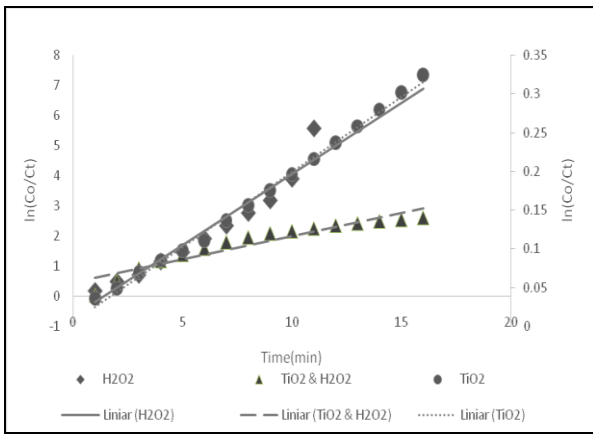


Fig. 4. Photolysis kinetics of Methylene Blue with catalysts TiO_2 , H_2O_2 used separately and simultaneously.

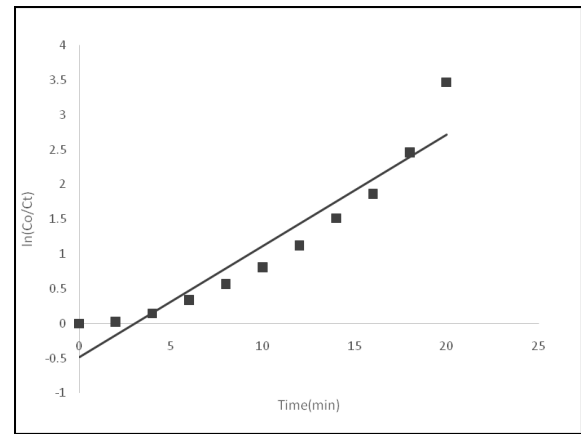


Fig. 7. Photolysis kinetics of Brilliant Green without catalyst.

Case 3: Photolytic degradation of Brilliant Green

(a) *Without catalyst:* The degradation is graphically represented in Fig. 7. Its statistical modeling indicated that degradation of Brilliant green followed a 1st order kinetic model and maximum dye removal occurred within 9.1 min. $t_{(1/2)} = 9.1$ min, $K = 0.159895 \text{ min}^{-1}$, $R^2 = 0.950303$.

(b) *With catalysts TiO_2 , H_2O_2 used separately and simultaneously:* Fig. 8 shows the degradation results for Brilliant Green with catalysts TiO_2 and H_2O_2 used separately and simultaneously. Their statistical modeling is as follows:

with TiO_2 : $t_{(1/2)} = 5.2$ min, $K = 0.364276 \text{ min}^{-1}$, $R^2 = 0.861151$

with H_2O_2 : $t_{(1/2)} = 0.8$ min, $K = 0.971629 \text{ min}^{-1}$, $R^2 = 0.993809$

with TiO_2 and H_2O_2 : $t_{(1/2)} = 0.9$ min, $K = 0.952320 \text{ min}^{-1}$, $R^2 = 0.98018$.

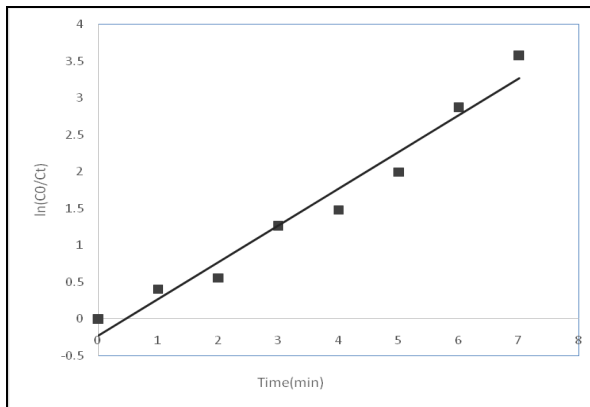


Fig. 5. Photolysis kinetics of Tartrazine without catalyst.

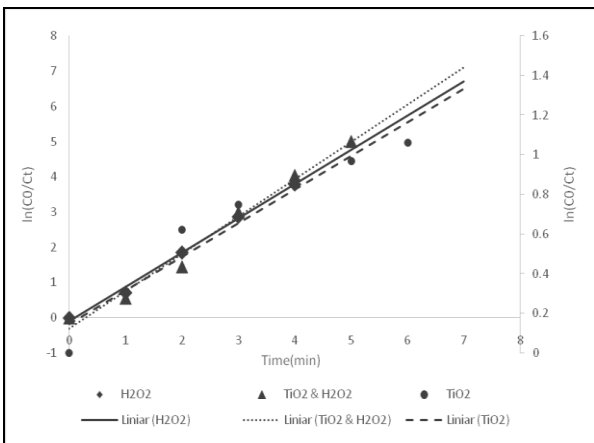


Fig. 6. Photolysis kinetics of Tartrazine with catalysts TiO_2 , H_2O_2 used separately and simultaneously.

Statistical correlation indicated that the catalysts can be effectively employed on a larger scale for removal of Tartrazine dye like any other methodology of removal of dyes [28-33].

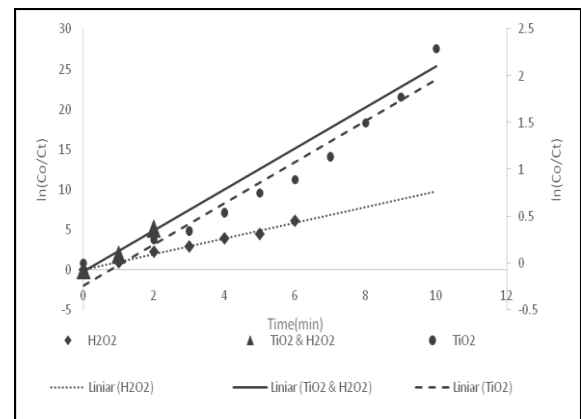


Fig. 8. Photolysis kinetics of Brilliant Green with catalysts TiO_2 , H_2O_2 used separately and simultaneously.

The same trend as for Tartrazine is shown: complete dye removal occurred within 0.8 min using H_2O_2 only. So, H_2O_2 can be efficiently employed for adsorptive removal of Methylene Blue or using other catalytic methods for removal of dyes [26-32].

CONCLUSIONS

The photodegradation of dyes was performed under UV light by using a modified method. Kinetic studies indicated that photolytic degradation of dyes followed a first-order kinetic model. The rate of degradation of dyes was very high in presence of catalysts such as TiO₂ and H₂O₂. The optimal result for Methylene Blue was $t_{(1/2)}=4$ min, $k = 0.4471 \text{ min}^{-1}$, $R^2 = 0.9650$, for Tartrazine was $t_{(1/2)} = 1.2$ min, $k = 0.9723 \text{ min}^{-1}$, $R^2 = 0.9980$ and for Brilliant Green was $t_{(1/2)} = 0.8$ min, $k = 0.9716 \text{ min}^{-1}$, $R^2 = 0.9938$. This developed methodology is economical, safe to use, developed from local resources and proved to be very efficient for degradation of dyes and other contaminants in an ecofriendly way.

REFERENCES

1. D. Pathania, G. Sharma, A. Kumar, M. Naushad, S. Kalia, A. Sharma, Z. A. AlOthman, *Toxicol. Env. Chem.*, **97**, 526 (2015).
2. M. Rauf, M. Meetani, S. Hisaindee, *Desalination*, **276**, 13 (2011).
3. A. Kumar, G. Sharma, M. Naushad, P. Singh, S. Kalia, *J. Industr. Eng. Chem. Res.*, **53**, 15549 (2014).
4. D. Pathania, D. Gupta, H. Ala'a, G. Sharma, A. Kumar, M. Naushad, T. Ahamad, S. M. Alshehri, *J. Photochem. Photobiol. A: Chem.*, **329**, 61 (2016).
5. U. Akpan, B. Hameed, *J. Hazard. Mat.*, **170**, 520 (2009).
6. R. Rehman, J. Anwar, T. Mahmud, *J. Chem. Soc. Pak.*, **34**, 460 (2012).
7. W. Subramanian, T.Y. Wu, *Water, Air & Soil Poll.*, **225**, 1 (2014).
8. H. Javadian, M. T. Angaji, M. Naushad, *J. Industr. Eng. Chem. Res.*, **20**, 3890 (2014).
9. N. Shanmugam, T. Sathya, G. Viruthagiri, C. Kalyanasundaram, R. Gobi, S. Ragupathy, *Appl. Surf. Sci.*, **360**, 283 (2016).
10. A. Houas, H. Lachheb, M. Ksibi, E. Elaloui, C. Guillard, J.M. Herrmann, *Appl. Catal. B: Env.*, **31**, 145 (2001).
11. I.K. Konstantinou, T.A. Albanis, *Appl. Catal. B: Env.*, **49**, 1 (2004).
12. R.J. Tayade, T.S. Natarajan, H.C. Bajaj, *Industr. Eng. Chem. Res.*, **48**, 10262 (2009).
13. J. Tang, Z. Zou, J. Yin, J. Ye, *Chem. Phys. Lett.*, **382**, 175 (2003).
14. S. Lakshmi, R. Renganathan, S. Fujita, *J. Photochem. Photobiol. A: Chem.*, **88**, 163 (1995).
15. P. Oancea, V. Meltzer, *Chem. Papers*, **68**, 105 (2014).
16. F. Parolin, U.M. Nascimento, E.B. Azevedo, *Env. Technol.*, **34**, 1247 (2013).
17. V.K. Gupta, R. Jain, A. Nayak, S. Agarwal, M. Shrivastava, *Mat. Sci. Eng., Part C*, **31**, 1062 (2011).
18. M.J.N. Gotostos, C.C. Su, M.D.G. De Luna, M.C. Lu, *J. Env. Sci. Health, Part A*, **49**, 892 (2014).
19. R. Khosravi, A. Zarei, M. Heidari, A. Ahmadvazeli, M. Vosoghi, M. Fazlzadeh, *Korean J. Chem. Eng.*, **35**, 1000 (2018).
20. H. Golestanifar, A. Asadi, A. Alinezhad, B. Haybati, M. Vosoughi, *Deswater*, **57**, 5480 (2016).
21. Y. Rashtbari, S. Hazrati, S. Afshin, M. Fazlzadeh, M. Vosoughi, *Data Brief*, **20**, 1434 (2018).
22. G. Sharma, M. Naushad, D. Pathania, A. Mittal, G. El-Desoky, *Deswater*, **54**, 3114 (2015).
23. G. Sharma, M. Naushad, A. Kumar, S. Rana, S. Sharma, A. Bhatnagar, F. J. Stadler, A. A. Ghfar, M. R. Khan, *Process Safety Env. Protect.*, **109**, 301 (2017).
24. M. Ahemad, M. Kibret, *Biochem. Mol. Biol.*, **1**, 19 (2013).
25. A. A. Alqadami, M. Naushad, M. A. Abdalla, M. R. Khan, Z. A. AlOthman, *J. Chem. Eng. Data*, **61**, 3806 (2016).
26. A. Kumar, G. Sharma, M. Naushad, A. Kumar, S. Kalia, C. Guo, G. T. Mola, *J. Photochem. Photobiol. A: Chem.*, **337**, 118 (2017).
27. M. Rauf, S.S. Ashraf, *Chem. Eng. J.*, **151**, 10 (2009).
28. H. Lachheb, E. Puzenat, A. Houas, M. Ksibi, E. Elaloui, C. Guillard, J.M. Herrmann, *Appl. Catal. B: Env.*, **39**, 75 (2002).
29. M. Naushad, T. Ahamad, B. M. Al-Maswari, A. A. Alqadami, S. M. Alshehri, *Chemical Engineering Journal*, **330**, 1351 (2017).
30. D. Pathania, R. Katwal, G. Sharma, M. Naushad, M. R. Khan, H. Ala'a, *Int. J. Biol. Macromol.*, **87**, 366 (2016).
31. A. B. Albadarin, M. N. Collins, M. Naushad, S. Shirazian, G. Walker, C. Mangwandi, *Chem. Eng. J.*, **307**, 264 (2017).
32. M. Naushad, T. Ahamad, G. Sharma, H. Ala'a, A. B. Albadarin, M. M. Alam, Z. A. AlOthman, S. M. Alshehri, A. A. Ghfar, *Chem. Eng. J.*, **300**, 306 (2016).
33. E. Daneshvar, A. Vazirzadeh, A. Niazi, M. Kousha, M. Naushad, A. Bhatnagar, *J. Cleaner Prod.*, **152**, 443 (2017).

Comparative study of the methods for the determination of organic carbon and organic matter in soils, compost and sludge

V. R. Angelova^{1*}, V. I. Akova², K. I. Ivanov¹

¹Department of Chemistry, Agricultural University-Plovdiv, 4000 Plovdiv, Bulgaria

²Fruit Growing Institute-Plovdiv, 4004 Plovdiv, Bulgaria

Received July 4, 2018; Revised March 19, 2019

The aim of this study was to compare the most commonly used methods for the determination of organic carbon (OC) and organic matter (SOM), and evaluate the capability of LOI (loss on ignition method) to estimate OC, using reference soils, compost and sludge as standards. The use of a titrimetric endpoint (adding phosphoric acid prior to titration) is more suitable for assessing the level of organic carbon in soils with low, medium, high and very high content. The use of a photometric endpoint is more appropriate for samples of medium and high carbon content. LOI 400 and LOI 450 may also be used for the determination of samples with a high organic content whereas LOI 450 - in the determination of samples with an average organic content. LOI 450 can be used to evaluate SOC in a wide range of organic matter concentrations (3-55%). Indirect assessment of the organic carbon content or organic matter using a correction coefficient is not very accurate for samples with average organic carbon content.

Keywords: methods, organic carbon, organic matter, certified samples

INTRODUCTION

For the study of soil reactions and soil contamination, reliable knowledge of soil organic matter (SOM) or soil organic carbon (OC) is required [1-3]. Soil organic matter affects many soil properties including: (i) the soil's capacity to deliver N, P and S and essential elements in plants; (ii) water infiltration and retention, (iii) degree of aggregation and general soil structure that influence air and water balance; (iv) cation exchange capacity; (v) soil colour; and (vi) adsorption or desorption of chemical pollutants.

Organic substances in the soil are generally classified as non-humus and humus [4], with humus substances being a major part of organic matter in most soils. There is a wide variety of methods for assessing the content and composition of humus. The main part of the methods used for quantification of humus is based on the determination of the amount of organic carbon as a predominant element in the composition of the soil organic matter. Carbon from soil samples is converted to carbon dioxide, which is measured directly or indirectly by different methods. Organic carbon can be measured by dry combustion at high temperatures in furnaces and CO₂ determination with automatic analyzers [5] or by oxidation with acidic mixtures followed by titration of the dichromate residue with ferric ammonium sulfate or photometric determination of Cr³⁺ [6]. The dry combustion method is considered to be one of the most precise and accurate procedures, but the high

cost of the apparatus is a major limiting factor determining the use of the method in few laboratories [7].

Oxidation with a bichromic mixture (wet combustion) is widely used as a routine method by most laboratories due to the simplicity and speed of the method as compared to the dry combustion method [8]. Titrimetric and photometric methods can be used for the quantification of organic carbon in the samples [8]. In titrimetric methods, the residue of Cr₂O₇²⁻ is titrated with Fe(NH₄)₂(SO₄)₂·6H₂O (Mohr's salt), while in the spectrophotometric methods the green colour due to Cr³⁺ is quantitated at a wavelength of 660 nm after pre-calibration of the standard glucose method [9,10].

In recent years, it has been increasingly preferred to use alternative methods such as the LOI (loss on ignition) method to wet combustion in order to eliminate the use and disposal of potassium bichromate containing Cr⁶⁺, which is carcinogenic and causes environmental pollution [7,11]. The use of the LOI method for the assessment of soil organic matter and SOC is recommended by many authors and criticized by others. The advantages of the method include the simultaneous analysis of a large number of samples and the low cost of equipment [7]. According to the procedure, soil samples are incinerated at high temperature in a muffle furnace where the organic matter is combusted. When determining the organic matter in soils by the LOI method, an incineration temperature of 400°C is recommended for 16 h [8] or 450°C for 4 h [12]. A combination of a higher

* To whom all correspondence should be sent:
E-mail: vileriz@abv.bg

V. R. Angelova *et al.*: Comparative study of the methods for the determination of organic carbon and organic matter ... temperature with a longer warm-up time may lead to an increase in the results obtained by this method [12]. This may be due to: (i) the removal of hygroscopic and intercrystalline H₂O from clay minerals [13,14], (ii) the loss of H₂O from hydroxyl groups in the sesquioxides [13] and (iii) the charring of the elemental C [15].

Various methods are available in the literature to determine the OC in soil samples. Several studies have been dedicated to the comparison of a traditional wet chemical method using sets of soil samples, others use dry combustion at high temperatures followed by the detection of evolved CO₂ or the SOC content is determined by weight loss on ignition [5,16,17]. Since all methods available have some limitations, the choice of assessment methodology is a critical decision for accurate quantification of SOC content.

The present study is an attempt to solve some of the discussion questions related to the quantification of organic carbon in soils, compost and sludge with low, medium and high content of organic matter using reference materials. Reference materials play a critical role in validating analytical methods and assessing accuracy and comparability of results among different laboratories.

The aim of the present paper was to compare the most commonly used methods for the determination of organic carbon (OC) and organic matter (SOM), evaluate the capability of LOI to estimate OC, as well as their comparability and compatibility, accuracy, precision, speed of determination and convenience, using reference soils, compost and sludge as standards.

EXPERIMENTAL

In the comparative study of the methods for determination of organic carbon, 7 certified soil samples and composts with total carbon content (%) and organic matter content (%) were used as follows: standard 1 (soil) NCS DC 73386 – 0.32 ± 0.13 (OC) and 9.1 ± 0.13 (OM), standard 2 (soil) NCS DC 85106a – 3.85 ± 0.133 (OM), standard 3 (chanel sludge) ISE 859 – 11.4 ± 1.13 (OC) and 21.7 ± 1.0 (OM), standard 4 (clay) ISE 952 – 1.66 ± 0.204 (OC) and 9.17 ± 1.005 (OM), standard 5 (organic ferrasol) ISE 998 - 1.66 ± 0.204 (OC) and 14.0 ± 0.093 (OM), standard 6 MARSE P205 (compost) – 42.4 ± 0.85(OM) and standard 7 MARSE P206 (sewage sludge) – 54.4 ± 0.76 (OM). Organic carbon in the certified samples was determined according to ISO 14235 [10] (oxidation with bichromate and subsequent photometric and titrimetric determination) and the content of organic matter was determined directly by the LOI measurement method at 400°C and 450°C and indirectly by recalculating

the organic carbon content, determined titrimetrically and photometrically by a correction coefficient.

For spectrophotometric determination, a spectrophotometer Pharo 100 (Merck KGaA) was used at a wavelength of 660 nm after preliminary calibration of the standard glucose method.

Titration was performed with an automatic burette with 0.2 N Fe(NH₄)₂(SO₄)₂•6H₂O and a phenylanthranilic acid indicator in two versions - addition of H₃PO₄ prior to titration and titration without addition of H₃PO₄.

According to the LOI methods, the glass (without sample) was heated in a muffle furnace at 400°C for 2 h, and after tempering, its weight was measured. To the tared glass 5 g of air-dry soil were added, heated at 105°C for 24 h. After the tempering of the glass in the desiccator, the weight of the cup and the sample was measured. The glass with the sample was again placed in a muffle furnace at 400°C for 16 h (LOI 400) or 6 h at 450°C (LOI 450).

The loss in soil weight, expressed as a percentage of the dry soil weight, was calculated according to the following equations:

$$\text{LOI (\%)} = (\text{Weight}_{105} - \text{Weight}_{400}) / \text{Weight}_{105} \times 100$$
$$\text{LOI (\%)} = (\text{Weight}_{105} - \text{Weight}_{450}) / \text{Weight}_{105} \times 100$$

All definitions were made in three iterations. Comparison of the results obtained for organic carbon and organic matter by titrimetric methods, photometric methods and LOI was performed by regression analysis using the Windows SPSS program.

RESULTS AND DISCUSSION

The results obtained for the 7 certified standard samples determined according to ISO 14235 [10] (oxidation with bichromate and subsequent photometric and titrimetric determination) are presented in Table 1 and Fig. 1. From the results presented in Table 1 it is evident that there is no significant difference in the quantification of organic carbon with photometric and titrimetric endpoint. In most of the samples tested no significant differences were observed between the values obtained by both methods except for standard 1. Table 1 also presents the results for titrimetric determination of organic carbon with addition and without addition of phosphoric acid prior to titration. A full match of the photometric and titrimetric results is observed with the addition of phosphoric acid prior to titration. The addition of phosphoric acid helps to more accurately determine the equivalent point. The addition of H₃PO₄ to the digestive mix after the sample has cooled was used

V. R. Angelova *et al.*: Comparative study of the methods for the determination of organic carbon and organic matter ... to help eliminate interferences from iron (Fe^{3+}) that may be present in the sample. (sulfochromic oxidation) and the certified values in the samples using linear regression analysis.

Figure 1a shows the relationship between organic carbon determined by ISO 14235 [10]

Table 1. Content of organic carbon in certified standard samples determined by oxidation with bichromate and subsequent photometric and titrimetric determination

Standard	St.1	St.2	St.3	St.4	St.5	St.6	St.7
Certified values	0.32±0.05		11.4±1.3	2.13±0.29	1.66±0.20		
Photometric	0.09±0.01	2.12±0.30	11.91±1.1	2.27±0.30	1.73±0.21	23.18±1.3	27.94±1.5
Titration	0.27±0.05	2.15±0.32	11.02±1.2	2.14±0.31	1.72±0.20	22.16±1.5	25.74±1.5
Titration + H_3PO_4	0.30±0.05	2.13±0.31	11.47±1.1	2.28±0.31	1.78±0.22	23.63±1.5	28.0±1.5

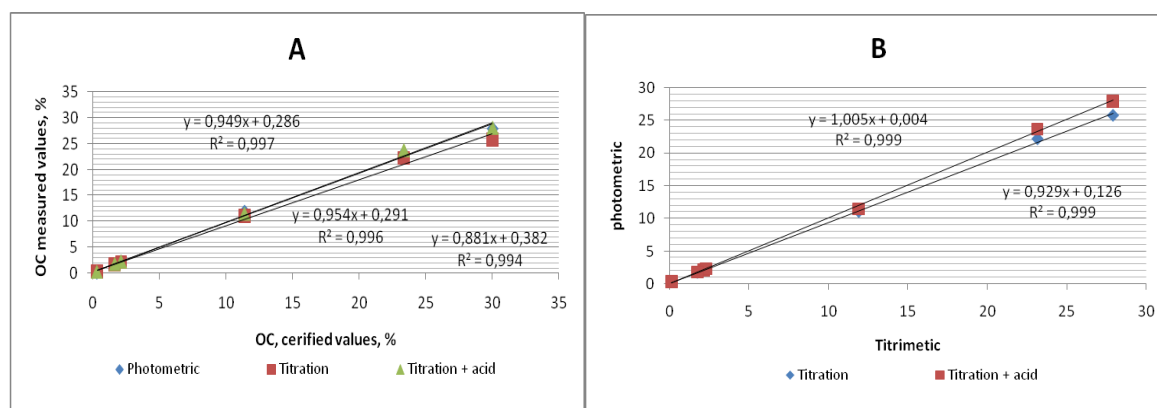


Figure 1. Linear regression analysis between organic carbon determined by sulfochromic oxidation and the certified values in samples (A) and organic carbon determined by photometric and titrimetric methods (B)

Table 2. Content of organic matter in the certified samples recalculated with a coefficient of 1.724

Standard	St.1	St.2	St.3	St.4	St.5	St.6	St.7
Certified values	9.1±0.5	3.85±0.13	21.71±1.0	9.17±1.005	14±0.93	42.4±0.85	54.4±0.74
Photometric	0.16	3.6	20.52	3.92	2.98	40.0	48.2
Titration	0.47	3.71	18.99	3.69	2.97	38.2	44.4
Titration + H_3PO_4	0.51	3.67	19.77	3.93	3.07	40.8	48.3

Table 3. Content of organic matter in the certified samples recalculated by the equation: % organic matter = $0.35 + (1.8 \times \% \text{ organic C})$

Standard	St.1	St.2	St.3	St.4	St.5	St.6	St.7
Certified values	9.1±0.5	3.85±0.13	21.71±1.0	9.17±1.005	14±0.93	42.4±0.85	54.4±0.74
Photometric	0.52	4.16	21.78	4.44	3.46	42.07	50.64
Titration	0.84	4.22	20.19	4.202	3.446	40.24	46.68
Titration + H_3PO_4	0.89	4.18	21.0	4.454	3.55	42.97	50.75

Figure 1b shows the relationship between organic carbon determined photometrically and titrimetrically using linear regression analysis. As seen, there is a well-defined linear dependence ($R = 0.999$) between the amount of organic carbon determined titrimetrically and photometrically, using oxidation with bichromate according to ISO 14235 [10].

There are two approaches to assessing organic matter in soils. The first one is an indirect method based on the recalculation of the results of the organic carbon content in soils with correction coefficient, while the second one is the direct determination of the organic matter by the LOI method. Nelson and Sommers [8] propose to use the correction coefficient 1.724 as

a factor for converting organic carbon into an organic substance. According to Ranney [18], however, the organic matter content in the surface horizons can be sufficiently accurately calculated by the equation:

$$\% \text{ organic matter} = 0.35 + (1.8 \times \% \text{ organic C}).$$

Tables 2 and 3 show the results obtained for the organic matter content of the certified samples recalculated on the basis of results obtained for organic C by the titrimetric and photometric methods.

As can be seen from Tables 2 and 3, the results for organic carbon obtained by sulfochromic oxidation using the ISO method with a photometric endpoint can be used for

V. R. Angelova *et al.*: Comparative study of the methods for the determination of organic carbon and organic matter ... assessing the organic matter in cases of low and high organic carbon content in the samples. A very good match of the results between the calculated organic matter based on the organic carbon obtained by the titrimetric methods is observed for standards 2, 3, 6 and 7. However, in standards 1, 4 and 5 (with an average organic content) unsatisfactory results are obtained.

The results obtained for the seven certified standard samples by LOI 400 and LOI 450 are presented in Table 4.

Table 4. Content of organic matter in the certified samples by LOI 400 and LOI 450

Standard	St.1	St.2	St.3	St.4	St.5	St.6	St.7
Certified values	9.1±0.5	3.85±0.13	21.71±1.0	9.17±1.005	14±0.93	42.4±0.85	54.4±0.74
LOI 400	3.76±0.5	5.92±0.20	20.72±1.1	6.65±0.85	7.58±0.56	42.80±0.90	53.14±0.80
LOI 450	6.33±0.5	6.34±0.20	21.08±1.2	9.03±0.95	13.66±0.99	41.85±0.90	53.39±0.85

There is a good match of results for both LOI 400 and LOI 450 in standard 3 (chanel sludge), 6 (compost) and 7 (sewage sludge), i.e. in samples with a high organic matter content. For these samples, the organic matter content determined at 400°C for 16 h is identical to that determined at 450°C for 6 h. The results presented in Table 4 show that the duration and temperature of the sample heating have influence. Increased temperature and shorter heating of samples with low and medium organic matter content lead to more accurate results corresponding to the certified values. For standards 1, 4 and 5, the organic matter content determined at 400°C is significantly lower than at 450°C, suggesting that the incomplete combustion of organic matter at this lower temperature and longer heating time cannot compensate for the low (400°C) incineration temperature. Apparently the sample processing time is not sufficient and should be increased (up to 24 h and more) to obtain correct results for standard samples 1, 4 and 5.

The temperature at which LOI is determined is important, as this method not only measures organic matter, but also the CO₂ losses from carbonates and the loss of structural water from clay minerals. Studies of Ball [15] and Ben-Dor and Banin [19] show that dehydroxylation of phyllosilicates occurs at temperatures below 450°C. Gibbsite is an exception, as it is reported that this clay mineral loses structural water when heated at 300 to 350° C [18]. This process depends not only on the amount of clay but also on its mineralogical nature. Standard sample 4 is clay, and 5 is organic ferrasol. It is known that organic ferrasol is predominant in kaolinite and has a high content of sesquioxides. A problem with the LOI method is that some clay minerals may lose structural water (i.e, water that is part of the matrix) or hydroxyl groups at temperatures (400-450°C) used in the incineration of samples.

The loss of structural water will increase the total weight loss of the sample, which will result

in higher results for the organic matter content of the samples. These weight losses can have a significant impact for soils containing little organic matter and high clay content. At a low organic content, the dehydroxylating of clays is much more likely and the loss of weight from the dehydroxylating of the clay may be greater.

Figure 2 shows the relationship between the organic matter determined by LOI 400 and LOI 450 and the certified values in the samples using a linear regression analysis.

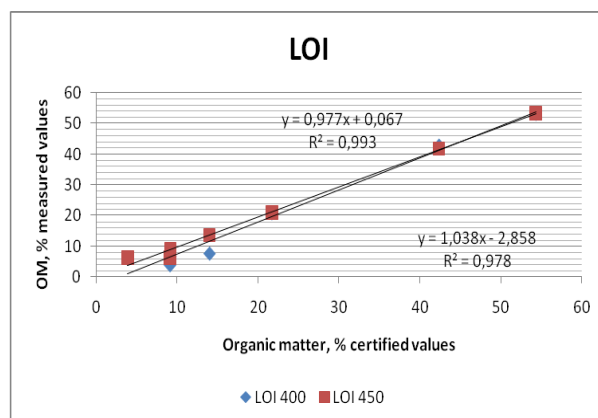


Fig. 2. Linear regression analysis between the organic matter determined by LOI 400 and LOI 450 and the certified values in the samples.

As can be seen from Fig. 2, there is a linear relationship between the amount of soil organic matter (SOM) determined by the LOI method and its content in the certified samples. The R² regression coefficient is 0.997 for LOI 450 and 0.991 for LOI 400. The values of the "b" regression coefficient below 1 suggest that some components other than organic matter are lost during heating while the coefficients greater than 1 indicate that an incomplete removal of organic matter has occurred [19,20]. The results we obtained show that the coefficient is higher than 1 (5.073) at the lower temperature (400°C), while at the higher temperature (450°C) the coefficient is close to 1 (1.094).

Most authors use regression analysis to

V. R. Angelova *et al.*: Comparative study of the methods for the determination of organic carbon and organic matter ... describe the relationship between OC and OM through LOI. The idea of using a factor that can turn LOI into organic C is attractive because OM can easily be determined by LOI, unlike organic C.

The results obtained for an organic substance by the LOI method were compared with the data for organic carbon, obtained by the titrimetric methods and photometric method (Fig. 3). A very good correlation between LOI 400 and LOI 450 with OC is found. The comparison of the organic substance obtained by oxidation with potassium dichromate with a titrimetric and photometric endpoint and LOI 400 and LOI 450 in a wide range of the organic matter concentration (approximately 3 - 55%) shows a correlation coefficient of 0.99.

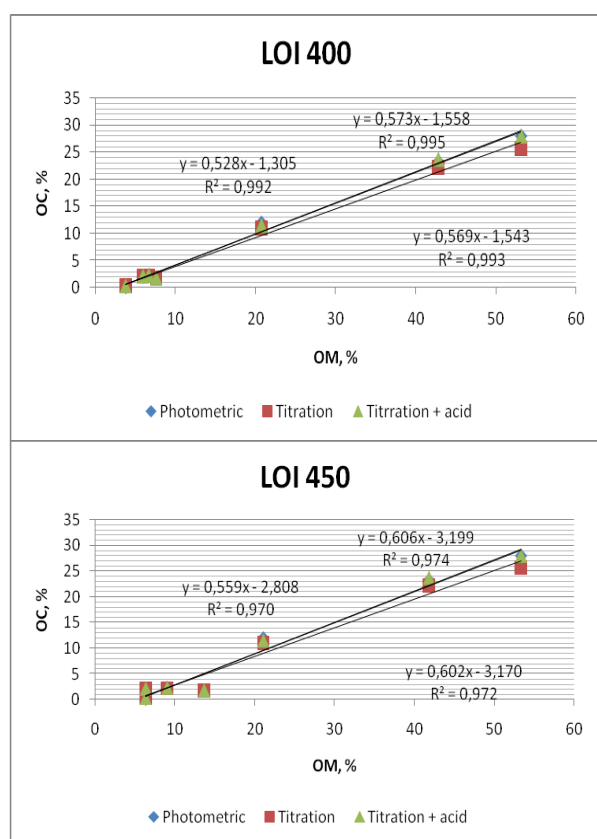


Fig. 3. Linear regression analysis between the organic matter determined by the LOI method and organic carbon, obtained by the titrimetric methods and the photometric method.

The results obtained show that LOI can be used to evaluate SOC in samples with low, medium and high organic carbon contents.

CONCLUSIONS

The most important criteria for choosing a method for determining organic carbon and organic matter in soils, composts and sludge are the reagent consumption, the duration of the

analysis, the accuracy of measurement and the reproducibility of the results. Considering these criteria, we can recommend the use of sulfochromic oxidation by ISO to determine organic carbon in the samples. The use of the titrimetric endpoint (adding phosphoric acid prior to titration) is more suitable for assessing the level of organic carbon in soils with low, medium, high and very high content. The use of a photometric endpoint is more appropriate for samples of medium and high carbon content.

LOI analyses have advantages primarily related to the ability to simultaneously determine a large number of samples. LOI 400 and LOI 450 may also be used for the determination of samples with a high organic content. We recommend the use of LOI 450 in the determination of samples with an average organic content.

LOI 450 can be used to evaluate SOC in a wide range of organic matter concentrations (3-55%).

Acknowledgement: The financial support by the Bulgarian National Science Fund Project DFNI H04/9 is greatly appreciated.

REFERENCES

1. J.-I. Drever, The geochemistry of natural waters, surface and groundwater environments, Prentice Hall, Upper Saddle River, New York, 1997.
2. J.-G. Smith, *Geograf. Annal., Series A: Phys. Geogr.*, **85**, 91 (2003).
3. N.-C. Brady, R. Weil, Nature and properties of soils, Prentice Hall, Upper Saddle River, New York, 2007.
4. M. Klavins, Aquatic Humic Substances: Characterisation, Structure and Genesis, University of Latvia, Riga, 1997.
5. B. Schumacher, Methods for the determination of total organic carbon in soils and sediments, NCEA-C-1282, EMASC-001, 1, 2002.
6. R.-H. Ellerbrock, H.-H. Gerke, J. Bachmann, M.-O. Goebel, *Soil Sci. Soc. Am. J.*, **69**, 57 (2005).
7. M.-E. Konen, P.-M. Jacobs, C.-L. Burras, B.-J. Talaga, J.-A. Mason, *Soil Sci. Soc. Am. J.*, **66**, 1878 (2002).
8. D.-W. Nelson, L.-E. Sommers, *Proc. Indiana Acad. Sci.*, **84**, 456 (1975).
9. D.-L. Heanes, *Commun. Soil Sci. Plant Anal.*, **15**, 1191 (1984).
10. ISO 14235, Soil quality. Determination of organic carbon by sulfochromic oxidation, 1988.
11. E. E. Schulte, A. Kaufmann, J. B. Peter, *Commun. Soil Sci. Plant Anal.*, **22**, 159 (1991).
12. C.-A. Cambardella, A.-M. Gajda, J.-W. Doran, B.-J. Wienhold, T.-A. Kettler, in: Assessment methods for soil carbon, R. Lal *et al.* (eds.), Lewis Publ., New York, 2001, p. 349.

- V. R. Angelova *et al.*: Comparative study of the methods for the determination of organic carbon and organic matter ...
13. A. Goldin, *Commun. Soil Sci. Plant Anal.*, **18**, 1111 (1987).
 14. M.-B. David, *Commun. Soil Sci. Plant Anal.*, **19**, 1593 (1988).
 15. D.-F. Ball, *J. Soil Sci.*, **15**, 84 (1964).
 16. S. Sleutel, S. De Neve, B. Singier, G. Hofman, *Communications in Soil Science and Plant Analysis*, **38**, 2647 (2007).
 17. H. Spiegel, E. Filcheva, P. Hegymegi, A. Gal, F. Verheijen, *Soil Sci. Agrochem. Ecol.*, **4**, 3 (2007).
 18. R.-W. Ranney, *Soil Sci. Soc. Am. Proc.*, **33**, 809 (1969).
 19. E. Ben-Dor, A. Banin, *Commun. Soil Sci. Plant Anal.*, **20**, 1675 (1989).
 20. T. T. Gorsuch, *The destruction of organic matter*, Oxford, New York, Pergamon Press, 1970.

Theory of staircase cyclic voltammetry of two electrode reactions coupled by a chemical reaction

Š. Komorsky-Lovrić, M. Lovrić

Divkovićevo 13, Zagreb 10090, Croatia

Received October 15, 2018, Accepted February 27, 2019

Two reversible electrode reactions that are connected by either reversible or totally irreversible chemical reactions are theoretically analysed by staircase cyclic voltammetry. The dependence of peak potentials on the thermodynamic and kinetic parameters is calculated. If the mechanism is permanently in equilibrium, the stability constant of the reversible chemical reaction can be determined. Furthermore, the critical kinetic parameter is determined and its application to the measurement of the forward rate constant of the chemical reaction is demonstrated. Also, the influence of the kinetics of electrode reactions is discussed.

Keywords: ECE mechanism; Cyclic voltammetry; Theory

INTRODUCTION

The acronym ECE denotes an electrochemical mechanism in which two electrode reactions are coupled by a chemical reaction in the way that the product of the first electrode reaction is the reactant in a chemical reaction and the product of the latter is a reactant in a second electrode reaction [1-7]. This mechanism can be considered as a special case of the general nine-member square scheme [8-11]. It was observed in electroreduction of p-nitrosophenol [12, 13], carbonylmanganese compounds [14-16], benzenesulfonyl fluoride [17, 18], 1-butyl-3-methylimidazolium bistriflimide [19], uranium complexes of acetylacetonate [20], hexacyanochromate(III) [21], bimetallic organometallic complexes [22] and adriamycin [23], as well as in electrooxidation of tocopherols [24], copper(II) complex of thyrotropin-releasing hormone [25], methylcatechol [26, 27], dopamine [28] and aromatic hydrocarbons [29, 30]. The theory of the ECE mechanism is developed for chronoamperometry [31-33], d. c. polarography [34-36], linear scan [37, 38], cyclic [21, 39] and square wave voltammetry [40-44], rotating disk [45] and ring-disk electrode measurements [46], the scanning electrochemical microscopy [47] and the surface reactions in protein film voltammetry [48, 49]. In this paper the main properties of responses of ECE mechanism in staircase cyclic voltammetry are recapitulated. The influences of both the thermodynamic constants under equilibrium conditions and the kinetic parameters of reversible and totally irreversible chemical reactions, as well as electrode reactions are considered.

MODELS

The following reactions are investigated:



It is assumed that the mass transport can be described by the stationary, planar, semiinfinite diffusion model and that the reagent X^- is present in great excess, so that the variation of its concentration can be neglected.

(1) The first model is based on the assumption that the chemical reaction is permanently in equilibrium. Its mathematical representation is given by the following differential equations and boundary conditions:

$$\partial c_A / \partial t = D \partial^2 c_A / \partial x^2 \quad (4)$$

$$\partial c_{Int} / \partial t = D \partial^2 c_{Int} / \partial x^2 \quad (5)$$

$$\partial c_F / \partial t = D \partial^2 c_F / \partial x^2 \quad (6)$$

$$c_{Int} = c_B + c_E \quad (7)$$

$$t = 0, x \geq 0: \quad c_A = c_A^*, \quad c_B = c_E = c_F = 0, \\ c_X = c_X^* \quad (8)$$

$$t > 0, x \rightarrow \infty: \quad c_A \rightarrow c_A^*, \quad c_X \rightarrow c_X^*, \quad c_B \rightarrow 0 \\ c_E \rightarrow 0, \quad c_F \rightarrow 0 \quad (9)$$

$$x = 0: \quad c_X = c_X^* \quad (10)$$

$$c_{B,x=0} = c_{A,x=0} \exp(F(E - E_1^0)/RT) \quad (11)$$

$$K c_X^* = c_{E,x=0} / c_{B,x=0} \quad (12)$$

$$c_{F,x=0} = c_{E,x=0} \exp(F(E - E_2^0)/RT) \quad (13)$$

* To whom all correspondence should be sent:
E-mail: mlovric@irb.hr

$$D(\partial c_A/\partial x)_{x=0} = I_1/FS \quad (14)$$

$$D(\partial c_{Int}/\partial x)_{x=0} = (I_2 - I_1)/FS \quad (15)$$

$$D(\partial c_F/\partial x)_{x=0} = -I_2/FS \quad (16)$$

$$x > 0: Kc_X^* = c_E/c_B \quad (17)$$

The meanings of symbols are reported in Table 1.

Table 1. Meanings of symbols

α_1, α_2	Transfer coefficients of the first and the second electrode reactions
c_A, c_B, c_E, c_F	Concentrations of species A, B ⁺ , E and F ⁺
c_A^*, c_X^*	Concentrations of species A and X ⁻ in the bulk of solution
D	Common diffusion coefficient
E	Electrode potential
E_1^0, E_2^0	Standard potentials of the first and the second electrode reactions
ΔE	Potential step in staircase cyclic voltammetry
$E_{p,a}, E_{p,c}$	Anodic and cathodic peak potentials
F	Faraday constant
I_1, I_2	Currents of the first and the second electron transfer
K	Equilibrium constant of the chemical reactions
k	Rate constant of irreversible chemical reaction
k_f, k_b	Rate constants of reversible chemical reaction
k_{s1}, k_{s2}	Rate constants of the first and the second electrode reactions
R	Gas constant
S	Electrode surface area
T	Temperature
t	Time
v	Scan rate

Differential equations are solved by the numerical method [50, 51]. In staircase voltammetry the potential is changed in a stepwise manner and the scan rate is defined as the ratio of the height and the duration of the step: $v = \Delta E/\tau$. The current is measured at the end of each step. The dimensionless current is defined as follows: $\Phi_k = I_k(FSc_A^*)^{-1}(DvF/RT)^{-1/2}$, where $k = 1$ or 2 . In the simulation the time increment $d = \tau/25$ and the fixed value $\Delta E = 5$ mV were used. The numerical solution is the system of recursive formulae for the dimensionless current:

$$\Phi_{2,m} = u_1 u_2 (1 + u_4)^{-1} - \sum_{j=1}^{m-1} \Phi_{2,j} S_{m-j+1} \quad (18)$$

$$\Phi_{1,m} = (u_1 u_5 + \sum_{j=1}^m \Phi_{2,j} S_{m-j+1})(1 + u_5)^{-1} - \sum_{j=1}^{m-1} \Phi_{1,j} S_{m-j+1} \quad (19)$$

$$u_1 = 5\sqrt{\pi RT/F\Delta E}/2 \quad (20)$$

$$u_2 = Kc_X^* \exp(F(E - E_1^0)/RT) \exp(F(E - E_2^0)/RT) \quad (21)$$

$$u_3 = Kc_X^* [1 + \exp(F(E - E_2^0)/RT)] \quad (22)$$

$$u_4 = (1 + u_3) \exp(F(E - E_1^0)/RT) \quad (23)$$

$$u_5 = (1 + Kc_X^*) \exp(F(E - E_1^0)/RT) \quad (24)$$

$$s_p = \sqrt{p} - \sqrt{p-1} \quad (25)$$

$$m = 1, 2, 3 \dots \quad (26)$$

The sum $\Phi = \Phi_1 + \Phi_2$ is reported as a function of electrode potential.

(2) In the second model it is assumed that the chemical reaction is totally irreversible and of the first order:



Consequently, equations (12) and (17) have to be replaced by the following equations:

$$\partial c_B/\partial t = D\partial^2 c_B/\partial x^2 - kc_B \quad (28)$$

$$D(\partial c_B/\partial x)_{x=0} = -I_1/FS \quad (29)$$

The following solution is obtained:

$$\Phi_{1,m} = [u_1 u_6 - \kappa^{-1/2} \sum_{j=1}^{m-1} \Phi_{1,j} P_{m-j+1} - u_6 \sum_{j=1}^{m-1} \Phi_{1,j} S_{m-j+1}] (P_1 \kappa^{-1/2} + u_6)^{-1} \quad (30)$$

$$\Phi_{2,m} = [\sum_{j=1}^m \Phi_{1,j} S_{m-j+1} - u_1 \kappa^{-1/2} \sum_{j=1}^m \Phi_{1,j} P_{m-j+1}] u_7 - \sum_{j=1}^{m-1} \Phi_{2,j} S_{m-j+1} \quad (31)$$

$$u_6 = \exp(F(E - E_1^0)/RT)/u_1 \quad (32)$$

$$u_7 = \exp(F(E - E_2^0)/RT) / [1 + \exp(F(E - E_2^0)/RT)] \quad (33)$$

$$\kappa = kRT/Fv \quad (34)$$

$$P_i = \operatorname{erf}\sqrt{\kappa qi} - \operatorname{erf}\sqrt{\kappa q(i-1)} \quad (35)$$

$$q = F\Delta E/25RT \quad (36)$$

(3) The third model extends the second one by assuming that electrode reactions are not fast and reversible. Under this condition, equations (11) and (13) must be replaced by the following equations:

$$I_1/FS = -k_{s1} \exp(-\alpha_1 F(E - E_1^0)/RT) [c_{B,x=0} - c_{A,x=0} \exp(F(E - E_1^0)/RT)] \quad (37)$$

$$I_2/FS = -k_{s2} \exp(-\alpha_2 F(E - E_2^0)/RT) [c_{F,x=0} - c_{E,x=0} \exp(F(E - E_2^0)/RT)] \quad (38)$$

The solution is as follows:

$$\Phi_{1,m} = [u_8 - u_9 \sum_{j=1}^{m-1} \Phi_{1,j} P_{m-j+1} - u_8 u_1^{-1} \sum_{j=1}^{m-1} \Phi_{1,j} S_{m-j+1}] / u_{10} \quad (39)$$

$$\Phi_{2,m} = [u_{11} u_1^{-1} \sum_{j=1}^m \Phi_{1,j} S_{m-j+1} - u_{11} \kappa^{-1/2} \sum_{j=1}^m \Phi_{1,j} P_{m-j+1} - u_{12} u_1^{-1} \sum_{j=1}^{m-1} \Phi_{2,j} S_{m-j+1}] / (1 + u_{12} u_1^{-1}) \quad (40)$$

$$u_8 = \lambda_1 \exp((1 - \alpha_1) F(E - E_1^0)/RT) \quad (41)$$

$$u_9 = \lambda_1 \exp(-\alpha_1 F(E - E_1^0)/RT) \kappa^{-1/2} \quad (42)$$

$$u_{10} = 1 + u_9 P_1 + u_8 / u_1 \quad (43)$$

$$u_{11} = \lambda_2 \exp((1 - \alpha_2) F(E - E_2^0)/RT) \quad (44)$$

$$u_{12} = \lambda_2 \exp(-\alpha_2 F(E - E_2^0)/RT) [1 + \exp(F(E - E_2^0)/RT)] \quad (45)$$

$$\lambda_1 = k_{s1} (DFv/RT)^{-1/2} \quad (46)$$

$$\lambda_2 = k_{s2} (DFv/RT)^{-1/2} \quad (47)$$

(4) The last model is a general solution for two reversible electrode reactions coupled by a kinetically controlled reversible chemical reaction. In this case equations (12) and (17) must be replaced by the following equations:

$$c_H = K c_X^* c_B - c_E \quad (48)$$

$$\partial c_H / \partial t = D \partial^2 c_H / \partial x^2 - \varepsilon c_H \quad (49)$$

$$D(\partial c_H / \partial x)_{x=0} = -K c_X^* I_1 / FS - I_2 / FS \quad (50)$$

$$\varepsilon = k_b (1 + K c_X^*) \quad (51)$$

$$K = k_f / k_b \quad (52)$$

The solution is given by the following recursive formulae:

$$\begin{aligned} \Phi_{2,m} = & -z_8 z_7^{-1} + z_9 z_7^{-1} \sum_{j=1}^{m-1} \Phi_{2,j} S_{m-j+1} + \\ & z_{10} z_7^{-1} \sum_{j=1}^{m-1} \Phi_{2,j} P_{m-j+1} + \\ & z_{11} z_7^{-1} \sum_{j=1}^{m-1} \Phi_{1,j} S_{m-j+1} + \\ & z_{12} z_7^{-1} \sum_{j=1}^{m-1} \Phi_{1,j} P_{m-j+1} \end{aligned} \quad (53)$$

$$\begin{aligned} \Phi_{1,m} = & z_8 + z_1 z_5^{-1} \sum_{j=1}^m \Phi_{2,j} S_{m-j+1} - \\ & z_2 z_5^{-1} \sum_{j=1}^m \Phi_{2,j} P_{m-j+1} - z_{13} \sum_{j=1}^{m-1} \Phi_{1,j} S_{m-j+1} - \\ & z_3 z_5^{-1} \sum_{j=1}^{m-1} \Phi_{1,j} P_{m-j+1} \end{aligned}$$

$$z_1 = u_1^{-1} (1 + K c_X^*)^{-1} \quad (55)$$

$$z_2 = (1 + K c_X^*)^{-3/2} \kappa_b^{-1/2} \quad (56)$$

$$z_3 = K c_X^* z_2 \quad (57)$$

$$z_4 = K c_X^* z_1 \quad (58)$$

$$z_5 = z_1 + u_1^{-1} \exp(F(E - E_1^0)/RT) + z_3 P_1 \quad (59)$$

$$z_6 = [z_4 + z_3 P_1] \exp(F(E - E_2^0)/RT) \quad (60)$$

$$z_7 = z_5^{-1} (z_1 - z_2) - z_6^{-1} [u_1^{-1} + (z_4 + z_2 P_1) \exp(F(E - E_2^0)/RT)] \quad (61)$$

$$z_8 = z_5^{-1} \exp(F(E - E_1^0)/RT) \quad (62)$$

$$z_9 = u_1^{-1} z_6^{-1} + z_4 z_6^{-1} \exp(F(E - E_2^0)/RT) - z_1 z_5^{-1} \quad (63)$$

$$z_{10} = z_2 z_6^{-1} \exp(F(E - E_2^0)/RT) + z_2 z_5^{-1} \quad (64)$$

$$z_{11} = z_{13} - z_4 z_6^{-1} \exp(F(E - E_2^0)/RT) \quad (65)$$

$$z_{12} = z_3 z_6^{-1} \exp(F(E - E_2^0)/RT) + z_3 z_5^{-1} \quad (66)$$

$$z_{13} = [z_1 + u_1^{-1} \exp(F(E - E_1^0)/RT)] / z_5 \quad (67)$$

$$\kappa_b = k_b RT / Fv \quad (68)$$

$$P_i = \frac{\operatorname{erf} \sqrt{\kappa_b (1 + K c_X^*) q i} - \operatorname{erf} \sqrt{\kappa_b (1 + K c_X^*) q (i - 1)}}{\operatorname{erf} \sqrt{\kappa_b (1 + K c_X^*) q i} - \operatorname{erf} \sqrt{\kappa_b (1 + K c_X^*) q (i - 1)}} \quad (69)$$

RESULTS AND DISCUSSION

Staircase cyclic voltammograms of the mechanisms (1) – (3) under equilibrium conditions depend on the standard potentials of electron transfers and the dimensionless constant $K c_X^*$ of the chemical reaction. We shall investigate an ideal case in which the concentration of reagent X^- can be changed experimentally from zero to the limit of solubility. If $E_1^0 = E_2^0$ and $K c_X^* = 1$, the response exhibits a single pair of peaks with the dimensionless peak currents $\Phi_{p,a} = 0.773$ and $\Phi_{p,c} = -0.574$ that appear at $E_{p,a} = 0.035$ V vs. E_1^0 and $E_{p,c} - E_1^0 = -0.040$ V. This is shown in Fig. 1. The real peak currents depend linearly on the square root of scan rate, but the peak potentials are independent of the scan rate. If the concentration of X^- is reduced to zero, only the first electrode reaction occurs and the peak currents are diminished to 0.3865 and -0.287, but the peak potentials do not change. The peak separation is 75 mV and the mid-potential is

close to the first standard potential. The difference of -2.5 mV is the consequence of changing the potential in discrete quantity ΔE .

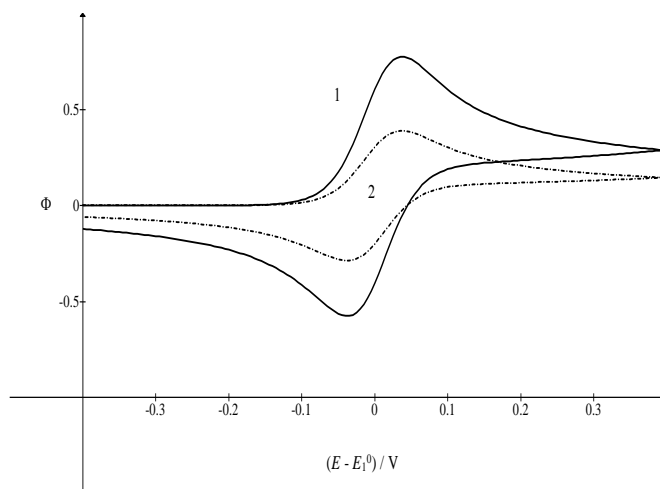


Fig. 1. Dimensionless staircase cyclic voltammograms of ECE mechanism under equilibrium conditions (eqs. 18 and 19). $\Delta E = 5$ mV, $E_2^0 = E_1^0$ and $Kc_X^* = 1$ (1) and 0 (2).

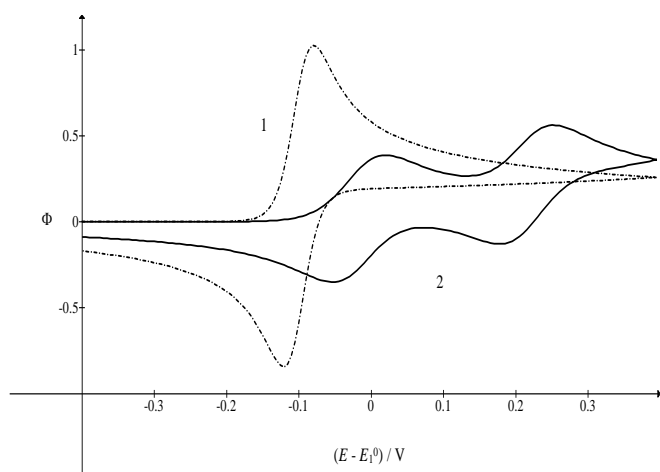


Fig. 2. Dimensionless staircase cyclic voltammograms of ECE mechanism under equilibrium conditions. $Kc_X^* = 1$ and $(E_2^0 - E_1^0) / V = -0.2$ (1) and 0.2 (2).

Fig. 2 shows the influence of the difference in standard potentials on cyclic voltammograms. If $E_2^0 - E_1^0 = -0.2$ V, the intermediate is unstable and only two peaks appear: $\Phi_{p,a} = 1.023$ and $\Phi_{p,c} = -0.844$. The peak potentials are $E_{p,a} - E_1^0 = -0.080$ V and $E_{p,c} - E_1^0 = -0.120$ V. In the case of stable intermediate, the voltammogram consists of two pairs of peaks: $\Phi_{p,1,a} = 0.387$ and $\Phi_{p,1,c} = -0.350$, appearing at $E_{p,1,a} - E_1^0 = 0.020$ V and $E_{p,1,c} - E_1^0 = -0.055$ V, and $\Phi_{p,2,a} = 0.562$ and $\Phi_{p,2,c} = -0.128$ that appear at $E_{p,2,a} - E_1^0 = 0.250$ V and $E_{p,2,c} - E_1^0 = 0.180$ V. Table 2 reports the peak potentials as a function of the difference between standard potentials.

Table 2. Dependence of anodic and cathodic peak potentials on the difference between standard potentials for $Kc_X^* = 1$.

$(E_2^0 - E_1^0) / V$	$E_{p,1,a} / V$	$E_{p,1,c} / V$	$E_{p,2,a} / V$	$E_{p,2,c} / V$
-0.300	-0.130	-0.170		
-0.250	-0.105	-0.145		
-0.200	-0.080	-0.120		
-0.150	-0.055	-0.095		
-0.100	-0.030	-0.075		
-0.050	0.000	-0.050		
0.000	0.035	-0.040		
0.050	0.090	-0.045		
0.060	0.105	-0.045		
0.070	0.115	-0.045		
0.080	0.125	-0.045		
0.090	0.135	-0.050		
0.100	0.030	-0.050	0.150	-
0.150	0.020	-0.050	0.200	0.125
0.200	0.020	-0.055	0.250	0.180
0.250	0.020	-0.055	0.305	0.230
0.300	0.020	-0.055	0.355	0.280

If $E_2^0 - E_1^0 < -0.1$ V, the peak separation is 40 mV and the mid-potential is equal to the average of standard potentials. The latter is in agreement with the properties of the simple EE mechanism [52 - 54]. The peak separation increases to 75 mV for $E_2^0 = E_1^0$ and to 185 mV for $E_2^0 - E_1^0 = 0.090$ V. This is the consequence of the development of the second pair of peaks, as can be seen in Fig. 3. The response is split into two pairs of peaks if $E_2^0 - E_1^0 > 0.1$ V. The peak separations are 75 mV and the mid-potentials are equal to $E_1^0 - 17.5$ mV and $E_2^0 + 17.5$ mV. In the further analysis the mid-potential will be neglected.

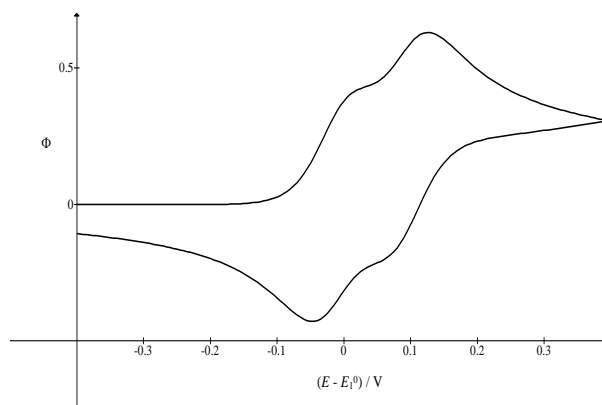


Fig. 3. CV of ECE in the equilibrium. $Kc_X^* = 1$ and $E_2^0 - E_1^0 = 0.080$ V.

The second variable that governs the response is the dimensionless constant Kc_X^* . An example is shown in Fig. 4.

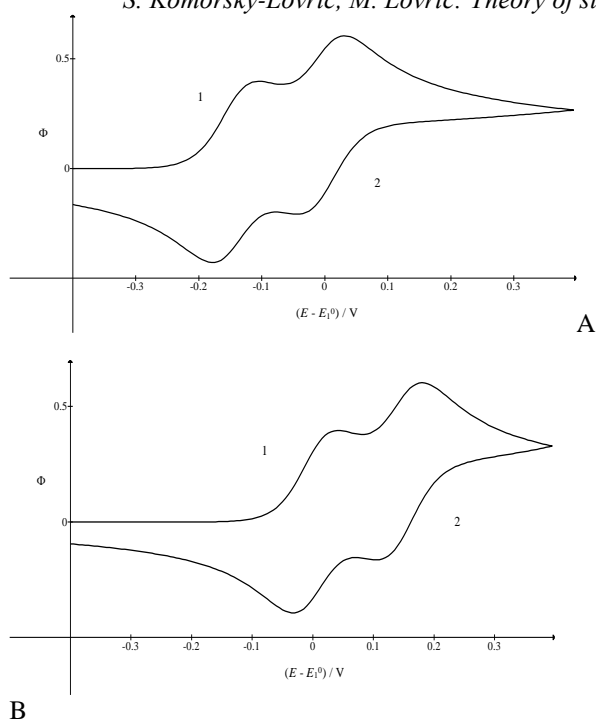


Fig. 4. CV of ECE in the equilibrium. $E_2^0 = E_1^0$ and $Kc_X^* = 300$ (A) and 0.003 (B). Two pairs of peaks are marked.

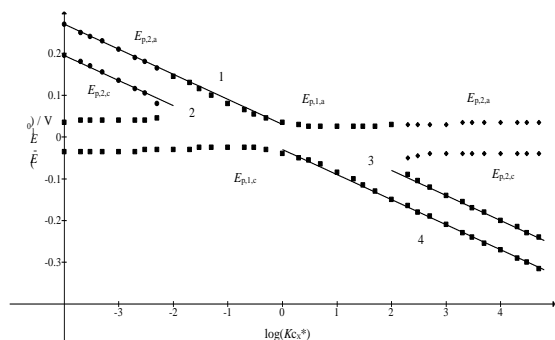


Fig. 5. Relationship between peak potentials in CV and the logarithm of dimensionless equilibrium constant of chemical reaction. ECE in the permanent equilibrium. $E_2^0 = E_1^0$. The straight lines are linear approximations.

If $E_2^0 = E_1^0$ and $Kc_X^0 = 300$, the first electron transfer occurs at the potential that is lower than the standard potential ($E_{p,1,a} - E_1^0 = -0.105$ V and $E_{p,1,c} - E_1^0 = -0.180$ V) while the second charge transfer remains unchanged ($E_{p,2,a} - E_1^0 = 0.030$ V and $E_{p,2,c} - E_1^0 = -0.045$ V). This is because the chemical reaction consumes the product of the first electrode reaction and decreases the formal potential of this reaction.

The situation is opposite if $Kc_X^* = 0.003$ and the chemical equilibrium is shifted towards B^+ species. In this case additional energy is required to surmount the chemical reaction preceding the second charge transfer [55]. For this reason the peak potentials corresponding to the second electrode reaction are higher than the second standard

potential: $E_{p,2,a} - E_1^0 = 0.180$ V and $E_{p,2,c} - E_1^0 = 0.105$ V. These explanations are confirmed by the dependence of anodic and cathodic peak potentials on the logarithm of the product Kc_X^* that is shown in Fig. 5 for $E_2^0 = E_1^0$. Under this condition the cyclic voltammogram splits in two pairs of peaks if either $Kc_X^* > 100$ or $Kc_X^* < 0.01$. Within these boundaries only two peaks appear, but their separation increases from 75 mV for $Kc_X^* = 1$ to 110 mV for $Kc_X^* = 10$, or $Kc_X^* = 0.1$, and to 180 mV for $Kc_X^* = 100$ or $Kc_X^* = 0.01$. In the split responses one pair of peak potentials depends linearly on the logarithm of Kc_X^* while the other pair is independent of this variable. The straight lines in Fig. 5 are defined by the following equations: $E_{p,2,a} - E_1^0 = -2.3 (RT/F) \log(Kc_X^*) + 0.030$ V (1), $E_{p,2,c} - E_1^0 = -2.3 (RT/F) \log(Kc_X^*) - 0.045$ V (2), $E_{p,1,a} - E_1^0 = -2.3 (RT/F) \log(Kc_X^*) + 0.040$ V (3) and $E_{p,1,c} - E_1^0 = -2.3 (RT/F) \log(Kc_X^*) - 0.030$ V (4). One can see that the equilibrium constant K can be estimated if the product Kc_X^* can be changed either from 0.1 to 100, or from 0.01 to 10. In the first case the cathodic peak potential changes from $E_{p,1,c} - E_1^0 = -0.030$ V to the straight line 4. The intersection of these two lines reveals the equilibrium constant: $\log(Kc_X^*)_{cross} = 0$ and $K = (c_X^*)_{cross}^{-1}$. The same applies to the intersection of the straight line $E_{p,2,a} - E_1^0 = 0.030$ V and the straight line 1. In experiments the condition $c_X^* \gg c_A^*$ must be satisfied.

The relationship between peak potentials and the equilibrium constant depends on the difference in standard potentials. This is shown in Figs. 6 and 7.

If two pairs of peaks appear at all values of $\log(Kc_X^*)$, the first electrode reaction is influenced by the chemical reaction if $Kc_X^* > 0.1$, while the peak potentials of the second electrode reaction depend on $\log(Kc_X^*)$ if it is smaller than 1. The straight lines 1 and 2 in Fig. 6 satisfy the equations: $E_{p,2,a} - E_1^0 = -2.3 (RT/F) \log(Kc_X^*) + E_2^0 - E_1^0 + 0.035$ V and $E_{p,2,c} - E_1^0 = -2.3 (RT/F) \log(Kc_X^*) + E_2^0 - E_1^0 - 0.040$ V. If $Kc_X^* > 10$ the peak potentials acquire constant values $E_{p,2,a} - E_1^0 = E_2^0 - E_1^0 + 0.035$ V and $E_{p,2,c} - E_1^0 = E_2^0 - E_1^0 - 0.040$ V. These relationships can be used for the calculation of equilibrium constant. The lines 3 and 4 in Figs. 5 and 6 are identical.

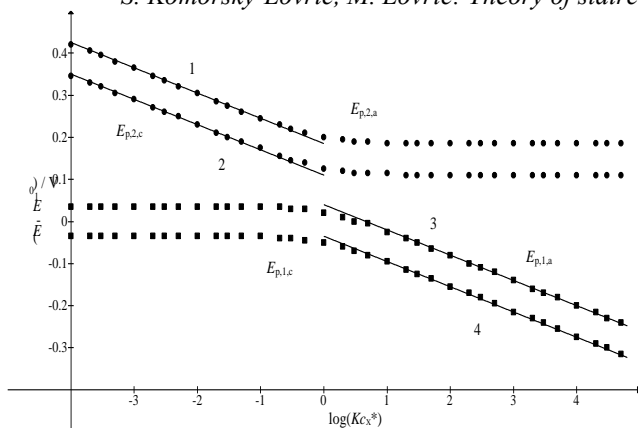


Fig. 6. Dependence of peak potentials on the logarithm of the product Kc_X^* . $E_2^0 - E_1^0 = 0.150$ V.

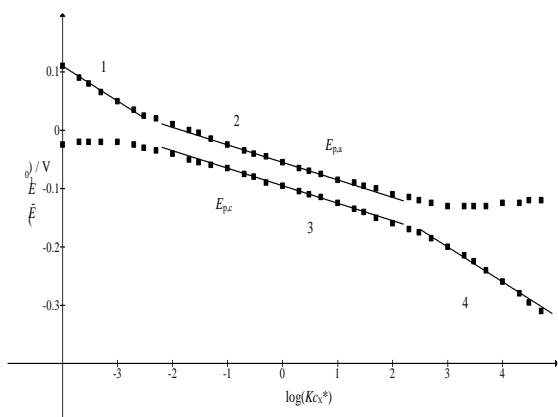


Fig. 7. Dependence of peak potentials on the logarithm of the product Kc_X^* . $E_2^0 - E_1^0 = -0.150$ V.

Fig. 7 shows that for $E_2^0 - E_1^0 = -0.150$ V a single pair of peaks appears within a wide range $-4 < \log(Kc_X^*) < 5$. The peak separation is constant if $-1 < \log(Kc_X^*) < 1$ and within these boundaries the slopes of linear dependence of peak potentials on the logarithm of Kc_X^* are equal to -0.030 V. This slope corresponds to the average of the formal potentials of the first and the second electrode reaction:

$$\bar{E} = [E_1^0 - (RT/F) \ln(Kc_X^*) + E_2^0]/2 \quad (70)$$

So, the straight lines 2 and 3 are defined by the equations:

$$E_{p,a} - E_1^0 = -2.3 (RT/2F) \log(Kc_X^*) + (E_2^0 - E_1^0)/2 + 0.020 \text{ V} \quad (71)$$

$$E_{p,c} - E_1^0 = -2.3 (RT/2F) \log(Kc_X^*) + (E_2^0 - E_1^0)/2 - 0.020 \text{ V} \quad (72)$$

For the biggest and the smallest values of Kc_X^* the shoulders develop, as in Fig. 3, and the responses start to split. The slopes of straight lines 1 and 4 are $-2.3 (RT/F)$, as in CE and EC mechanisms.

The figures 5, 6 and 7 show that the form of response depends on the product Kc_X^* and the difference in standard potentials. One may define a critical value of Kc_X^* above which the voltammogram consists of two pairs of peaks. Our calculation shows that the logarithm of this critical value is a linear function of the difference between standard potentials expressed in volts: $\log(Kc_X^*)_{crit.} = -17.16 (E_2^0 - E_1^0) + 2.255$.

Fig. 8 shows the influence of the kinetics of irreversible chemical reaction on the response of ECE mechanism. Dimensionless voltammograms depend on the dimensionless rate constant $\kappa = kRT/Fv$. If the intermediate is stable, the second pair of peaks develops with the increasing rate constant, but the first cathodic peak is diminished. If $\kappa = 0.01$ there is no second pair of peaks and the response is characterised by $\Phi_{p,a} = 0.387$, $E_{p,a} - E_1^0 = 0.035$ V, $\Phi_{p,c} = -0.242$ and $E_{p,c} - E_1^0 = -0.035$ V. For $\kappa = 0.001$ the anodic branch does not change, but the cathodic peak current decreases to -0.287 and appears at -0.040 V vs. E_1^0 . This is identical to the curve 2 in Fig. 1. If the rate constant is increased to 1, the following characteristic currents and potentials are obtained: $\Phi_{p,1,a} = 0.421$, $E_{p,1,a} - E_1^0 = 0.020$ V, $\Phi_{p,1,c} = -0.060$, $E_{p,1,c} - E_1^0 = -0.075$ V, $\Phi_{p,2,a} = 0.504$, $E_{p,2,a} - E_1^0 = 0.235$ V, $\Phi_{p,2,c} = -0.142$ and $E_{p,2,c} - E_1^0 = 0.160$ V. The response of the second electrode reaction is similar to the curve 2 in Fig. 2, but the first electrode reaction appears totally irreversible. This is because the product B^+ is irreversibly transformed into the species E and cannot be reduced back to the reactant A.

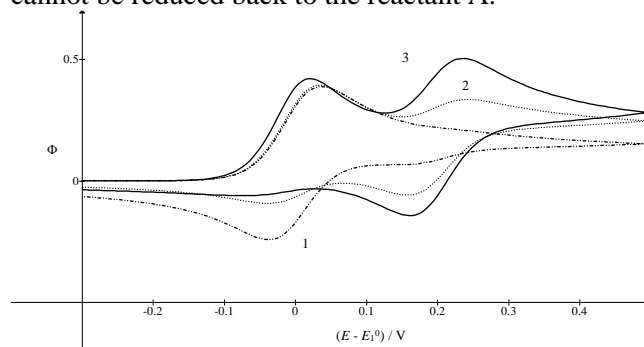


Fig. 8. Dimensionless staircase cyclic voltammograms of ECE mechanism influenced by the kinetics of totally irreversible chemical reaction (eqs. 30 and 31). $\Delta E = 5$ mV, $E_2^0 - E_1^0 = 0.2$ V and $\kappa = 0.01$ (1), 0.1 (2) and 1 (3).

Fig. 9 shows the relationship between dimensionless peak currents and peak potentials and the logarithm of dimensionless rate constant. One can notice that the second anodic peak appears for $\kappa_{crit.} = 0.03$. If the parameter κ is changed by the variation of scan rate, the real rate constant is related to the critical scan rate, at which the second peak

appears, by the following equations: $k = \kappa_{crit} v_{crit} / (RT/F)$ and $k = 1.17 v_{crit}$.

Fig. 10 shows a simulation of a real experiment in which the critical scan rate is determined. The second anodic peak can be observed below $v = 0.1$ V/s and disappears for higher scan rates. This suggests that $k = 0.117 \text{ s}^{-1}$. The rate constant influences mainly the peak potentials of the first electrode reaction, as can be seen in Fig. 9B.

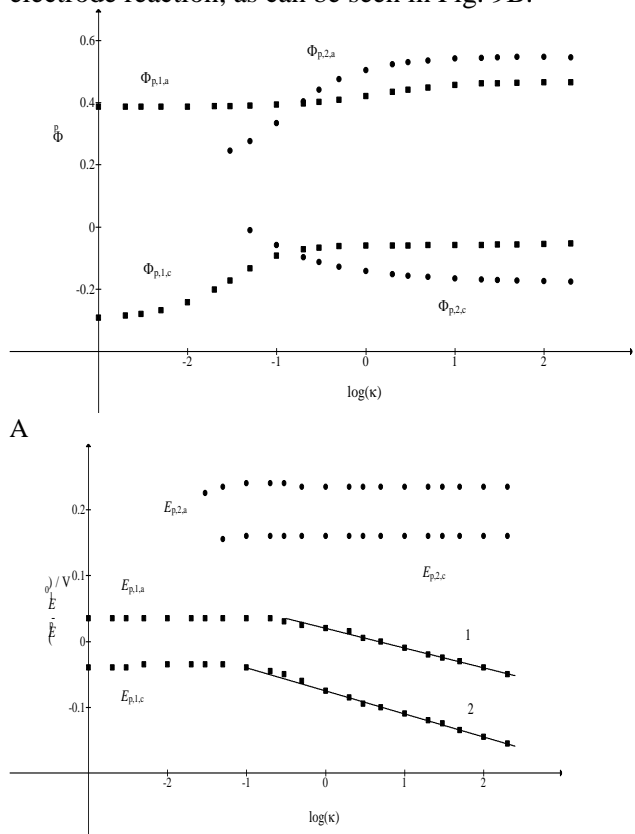


Fig. 9. Dependence of dimensionless peak currents (A) and peak potentials (B) on the logarithm of dimensionless rate constant of irreversible chemical reaction. $E_2^0 - E_1^0 = 0.2 \text{ V}$.

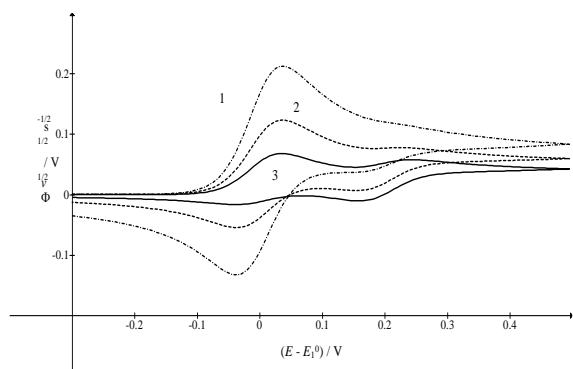


Fig. 10. Normalized cyclic voltammograms of ECE mechanism controlled by the chemical kinetics. $E_2^0 - E_1^0 = 0.2 \text{ V}$, $k = 0.117 \text{ s}^{-1}$ and $v/(V/s) = 0.3$ (1), 0.1 (2) and 0.03 (3).

The straight lines 1 and 2 satisfy the following equations: $E_{p,1,a} - E_1^0 = -0.030 \log(\kappa) + 0.020 \text{ V}$ and $E_{p,1,c} - E_1^0 = -0.035 \log(\kappa) - 0.075 \text{ V}$. The effect of chemical kinetics may be hidden if the intermediate is not stable. Fig. 11 shows the change of a single pair of peaks under the influence of diminishing dimensionless rate constant. Dimensionless anodic peak current decreases from 0.675 to 0.393 , but the cathodic peak current changes from -0.230 to -0.265 .

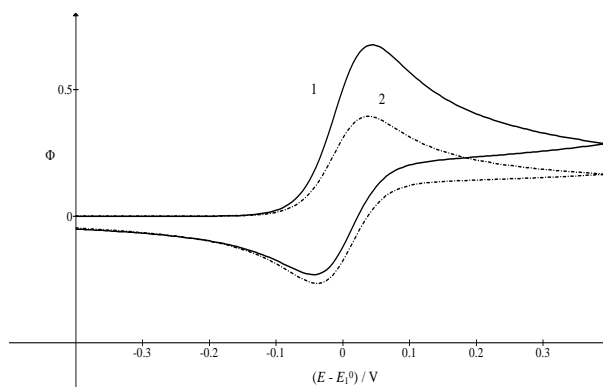


Fig. 11. Cyclic voltammograms of kinetically controlled ECE mechanism. $E_2^0 = E_1^0$ and $\kappa = 1$ (1) and 0.01 (2).

Comparing to Fig. 1, a reversible transfer of single electron that appears for $\kappa = 0.01$ turns into irreversible two-electrons electrode reaction for $\kappa = 1$. In the experiments one can observe that the relationship between peak current and the square root of scan rate is not linear. This is shown in Fig. 12.

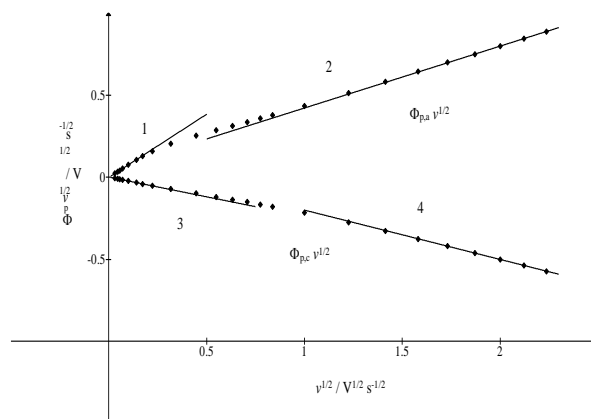


Fig. 12. Dependence of normalized peak currents on the square root of scan rate. ECE mechanism controlled by the kinetics of totally irreversible chemical reaction. $E_2^0 = E_1^0$ and $k = 3 \text{ s}^{-1}$.

The slopes of straight lines 1 and 2 are 0.77 and 0.38 , respectively. The first slope corresponds to two electrons oxidation appearing for higher values of the dimensionless kinetic parameter, while the second one belongs to the single electron oxidation.

However, the slopes of straight lines 3 and 4 are -0.24 and -0.30 because the cathodic current originates from the reduction of either the species F^+ , at higher κ values, or B^+ at lower κ values.

The variation of scan rate may influence the kinetics of both chemical and electrode reactions [5]. An example is shown in Fig. 13. The kinetics of electrode reactions depends on the dimensionless parameters λ_1 and λ_2 (see eqs. 46 and 47), but the ratio of electrochemical and chemical kinetic parameters depends on the scan rate: $\lambda_1/\kappa = k_{s1}\sqrt{Fv/DRT}/k$.

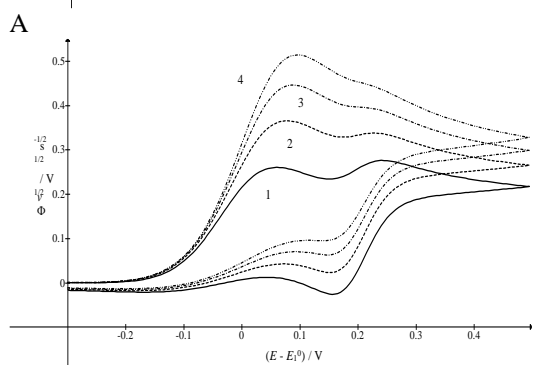
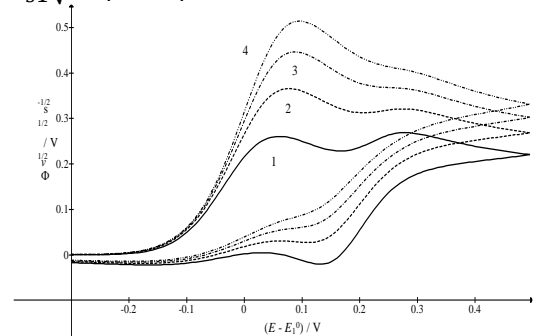


Fig. 13. Normalized cyclic voltammograms of ECE mechanism influenced by the kinetics of both chemical and electrode reactions (eqs. 39 and 40). $E_2^0 - E_1^0 = 0.2$ V, $\Delta E = 5$ mV, $D = 9 \times 10^{-6}$ cm²/s, $k = 3$ s⁻¹, $\alpha_1 = 0.5$, $\alpha_2 = 0.5$, $k_{s1} = 0.01$ cm/s, $k_{s2}/(\text{cm/s}) = 0.01$ (A) and 1 (B) and $v / (\text{V/s}) = 1$ (1), 2 (2), 3 (3) and 4 (4).

For this reason Fig. 13 shows the influence of scan rate on the normalized voltammograms. The chemical kinetic parameter decreases with the scan rate as follows: $\kappa = 0.0771$ (1), 0.0386 (2), 0.0257 (3) and 0.0193 (4). One can notice that the second anodic peak disappears if the scan rate is higher than 2 V/s regardless of the ratio between rate constants of the first and the second electrode reaction. This is in agreement with the critical chemical kinetic parameter $\kappa_{crit} = 0.03$ that is predicted for reversible electrode reactions. Comparing with Fig. 10, it can be noticed that the anodic peak potentials increase with the scan rate, but two peaks do not overlap if the difference between standard potentials is high enough. However, if these conditions are not

satisfied, the critical scan rate cannot be determined. This is shown in Fig. 14. The second anodic peak is diminished with the scan rate because the parameter κ decreases from 1.54, for $v = 0.050$ V/s, to 0.0386 for $v = 2$ V/s. As the first anodic peak potential increases with the scan rate and the second one does not, two anodic peaks overlap and the second peak disappears at the scan rate that is lower than the theoretical one.

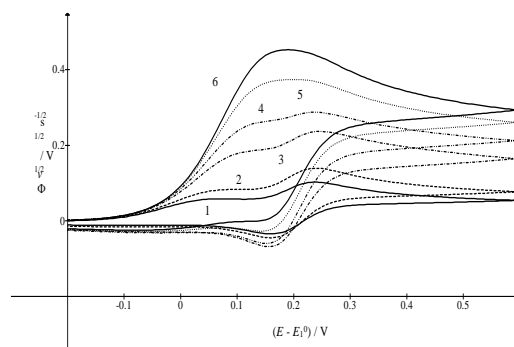


Fig. 14. CV of ECE mechanism (eqs. 39 and 40); $k_{s1} = 0.002$ cm/s, $k_{s2} = 0.1$ cm/s and $v / (\text{V/s}) = 0.05$ (1), 0.1 (2), 0.5 (3), 1 (4), 2 (5) and 3 (6). All other data are as in Fig. 13.

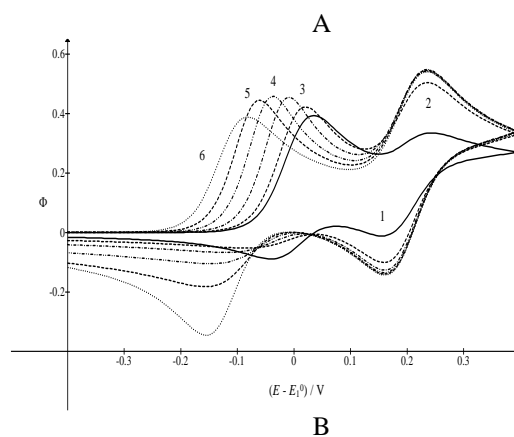
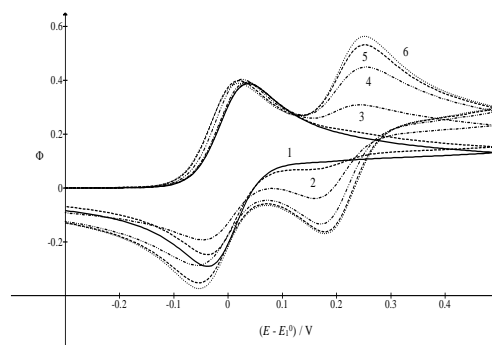


Fig. 15. Dimensionless voltammograms of ECE mechanism controlled by the kinetics of reversible chemical reaction (eqs. 53 and 54). $E_2^0 - E_1^0 = 0.2$ V, $Kc_X^* = 1$ (A) and 100 (B) and $\kappa_b = 0.001$ (1), 0.01 (2), 0.1 (3), 1 (4), 10 (5) and $\rightarrow \infty$ (6).

The equilibrium constant and the kinetics of the reversible chemical reaction are considered in the last theoretical model. The reaction (2) depends on

dimensionless rate constants $\kappa_b = k_b RT/Fv$ and $\kappa_f = \kappa_b Kc_X^*$. The latter corresponds to the dimensionless rate constant κ of totally irreversible chemical reaction. The responses depend on κ_b and Kc_X^* , as can be seen in Fig. 15. These parameters can be changed by the variation of scan rate and the concentration of the reactant X^- . If $Kc_X^* = 1$ the forward and backward kinetic parameters are equal ($\kappa_f = \kappa_b$) and the response tends to the equilibrium conditions with increasing κ_b . The curve 6 is calculated by the first model. The second anodic peak appears if $\kappa_{f,crit} = 0.03$, which means that $k_{f,crit} = 1.17 v_{crit}$. The same was predicted by the second model. Fig. 15B shows that for $Kc_X^* = 100$ and $\kappa_b = 10$ the first electrode reaction appears irreversible and out of equilibrium. Under these conditions the second electrode reaction is in the equilibrium, but the backward chemical reaction limits the first cathodic peak current. This is because the equilibrium is shifted towards the species E and the value of κ_b that is required for the approaching to the equilibrium is higher than in Fig. 15A.

The influence of the reagent X^- is shown in Fig. 16 for various scan rates. The relationships between the first anodic peak potential and the logarithm of the product Kc_X^* are curves that tend to the asymptotes with the slope -0.030 V (see curves 1 – 4). The straight line 5 is calculated by the first model and its slope is $-2.3RT/F$. The difference in slopes is caused by the fact that the first electrode reaction appears irreversible for the chosen kinetic parameters. This is confirmed by Fig. 17 in which the voltammograms influenced by the variation of the concentration of the reagent X^- at the constant scan rate are shown. It can be seen that the first cathodic peak current vanishes with the increasing product Kc_X^* . Fig. 18 shows that for the given value of the product Kc_X^* the scan rate has to be decreased as to increase the parameter κ_b in order to approach the equilibrium conditions. The curve 5 is calculated by the first model.

Generally, the equilibrium constant cannot be measured by the variation of the reactant X^- concentration, but it can be estimated by the simulation using the value of the forward rate constant of chemical reaction that is determined from the critical scan rate at which the second anodic peak appears.

CONCLUSIONS

Four mathematical models of ECE mechanism are described. The first two models are simplified in order to determine the parameters that can be measured by the cyclic voltammetry.

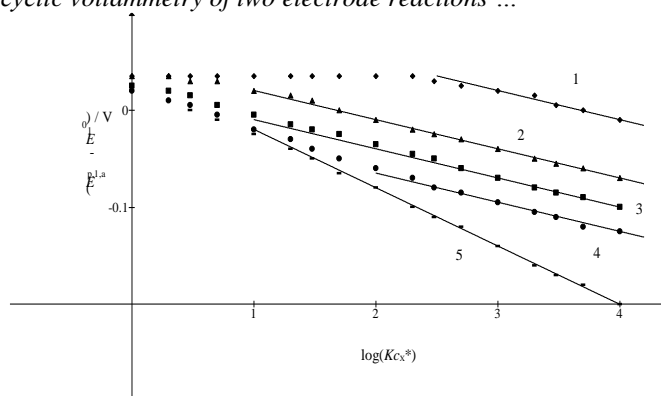


Fig. 16. Dependence of the first anodic peak potential on the logarithm of the dimensionless equilibrium constant of the kinetically controlled reversible chemical reaction. $E_2^0 - E_1^0 = 0.2$ V and $\kappa_b = 0.001$ (1), 0.1 (2) 1 (3), 10 (4) and $\rightarrow\infty$ (5).

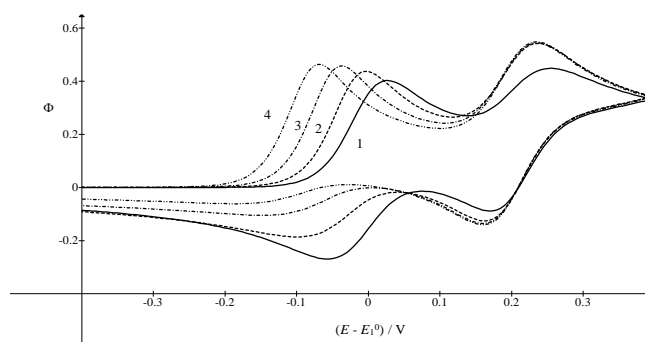


Fig. 17. CV of ECE mechanism. $E_2^0 - E_1^0 = 0.2$ V, $\kappa_b = 1$ and $Kc_X^* = 1$ (1), 10 (2), 100 (3) and 1000 (4).

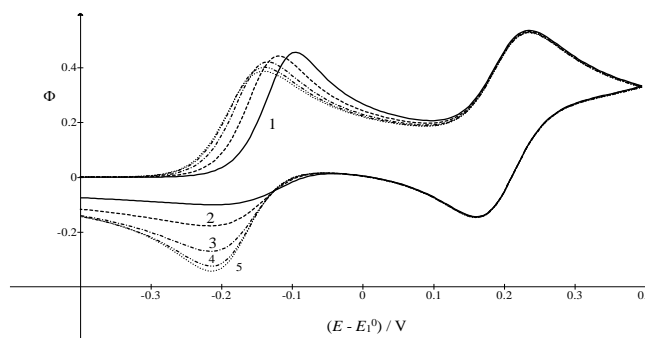


Fig. 18. CV of ECE mechanism. $E_2^0 - E_1^0 = 0.2$ V, $Kc_X^* = 1000$ and $\kappa_b = 10$ (1), 100 (2), 1000 (3), 10000 (4) and $\rightarrow\infty$ (5).

The other two models are general and they define the conditions under which the first two models are realistic. The simulation demonstrates that the equilibrium constant of chemical reaction can be measured by the variation of the concentration of the reagent X^- if the chemical reaction is permanently in equilibrium. Furthermore, the critical kinetic parameter is calculated that enables the measurement of the rate constant of totally irreversible chemical reaction. However, it is shown that the kinetics of electrode reactions may hinder the proper estimation of the chemical rate constant.

Finally, the last model shows that the chemical reaction appears irreversible if the concentration of the reagent X⁻ is increased and that the critical kinetic parameter applies under this condition. Also, the determination n of the equilibrium constant by the fitting procedure is discussed.

REFERENCES

- L. Nadjo, J.M. Saveant, *J. Electroanal. Chem.*, **33**, 419 (1971).
- S. W. Feldberg, *J. Phys. Chem.*, **75**, 2377 (1971).
- C. Amatore, J. M. Saveant, *J. Electroanal. Chem.*, **86**, 227 (1978).
- M. J. Palys, M. Bos, W. E. van der Linden, *Anal. Chim. Acta*, **283**, 811 (1993).
- P. T. Sanecki, C. Amatore, P. M. Skital, *J. Electroanal. Chem.*, **546**, 109 (2003).
- P. T. Sanecki, P. M. Skital, *Electrochim. Acta*, **53**, 7711 (2008).
- R. Gulaboski, V. Mirčeski, I. Bogeski, M. Hoth, *J. Solid State Electrochem.*, **16**, 2315 (2012).
- J. Jacq, *J. Electroanal. Chem.*, **29**, 149 (1971).
- E. Laviron, R. Meunier-Prest, *J. Electroanal. Chem.*, **324**, 1 (1992).
- R. Gulaboski, V. Markovski, Z. Jihe, *J. Solid State Electrochem.*, **20**, 3229 (2016).
- A. Molina, E. Laborda, J. M. Gomez-Gil, R. G. Compton, *J. Solid State Electrochem.*, **20**, 3239 (2016).
- R.S. Nicholson, I. Shain, *Anal. Chem.*, **37**, 190 (1965).
- G.S. Alberts, I. Shain, *Anal. Chem.*, **35**, 1859 (1963).
- B. D. Rossemaer, F. Hartl, D. J. Stufkens, C. Amatore, E. Maisonhaute, J. N. Verpeaux, *Organometallics*, **16**, 4675 (1997).
- J. W. Hersherberger, R. J. Klinger, J. K. Kochi, *J. Am. Chem. Soc.*, **105**, 61 (1983).
- C. C. Neto, S. Kim, Q. Meng, D. A. Sweigart, Y. K. Chung, *J. Am. Chem. Soc.*, **115**, 2077 (1993).
- P. Sanecki, K. Kaczmarski, *J. Electroanal. Chem.*, **471**, 14 (1999).
- P. Sanecki, P. Skital, K. Kaczmarski, *Electroanalysis*, **18**, 981 (2006).
- S. O'Toole, S. Pentlavalli, A. P. Doherty, *J. Phys. Chem. B*, **111**, 9281 (2007).
- T. Yamamura, K. Shirasaki, H. Sato, Y. Nakamura, H. Tomiyasu, I. Satoh, Y. Shiokawa, *J. Phys. Chem. C*, **111**, 18812 (2007).
- S. W. Feldberg, L. Jeftić, *J. Phys. Chem.*, **76**, 2439 (1972).
- R.D. Moulton, D.J. Chandler, A.M. Arif, R.A. Jones, A.J. Bard, *J. Am. Chem. Soc.*, **110**, 5714 (1988).
- Š. Komorsky-Lovrić, M. Lovrić, *Collect. Czech Chem. Commun.*, **72**, 1398 (2007).
- G. J. Wilson, C. Y. Lin, R. D. Webster, *J. Phys. Chem. B*, **110**, 11540 (2006).
- R. Meng, S. G. Weber, *J. Electroanal. Chem.*, **600**, 325 (2007).
- R. N. Adams, M. D. Hawley, S. W. Feldberg, *J. Phys. Chem.*, **71**, 851 (1967).
- D. Nematollahi, S. M. Golabi, *J. Electroanal. Chem.*, **481**, 208 (2000).
- Y. Li, M. Liu, C. Xiang, Q. Xie, S. Yao, *Thin Solid Films*, **497**, 270 (2006).
- G. Manning, V. D. Parker, R. N. Adams, *J. Am. Chem. Soc.*, **91**, 4584 (1969).
- M. Fleischmann, F. Lasserre, J. Robinson, *J. Electroanal. Chem.*, **177**, 115 (1984).
- S. O. Engblom, J. C. Myland, K. B. Oldham, *Anal. Chem.*, **66**, 3182 (1994).
- M. D. Hawley, S. W. Feldberg, *J. Phys. Chem.*, **70**, 3459 (1966).
- C. Amatore, J. M. Saveant, *J. Electroanal. Chem.*, **86**, 227 (1978).
- J. Galvez, A. Molina, R. Saura, F. Martinez, *J. Electroanal. Chem.*, **127**, 17 (1981).
- B. Kastening, *Anal. Chem.*, **41**, 1142 (1969).
- H. R. Sobel, D. E. Smith, *J. Electroanal. Chem.*, **26**, 271 (1970).
- M. Mastragostino, L. Nadjo, J. M. Saveant, *Electrochim. Acta*, **13**, 721 (1968).
- C. Amatore, J. M. Saveant, *J. Electroanal. Chem.*, **85**, 27 (1977).
- R.S. Nicholson, I. Shain, *Anal. Chem.*, **37**, 178 (1965).
- M. A. Mann, J. C. Helfrick Jr., L. A. Bottomley, *J. Electrochem. Soc.*, **163**, H3101 (2016).
- A. B. Miles, R. G. Compton, *J. Electroanal. Chem.*, **499**, 1 (2001).
- J. J. O'Dea, K. Wikiel, J. Osteryoung, *J. Phys. Chem.*, **94**, 3628 (1990).
- A.B. Miles, R.G. Compton, *J. Phys. Chem. B*, **104**, 5331 (2000).
- Š. Komorsky-Lovrić, M. Lovrić, *Anal. Bioanal. Electrochem.*, **5**, 291 (2013).
- S. Karp, *J. Phys. Chem.*, **72**, 1082 (1968).
- K. B. Prater, A. J. Bard, *J. Electrochem. Soc.*, **117**, 1517 (1970).
- C. Demaille, P. R. Unwin, A. J. Bard, *J. Phys. Chem.*, **100**, 14137 (1996).
- R. Gulaboski, *J. Solid State Electrochem.*, **13**, 1015 (2009).
- R. Gulaboski, P. Kokoškarova, S. Mitrev, *Electrochim. Acta*, **69**, 86 (2012).
- M. L. Olmstead, R. S. Nicholson, *J. Electroanal. Chem.*, **16**, 145 (1968).
- L.K. Bieniasz, *Modelling Electroanalytical Experiments by the Integral Equation Method*, Springer, Berlin, 2015.
- M. Lopez-Tenes, A. Molina, C. Serna, M.M. Moreno, J. Gonzalez, *J. Electroanal. Chem.*, **603**, 249 (2007).
- A. Molina, J. Gonzalez, E. Laborda, R. G. Compton, *Int. J. Electrochem. Sci.*, **7**, 5765 (2012).
- Š. Komorsky-Lovrić, M. Lovrić, *Croat. Chem. Acta*, **90**, 27 (2017).
- D. DeFord, N. Hume, *J. Am. Chem. Soc.*, **73**, 5321 (1951).

IR/Raman characterization of Au-mercaptopotriazole crystals

S. B. Dimitrijević^{1*}, S. Č. Alagić², M. M. Rajčić-Vujasinović², S. P. Dimitrijević³, A. T. Ivanović²¹Mining and Metallurgy Institute Bor, Zeleni bulevar 35, 19210 Bor, Serbia²University of Belgrade, Technical Faculty in Bor, VJ 12, 19210 Bor, Serbia³Innovation Center, Faculty of Technology and Metallurgy, University of Belgrade, Belgrade, Serbia

Received November 13, 2018; Accepted February 14, 2019

The aim of this study was a characterization of the crystals of gold complexes based on mercaptopotriazole, obtained from solutions with different pH values (2, 4, 7, and 9), using the methods of infrared (IR) and Raman spectroscopy. Both methods provided very useful information on the investigated systems and signaled existence of the Au-S bond in the complexes obtained at pH = 2 and 9. Recorded spectra clearly illustrated the changes that occur in the systems as a consequence of pH change. At the same time, the results also showed that the pyrrole nitrogen atoms stay protonated at pH = 9, which is not in favor of the assumption evolved from the previous UV-vis analysis of possible additional coordination between Au and possible deprotonated nitrogen atoms at this particular pH.

Keywords: synthesis; gold-mercaptopotriazole (Au-MT); IR and Raman spectroscopy

INTRODUCTION

Gold coatings are widely used in many fields of industry. This is the result of their exceptional electrical, chemical and optical properties, such as excellent electrical conductivity, high abrasion resistance and excellent corrosion resistance [1]. A wide area of these applications is the subject of research of many authors [2-7].

Traditionally, gold has been plated from cyanide electrolytes, where Au⁺ is ligated with cyanide (CN⁻). Cyanide electrolytes are extremely stable, but the main problem with the use of cyanide is in their poor compatibility with many standard photoresist layers on printed circuit boards, as well as the high toxicity [4,7-13].

Also, the presence of cyanides in solutions, wastewater and in atmosphere causes high costs of wastewater treatment and potential risks to the safety of workers in these facilities. Their negative redox potential makes difficult the formulation of a chemical bath, while low exchange current density leads to limits of reaction rates in cyanide complex solutions [14,15].

These disadvantages of cyanide electrolytes lead to a large number of investigations related to baths based on non-cyanide electrolytes such as: sulphite and aminosulphite, thiosulphate, thiosulphate-sulphite, thiourea, ascorbic acid, baths without a reducing agent, Au(III) halide baths, Au(I) thiomalate baths, etc.

In recent time the results of the research on formulation and characterization of a new non-cyanide electrolyte, the organic complex of gold based on mercaptopotriazole (C₂H₃N₃S), are

published in studies of Dimitrijević *et al.* [16-24], which showed that the resulting coatings fully meet the requirements of decorative coatings.

In general, five-membered heterocyclic compounds such as triazoles are of great importance because of their wide application as anticonvulsants, but also as bactericides, insecticides, herbicides, etc. [25]. It should be mentioned here that thiazole and its derivatives were also successfully used in the synthesis of antibiotics [26].

By analogy with palladium and platinum complexes that can build colored complexes with mercaptopotriazole (MT) [27], Dimitrijević *et al.* [16] assumed that gold can also build a complex with this compound, so that the synthesis of Au-MT complex has been achieved several years ago in the chemical laboratory of the Mining and Metallurgy Institute in Bor.

Briefly, as the first step in the procedure of Au-MT synthesis, the Beyer and Kroger [28] method for MT preparation was performed using thiosemicarbazide (min 98%, Merck, Germany) and formamide (p.a. Alkaloid, Skopje) as the basic chemicals. The structure of the obtained MT crystals (melting point 215°C) was characterized by infrared (IR) and Raman spectroscopy (RS) [16]. The recorded spectra were in a good agreement with the published data of Krishnakumar and Xavier (2004) [26], who studied the vibrational spectra of 3-mercaptopotriazole using FT-IR and FT-Raman spectroscopy (Table 1). The Raman spectrum of the obtained crystals of MT provided evidence of the thione form of MT molecule, while the IR spectrum confirmed the existence of thione-thiol tautomerism (Table 1). Finally, the novel Au-MT electrolyte was synthesized in the system

* To whom all correspondence should be sent:
E-mail: silvana.dimitrijevic@irmbor.co.rs

formulated of MT, glycine (Gly, min. 99%, Alkaloid, Skopje), and chloroauric acid (HAuCl₄), obtained by dissolution of gold (gold powder, 99.99%, Mining and Metallurgy Institute Bor) in *aqua regia* (HCl:HNO₃ = 3:1); the final concentration of gold in HAuCl₄ was 2.5 g/dm³, which is desirable in decorative gold coating electrodeposition [16]. The experiments were performed in a wide range of pH values, so solutions with different pH (pH = 2, 4, 7, 9) were prepared (using 1 M KOH for the pH adjustment), and the obtained electrolytes were further analyzed using different methods such as: inductively coupled plasma atomic emission spectroscopy, ultraviolet–visible spectroscopy, polarization measurements, open circuit potential measurements, cyclic voltammetry [16-20]. The obtained results showed that: (1) the highest stability of the complex is at pH = 9; (2) the best coatings are obtained from the complex formed at pH = 9; and (3) the connection of gold with MT molecule is most probably formed *via* an exocyclic sulfur atom of MT [16-20].

Table 1. Vibrational frequencies (cm⁻¹) and their probable assignments for the crystalline MT.

MT		Vibrational assignments*
IR	Raman	
	3155 w	N–H stretching, $\nu(\text{NH})$
3075 vs	3091 vw	C–H stretching, $\nu(\text{CH})$
2616 w	/	S–H stretching, $\nu(\text{SH})$
1558 s	1557 w	C=N stretching, $\nu(\text{CN})$
1471 s	1468 s	N–C stretching, $\nu(\text{NC})$
1430 s	1428 w	C–N stretching, $\nu(\text{CN})$
1259 w	1256 ms	N–N stretching, $\nu(\text{NN})$
1186 s	1190 s	N–H in-plane bending, $\beta(\text{NH})$
1057 ms	1065 ms	C–H in-plane bending, $\beta(\text{CH})$
/	991 s	Ring in-plane bending, $\beta(\text{ring})$
942 ms	941 ms	C–S stretching, $\nu(\text{CS})$
844 s	845 w	NCN in-plane bending, $\beta(\text{NCN})$
700 ms	708 w	CSH in-plane bending, $\beta(\text{CSH})$
665 ms	/	CNN in-plane bending, $\beta(\text{CNN})$ and CSH in-plane bending, $\beta(\text{CSH})$
/	530 s	NCS in-plane bending, $\beta(\text{NCS})$
/	354 s	NCN out-of-plane bending, $\gamma(\text{NCN})$

* Probable vibrational assignments are in accordance with Krishnakumar and Xavier (2004) [25].

Additionally, the structures of UV–vis absorption spectra, recorded for the electrolytes obtained at pH values of 2, 7, and 9, allowed a

possibility of an assumption that, at pH = 9, the molecules of MT may interact with Au not only through sulfur, but also through the nitrogen atoms of triazole rings [16], which can be deprotonated in the circumstances of increased pH [29]. Namely, Wrzosek and Bukovska [29] demonstrated that, depending on pH change, which is followed by processes of protonation (low pH)/deprotonation (increased pH) of the rings of AMT (3-amino-MT), the orientation of these rings in the system may also be further changed affecting the complete system state and providing different possibilities for the interactions between Au and AMT.

Following these findings, our team decided to subject the crystals of Au-MT, obtained from the solutions at different pH by simple evaporation at ambient temperature, to further analysis by IR and Raman spectroscopy in terms of obtaining additional information on the Au-MT structure, and especially regarding the evidence of the established coordination between Au and sulfur, or nitrogen atoms of MT. The results of the applied methods, together with the following discussion are represented in this paper.

EXPERIMENTAL

IR/Raman spectroscopy

Infrared spectrometry of the crystalline Au-MT synthesized at pH = 2, 7 and 9 was performed on a Perkin-Elmer 983G Infrared spectrophotometer using the KBr technique (finely pulverized sample), in the range 100–4000 cm⁻¹.

The Raman spectra of Au-MT obtained at pH = 2, 4, 7, and 9 were acquired in "backscattering geometry", using a μ -Raman system with a Jobin Yvon T64000 triple monochromator, and a CCD (charge-coupled-device) detector. The Ar laser 514 nm was used as a source for the excitation. All measurements were conducted at a laser power of 80 mW. The Raman spectra were recorded in the frequency range 100–3500 cm⁻¹ with a resolution of 4 cm⁻¹.

RESULTS AND DISCUSSION

The IR spectra of the crystalline Au-MT, synthesized at different pH: 2 (Fig. 1); 7 (Fig. 2); and 9 (Fig. 3), showed several relevant differences in comparison with the recorded IR spectrum of MT. The main indices on formation of a chemical bond between the metal and exocyclic sulfur atom of MT were evident in few cases. At the first place, according to Shalini and Sharma (2011) [26], who studied the iron and cobalt complexes with substituted MT, the appearance of a band that reveals the conversion of C=S into C-S- (which can be positioned in the frequency range 650-700 cm⁻¹

in the IR spectra) may represent a basis for further conclusion of probable coordination through the sulfur atom. It is noticeable that this band is one of the strongest in the spectrum of Au-MT obtained at pH = 9: 699 cm^{-1} (Fig. 3), whereas in the spectra of Au-MT, obtained at pH = 2 (Fig. 1) and pH = 7 (Fig. 2), two weak bands are present at 674 cm^{-1} and 637 cm^{-1} . In addition, in the IR spectra of the complexes (Figs. 1-3), as well as in the corresponding Raman spectra (Figs. 4-7), the deprotonation of a thiol group and further complexation through S atom is indicated by the absence of a band in the frequency range of $2450\text{--}2560\text{ cm}^{-1}$, which is usually assigned to the $\nu(\text{S-H})$ stretching vibration [26, 30]. It should be mentioned here that this band is only found in the IR spectrum of MT (Table 1) proving the existence of thione–thiol tautomerism in the molecule.

According to Little and Ottewill (1962) [31], who studied the adsorption of MT on silver iodide by IR spectroscopy, the presence of a strong band at 1050 cm^{-1} may be assigned to the $\nu(\text{C=S})$ stretching vibration of the thione form of MT molecule, and this band was found at 1057 cm^{-1} in the IR spectrum of the synthesized MT (Table 1). In the IR spectrum of Au-MT, obtained at pH = 2 (Fig. 1), this band is displaced at 995 cm^{-1} , and at 1014 cm^{-1} in the IR spectrum of Au-MT, obtained at pH = 9 (Fig. 3), which is most probably due to the elongation of the C=S bond caused by the complex formation [30]. However, in both latter cases, this band is rather weak. Analogous weak bands can be found in the recorded Raman spectra as follows: 995 cm^{-1} for Au-MT obtained at pH = 2 and 1017 cm^{-1} for Au-MT obtained at pH = 9. Finally, this band was not manifested in the IR spectrum of Au-MT obtained at pH = 7 (Fig. 2), nor in the corresponding Raman spectrum (Fig. 6). It can be said that in general, the IR spectrum of Au-MT, obtained at neutral pH (Fig. 2), has shown a notable declination with regard to the IR spectra of Au-MT obtained at pH 2 and 9 (Figs. 1 and 3, respectively), and suggested that a very specific situation may be present in the system at pH = 7, indicating a possibility of some specific molecular (re)arrangements.

An additional support of this assumption can be found from the analysis of the recorded Raman spectra of Au-MT complexes, formed at different pH = 2, 4, 7, and 9 (Figs. 4, 5, 6, and 7,

respectively). Namely, very specific structures of the Raman spectra of Au-MT, obtained at pH 4, and 7, which are reflected in the absence of any expressive band in the spectrum for pH = 4 (Fig. 5), or in the presence of numerous bands, which are not well defined and differentiated ("noise") in the spectrum for pH = 7 (Fig. 6), are rather different in comparison with the Raman spectra of Au-MT, obtained at pH 2 and 9 (Figs. 4 and 7, respectively). Most importantly, in the latter spectra, the appearance of bands at 245 cm^{-1} (for pH = 2) and 268 cm^{-1} and 241 cm^{-1} (for pH = 9) is noticeable, which may represent an additional and final signal of the formed bond: metal-S [30]. There were no such bands in the Raman spectrum of MT in which the band of the bending $\beta(\text{NCS})$ vibration at 530 cm^{-1} appeared as one of the strongest (Table 1). Medium strong bands, which may be ascribed to the stretching $\nu(\text{C=S})$ vibration [29], are present in the Raman spectra of the crystalline Au-MT, as follows: at 406 cm^{-1} for pH = 2 (Fig. 4), and 407 cm^{-1} and 510 cm^{-1} for pH = 9 (Fig. 7). Finally, it should be pointed out that both applied methods indicated that the nitrogen atoms of the triazole rings in the complex, formed at pH = 2, as well as at pH = 9, are protonated, which is not in support of previous assumptions, based on the analysis of UV-vis spectra that, at pH = 9, additional coordination between Au and deprotonated nitrogen atoms, is also possible [16]. This can be concluded on the basis of the presence of strong broad bands in the high-frequency region, which can be assigned to the NH stretching vibrations such as the bands in the range of $2600\text{--}3400\text{ cm}^{-1}$ in the IR spectra [26], and bands at 3151 cm^{-1} (Fig. 4), 3076 cm^{-1} and 3122 cm^{-1} (Fig. 7) in the Raman spectra [29]. The presence of bands in the frequency range $1000\text{--}1600\text{ cm}^{-1}$, which may be assigned not only to several modes of ring vibrations, but also to the NH deformation vibrations [25, 29], additionally supports the conclusion on protonated nitrogen. The bands from the same frequency range ($1000\text{--}1600\text{ cm}^{-1}$), in all recorded spectra of the obtained complexes, did not significantly change their positions in regard to the spectra of MT. It can be said that many of the bands from this region appeared as the most intensive in all spectra (except in the Raman spectra of complexes, obtained at pH 4 and 7).

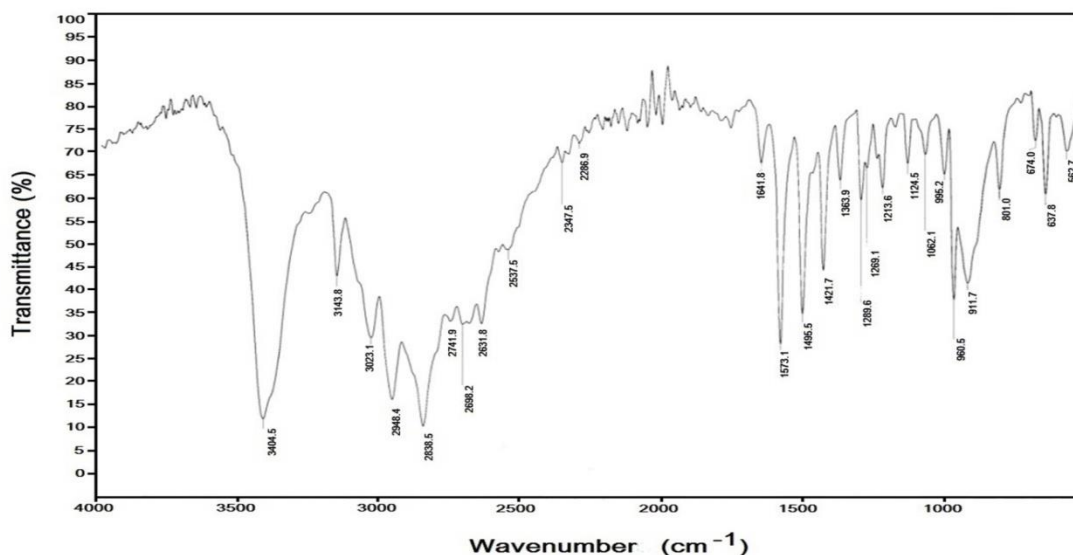


Figure 1. IR spectrum for the gold complex based on mercaptotriazole, obtained from a solution with pH = 2

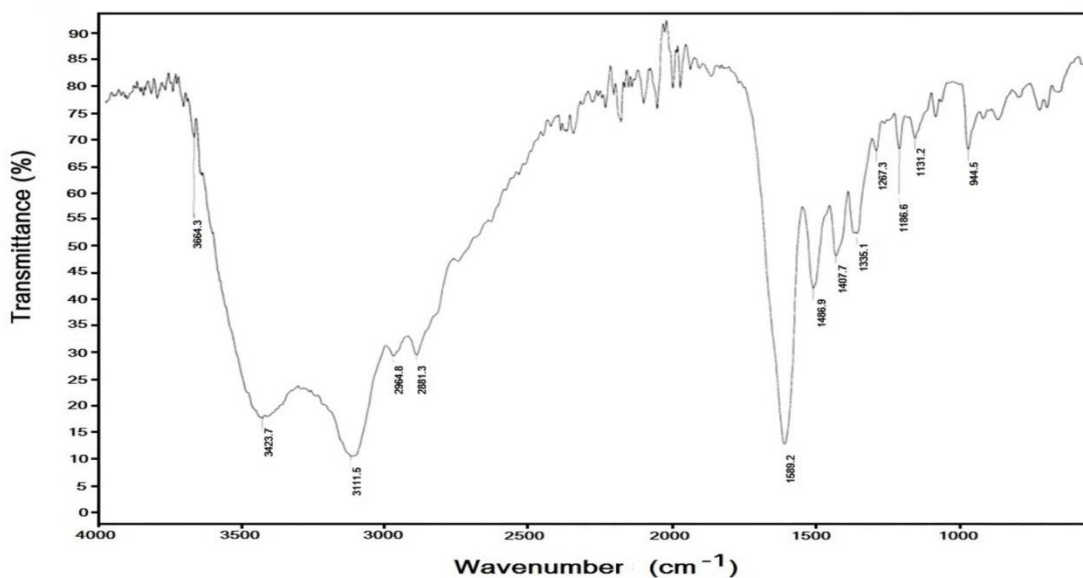


Figure 2. IR spectrum for the gold complex based on mercaptotriazole, obtained from a solution with pH = 4

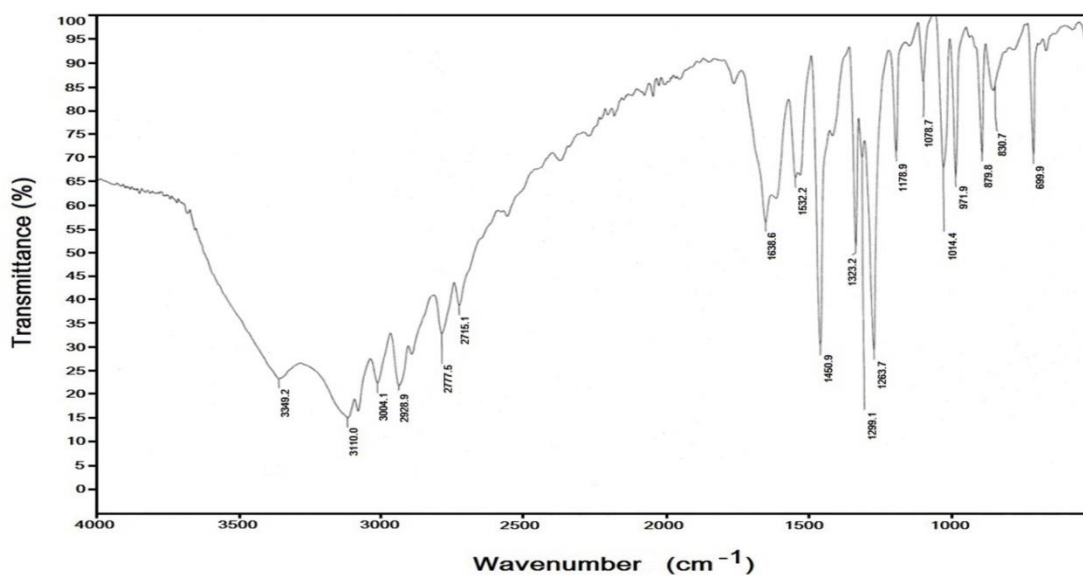


Figure 3. IR spectrum for the gold complex based on mercaptotriazole, obtained from a solution with pH = 9

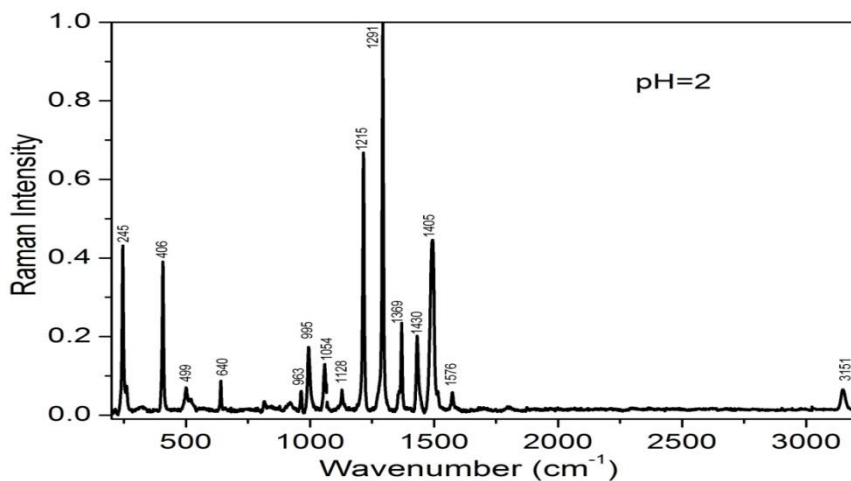


Figure 4. Raman spectrum for the gold complex based on mercaptopotriazole, obtained from a solution with pH = 2

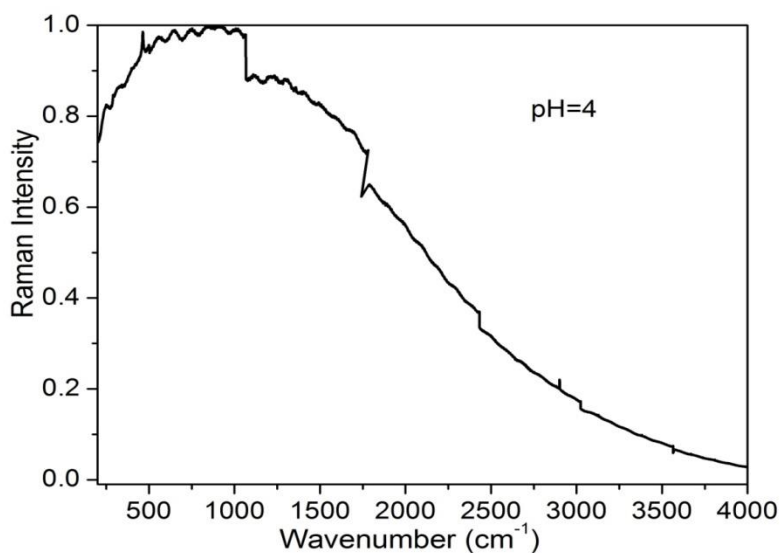


Figure 5. Raman spectrum for the gold complex based on mercaptopotriazole, obtained from a solution with pH = 4

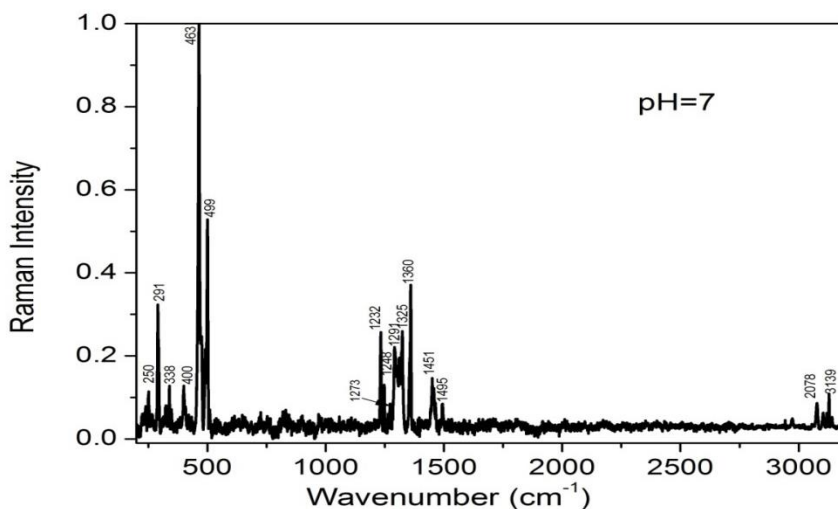


Figure 6. Raman spectrum for the gold complex based on mercaptopotriazole, obtained from a solution with pH = 7

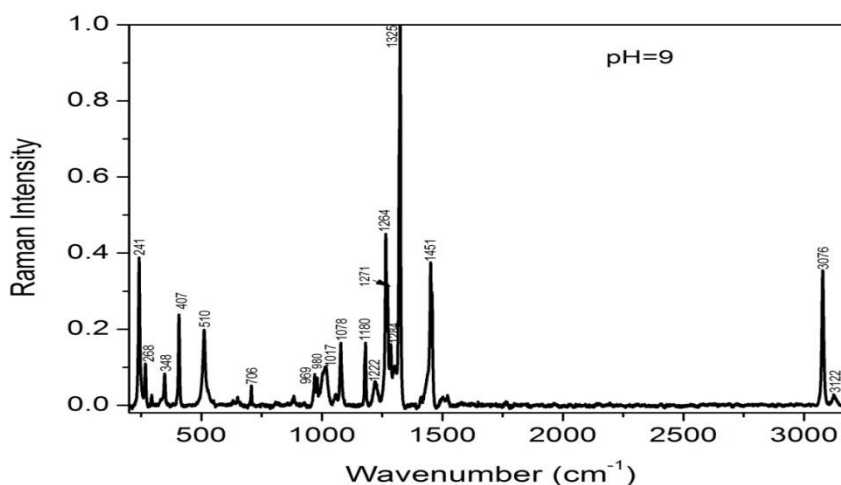


Figure 7. Raman spectrum for the gold complex based on mercaptotriazole, obtained from a solution with pH = 9

CONCLUSION

The methods of IR and Raman spectroscopy, applied in this work for the characterization of the crystals of Au-MT obtained from the solutions at different pH, provided very useful information on their structures, and signaled the existence of Au-S bond in the complexes, obtained at pH = 2 and pH = 9. The recorded spectra clearly illustrated the changes occurring in the systems as a consequence of pH change. However, the obtained results also showed that, at pH = 9, the pyrrole nitrogen atoms more likely stay protonated, which is not in favor of the assumption evolved from the UV-vis analysis of possible additional coordination between Au and deprotonated nitrogen atoms of MT at this particular pH.

Acknowledgement: This work has resulted from the Projects No: 34024 and 34033 funded by the Ministry of Education, Science and Technological Development of the Republic of Serbia.

REFERENCES

- M. J. Liew, S. Roy, K. Scott, *Green Chem.*, **5**, 376 (2003).
- Y. Okinaka, M. Hoshino, *Gold Bull.*, **31**, 3 (1998).
- S. Roy, *ECS Transac.*, **16**, 667, (2009).
- K. Kosaki, M. Matsuoka, Y. Seiwa, S. Orisaka, K. Nishitani, M. Otsubo, in: M. Datta, K. Sheppard, D. Snyder (eds.), In The Electrochemical Society Proceedings Series, PV 92-3, Pennington, NJ, 1992, p. 317.
- H. Honma, Y. Kagaya, *J. Electrochem. Soc.*, **140**, L135 (1993).
- T. A. Green, *Gold Bull.*, **40**, 105 (2007).
- W. S. Rapson, T. Groenewald, *Gold Usage*, Academic Press, London, 1978.
- J. Traut, J. Wright, J. Williams, *Plat. Surf. Finish.*, **77**, 49 (1990).
- A. Sullivan, P. Kohl, *J. Electrochem. Soc.*, **144**, 1686 (1997).
- R. J. Morrissey, A. Versatile, *Plat. Surf. Finish.*, **80**, 75 (1993).
- A. Osaka, T. Kodera, T. Misato, T. Homma, Y. Okinaka, *J. Electrochem. Soc.*, **144**, 3462 (1997).
- M. J. Liew, S. Sobri, S. Roy, *Electrochim. Acta*, **51**, 877 (2005).
- T. A. Green, M.-J. Liew, S. Roy, *J. Electrochem. Soc.*, **150**, C104 (2003).
- S. Đorđević, *Metal Coating*, Tehnička knjiga, Belgrade, 1990, p. 28.
- S. Đorđević, M. Maksimović, M. Pavlović, K. Popov, *Electroplating*, Tehnička knjiga, Belgrade, 1998.
- S. Dimitrijević, M. Rajčić-Vujasinović, S. Alagić, V. Grekulović, V. Trujić, *Electrochim. Acta*, **104**, 330 (2013).
- S. B. Dimitrijević, M. M. Rajčić-Vujasinović, R. M. Jančić-Hajneman, J. B. Bajat, V. K. Trujić, D. D. Trifunović, *Int. J. Mater. Res.*, **105**, 271 (2014).
- S. B. Dimitrijević, M. M. Rajčić-Vujasinović, D. D. Trifunović, B. T. Trumić, Z. M. Stević, S. P. Dimitrijević, *Int. J. Mater. Res.*, **107**, 624 (2016).
- S. B. Dimitrijević, V. K. Trujić, M. M. Rajčić-Vujasinović, 42nd International October Conference on Mining and Metallurgy, Proceedings, Kladovo, Serbia, 2010, p. 294.
- S. B. Dimitrijević, V. K. Trujić, M. M. Rajčić-Vujasinović, 14th International Research/Expert Conference "Trends in the Development of Machinery and Associated Technology" TMT 2010, Proceedings, Mediterranean Cruise, 2010, p. 669.
- S. Dimitrijević, M. Rajčić-Vujasinović, S. Alagić, V. Grekulović, V. Trujić, XXI International Scientific and Professional Meeting Ecological Truth, Proceedings, Bor Lake, Bor, Serbia, 2013, p. 148.
- S. Dimitrijević, M. Rajčić-Vujasinović, R. Jancic-Hajneman, D. Trifunović, J. Bajat, V. Trujić, S. Alagić, International Scientific and Professional Meeting Eco-Ist'12, Proceedings, 2012, p. 194.
- S. Dimitrijević, M. Rajčić-Vujasinović, S. Alagić, V. Grekulović, V. Trujić, Chemical and Electrochemical, 17th International Research/Expert Conference "Trends in the Development of

- Machinery and Associated Technology” TMT 2013, Istanbul, Turkey, 2013, p. 165.
24. S. Dimitrijević, M. Rajčić-Vujasinović, R. Jančić-Hajneman, J. Bajat, D. Trifunović, N. Vuković, V. Trujić, 18th International Research/Expert Conference ”Trends in the Development of Machinery and Associated Technology” TMT 2014, Budapest, Hungary, 2014, p. 125.
 25. N. T. Shalini, V. K. Sharma, Synthesis, *Rev. Roum. Chim.*, **56**, 189 (2011).
 26. V. Krishnakumar, R. John Xavier, *Spectrochim. Acta*, Part A, **60**, 709 (2004).
 27. D.D. Perrin, Organic Complexing Reagents, John Wiley and Sons, London, 1964.
 28. C. H. Beyer, C. F. Kroger, *Liebigs Ann. Chem.*, **637**, 135 (1960).
 29. B. Wrzosek, J. Bukowska, *J. Phys. Chem.* **111**, 17397 (2007).
 30. K. M. Marzec, B. Gaweł, W. Lasocha, K. Malek, *J. Raman Spectrosc.*, **41**, 543 (2010).
 31. L.H. Little, R.H. Ottewill, *Canad. J. Chem.*, **40**, 20110 (1962).

Removal of LAS from water by activated carbon and resins in continuous process

M. R. Franco Júnior^{1*}, N. R. A. F. Rocha², W. A. Pereira², N. P. Merlo²

¹ Post-Graduation Program in Biofuels, Chemistry Institute, Federal University of Uberlândia, Avenida João Naves de Ávila, 2121 Santa Monica, 38 408 100, Uberlândia MG Brazil

² UniRV, Rio Verde University, Fazenda Fontes do Saber, Rio Verde, Goiás, Brazil

Received November 21, 2018; Revised February 27, 2019

In this study, Purolite resins and activated carbon (AC) were used to remove LAS (linear dodecyl benzene sulfonate) from water. In some cases the conventional filtration at constant pressure released a negligible amount of residual surfactant ($< 0.1 \text{ mg L}^{-1}$). Adsorption characteristics were investigated with anionic, cationic and mixed resins and activated carbon with different sizes. LAS adsorption onto the solid material was studied in a solution of low concentration (0.50 mg L^{-1}). For comparison, some filters filled with resins and activated carbon were prepared, characterized and connected to the recipient bottom for filtration. The size of carbon particles really influenced the results, and the anionic resin exhibited better adsorption capacity than the others in this study. The ANOVA response surface analyses properly confirmed the experimental results.

Keywords: resins; activated carbon; filtration; continuous process; adsorption.

INTRODUCTION

Surfactants (surface active agents) are amphiphilic molecules containing two distinct parts: a hydrophilic group and a lipophilic group [1] and have negative impact both on the wastewater treatment process and more importantly on the environment. There are numerous papers published regarding the negative effect that surfactants had on the environment, wildlife and humans [2,3].

Palmer and Hatley [4] have published a critical review informing that numerous studies have shown that whilst activated sludge tanks can achieve removal efficiencies of between 98.9 and 99.9% for LAS, a trickling filter has a much wider range of removal efficiencies between 89.1 and 99.1% [5], whilst for alkylphenol ethoxylates the removal efficiency was more in the region of 90% [6].

The LAS removal can occur in several ways, such as precipitation, adsorption or degradation [7]. Berna *et al.* [8] considered that among these mechanisms biodegradation is of greater importance for the removal of chemical compounds present in aquatic environments. Scott and Jones [9] concluded that bacteria can use LAS as a source of carbon and energy or even co-metabolize it through biochemical microbial reactions [10]. Besides, recently, Motteran *et al.* [11] performed the characterization and identification of metabolic pathways of the microorganisms involved in the degradation of the linear alkylbenzene sulfonate in commercial laundry wastewater in an enlarged scale fluidized bed reactor.

Ten years ago, Yoona and co-workers [12] investigated the mechanisms of perchlorate

adsorption on activated carbon (AC) and anion exchange resin (SR-7 resin) using Raman, FTIR, and zeta potential analyses. Batch adsorption and desorption results demonstrated that the adsorption of perchlorate by AC and SR-7 resin was reversible. The reversibility of perchlorate adsorption by the resin was also proved by column regeneration test.

In recent years, Yu *et al.*, 2009 [13] trying to adsorb perfluorooctane sulfonate (PFOS) and perfluorooctanoate (PFOA) on powdered activated carbon (PAC), granular activated carbon (GAC) and anion-exchange resin (AI400) to remove PFOS and PFOA from water, have realized that time of filtration was really important for the adsorbent choice. Sorption kinetic results showed that the adsorbent size influenced greatly the sorption velocity, and both the GAC and AI400 required over 168 h to achieve the equilibrium, much longer than the 4 h needed for the PAC.

The objectives of this study are to investigate the sorption behavior of LAS on the commercial adsorbents including activated carbon with four sizes and resins (anionic, cationic and mixed), and evaluate their sorption in terms of turbidity and conductivity at ambient temperatures with no pH correction. The possible influences of carbon size and type of resins among the adsorbents and adsorbate were also discussed.

EXPERIMENTAL

The equipment is shown in Fig. 1. The fixed bed filter was built in the Laboratório de Bromatologia from University of Rio Verde - UniRV. Experiments were performed using filters filled with activated carbon and resins to evaluate LAS

* To whom all correspondence should be sent.

E-mail: moilton@ufu.br

adsorption from residual water. The resins used were purchased from Purolite (anionic, cationic and mixed) and the activated carbon from Vetec. The activated carbon (AC) was prepared by using sieves to obtain four different sizes: 48, 60, 100 and 300 mesh. The solid material was packed into a glass column and weighed on an analytical balance. Filters (4) were connected in the bottom of the tank

(1). The filtration tests were conducted by passing LAS solutions through the resin or AC column at the same drop pressure. The effluent samples or filtrates were collected at different times for analysis. All effluent samples were collected into a container for measurement of conductivity, turbidity and LAS concentration.

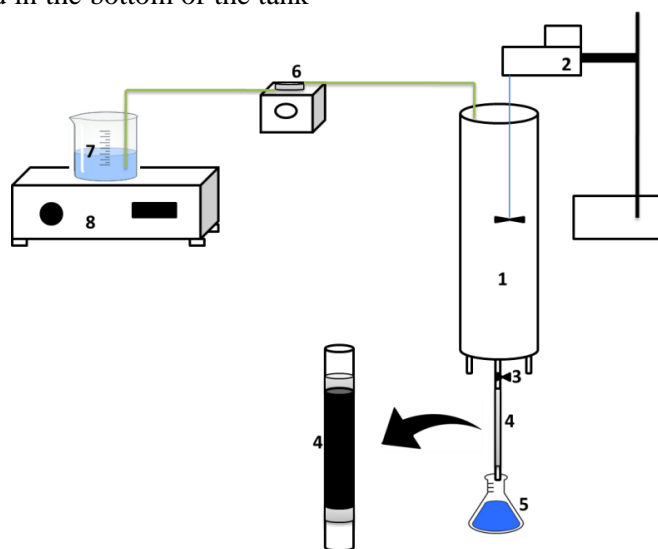


Fig. 1. Schematic view of the equipment used in this work (1 - tank, 2 - agitator engine, 3 - valve, 4 - filter, 5 - filtrate, 6 - metering pump, 7 - LAS solution or residual water, 8 - magnetic stirrer).

The contaminated water was put in the tank that was made of PVC cylindrical tube (1), with internal diameter of 0.08 m. The residual water inside was stirred using a mechanical agitator (2) (IKA Model RW 20 D S1), with rotation frequency of 350 rpm. There were three outing tubes or fixed bed filters, with internal diameter of 0.007 m, made of glass connected in the base of the PVC tube. They were filled with the adsorbent material for extracting LAS from the liquid. Also, all link tubes were made of flexible Teflon and had 0.0008 m internal diameter. All experiments were carried out at ambient temperature which varied around (25 ± 1) °C. To maintain constant pressure and LAS concentration ($C_0=0.50 \text{ mg L}^{-1}$) fed to the filters, the metering bomb (BIOTEC- Model FCE 0505 FP) (6) was used to constantly feed stirred (Tecnal modelo TE-0852 - 10 rpm) solution from tank (7) to tank (1).

Materials and methods

All chemicals were obtained from Vetec and Reagan In. Químicas, Brazil, including LAS – linear dodecyl benzene sulfonate. All chemicals were of A.R. grade and used without further purification. Ultrapure water was used throughout the study to prepare aqueous solutions. Resins were acquired from Purolite Company Ltd.

The activated carbon (AC) used as adsorbent had the following sizes (mesh): 48, 60, 100 and 300. In addition, three types of resins were employed as follows: anionic, cationic and mixed. Table 1 shows the material, amount (m) and length (h) of each filter used.

Table 1. Description of the filters connected in the base of the fixed reactor.

Filter	Material	m (g)	h (cm)
F1	AC 48	1.2820	10
F2	AC 60	1.2631	10
F3	AC 100	1.3774	10
F4	AC 300	1.3976	10
F5	AR	1.3494	10
F6	CR	2.3367	10
F7	MR	2.0792	10

Legend: F- filter, AC - activated carbon (size), AR - anionic resin, CR - cationic resin, MR - mixed resin.

For turbidity measurements, the turbidity meter model AP 2000 from Poli Control (± 0.01 NTU or ± 0.1 NTU) was employed. The filtrate conductivities were determined on a conductivity meter model CD 850 in μS (micro Siemens/cm). The concentration of surfactant was determined indirectly using a spectrophotometer (UV-VIS)

M. R. Franco Júnior et al.: Removal of LAS from water by activated carbon and resins in a continuous process. TECNAL- Model SP-1105 at a wavelength of 650 nm.

RESULTS AND DISCUSSION

Surfactant concentration, filtrate turbidity and conductivity in aqueous phase are shown in tables 2-4 when activated carbon was used as filter filling. Turbidity and conductivity of filtrate significantly

decreased with the time of filtration, especially for meshes 48-100. For mesh 300 it was observed that the small particles of carbon undetermined the result. It clearly indicated that filtration has better removal efficiency (88%) after 6 h of filtering and the filter with mesh 300 can be distinguished among the others.

Table 2. LAS concentration in the filtrate as a function of time for all AC meshes at the exit of the fixed bed. ($C_0=0.50 \text{ mg L}^{-1}$)

Mesh	Filtration Time							
	1h	2h	3h	4h	5h	6h	7h	8h
48	0.263136	0.249124	0.201485	0.152445	0.153846	0.117416	0.180468	0.24352
60	0.249124	0.2197	0.194479	0.166456	0.152445	0.166456	0.187474	0.214096
100	0.298164	0.230909	0.190276	0.120219	0.15805	0.062771	0.075382	0.117416
300	0.335996	0.221101	0.148242	0.156648	0.089393	0.059969	0.075382	0.106207

Table 3. Turbidity of the filtrate as a function of time for all AC meshes at the exit of the fixed bed.

Mesh	Filtration Time							
	1h	2h	3h	4h	5h	6h	7h	8h
48	0.36	0.14	0.02	0.15	0.02	0.29	0.02	0.22
60	0.45	0.16	0.4	0.02	0.02	0.02	0.12	0.16
100	0.41	0.33	0.2	0.02	0.23	0.26	0.31	0.06
300	0.69	0.52	0.44	0.35	0.31	0.47	0.41	0.35

Table 4. Conductivity of the filtrate as a function of time for all AC meshes at the exit of the fixed bed.

Mesh	Filtration Time							
	1h	2h	3h	4h	5h	6h	7h	8h
48	18.6	7.5	6.1	4.5	3.9	3.5	3.1	2.9
60	36.6	13.2	8.4	5.8	5	4.4	4.4	3.2
100	5.2	4.5	4.3	4.3	5.1	4.1	4.1	3.9
300	17.1	15.5	14	13.7	13.7	12.4	12.2	11.1

Table 5. LAS concentration (mg.L^{-1}) of the filtrate as a function of time for all resins at the exit of the fixed bed.

Resin	Filtration Time							
	1h	2h	3h	4h	5h	6h	7h	8h
ANI	0.1265	0.141	0.08	0.064	0.1195	0.156	0.1205	0.139
CAT	0.213	0.226	0.331	0.263	0.206	0.296	0.299	0.262
MIX	0.107	0.103	0.064	0.082	0.116	0.072	0.085	0.089

Table 6. Turbidity (NTU) of the filtrate as a function of time for all resins at the exit of the fixed bed.

Resin	Filtration Time							
	1h	2h	3h	4h	5h	6h	7h	8h
ANI	0.211994	0.23231	0.14684	0.124422	0.202186	0.253328	0.203587	0.229508
CAT	0.333193	0.351408	0.498529	0.403251	0.323385	0.449489	0.453692	0.40185
MIX	0.184671	0.179067	0.124422	0.149643	0.197282	0.135631	0.153846	0.159451

Table 7. Conductivity ($\mu\text{S cm}^{-1}$) of the filtrate as a function of time for all resins at the exit of the fixed bed.

Resin	Filtration Time							
	1h	2h	3h	4h	5h	6h	7h	8h
ANI	5.8	3.4	3.75	3.9	3.85	3.4	3.9	3.75
CAT	14.9	6.3	7.3	7.1	7.1	3.3	4	4.4
MIX	14	0.8	0.7	0.8	0.8	1.3	0.8	0.7

Table 8. The ANOVA results of the regression model for filtrate LAS concentration (mg/L).

Parameter	SQ	GL	MQ	F ₀ C	F ₀ T
A	0.267688627	2	0.133844313	47.74252	3.74
B	0.00629324	7	0.000899034	0.320687	2.76
AB	0.039248457	14	0.002803461		
TOTAL	0.313230323				

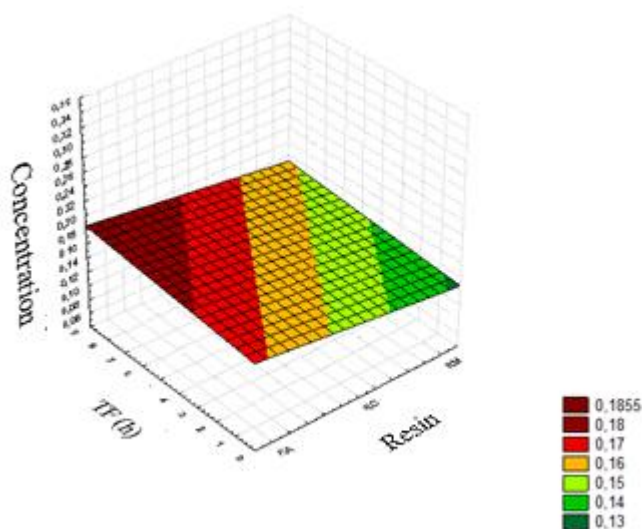


Fig. 2. Response surface for the effect of type of resin and filtration time (FT) on the filtrate LAS concentration (mg/L).

Tables 5-7 show the results of LAS concentration, turbidity and conductivity of filtrate for filters filled with resins. For all resins, turbidity does not change in the filtrate as time of filtration reached 8 h. It seems that the anionic resin was the best one to remove LAS (87.2%) from the aqueous solutions. This result is distinguished when compared to other adsorbents published by Nie *et al.* [14] that attribute the range of 30-70% to LAS removal efficiency. A better discussion will be done using response surfaces as follows.

The ANOVA results for the fixed effect model are shown in tables 8-10. In all tables A, B, AB are significant model terms that affect the parameter analysed. Also, in these tables each variable means: SQ (sum of squares), DF (degree of freedom), MQ (mean square), F₀C (F-value) and F₀T (P-value). P-value (or F₀T) is the tool to check the significance of each term. The term is more significant with a lower P-value and higher (or F₀C) F-value. Values of Prob > F < 0.0500 indicate that model terms are significant.

The response surfaces were generated by Design Expert after model fitting, as shown in Figs. 2-4. The influences of each factor (A: type of resin, B: filtration time) and their interactions (AB) on the each variable could be analyzed according to the response surfaces.

Table 8 presents the analysis of variance to verify the effects of A and B on the LAS filtrate concentration. It can be seen that the high F-value of 47.74 and low P-value of 2.76 implied that the type of resin was highly significant. Between the two variables, the type of resin was the more significant one that affected the filtrate concentration according to the statistical analysis.

Fig. 2 confirms that the concentration is clearly affected by the type of resin (A) and is not so affected by the time of filtration (B) when the pressure drop is fixed at level 0 (0.45 m water column). With the increase in filtration time, LAS concentration generally decreased for the anionic resin and kept the same for the others. Table 9 illustrates the analysis of variance to verify the effects of A and B in the filtrate turbidity. It can be seen that the small F-value of around 2.00 and relatively high P-value of 3.74 implied that the type of resin and time of filtration had similar significance in the results. Between the two

variables, the type of resin was the more significant one that affected the filtrate concentration according to the statistical analysis.

Fig. 3 confirms that apart from the anionic resin in the four initial times the turbidity is not clearly affected by the type of resin (A) and is not affected by the time of filtration (B) when the pressure drop is fixed (0.45 m water column). With the increase in filtration time, turbidity was maintained the same for all tested resins. This was consistent with the ANOVA results in Table 9 that the F-values for A and B were similar to their P-values.

Table 10 illustrates the analysis of variance to verify the effects of A and B on the filtrate conductivity. It can be seen that the reasonable F-value of around 8.00 and the relatively high P-value of 3.74 implied that the type of resin had more significance than time of filtration on the results. Between the two variables, the type of resin was the more significant one that affected the filtrate conductivity according to the statistical analysis. In addition, the small values of conductivity at the end of the filtration mean low LAS concentration.

Fig. 4 confirms that the anionic resin had particularly good performance in LAS adsorption, followed by the mixed resin.

Table 9. The ANOVA results of the regression model for filtrate turbidity.

Parameter	SQ	GL	MQ	F ₀ C	F ₀ T
A	0.033475	2	0.016738	1.98763	3.74
B	0.123083	7	0.017583	2.088075	2.76
AB	0.117892	14	0.008421		
TOTAL	0.27445				

A = Resin (anionic (1), cationic (2) and mixed (3)); B = filtration time (1 to 8 h).

Table 10. The ANOVA results of the regression model for filtrate conductivity.

Parameter	SQ	GL	MQ	F ₀ C	F ₀ T
A	76.82062	2	38.41031	7.983413	3.74
B	180.6307	7	25.80439	5.363328	2.76
AB	67.35771	14	4.811265		
TOTAL	324.8091				

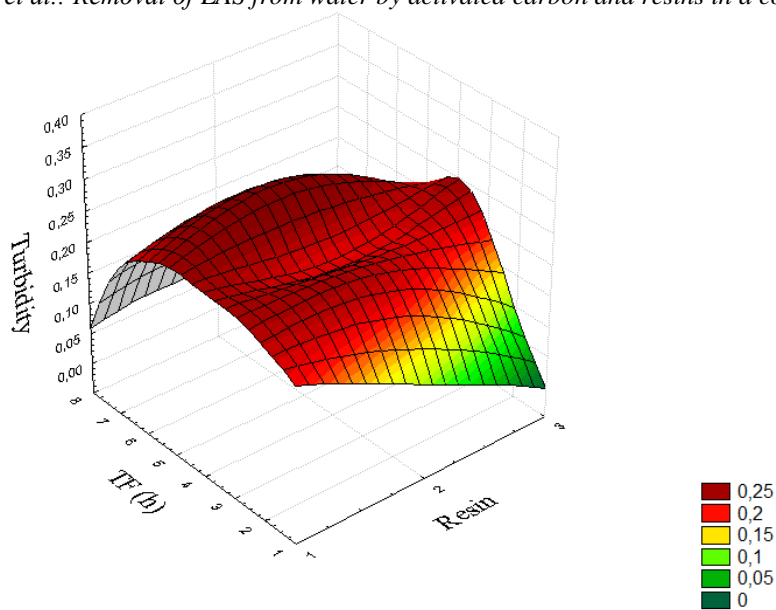


Fig. 3. Response surface for the effect of type of resin and filtration time (FT) on filtrate turbidity. (1- RA; 2-RC; 3- RM)

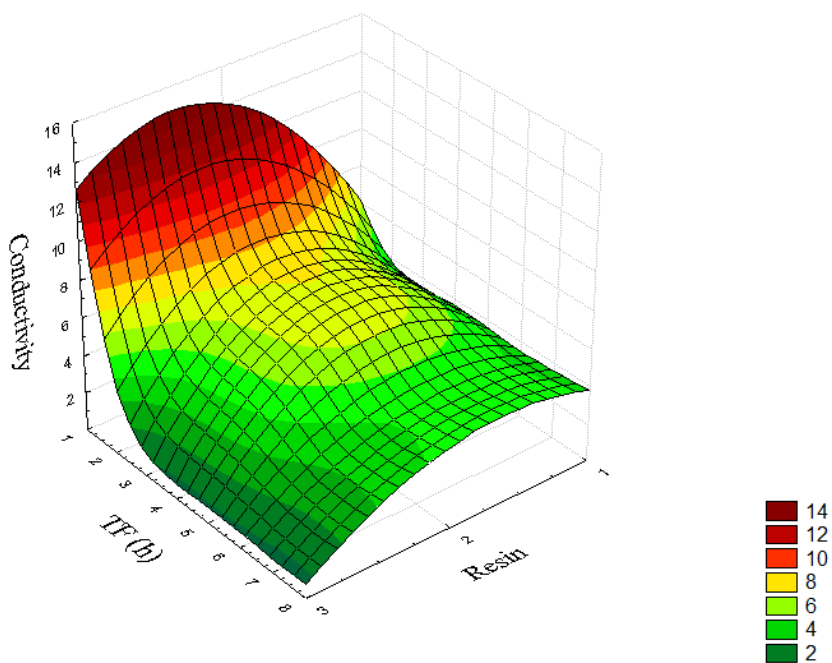


Fig. 4. Response surface for the effect of type of resin and filtration time (FT) on the filtrate conductivity. (1- RA; 2-RC; 3- RM)

CONCLUSIONS

In this study, adsorption of LAS on three types of resins and four different sizes of activated carbon were investigated. The conventional constant pressure filtration method was used and the LAS initial concentration was maintained by using simple recirculation of the solution. In a single contaminant system, LAS has the highest affinity to the anionic resin and AC with 300 mesh.

Maximum adsorbed mass of LAS was similar comparing anionic and mixed resins. The maximum adsorbed amount (87.2%) was reached after six hours of filtering.

Acknowledgement: This research was partially supported by the Rio Verde University (Proposal approved in CHAMADA INTERNA 02/2018 – PRPI/UniRV – Scholarship of N. A. F. Rocha).

Conflict of interests: The authors declare that there is no conflict of interests regarding the publication of this paper.

REFERENCES

1. C. L. Yuan, Z. Z. Xu, M. X. Fan, H. Y. Liu, *J. Chem. Pharmaceut. Res.* **6** (7), 2233 (2014).
2. HERA, Human & Environmental Risk Assessment on Ingredients of European Household Cleaning Products. Substance: Fluorescent Brightener FWA-1 (CAS 16090-02-1), vol 69, 2002.
3. HERA, Linear alkylbenzene sulphonate, available at: http://www.heraproject.com/files/HERA-LAS_revised_April_2013_Final1.pdf.
4. M. Palmer, H. Hatley, *Water Research* **147**, 60 (2018).
5. A. K. Mungray, P. Kumar, *Bioresour. Technol.*, **99**(8), 2919 (2008), <https://doi.org/10.1016/j.biortech.2007.06.025>.
6. S. Gonzalez, M. Petrovic, D. Barcel, *Chemosphere*, **67**(2), 335 (2007). <https://doi.org/10.1016/j.chemosphere.2006.09.056>.
7. HERA, Human & Environmental Risk Assessment on Ingredients of European Household Cleaning Products, 2009, p. 1.
8. J. L. Berna, G. Cassani, C.-D. Hager, N. Rehman, L. López, D. Schowanek, J. Steber, K. Taeger, T. Wind, *Tenside Surfactant Deterg.* **44**, 312 (2007). <https://doi.org/10.3139/113.100351>.
9. M. J. Scott, M. N. Jones, *Biochim. Biophys. Acta Biomembr.*, **1508**, 235 (2000). [https://doi.org/10.1016/S0304-4157\(00\)00013-7](https://doi.org/10.1016/S0304-4157(00)00013-7).
10. G. G. Ying, *Environ. Int.*, **32**, 417 (2006). <https://doi.org/10.1016/j.envint.2005.07.004>.
11. F. Motteran, B. M. Nadai, J. K. Braga, E L. Silva, M. B. A. Varesche, *Science of the Total Environment*, **640–641**, 1411 (2018).
12. I.-H. Yoona, X. Meng, C. Wang, K.-W. Kim, S. Bang, E. Choe, L. Lippincott, *Journal of Hazardous Materials*, **164**, 87 (2009).
13. Q. Yu, R. Zhang, S. Deng, J. Huang, G. Yu, *Water Research*, **43**, 1150 (2009).
14. Y. Nie, H. Kato, T. Sugo, T. Hojo, X. Tian, Y.-Y. Li, *Chemical Engineering Journal*, **315**, 83 (2017).

The influence of isochronal aging on the mechanical and thermophysical properties of the EN AW-6060 aluminum alloy

U. Stamenković*, S. Ivanov, I. Marković

University of Belgrade, Technical Faculty in Bor, Vojske Jugoslavije 12, Bor, Serbia

Received December 5, 2018; Revised March 7, 2019

The scope of this paper is the investigation of the effect of precipitation on an EN AW-6060 aluminum alloy by measuring mechanical, physical, and thermal properties. According to the exothermic peaks that appeared on the DSC thermogram and thermal diffusivity curve, parameters for isochronal aging treatment were defined. Thermal, mechanical, physical, and structural properties were investigated during the isochronal aging. The maximal enhancement of mechanical properties was achieved after aging at 230 °C for 30 min, whereas the most favorable thermal properties were obtained after aging at the same temperature for 60 min. During the aging, the precipitation from the solid solution caused a gradual increase in electrical conductivity. SEM/EDS microstructural investigations confirmed the existence of precipitated phases and provided the insight into their distribution within the microstructure.

Keywords: aluminum alloys, EN AW-6060, aging, heat treatment, thermal properties

INTRODUCTION

A good combination of properties such as good ductility, high strength-to-weight ratio, formability, corrosion resistance, and non-toxicity makes the aluminum alloys from the 6000 series common industry materials [1, 2]. Besides that, aluminum alloys generally have a good electrical and thermal conductivity with high reflectivity to light and heat [3]. All of these properties are highly affected by the alloy's microstructure. In order to change the microstructure and to improve the properties, alloys from this series are usually subjected to various treatments. Generally, heat treatable aluminum alloys are strengthened by precipitation hardening (aging). The chosen alloy for such investigation is a low-alloyed (lean) EN AW-6060 alloy which is usually strengthened by thermo-mechanical treatment. Many authors have studied the influence of different thermo-mechanical parameters on the properties enhancement. The role of co-clusters on the artificial aging for this alloy was investigated by Pogatscher *et al.* [4]. Abid *et al.* [5] discovered that pre-aging enhances the hardening effect. Strobel *et al.* [6] suggested that prolonged natural aging leads to an increase in hardness and has a positive effect on quench sensitivity. Teichmann *et al.* [1] investigated the effect of simultaneous deformation and annealing on the precipitation behavior and mechanical properties of this alloy. They confirmed the beneficial influence of simultaneous deformation on the strengthening, i.e., the peak hardness for the deformed alloy was achieved after a shorter annealing time. Milkereit *et al.* [7] constructed the continuous cooling precipitation

diagrams for Al-Mg-Si alloys using DSC analysis, SEM/TEM investigations, and hardness measurement. Kim *et al.* [8] obtained results for thermal diffusivity as a function of temperature and the amount of Mg₂Si precipitated phase on the quenched samples. Choi *et al.* [9] investigated the precipitation dependence of thermal diffusivity for Al-6%Si-0.4%Mg-0.9%Cu-(Ti) alloys with various heat treatments.

According to the literature, it can be concluded that the researchers' focus was on the investigation of the improvement of properties during thermo-mechanical treatment rather than heat treatment. Also, researchers are mainly focused on investigating the influence of isothermal heat treatment rather than the isochronal one. Therefore, our aim was to investigate the influence of the heat treatment (isochronal aging) alone on the thermal, mechanical, and physical properties of the EN AW-6060 aluminum alloy. Based on these investigations, the parameters for isochronal aging treatment involving temperatures higher than conventional and shorter periods of time were defined to provide the optimal values of the studied properties.

EXPERIMENTAL PART

The EN AW-6060 alloy was chosen for the experimental investigation. The alloy was delivered by "AlCu metali d.o.o." company, in peak-aged state (T6 temper). The chemical composition was determined by using an optical emission spectrometer "Belec Compact Port" and is presented in Table 1. Peak-aged state was removed and O-temper achieved by annealing at 550 °C for 6 h in the electric resistance furnace Heraeus K-1150/2.

* To whom all correspondence should be sent:

E-mail: : ustamenkovic@tbor.bg.ac.rs

Table 1. Chemical composition of the investigated alloy (mass %)

Si	Fe	Cu	Mn	Mg	Cr	Ni	Zn
0.49	0.182	0.012	0.006	0.594	<0.003	0.028	0.01
Ti	Pb	V	Co	Sn	Zr	Al	
0.005	<0.003	0.014	<0.003	<0.003	<0.003	98.62	

The samples were solution heat treated at 550 °C for 1 h and then quenched in ice water in order to obtain the supersaturated solid solution (α_{SSS}). Immediately after the quenching, the samples were isochronally aged at different temperatures ranging from 160 °C to 330 °C, for 30 min and 60 min. The properties of the aged samples were compared to those of the quenched one (sample Q in Figures).

The sample of the supersaturated EN AW-6060 alloy designated for DSC analysis was investigated with the SDT Q600 (TA Instruments) simultaneous DSC/TGA analyzer by heating the sample up to 600 °C at the rate of 10 °C min⁻¹.

Hardness measurements were performed on the VEB Leipzig Vickers hardness tester with a 10 kg load and a 15 s dwelling time. In addition, microhardness values were measured using a PMT-3 Vickers microhardness tester using 100 gf loads with load duration of 15 s. Both hardness and microhardness measurements followed the ASTM E384 standard [10].

The electrical conductivity tester “Sigma test 2.063” was used to measure electrical conductivity.

Thermal properties were investigated on the DXF 500 thermal analyzer manufactured by TA Instruments using a flash method. The thermal diffusivity of the quenched sample was studied during the continuous heating at the rate of 10 °C min⁻¹. Based on the obtained hardness/microhardness values, three aging temperatures were selected for further thermal diffusivity and thermal conductivity measurements. These properties were measured at room temperature after aging at 160 °C, 230 °C and 330 °C.

Metallographic phase investigations, as well as the distribution of phases, were investigated using the TESCAN Vega 3 LMU scanning electron microscope equipped with an EDS X-act detector by Oxford Instruments.

RESULTS AND DISCUSSION

DSC analysis

Fig. 1 shows the DSC thermogram of the quenched EN AW-6060 alloy. The precipitation sequence in Al-Mg-Si alloys is rather complex. The largely accepted sequence can also be seen on the presented thermogram, which is: $\alpha_{\text{SSS}} \rightarrow \text{Mg:Si clusters} \rightarrow \text{G.P. zones} \rightarrow \beta'' \rightarrow \beta' \rightarrow \text{Si}$ (if excess silicon is present) $\rightarrow \beta$ [7, 8, 11-16]. There are six

exothermic peaks presented in Fig. 1, some of which are less pronounced due to low calorimetric effect [16].

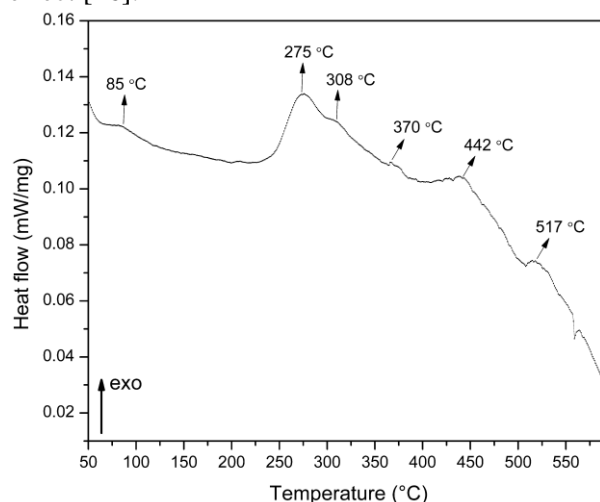


Fig. 1. DSC thermogram for the EN AW-6060 alloy

The peak associated with the Mg:Si clustering can be seen at around 85 °C [1, 7, 13, 17]. The formation of metastable β'' and β' precipitates is represented by the two exothermic peaks at 275 °C and 308 °C, respectively [5, 8, 11-18]. The β'' metastable phase is the phase that attracted the most attention of the researchers. Marioara *et al.* [19] characterized it as a needle-like phase with a monoclinic structure that precipitates along the $\langle 100 \rangle$ Al direction, with the unit cell characteristics being: $a = 15.16 \text{ \AA}$, $b = 4.05 \text{ \AA}$, $c = 6.74 \text{ \AA}$, $\beta = 105.3^\circ$.

The last three exothermic peaks that appear at 370 °C, 442 °C, and 517 °C represent the precipitation of the excess Si and the formation of the equilibrium β phase [11, 12]. Gupta *et al.* [12] gave the equation for calculating the excess Si in Al-Mg-Si alloys. For this alloy it is 0.1%. According to Gupta *et al.* [12], excess Si can have significant influence on the precipitation and strengthening, but in this case the influence is less significant, due to only 0.1% excess. According to the exothermic peaks that appeared on the DSC thermogram, the temperature of isochronal aging treatment was defined. DSC curves often shift to the right side of the diagram which can be attributed to the sample preparation, measuring equipment and a sample weight that is often very low - in this case about 10 mg [5, 12, 17]. Based on that fact, the temperature ranging from 160 °C to 330 °C was chosen. During the defined isochronal

treatment, hardness and microhardness values were measured.

Absolute hardness values as a function of aging temperature for the two applied times can be seen in Fig. 2. During the aging at lower temperatures, the hardness values decrease compared to the quenched state. This is most probably due to quenched-in vacancies and solutes causing the movement reduction of dislocations. Afterwards, the hardness gradually increases with the aging temperature reaching the peak age state at 230 °C for both aging times. This hardening is caused by the precipitation of the metastable β'' phase, which is the main hardening phase in aluminum alloys from the 6000 series [5, 11, 12, 20].

Compared to the quenched sample which had a 56 HV₁₀ hardness value, the peak-aged sample had a hardness value of 85 HV₁₀ when aged for 30 min, and 80 HV₁₀ when aged for 60 min. That is a 51.7% relative increase in hardness for the sample aged for 30 min and a 42.8% relative increase for the sample aged for 60 min.

As the aging temperature increases the hardness values decrease due to the overaging of the alloy. The change in precipitate type, size, and density, as well as the loss of matrix coherency, leads to the loss of hardening effect [21]. Metastable phases can increase the hardness values, but only for a small amount, as seen in Fig. 2 in the temperature interval from 260 to 330 °C. It can also be seen that in the temperature range from 200 °C to 330 °C aging for a shorter time (30 min) results in higher hardness values than for the longer aging time (60 min).

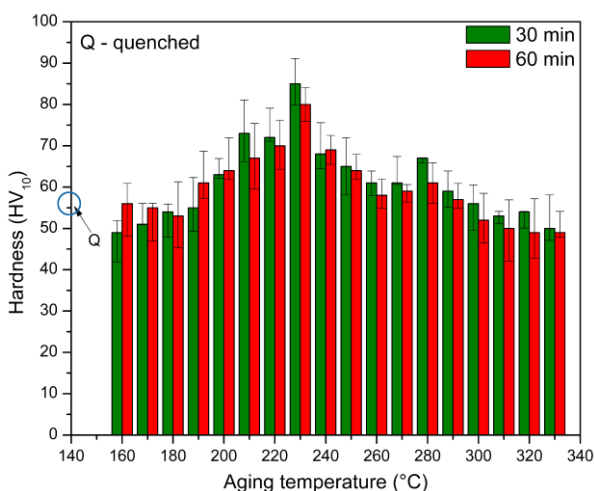


Fig. 2. Hardness values of the EN AW-6060 alloy after the isochronal aging treatment.

Study of mechanical properties

Microhardness measurements gave somewhat similar conclusions, as shown in Fig. 3. Maximal microhardness values were achieved at 230 °C for both aging times.

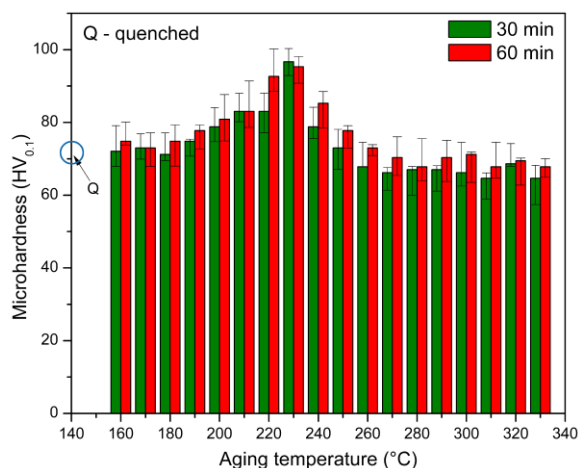


Fig. 3. Microhardness values of the EN AW-6060 alloy after the isochronal aging treatment.

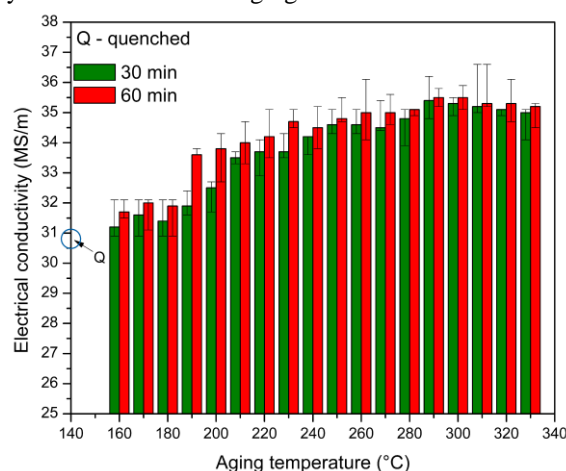


Fig. 4. Electrical conductivity values of the EN AW-6060 alloy after the isochronal aging treatment.

Aging for 30 min caused a 26% relative increase in microhardness value compared to the quenched sample, i.e., microhardness increased from 77 HV_{0.1} to 97 HV_{0.1}. When aged for 60 min there was a 19% relative increase in microhardness value compared to the quenched sample, i.e., microhardness increased from 77 HV_{0.1} to 95 HV_{0.1}. Overaging is particularly well illustrated in the part of the diagram covering the temperature range from 260 °C to 330 °C. In this case, almost all of the microhardness values of the aged samples are lower than those of the quenched one.

Investigation of electrical conductivity

The electrical conductivity values obtained during the isochronal aging treatment are presented in Fig. 4. The measurement of electrical conductivity can indirectly give information about precipitation, especially in Al-Mg-Si alloys where a strong connection between electrical conductivity and precipitation exists [22, 23].

The electrical conductivity of the quenched sample is 30.8 MS/m. Quenching caused the

increase in vacancies and solutes in the matrix causing the electron scattering effect [13, 23, 24]. During the aging, clusters and early-stage precipitates coarsen as a result of the diffusion process, which causes a gradual increase in electrical conductivity values. The metastable β'' and β' are formed, causing the dilution of the solid solution resulting in electrical conductivity increase [22, 23].

The electrical conductivity peak values are achieved at 290 °C for both aging times. The absolute increase in electrical conductivity is 4.6 MS/m during the aging at 290 °C for 30 min and 4.7 MS/m during the aging for 60 min. Aging for a longer time (60 min) caused higher electrical conductivity values than the shorter aging time (30 min). Prolonged aging time increases the precipitations dissolution and causes the easier formation of pre- β'' and β'' phases [23].

Investigation of thermal properties

Fig. 5 shows the thermal diffusivity of the quenched EN AW-6060 alloy during continuous heating at the rate of 10 °C min⁻¹.

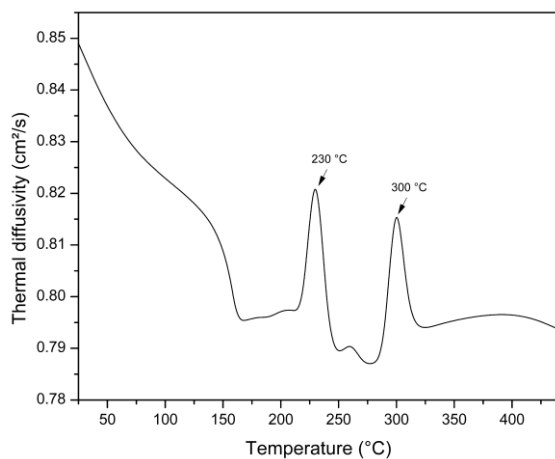


Fig. 5. Thermal diffusivity of quenched EN AW-6060 alloy during the continuous heating.

Usually, with an increase in temperature thermal diffusivity linearly decreases. This is caused by heat vibrations of the atoms in the matrix that interrupt the movements of electrons [25].

However, in Fig. 5 two peaks at 230 °C and 300 °C can be observed. The temperatures of the peaks coincide with the temperatures where the maximal values of hardness and electrical conductivity were obtained during the aging. Hence, the diffusivity peaks are the proof that metastable phases have an influence on thermophysical properties. The first peak that appears at 230 °C represents the formation of β'' precipitates. The second peak that appears at 300 °C is related to the formation of β' phase. Heat transfer is increased because the concentration of alloying elements in the solid

solution is reduced [8, 9]. Peaks that represent the formation of clusters and excess Si are not registered on the thermal diffusivity curve. This is most probably due to the fact that the thermal diffusivity measurements are not sensitive enough to register such small change in the structure, unlike the measurements in DSC analysis.

Thermal diffusivity and thermal conductivity were measured at room temperature after aging at 160 °C, 230 °C and 330 °C. These temperatures were chosen to represent three different stages in the precipitation process. G.P. zones were formed at the lowest chosen temperature; metastable phases were formed at the medium chosen temperature, while the highest chosen temperature indicates over-aging. The measured values of thermal diffusivity and thermal conductivity in the function of the aging temperature are given in Fig. 6. The presented results demonstrate that aging has an influence on the thermal properties.

Aging at 160 °C caused a decrease in thermal diffusivity and thermal conductivity values compared to the quenched state. This can be ascribed to the strong electron scattering effect caused by the formation of closely spaced G.P. zones and fine early-stage precipitates [13, 23, 26]. The highest values of thermal diffusivity were obtained at 230 °C for both aging times, as well as the values of hardness and microhardness.

This increase is also evident in Fig. 5 and is related to the formation of β'' precipitates. Aging at 330 °C caused a slight decrease in thermal diffusivity as a result of the precipitation of semi-coherent β' particles. During aging, thermal conductivity continuously increased up to 330 °C for the samples aged for 30 min. The thermal conductivity curve for the sample aged for 60 min follows the same trend as the curves for thermal diffusivity.

Microstructural investigation

In order to complete the investigation in more detail and study the effect of the aging process on the alloy's microstructure, SEM and EDS analysis were performed on the sample in peak hardness state, as presented in Fig. 7. It can be seen that the solid solution matrix is covered with finely dispersed particles of the metastable β'' phase, represented by the spectrum 3 in Fig. 7. Marioara *et al.* [20, 27] suggested that the ideal ratio of Mg:Si in the β'' phase should be 5 to 6, as presented in our analysis. It is very difficult to detect the ultra-fine particles of the β'' phase at these magnifications; however, the other results obtained in this study indirectly indicate their existence. This indication is evident through the hardness and microhardness

U. Stamenković et al.: The influence of isochronal aging on the mechanical and thermophysical properties of ... measurements that are enhanced by the precipitation of β'' phase after aging at 230 °C.

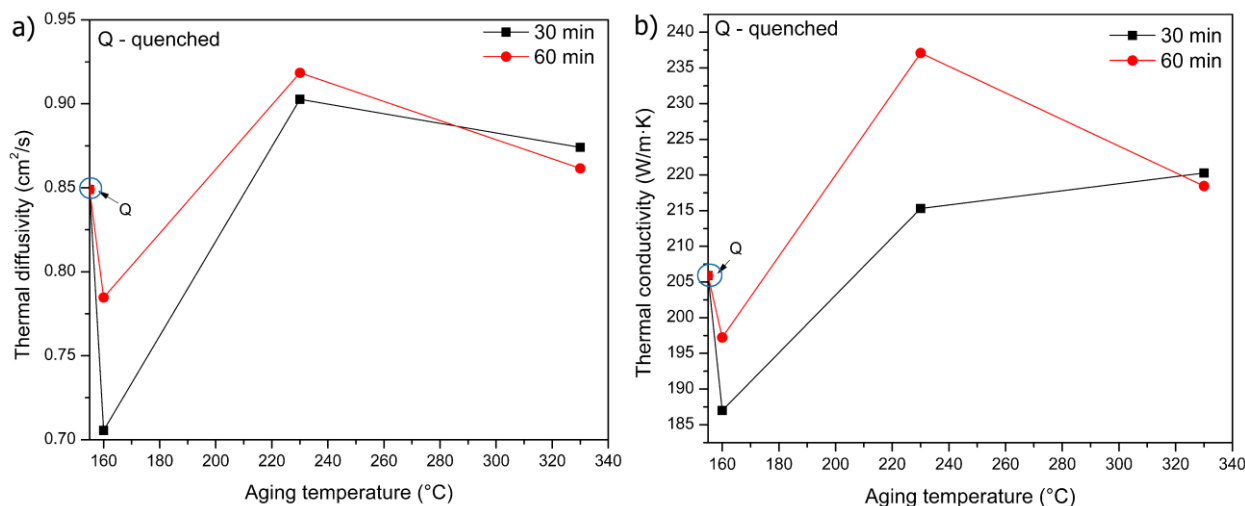


Fig. 6. Thermal diffusivity (a) and thermal conductivity (b) of EN AW-6060 alloy as a function of aging temperature

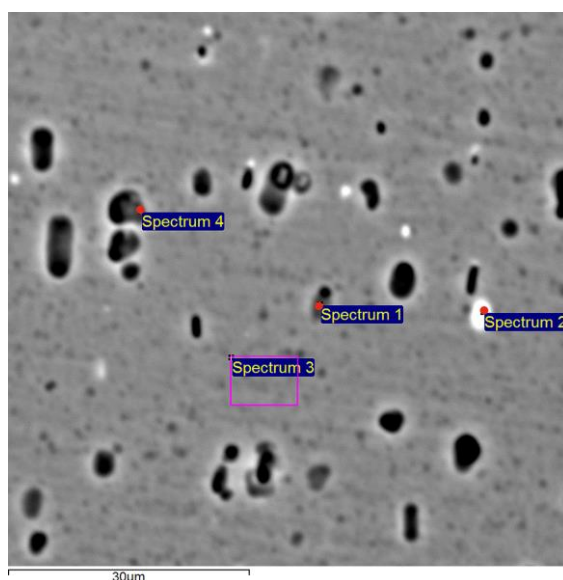


Fig. 7. SEM and EDS analyses of EN AW-6060 alloy after aging at 230 °C for 30 min

Table 2. Chemical composition of the analyzed spectra (at. %)

Spectrum	Mg	Al	Si	Fe
Spectrum 1	0.58	98.36	1.06	
Spectrum 2	0.51	95.55	1.48	2.46
Spectrum 3	0.50	98.93	0.57	
Spectrum 4	0.48	98.4	1.12	

CONCLUSIONS

Within the presented microstructure in Fig. 7 the precipitates that appear as a dark phase can be observed. This phase is illustrated by the spectra 1 and 4 and its chemical composition is provided in Table 2. There is also an additional white phase that appears throughout the microstructure. This is the quaternary AlMgSiFe phase, especially rich in iron represented by spectrum 2.

Based on the results obtained during the study of the influence of isochronal aging on the mechanical and thermophysical properties of the EN AW-6060 aluminum alloy, the following conclusions were drawn:

- Largely accepted precipitation sequence due to the precipitation of metastable phases (which is: $\alpha_{SSSS} \rightarrow \text{Mg:Si clusters} \rightarrow \text{G.P. zones} \rightarrow \beta'' \rightarrow$

$\beta' \rightarrow \beta$) was detected by the presence of exothermic peaks during the DSC analysis.

- Isochronal aging caused significant increase in mechanical and physical properties. The highest improvement in hardness and microhardness values was obtained after aging at 230 °C by the precipitation of metastable β'' phase. The formation of metastable β'' and β' phases caused the solid solution matrix to get less saturated, which increased electrical conductivity.
- Thermal diffusivity peaks obtained during the continuous heating confirmed the existence of β'' and β' precipitates. The highest values of thermal diffusivity and thermal conductivity were obtained at 230 °C for both aging times.
- Microstructural investigation confirmed the existence of finely dispersed metastable β'' phase with the ideal ratio of Mg:Si = 5:6, which caused the enhancement of physical, thermal and mechanical properties.

Acknowledgement: The research results were developed with the assistance of the Ministry of Education, Science and Technological Development of the Republic of Serbia under the projects OI 172037 and TR34003.

REFERENCES

1. K. Teichmann, C. D. Marioara, K. O. Marioara, K.O. Pedersen, K. Marthinsen, *Mater. Sci. Eng., A*, **565**, 228 (2013).
2. M. Kolar, K.O. Pedersen, S. Gulbrandsen-Dahl, K. Teichmann, K. Marthinsen, *Mater. Trans.*, **52**, 1356 (2011).
3. I.M. Masoud, T. Abu Mansour, J.A. Al-Jarrah, *Journal of Applied Sciences Research*, **8**, 5106 (2012).
4. S. Pogatscher, H. Antrekowitsch, T. Ebner, P.J. Uggowitzer, in: *Light Metals*, C. E. Suarez (ed.), Springer, Cham, 2012, p. 415.
5. T. Abid, A. Boubertakh, S. Hamamda, *J. Alloy. Compd.*, **490**, 166 (2010).
6. K. Strobel, M.D.H. Lay, M.A. Easton, L. Sweet, S. Zhu, N.C. Parson, A.J. Hill, *Mater. Charact.*, **111**, 43 (2016).
7. B. Milkerit, N. Wanderka, C. Schick, O. Kessler, *Mater. Sci. Eng., A*, **550**, 87 (2012).
8. Y.M. Kim, S.W. Choi, Y.C. Kim, C.S. Kang, S.K. Hong, *Appl. Sci.*, **8**, 2039 (2018).
9. S.W. Choi, Y.M. Kim, Y.C. Kim, *J. Alloy. Compd.*, **775**, 132 (2019).
10. <https://www.astm.org/Standards/E384.htm>
11. Y. Birol, *Trans. Nonferrous Met. Soc. China*, **23**, 1875 (2013).
12. A.K. Gupta, D.J. Lloyd, S.A. Court, *Mater. Sci. Eng., A*, **316**, 11 (2001).
13. G.A. Edwards, K. Stiller, G.L. Dunlop, M.J. Couper, *Acta Mater.*, **46**, 3893 (1998).
14. B.C. Shang, Z.M. Yin, G. Wang, B. Liu, Z.Q. Huang, *Mater. Design.*, **32**, 3818 (2011).
15. M. Vedani, G. Angella, P. Bassani, D. Ripamonti, A. Tuissi, *J. Therm. Anal. Calorim.*, **87**, 277 (2007).
16. L. Zhen, W.D. Fei, S.B. Kang, H.W. Kim, *J. Mater. Sci.*, **32**, 1895 (1997).
17. Y. Birol, *J. Mater. Process. Tech.*, **173**, 84 (2006).
18. S.W. Choi, H.S. Cho, C.S. Kang, S. Kumai, *J. Alloy. Compd.*, **647**, 1091 (2015).
19. C.D. Marioara, S.J. Andersen, J. Jansen, H.W. Zandbergen, *Acta Mater.*, **49**, 321 (2001).
20. C.D. Marioara, S.J. Andersen, J. Jansen, H.W. Zandbergen, *Acta Mater.*, **51**, 789 (2003).
21. O.R. Myhr, O. Grong, K.O. Pedersen, *Metall. Mater. Trans. A*, **41A**, 2276 (2010).
22. S. Karabay, *Mater. Design*, **27**, 821 (2006).
23. L. Cui, Z. Liu, Xi. Zhao, J. Tang, K. Liu, X. Liu, C. Qian, *Trans. Nonferrous Met. Soc. China*, **24**, 2266 (2014).
24. T.R. Prabhu, *Engineering Science and Technology, an International Journal*, **20**, 133 (2017).
25. T.M. Tritt, *Thermal Conductivity: Theory, Properties and Applications*, Kluwer Academic /Plenum Publisher, New York, 2004.
26. R.G. Lumley, N. Deeva, R. Larsen, J. Gemberovic, J. Freeman, *Metall. Mater. Trans. A*, **44**, 1074 (2013).
27. C.D. Marioara, H. Nordmark, S.J. Andersen, R. Holmestad, *Mater. Sci.*, **41**, 471 (2006).

Phytochemical screening and antimicrobial activity of extracts of *Cassia alata* L. leaves and seeds

P. T. Q. Le

Institute of Biotechnology and Food Technology, Industrial University of Ho Chi Minh City, No. 12 Nguyen Van Bao, Ward 4, Go Vap district, Ho Chi Minh city, Vietnam

Received January 11, 2019; Revised March 25, 2019

The aim of the study is to determine the presence of some bioactive compounds in *Cassia alata* L. leaves and seeds extracts such as tannins, saponins, anthraquinones and flavonoids. Total polyphenol contents (TPC) of leaves and seeds extracts are 59.211 mg GAE/g DW and 1.816 mg GAE/g DW, respectively, while their antioxidant capacities (AC) are 8.14 $\mu\text{mol Fe/g DW}$ and 2.75 $\mu\text{mol Fe/g DW}$, respectively. The antimicrobial activity is determined by the paper disc diffusion method combined with the minimum inhibitory concentration (MIC). Leaves extract inhibits *S. aureus* and *E. coli* at MIC of 400 mg/mL; *S. enteritidis* and *B. subtilis* at MIC of 800 mg/mL. Besides, seeds extract also inhibits *S. aureus* at MIC of 200 mg/mL; *E. coli*, *S. enteritidis* and *B. subtilis* at MIC of 400 mg/mL. However, leaves and seeds extracts of *C. alata* do not show any inhibitions on the growth of *A. niger*.

Keywords: Antibacterial activity, Antioxidant, *Cassia alata* L., Extract, MIC.

INTRODUCTION

Currently, there are many synthetic chemical compounds, which can inhibit the growth of microorganisms, that are widely used in food industry and medical technology. However, these compounds can affect consumer health and cause antimicrobial resistance. Therefore, it is an important challenge in chemical and medical field [1]. Until now, many studies have demonstrated that the roots, stems, leaves, and fruits of some plant species contain antimicrobial substances called phytoncides or plant antibiotics [2,3]. Therefore, some plant extracts can inhibit many microorganisms, for example, *Polygonum multiflorum* Thunb. root extract inhibited *S. aureus* and *S. enteritidis* [4]; extract of *Hyphaene thebaica* L. Mart. (Arecaceae) fruit inhibited *S. aureus* and *S. typhi* [5], etc.

In Vietnam, there are many herbal plants such as ginseng, dangshen, lingzhi mushroom, etc., that contain precious substances and are used in food industry or medicine [6]. Among them, *Cassia alata* L., which is planted as ornamental plant in Vietnam, contains various bioactive substances. According to the study of Meenupriya *et al.* [7], the authors identified phytochemical compounds such as alkaloids, flavonoids, saponins, tannins, coumarins, terpenoids, steroids, glycosides in *Cassia alata* L. leaves extract collected from India. The ethnomedical uses of *Cassia alata* L. have been recorded in many provinces in Vietnam. It can cure many diseases such as scabies, tokelau, etc. [6].

* To whom all correspondence should be sent:
E-mail: lephantanquoc@iuh.edu.vn

There are many researches on the extraction of bioactive compounds and their antifungal activity from *Cassia alata* L. leaves extract [8] but until now there is no report on phytochemical screening and antimicrobial activities of leaves and seeds extracts of *Cassia alata* L. in Vietnam by the combination of minimum inhibitory concentration and the paper disc diffusion method. Therefore, the current research was undertaken to determine some bioactive compounds and antimicrobial activities of ethanol extracts of *Cassia alata* L. leaves and seeds.

EXPERIMENTAL

Plant collection

Cassia alata L. leaves and seeds were collected from Ho Chi Minh city (Vietnam), cleaned by tap water, then dried at 60°C until moisture is lower than 13%. After that, the samples were milled and sieved with a sieve diameter of 500 μm ; packed under vacuum condition and stored at room temperature.

Organisms collection

A total of five tested microorganisms including: two gram-positive bacteria as *Bacillus subtilis* (ATCC 11774), *Staphylococcus aureus* (ATCC 25923), two gram-negative bacteria as *Escherichia coli* (ATCC 25922), *Salmonella enteritidis* (ATCC 13076) and the fungus *Aspergillus niger* were used in this study to determine the antimicrobial activity of extracts. All microorganisms were kindly provided by the Institute of Biotechnology and Food Technology, Industrial University of Ho Chi Minh city.

Ethanol extraction

The dried samples were extracted by microwave-assisted extraction (MAE) with 50% aqueous ethanol, dried seeds/ethanol ratio of 1/20 (w/v), dried leaves/ethanol ratio 1:10 (w/v) and microwave power of 194 W for 5 min. After the extraction process, the extract was filtered by Whatman paper no. 4 and the solvent was evaporated under vacuum conditions in a water bath at 45°C for 30 min. After that, the residue was freeze-dried during 7 h at -20°C, <1 mbar, then the dry extract was stored at 4°C until further experiments.

Phytochemical analysis

Identification of flavonoids. Ferric chloride test: Three drops of 5% FeCl₃ solution were added to the extract. The formation of greenish-black color indicated the presence of phenolic nucleus [9].

Identification of tannins. Gelatin test: Few drops of 10% gelatin solution were added to the extract. Formation of a precipitate indicated the presence of tannins [10].

Identification of anthraquinones. Borntrager's test: 2 mL of the extract were added to 5 mL of chloroform in a test tube and shaken for a few mins with an equal volume of 10% ammonia solution. The presence of free anthraquinones was evidenced by layering such as violet, pink or red [10].

Identification of saponins. Frothing test: The extract was placed in a test tube and added to 10 mL of distilled water; shook vigorously for 30 sec, then kept for 30 min and observed. The formation of foam indicated the presence of saponins [9].

Haemolysis test: Few drops of animal blood were added to the extract (dissolved in normal saline) by a syringe and mixed gently by inverting the tube and kept for 15 min. The settling down of red blood cells denoted the presence of saponins [11].

Determination of total polyphenol content (TPC) and antioxidant capacity (AC) of polyphenols by the phenanthroline method

The TPC of the extract was determined by the Folin Ciocalteu colorimetric method [12] with slight modifications. The results were calculated from a standard curve of gallic acid. TPC was expressed as mg of gallic acid equivalent per gram of dry weight (mg GAE/g DW).

The AC of the extract was slightly modified and determined by the phenanthroline method [13]. The reaction between iron and 1,10-phenanthroline produces orange-red complex. AC was presented as

μmol of Fe per gram of dry weight (μmol Fe/g DW).

Determination of antimicrobial activity and minimum inhibitory concentration (MIC) evaluation

The minimum inhibitory concentration (MIC) evaluation was performed by the paper disc diffusion method for antibiotic susceptibility testing according to the Kirby-Bauer test. The sterile paper discs of 6 mm diameter were prepared using various concentrations of dryness extract of leaves and seeds (50, 100, 200, 400 and 800 mg/mL); gentamicin (10 μg/disc) and ketoconazole (50 μg/disc) were used as positive controls to compare the antibacterial activity and antifungal activity, respectively; 5% dimethylsulfoxide (DMSO) was used as negative control. Firstly, 0.1 mL of bacteria suspension (0.5 McFarland standard, approximately 1.5×10⁸ cfu/mL) and 0.1 mL of fungus suspension (approximately 0.4×10⁴ – 5×10⁴ cfu/mL) were spread on the surface of the Mueller-Hinton agar media for bacterial strains and potato dextrose agar media for fungal strains by a sterile hockey stick, respectively. Then, the sterile paper discs were impregnated with 20 μL of each of extracts. The dishes were incubated during 24 h at 37°C for bacterial strains and 72 h at 30°C for fungal strain. After that, the zones of inhibition were expressed in mm as the diameters of clear zones around the discs.

Data analysis

Experimental results were analyzed by the one-way analysis of variance (ANOVA) method and significant differences among the means from triplicate analyses at (p<0.05) were determined by Fisher's least significant difference (LSD) procedure using Statgraphics software (Centurion XV). The values obtained were expressed in the form of a mean±standard deviation (SD).

RESULTS AND DISCUSSION

Identification of bioactive compounds

Phytochemical analysis of *Cassia alata* L. leaves and seeds was successfully performed; ethanol is a good solvent for the extraction of bioactive compounds of this plant. There are tannins, saponins and flavonoids in both *Cassia alata* L. leaves and seeds (Table 1). These results suggest that these parts of the plant can have an antibacterial capacity and antioxidant capacity because of the presence of these compounds. Tannins are polyphenols that are commonly found in plants such as *Cleome Ciliata* leaves [14] or

P.T.Q. Le: Phytochemical screening and antimicrobial activity of extracts of Cassia alata L. leaves and seeds Polygonum multiflorum Thunb. roots [4], etc. Tannins can be used to treat various human diseases, including diarrhea, stomach ulcers, snake bites and wounds [15]. In addition, they are good antioxidants, anti-aging, anti-inflammatory, anti-cancer agents [16]. The presence of flavonoids in this material is similar to that in *Paullinia pinnata* Linn leaves [11] or *Polygonum multiflorum* Thunb. roots [4] and these bioactive compounds have a strong antioxidant capacity. Several previous studies indicated that secondary metabolites of phenolic compounds such as flavonoids are responsible for a variety of pharmacological activities [17]. Note that free anthraquinones are only present in seeds extract; they are an important bioactive ingredient which possesses anti-cancer, anti-bacterial, anti-inflammatory effects [18]. In addition, it can activate the nucleotide repair system in human cells [19].

Apart from phenolic compounds, saponins were also detected in both *Cassia alata* L. leaves and seeds extracts. They also exist in other plants such as *Polygonum multiflorum* Thunb. roots [4],

Paullinia pinnata Linn leaves [11]. Basically, both *Cassia alata* L. leaves and seeds extracts contain many bioactive compounds. This is advantageous for the application of these compounds in medical technology.

Determination of total polyphenol content (TPC) and antioxidant capacity (AC) of extracts

Table 2 shows that TPC of leaves extract is 32 times higher than that of seeds extract while AC of leaves extract is 3 times higher than that of seeds extract. TPC of leaves extract is also higher than that of *Polygonum multiflorum* Thunb. root extract [4]. At the same time, AC of leaves and seeds extracts is higher than that of some vegetable oils extracts [13] or fresh garlic clove, garlic capsule, and baked garlic extracts [20]. This indicates that *Cassia alata* L. leaves and seeds are potential materials, especially the leaves, to be used for medical applications or functional products.

Table 1. Phytochemical constituents of *Cassia alata* L. leaves and seeds extracts

No.	Phytoconstituents	<i>Cassia alata</i> L. leaves extract	<i>Cassia alata</i> L. seeds extract
1	Tannins		
	FeCl ₃ test	+	+
2	Saponins		
	a. Frothing test	+	+
	b. Haemolysis test	+	+
3	Anthraquinones		
	Borntrager's test	-	+
4	Flavonoids		
	a. FeCl ₃ test	+	+
	b. NaOH test	+	+

“+”: Positive test

“-”: Negative test

Table 2. TPC and AC of *Cassia alata* L. leaves and seeds extracts

Materials	<i>Cassia alata</i> L. seeds extract	<i>Cassia alata</i> L. leaves extract
TPC (mg GAE/g DW)	1.82±0.17 ^a	59.21±3.02 ^b
AC (µmol Fe/g DW)	2.75±0.11 ^a	8.14±0.59 ^b

Various lowercase letters in the same row denote significant difference (p<0.05)

Table 3. Moisture and yield of dry extracts of *Cassia alata* L. seeds and leaves

Physicochemical characteristic	<i>Cassia alata</i> L. seeds dry extract	<i>Cassia alata</i> L. leaves dry extract
Moisture (%)	3.18±0.43 ^a	3.31±0.51 ^a
Yield (%)	16.67±2.8 ^b	8.16±2.01 ^a

Various lowercase letters in the same row denote significant difference (p<0.05)

P.T.Q. Le: Phytochemical screening and antimicrobial activity of extracts of Cassia alata L. leaves and seeds
Identification of moisture and yield of dry extracts

Based on the results of this study, the moisture of extracts of *Cassia alata* L. leaves and seeds is 3.31% and 3.18%, respectively (Table 3). They are similar to the dry extract of *Polygonum multiflorum* Thunb. root (3.03%) [4]. The dry extract should be stored at 4°C to avoid oxidation reaction and degradation of bioactive compounds.

The results suggest that the yield of recovery extracts from *Cassia alata* L. is quite high, extracts of leaves and seeds are 8.16% and 16.67%, respectively. These results are higher than those in the recent study of Vö *et al.* [21] (the dry extract from trunk and leaves of *Pouzolzia zeylanica* L. was nearly 2.96%) and the study of Đái *et al.* [22] (the extract from trunk and leaves of *Streptocaulon juventas* Merr. was 3.55%). This study proves that the obtained yields depend on various factors such as material, solvent, extraction methods, etc.

Antibacterial activity and minimum inhibitory concentration (MIC) evaluation

DMSO is a sulfur-containing organic compound with the formula (CH₃)₂SO, a colorless liquid that can be mixed with a wide range of organic solvents as well as with water. It is used as a negative control for various anti-microorganism tests of herbal plant extracts such as *Polygonum multiflorum* Thunb. root [4], the fruit pulp of wood apple [23], etc. In addition, gentamycin and ketoconazole are also positive controls for various antibacterial and antifungal tests [4,24]. The results show that these positive controls have high anti-microorganism capacities (zone of inhibitions ≥14 mm for fungus and ≥18 mm for bacteria) (Tables 4, 5, 6). Gentamycin binds quickly to the ribosome of bacteria, inhibits protein synthesis process and reduces the accuracy of the information RNA which leads to wrong combination of amino acids in the polypeptide chain of bacteria [25]. Furthermore, ketoconazole can inhibit the uptake of precursors of RNA and DNA, inhibits synthesis of peroxidative and oxidative enzymes and increases membrane permeability, which inhibits the growth of fungi [26].

Tables 4 and 5 show that dry seeds and leaves extracts of *Cassia alata* L. have antimicrobial activity against *S. aureus*, *E. coli*, *S. enteritidis* and *B. subtilis*. For seeds extract of *Cassia alata* L., *S. aureus* is inhibited at MIC of 200 mg/mL while the rest of bacteria are inhibited at MIC of 400 mg/mL. At the same time, leaves extract of *Cassia alata* L. can inhibit *S. aureus*, *E. coli* at MIC of 400 mg/mL and *S. enteritidis*, *B. subtilis* at MIC of 800 mg/mL. All inhibition zones are broader than 10 mm and

the antimicrobial effect increases with the increase in extract concentration. However, seeds and leaves extract of *Cassia alata* L. did not inhibit *A. niger* (Table 6); this result is similar with that in the study of Khan *et al.* [8] who reported that all parts of *Cassia alata* L. did not inhibit *A. niger*. In general, the antibacterial capacity of the extract of *Cassia alata* L. seeds is better than that of *Cassia alata* L. leaves mainly because it has antibacterial capacity at lower MIC.

Antibacterial capacity depends on the bioactive compounds in the extract, especially tannins, anthraquinones, flavonoids and saponins. For tannins, there are many antimicrobial mechanisms, such as alteration of the microorganism metabolism through the inhibition of oxidative phosphorylation, inhibition of enzyme activity by formation of complex with substrates of bacteria, etc. [27,28].

Some flavonoids have been shown to have strong antibacterial activity such as apigenin, galangin, flavon and flavonol glycosides, isoflavones, flavanones and chalcones [29]. Lipophilic flavonoids can also break down microbial membranes [30]. Mori *et al.* [31] suggested that the B ring of flavonoids could interleave or form hydrogen bonds with the overlap of bases in the nucleic acid molecule and further lead to inhibition of DNA and RNA synthesis of bacteria. Another study demonstrated the inhibition of quercetin, apigenin, and 3,6,7,3',4'-pentahydroxyflavone against DNA replication of *E. coli* [32].

The presence of anthraquinones in *Cassia alata* L. seeds extract can improve the antibacterial capacity. They have been used as a colorant in food, medicine, cosmetics, hair dyes and textiles. Currently, more than 300 naturally occurring anthraquinones are discovered. Some anthraquinones are found in many traditional Chinese medicine herbs such as *Rheum*, *Cassia*, *Aloe* and *Polygonum* [33]. Anthraquinones can inhibit respiration of some bacteria [34], interfere in redox of enzyme NADH dehydrogenase in bacteria [35]. Apart from the above phenolic compounds, saponins are also detected in *Cassia alata* L. seeds and leaves extracts. Various biological effects of saponins are reported including hemolytic and antibacterial activities [36]. The antimicrobial activity of saponins depends on the structure of aglycone of saponins. The efficiency of glucose utilization of microorganisms is quickly reduced by the presence of saponins, which in turn affects the development of microbes, reduces the activity of key enzymes in physiological metabolism, suppresses the synthesis of relevant proteins, and finally executes the antibacterial effect [37].

Table 4. Antibacterial activities of dry extract of *Cassia alata* L. seeds

Bacterial strains	Zone of inhibition (mm)						
	Gentamycin (10 µg/disc)	DMSO 5%	Concentrations of <i>Cassia alata</i> L. seeds dry extract (mg/mL)				
			800	400	200	100	50
<i>S. aureus</i>	27.3±0.5 ^{Cd}	-	16.7±0.5 ^{Cc}	14.7±0.5 ^{Cb}	12.7±0.5 ^a	-	-
<i>E. coli</i>	19.7±0.5 ^{Bb}	-	10.0±0.8 ^{Aa}	9.7±0.5 ^{Aa}	-	-	-
<i>S. enteritidis</i>	18.5±0.4 ^{Ac}	-	12.3±0.5 ^{Bb}	11±0 ^{Ba}	-	-	-
<i>B. subtilis</i>	20.3±0.5 ^{Bc}	-	11±0 ^{Ab}	9.7±0.5 ^{Aa}	-	-	-

Various lowercase letters in the same row denote significant difference (p<0.05).

Various uppercase letters in the same column denote significant difference (p<0.05).

“-”: Negative test.

Table 5. Antibacterial activities of dry extract of *Cassia alata* L. leaves

Bacterial strains	Zone of inhibition (mm)						
	Gentamycin (10 µg/disc)	DMSO 5%	Concentrations of <i>Cassia alata</i> L. leaves dry extract (mg/mL)				
			800	400	200	100	50
<i>S. aureus</i>	27±1.4 ^{Cb}	-	15.3±0.5 ^{Ba}	14.7±1.7 ^{Ba}	-	-	-
<i>E. coli</i>	20±1.4 ^{Bb}	-	11±0.8 ^{Aa}	10.3±0.5 ^{Aa}	-	-	-
<i>S. enteritidis</i>	18.3±0.5 ^{Ab}	-	12.3±1.7 ^{Aa}	-	-	-	-
<i>B. subtilis</i>	20±0.5 ^{Bb}	-	14.7±0.5 ^{Ba}	-	-	-	-

Various lowercase letters in the same row denote significant difference (p<0.05).

Various uppercase letters in the same column denote significant difference (p<0.05).

“-”: Negative test

Table 6. Antifungal activities of dry extract of *Cassia alata* L. leaves and seeds

Bacterial strains	Ketoconazole (50 µg/disc)	DMSO (5%)	Concentrations of <i>Cassia alata</i> L. leaves and seeds dry extract (mg/mL)				
			800	400	200	100	50
Zone of inhibition of <i>Cassia alata</i> L. seeds dry extract (mm)							
<i>A. niger</i>	15.7±1.2 ^A	-	-	-	-	-	-
Zone of inhibition of <i>Cassia alata</i> L. leaves dry extract (mm)							
<i>A. niger</i>	14±1.6 ^A	-	-	-	-	-	-

Various uppercase letters in the same column denote significant difference (p<0.05).

“-”: Negative test

CONCLUSION

The results show that the extracts of *Cassia alata* L. leaves and seeds contain some bioactive compounds such as tannins, flavonoids, anthraquinones and saponins. TPC and AC of leaves extract are higher than those of seeds extract.

The dry extracts of seeds and leaves can inhibit some bacteria but they can not inhibit *A. niger*.

Acknowledgement: The author wishes to thank Vo Thi Dung, Nguyen Thi Tuyet Nhung, Nguyen Tran Ky Duyen and Duong Thi Men for their supports in this study.

REFERENCES

1. C. K. Amadou, *Afric. Health J.*, **2**, 20 (1998).
2. D. Portz, E. Koch, A.J. Slusarenko, *Eur. J. Plant Pathol.*, **122**, 197 (2008).
3. H. A. Mabrouk, E. M. H. Labib, M. A. Zaki, *Egypt. J. Aquat. Res.*, **37**, 199 (2011).
4. L. P. T. Quoc, N. V. Muoi, *Carpathian J. Food Sci. Technol.*, **10**, 137 (2018).
5. W. Aboshora, Z. Lianfu, M. Dahir, M. Qingran, S. Qingrui, L. Jing, N. Q. M. Al-Haj, A. Ammar, *Trop. J. Pharm. Res.*, **13**, 2057 (2014).
6. T. L. Đõ, *Herbal Plants and their Medicine in Vietnam*, Medicine Press, Ha Noi, 2004.
7. J. Meenupriya, A. S. Vinisha, P. Priya, *World J. Pharm. Sci.*, **2**, 1723 (2014).
8. M. R. Khan, M. Kihara, A.D. Omoloso, *Fitoterapia*, **75**, 561 (2001).
9. A. Sofowora, in: *Textbook of Pharmacognosy*, W. C. Evans (eds.), Spectrum Books Limited, Ibadan, 1993, p. 50.
10. W. C. Evans, *Trease and Evans Pharmacognosy*, W.B Saunders Press, London, 2002.
11. A. Z. Yusuf, A. Zakir, Z. Shemau, M. Abdullahi, S. A. Halima, *J. Pharmacogn. Phytother.*, **6**, 10 (2014).
12. A. Siddiqua, K. B. Premakumari, R. Sultana, S. Vithya, *Int. J. Chem. Tech. Res.*, **2**, 205 (2010).
13. A. S. Szydłowska-Czerniak, C. Dianoczki, K. Recseg, G. Karlovits, E. Szyk, *Talanta*, **76**, 899 (2008).
14. S. C. Umerie, N. H. Okorie, S. C. Ezea, A. N. Okpalaononuju, *Int. J. Curr. Res. Rev.*, **4**, 5 (2012).
15. L. M. S. Perera, D. Ruedas, B. C. Gomez, *J. Ethnopharmacol.*, **77**, 1 (2001).
16. M. Atanassova, V. Christova-Bagdassarian, *J. Univ. Chem. Technol. Metall.*, **44**, 413 (2009).
17. A. K. Pandey, *Natl. Acad. Sci. Lett.*, **30**, 383 (2007).
18. G. Srinivas, R. J. Anto, P. Srinivas, S. Vidhyalakshmi, V. P. Senan, D. Karunagaran, *Eur. J. Pharmacol.*, **473**, 117 (2003).
19. L. C. Chang, H. M. Sheu, Y. S. Huang, T. R. Tsai, K. W. Kuo, *Biochem. Pharmacol.*, **58**, 49 (1999).
20. J. Songsungkan, S. Chanthai, *Int. Food Res. J.*, **21**, 2377 (2014).
21. T. T. A. Võ, C. L. Trần, T. T. T. Trần, P. Q. Đõ, *Can Tho Univ. J. Sci.*, **52**, 29 (2017).
22. T. X. T. Đái, H. B. N. Lâm, T. T. A. Võ, *Can Tho Univ. J. Sci.*, **40**, 1 (2015).
23. A. Senthilkumar, V. Venkatesalu, *Ind. Crops Prod.*, **46**, 66 (2013).
24. M. Masibo, Q. He, *Malays. J. Microbiol.*, **5**, 73 (2009).
25. T. R. Zembower, G. A. Noskin, M. J. Postelnick, C. Nguyen, L. R. Peterson, *Int. J. Antimicrob. Agents*, **10**, 95 (1998).
26. J. H. Van-Tyle, *Pharmacotherapy*, **4**, 343 (1984).
27. A. Scalbert, *Phytochemistry*, **30**, 3875 (1991).
28. M. A. Rebecca, E. L. Ishii-Iwamoto, R. Grespan, R. K. N. Cuman, S. M. Caparroz-Assef, J. C. P. Mello, C. A. Bersani-Amado, *J. Ethnopharmacol.*, **83**, 101 (2002).
29. T. P. T. Cushnie, A. J. Lamb, *Int. J. Antimicrob. Agents*, **26**, 343 (2005).
30. D. E. Moerman, *J. Ethnopharmacol.*, **52**, 1 (1996).
31. A. Mori, C. Nishino, N. Enoki, S. Tawata, *Phytochemistry*, **26**, 2231 (1987).
32. K. A. Ohemeng, C. F. Schwender, K. P. Fu, J. F. Barrett, *Bioorg. Med. Chem. Lett.*, **3**, 225 (1993).
33. Y. W. Wu, J. Ouyang, X. H. Xiao, W. Y. Gao, Y. Liu, *Chi. J. Chem.*, **24**, 45 (2006).
34. C. H. Chen, T. T. Li, H. L. Su, C. I. Wang, *Acta Biochim. Biophys. Sin.*, **3**, 426 (1963).
35. Y. Zhang, Q. H. Chen, *Acta Biochim. Biophys. Sin.*, **18**, 239 (1986).
36. E. Karimi, H. Z. Jaafar, S. Ahmad, *Molecules*, **16**, 4438 (2011).
37. Yu, Z. H., X. Z. Ding, L. Q. Xiz, X. Q. Xiao, Z. P. Cao, S. Xu, S. Liu, X. M. Liu, *Food Sci.*, **34**, 75 (2013).

Degradation of cyanide from gold processing effluent by H₂O₂, NaClO and Ca(ClO)₂ combined with sequential catalytic process

M. S. Kamrani¹, K. Seifpanahi-Shabani^{1*}, A. Seyed-Hakimi², G.A.M. Al^{3,4}, Sh. Agarwa⁵, V. K. Gupta⁵

¹ Faculty of Mining, Petroleum and Geophysics Engineering, Shahrood University of Technology, Shahrood, Iran

² Quality Control and Environment Department, Aq-Dareh Gold Mine, Takab, Iran

³ Chemistry Department, Faculty of Science, Al-Azhar University, Assiut 71524, Egypt

⁴ Faculty of Industrial Sciences & Technology, University Malaysia Pahang, 26300 Gambang, Kuantan, Pahang, Malaysia

⁵ Department of Biological Sciences, Faculty of Science, King Abdulaziz University, Jeddah, Saudi Arabia

Received January 16, 2018; Revised March 23, 2019

This work investigates the removal of cyanide as a noxious pollutant in the gold processing effluent (Aq-Dara mine, Takab, Iran) using H₂O₂, H₂O₂+Fe(II) (Fenton), H₂O₂+Cu(II), NaClO and Ca(ClO)₂ oxidants. Implementation of purification operation was carried out by varying the parameters including pH, oxidant dosage, temperature and time of the reaction. The results show that the oxidants have the highest efficacy at pH 10-12, while the Fenton process has the highest efficiency at pH 8. The results confirm that Ca(ClO)₂ is the best oxidant due to the shorter time, low reaction rate, high degradation of cyanide and low cost. The obtained results of response surface methodology optimization show that cyanide degradation has a direct relation to temperature, amount of oxidant, time and catalyst dosage parameters and has an inverse relation to pH. Also, the cyanide elimination efficiency is more than 99.5% and residual cyanide less than Environmental Protection Agency standards and 40% of the consumed water can be compensated by the effluent treatment and its return to the factory's processing circuit.

Keywords: Oxidation Process; Gold Processing Effluents Treatment; Cyanide Degradation; Non-linear Kinetic Modeling, Response Surface Method.

INTRODUCTION

Water pollution by organic and inorganic substances became a critical environmental problem [1-5]. Cyanide is a highly toxic, dangerous and hazardous chemical compound in gaseous, liquid and solid phases [6-8]. Cyanide is an important industrial chemical which is produced on a large scale for use in gold ore extraction, electroplating and many other industries [9, 10]. Such industries discharge large amounts of cyanide-containing liquid waste which often contains significant amounts of heavy metals and is a highly toxic and hazardous effluent [11-13]. Accordingly, environmental contamination by harmful compounds is considered as a big challenge [14, 15]. It is estimated that more than 100,000 tons of anthropogenic cyanide enter the environment annually [16-18]. Because of the potential hazards associated with cyanide, the discharge of these effluents into the environment without treatment is forbidden [19]. Literally, several methods are reported for removal of cyanide from wastewater such as alkaline chlorination [20], destruction on trickling filters

[21], oxidation with ozone [22], Fenton oxidation [23], sulfur dioxide [24], ultrasonic [25], ion exchange [26], Caro's acid [27, 28], photocatalytic degradation [29], adsorption process [30, 31], polymerization with formaldehyde [32], biodegradation [33] and Fenton catalytic degradation [34]. Hydrogen peroxide (H₂O₂) is widely used in the industry for the treatment of cyanide-containing effluents, as it is a strong oxidant [35]. H₂O₂ reacts with cyanide to produce cyanate which hydrolyzes ammonium and carbonate ions [36]. The reaction is conducted at a pH value of around 10 [37]. H₂O₂ can oxidize cyanide to cyanate in the presence of a transition metal (Cu, Ag, V, Ru, Mg) as a catalyst [38]. The final products are carbonate and ammonia compounds [25]. Fenton's oxidation is one of the best-known metal-catalyzed oxidation reactions of water-miscible organic compounds [39]. The mixture of FeSO₄ or any other ferrous complex and H₂O₂ (Fenton's reagent) at enough low pH, results in Fe(II) catalyzed decomposition of H₂O₂ and proceeds *via* a free radical chain process that produces hydroxyl radicals which have extremely high oxidizing ability [40]. Transition metal salts can activate H₂O₂ to form hydroxyl radicals which are strong oxidants [41]. The main advantage is the complete destruction of contaminants to harmless

* To whom all correspondence should be sent:

E-mail: q.s11063@yahoo.com,
seifpanahi@shahroodut.ac.ir
vinodfcy@gmail.com

compounds, water and inorganic salts [42]. Two major advantages of Fenton over other advanced oxidation processes include the lack of sophisticated equipment and facilities requirement and lack of limitation effects on mass transfer. In addition, it is a cost-effective and environmentally friendly method [23].

Likewise, alkaline chlorination has been well known for a long time as an effective means of treatment for industrial wastewaters [43], does not require a catalyst and is reported to be easy to operate [23]. Cyanide oxidation by calcium or sodium hypochlorite (Ca(ClO)₂ or NaClO) is an acceptable technique for cyanide wastewater treatment [44], where the reaction occurs in two stages. The first stage is the free cyanide rapid reaction with the hypochlorite ion ClO⁻ in aqueous solution forming as the intermediate compound the cyanogen chloride (CNCl) [45]. The second stage of the process involves cyanate (OCN⁻) hydrolysis and bicarbonate/nitrogen decomposition. This process needs strict pH control in order to prevent the release of cyanogen chloride which is highly toxic [46].

So this work focused on comparing the efficiency and conducting an experimental study on the kinetics of the oxidation of aqueous cyanide ion by alkaline chlorination and hydrogen peroxide by different catalyst processes in the removal of cyanide from gold processing wastewater (Aq-Dareh gold mine, Iran). In addition, nonlinear kinetic modeling and wastewater treatment economical assessment were done for each reaction. So, this paper presents the fundamentals and the approaches utilized in the development of the most efficient, economical and environmentally acceptable water management system possible for a particular mineral processing operation utilizing the cyanidation process.

MATERIALS AND METHODS

Samples and chemicals

Samples were collected from the wastewater that is contaminated with cyanide from the Aq-Dareh mine and gold processing plant located 32 km from Takab city in Western Azerbaijan province, Iran. The wastewater consists of a colorless solution that is clear but contains 40 mg/L of cyanide plus sewage. Calcium hypochlorite (Ca(ClO)₂), sodium hypochlorite (NaClO), iron sulfate heptahydrate (FeSO₄·7H₂O), hydrogen peroxide (H₂O₂, 30%) and copper sulfate pentahydrate (CuSO₄·5H₂O) of analytical grade were purchased from Merck. Solution pH values

were adjusted using reagent-grade NaOH and HCl solutions with different molar concentrations. All chemicals were used without further purification and all solutions were prepared using freshly prepared distilled water.

Experimental apparatus and procedures

All experiments were performed at room temperature and ambient light in order to reproduce full-scale operational conditions. Homogeneous samples were taken at different times from the part of the gold processing flow sheet that is named Paste Production and Storage Mechanism (PPSM). The samples were collected in sterile plastic containers and kept in the dark at the environmental temperature for less than one hour before being analyzed in the laboratory. Cyanide concentrations were determined by a colorimetric method on a UV-Visible spectrophotometer (Unico-2300) at a wavelength of 578 nm [16]. A pH meter Metrohm 827 model (Swiss mode) was used for pH measurements or adjustment. All samples were agitated with a magnetic stirrer (200 rpm) to provide an aerated environment and perfect mix. Chemical oxidation processes have higher operating costs but they are faster, more efficient and reliable for the breakdown of cyanide by comparison with natural degradation. This experimental study was designed to compare cyanide removal using H₂O₂ (no catalyst), Fenton (H₂O₂+Fe(II)), H₂O₂+Cu(II), and alkaline chlorination processes on a laboratory scale. During the processes, the effect of the main parameters, namely, pH, oxidant dosage, temperature and reaction time on the removal of cyanide from gold processing wastewater was studied (Table 1).

According to Table 1, the pH values were changed from 8 to 13, where at pH values less than 8 the soluble cyanide is volatile [16, 47] and same when temperatures values are more than 35 °C [48]. Obtained data from temperature changing on cyanide removal were used for thermodynamical studies [49]. Different oxidant with various dosages was used. The result of oxidants dosages changes was utilized for nonlinear kinetic modeling. At pre-selected times, 100 mL of contaminated wastewater was collected from the PPSM and added oxidant reagents solution to quench the residual radical reaction. At least three replicate runs were carried out for each experiment in order to ensure reproducible data and the results presented herein represent the average of these replicates, with a standard deviation of 0.16.

Table 1. The ranges of main parameters applied to the wastewater treatment process

Oxidant	pH	Reaction time (min)	Temperature (°C)	Dosage (g/L)
H ₂ O ₂		0-300		0.04-4.78
Fenton		0-130		0.05-1.00
H ₂ O ₂ /Cu(II)	8-13	0-220	20-35	0.04-1.09
Ca(ClO) ₂		0-25		0.08-0.90
NaClO		0-35		0.07-1.32

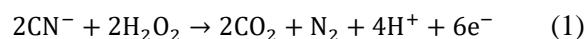
RESULTS AND DISCUSSION

Effect of pH

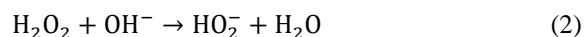
The pH effect on cyanide degradation efficiency was investigated and is shown in Fig. 1. Based on Eh-pH diagram of the aqueous cyanide system and pH-dependent fractionation of HCN and CN⁻, cyanide essentially exists in the form of HCN at pH below 9.3 under non-oxidizing conditions [50]. The level of free cyanide (CN⁻) in equilibrium with HCN decreases by increasing acidity. In order to avoid the cyanide volatilization, the pH was selected in the range of 8-13.

Figure 1 depicts the influence of pH on various oxidation processes for cyanide (40 mg/L) degradation. The optimum pH value for effective treatments in H₂O₂, Fenton, H₂O₂+Cu(II), Ca(ClO)₂ and NaClO process are equal to 10, 8, 10, 11.5 and 12, respectively. The amount and rate of cyanide degradation increased at higher pH by all oxidants except Fenton. Based on Fig. 1, with pH value increasing, the cyanide degradation by Fenton decreased from 60 to 2.5%. Whereas for other oxidants by increasing pH, the cyanide removal increased. The findings support that the Fenton process has better efficiency at low pH. On the other hand, cyanide at pH lower than 8 produces HCN - a dangerous gas. As mobility and solubility of toxic elements increased and hydrogen radicals competed with metal ions for cation exchange, thereupon the efficiency decreased. Fenton process with higher degradation efficiencies has been also reported at acidic conditions (pH ≈ 3) for some other contaminants such as citrate, Reactive Black 5 dye, and arsenic compounds [51]. As the amount of generated OH radicals increases at alkaline pH value and by rising pH up to 11, cyanide removal was increased. At pH 11, cyanide is entirely in ionic form, but at pH > 11, because of the competitive absorption between CN⁻ and HO⁻, the cyanide removal rate decreases, hence the maximum cyanide degradation occurs at pH 11. When cyanide is completely oxidized to CO₂ and N₂ (as illustrated in reaction 1), two moles of H⁺ are possibly produced when one mole of cyanide was degraded by H₂O₂. Thus, as pH decreases the reaction cannot be favored to produce CO₂ and N₂

as final products.



Significant enhancement of H₂O₂ decomposition was observed at pH 11 in the presence of Cu(II) ions. This was possible because Cu(II) ions would consume OH⁻ to hydroxyl complexes or hydroxide precipitate and accelerate the reactions [25]. The generated H₂O₂ could be decomposed to HO₂⁻ via reaction 2 when the solution pH is higher than 10. HO₂⁻ anions have good stability, but their oxidation potential is lower than that of H₂O₂ (oxidation potential E = 1.763 V at pH = 0 and E = 0.878 V at pH = 14). Therefore, it is found that the oxidation of cyanide proceeds rather slowly in this system [52].



For NaClO and Ca(ClO)₂ oxidants, by increasing pH the cyanide removal increased and high degradation occurred at pH 12 and 11.5, respectively. For higher pH values the efficiency severely decreased and this phenomenon refers to the evaporation process. Therefore, the degradation reaction was done at highly alkaline pH. On the other hand, for pH above 12, Cl⁻ ion consumption increased and consequently, cyanide treatment decreased. At lower pH, as illustrated by reactions 3 and 4, the dominant form of active chlorine is hypochlorous acid (E_(HClO/Cl₂) = 1.63 V or E_(HClO/Cl⁻) = 1.48 V), which exhibits considerably higher oxidation potential than hypochlorite (E_(ClO⁻/Cl⁻) = 0.89 V) in alkaline media. In this study, removal of cyanide was performed at the optimal alkaline condition in order to avoid the generation of evaporated HCN. Therefore, the cyanide oxidation process by ClO⁻ is limited [45]:



Effect of oxidant dosage

Different tests were performed to study cyanide oxidation. In these tests, an industrial solution of pH 10 containing 40 mg/L of cyanide was used.

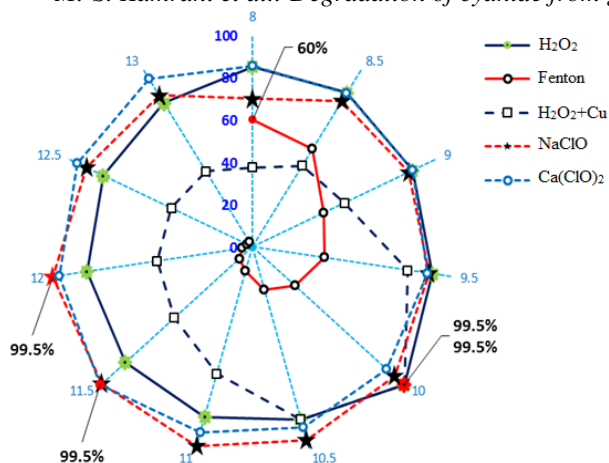


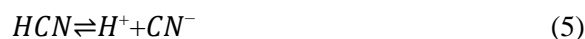
Fig. 1. Effect of different pH on the cyanide removal for five processes

The effect of oxidant dosage on cyanide removal was studied in the presence of different oxidants. The obtained results for oxidants dosage are shown in Fig. 2. The suitable dosages for effective treatments by H₂O₂ (no catalyst), Fenton, H₂O₂+Cu(II), Ca(ClO)₂ and NaClO process are 4.78, 1.00, 1.09, 0.90 and 1.19 g/L, respectively. As shown in Fig. 3, the hypochlorites are effective for chemical oxidation, which leads to reduced concentration of cyanide below the permitted level (less than 0.2 mg/L). However, to reach complete cyanide degradation, the amount of calcium hypochlorite used is lower than that of sodium hypochlorite, which is due to the stronger reactivity of calcium than sodium. The increase in other oxidants amounts also has similar results and with the increase in oxidant dosage, the cyanide degradation increases, but it is different for each one. When H₂O₂ was used, the oxidation was less evident due to the lack of a catalyst and almost three times the amount of catalyst that was used to increase the H₂O₂ consumption to cyanide degradation, completely oxidation of cyanide when copper is used as a catalyst is rapidly increased and the amount of hydrogen peroxide is lower. Hydroxyl radicals are devoid of any charge and have a high affinity for electrons, they can quickly strip any chemical of electrons including cyanide thus causing their oxidation. Depending on the amount of used H₂O₂, hydroxyl radicals react with cyanide thus causing its oxidation to form cyanate which further oxidizes to bicarbonate and nitrogen. Reaction stoichiometry is 1:1 when cyanate is formed and it increases further to 1:3 when nitrogen is formed [53]. Besides this decomposition reaction, it has been suggested for the removal of pollutants using different advanced oxidation processes combined with H₂O₂ that the hydroxyl

radicals formed can be scavenged by an excess of H₂O₂ to form much less oxidative H₂O₂ radicals [54]. Due to the fact that the reaction of Fenton was carried out at alkaline pH, the increase in the amount of H₂O₂ has increased the oxidation of cyanide up to 36% and did not show any increase in the amount of H₂O₂ oxidation by adding cyanide. Fe(OH)₃ sediment formed and prevented the reaction of free radicals [55]. Oxidant consumption during the process in aqueous solution is higher than the values predicted by stoichiometric number in the concentration. This behavior is probably due to the presence of other species that may also react with oxidation, thus the oxidant consumption was increased [56].

Effect of temperature on cyanide degradation

Temperature is an important parameter for the determination of cyanide oxidation rate. The effect of temperature on cyanide degradation was evaluated by changing the temperature between 20 and 35 °C. As mentioned, free cyanide would volatilize at temperatures slightly above ambient temperatures because its boiling point is 25.6 °C. However, the availability of metals would stabilize cyanide in the metallic complex form and thereby cause its retention in the environment at temperatures far above ambient temperature. As a consequence of reaction 5, the relative abundances of CN and HCN depend on pH.



So, the temperature has the most significant effect on the volatilization rate of free cyanide and most metal cyanide complexes were studied. The highest level of toxicity was observed at low pH and high temperature. As shown in Fig. 3, the rate of cyanide degradation increases by increasing temperature for all of the oxidants, which may be explained by the following presumption: for 25 °C in the solutions prepared with pure water CN and HCN are equally abundant at pH 9.2. The pH changes with temperature, increasing to 9.6 as the temperature is lowered to 10 °C and decreasing to 8.9 as the temperature is raised to 40 °C. Ionic strength also affects the abundances of CN⁻ and HCN, but the effect is relatively small. For ionic strengths like those encountered in actual leach solutions, pH for 25 °C decreases from 9.2 to 9. As explained, a part of cyanide degradation at high temperature is the concern to the cyanide evaporation process.

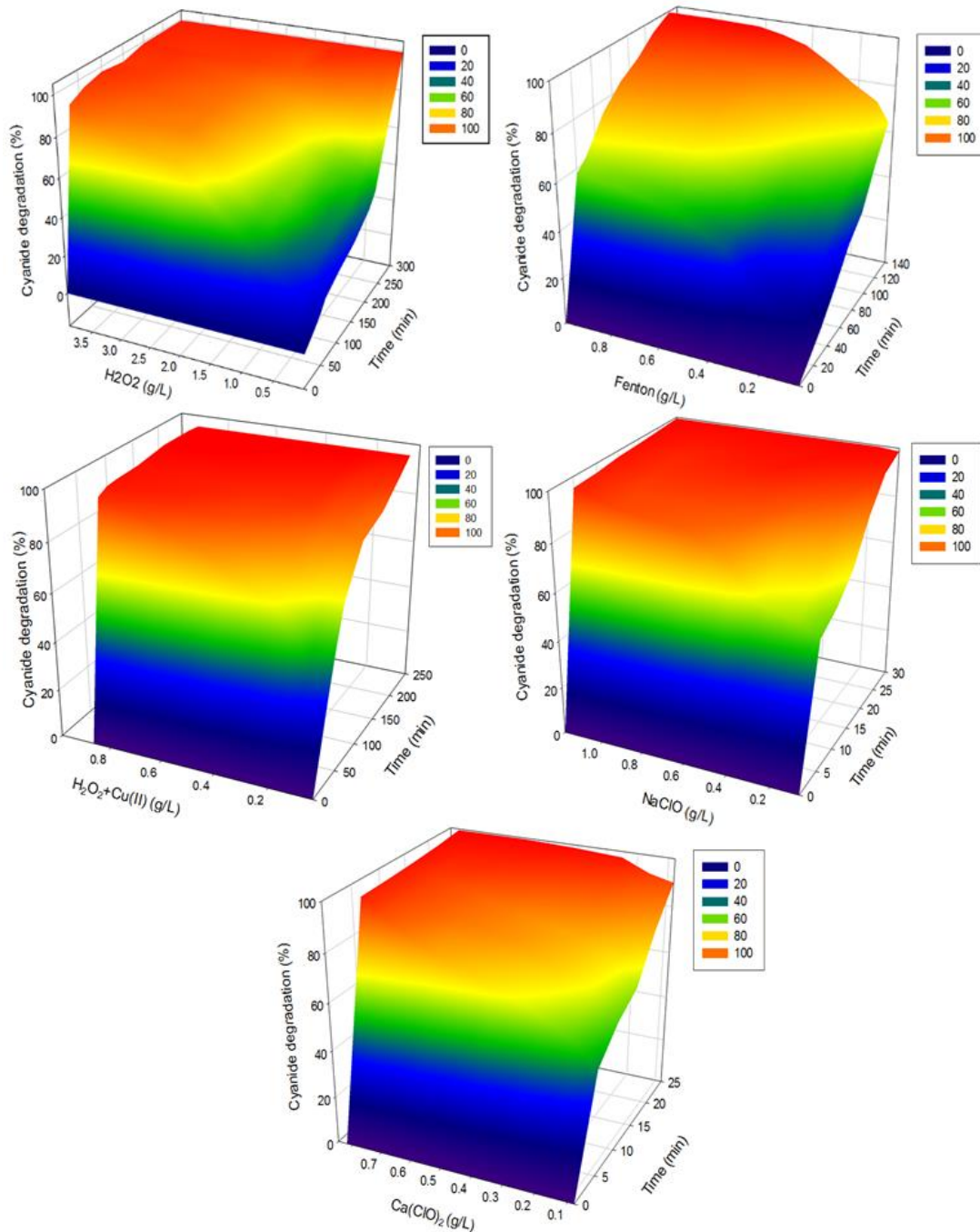
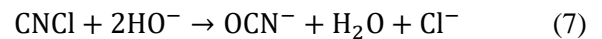
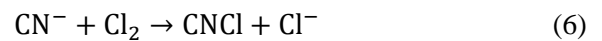


Fig. 2. Effect of oxidant dosage on the cyanide removal using different oxidants

According to Fig. 3, with increasing temperature the cyanide degradation decreases which is the least degradation regarding H₂O₂ (no catalyst). This phenomenon is a concern to cyanide degradation and reaction rate. Also for Fenton the low degradation is observed for wastewater with alkaline pH. Increase in the temperature for alkaline chloride has the strongest impact that has specified complexity. According to reactions 6 and 7, cyanide degradation leads to cyanogen chloride gas that as a mediator or catalyzer can generate Cl⁻ ion which leads to further degradation. On the other hand, the reaction was done in temperature range between 40-50 °C because in this temperature range

O₃Cl⁻ ion was practically not produced and in this situation chloride anion is dominant.



Both the initial rate and ultimate extent of cyanide degradation were generally higher at higher temperatures compared with those found at lower values. The presence of excess catalyst dosage overcomes the negative impacts of lower temperatures.

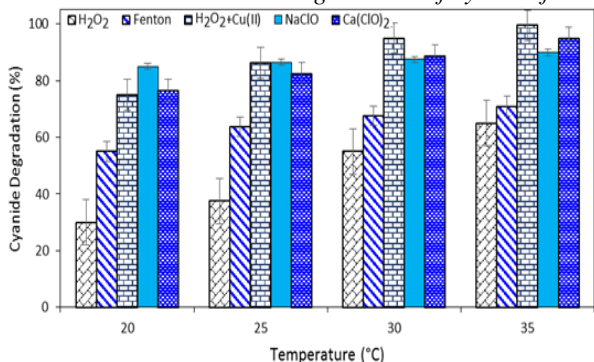


Fig. 3. Effect of temperature on cyanide degradation using different oxidants.

Non-linear kinetic modeling

Chemical kinetics help in identification of the reaction parameters and deal with experimental measurements of the velocities in batch, semi-batch or continuous reactors [57]. The matching of experimental data and the predicted value models were expressed by the correlation coefficients (R²). For all of the oxidants, based on reaction stoichiometry and using the initial rates from the previous performance to calculate the real, exact and quantitative order of reaction (a) with respect to [CN], according to an empirical equation ($[CN]/dt=k[CN]^{\beta}$), taking the $\log(d[CN]/dt) / \log[CN]$ linear representation, gave a slope value of β and values of k and α according to the least squares method that is obtained using the code

logging of the MATLAB program. The reaction rate or velocity (v) is defined mathematically as follows [27, 58].

$$v = \frac{d[CN^-]}{dt} = k[CN^-]^{\alpha}[\text{oxidant}]^{\beta} \quad (8)$$

$$\beta = \log(d[CN^-]/\log[\text{oxidant}]) \quad (9)$$

where [CN] and [oxidant] are the molar concentrations of the reactants; α and β exponents represent the order of the reaction between cyanide and oxidant, respectively, and k is the reaction rate constant. Sometimes the values for the exponents in the rate expression are equal to the coefficients in the equilibrium equation. The coefficients in the equilibrium equation are a consequence of the reaction stoichiometry. According to Fig. 2, cyanide degradation was studied as a function of time for each oxidant with variables dosage. In Fig. 4, the kinetic plot of cyanide degradation is shown for all oxidants.

Oxidants reaction rate can be determined by plotting $\log(-d[CN^-]/dt)$ versus $\log[\text{oxidant}]$ as shown in Fig. 4. The obtained results show that R² for all oxidants is less than 1. After calculating the velocity and reaction orders, the non-linear kinetic model (Eq. 10) and its parameters (a, b, c and R²) are listed in Table 2:

$$-\frac{d[CN^-]}{dt} = k[CN^-]^a[H_2O_2]^b \quad (10)$$

Table 2. Non-linear kinetic models and its parameters

Oxidant	Parameters			R ²
	k	a	b	
H ₂ O ₂	0.0000918	1.1774	1.1887	0.9724
Fenton	0.1692950	1.1289	0.1599	0.9852
H ₂ O ₂ +Cu(II)	0.0036600	1.1165	0.3000	0.9989
Ca(ClO) ₂	0.0008020	1.1472	0.5017	0.9886
NaClO	0.0274700	1.1329	0.2260	0.9771

A series of experiments were performed to determine the relationship between the rate of reaction and the concentration of reactants. Perfect cyanide degradation by oxidants does not happen in one step but to convert to the fewer toxicity products multi-steps were required.

As explained, cyanide concentration reduction was not equal for oxidants and did not follow a regular trend. This phenomenon was confirmed by different reaction rates. Cyanide degradation reaction orders for all oxidants are non-integer numbers between 1 and 2 ($1 < (\alpha+\beta) < 2$). Moreover, the reaction rate constant (k) for H₂O₂ (no catalyst), Fenton, H₂O₂+Cu(II), Ca(ClO)₂ and NaClO oxidants are 0.0000918, 0.1692950, 0.0036600, 0.000802 and 0.0244700 min⁻¹,

respectively. So, kinetic rate constants show that the reaction velocity of cyanide degradation is higher for NaClO and Fenton than for others and it is predictable for H₂O₂ less than all oxidants. Fenton and H₂O₂+Cu(II) oxidants in the presence of more free radicals due to the existence of catalysts have a higher velocity than H₂O₂.

In addition, Visual MINTEQ 3.1 software output (NaClO system: HCN_(aq) = 0.419 mg/L, ionic strength = 0.0441, CN⁻¹_(g) = 99.581%; Ca(ClO)₂ system: HCN_(aq) = 0.128 mg/L, ionic strength = 0.0662, CN⁻¹_(g) = 99.872%) in optimized conditions for cyanide reaction with Ca(ClO)₂ and NaClO obtained results show that the Ca(ClO)₂ reaction rate should be above NaClO reaction rate.

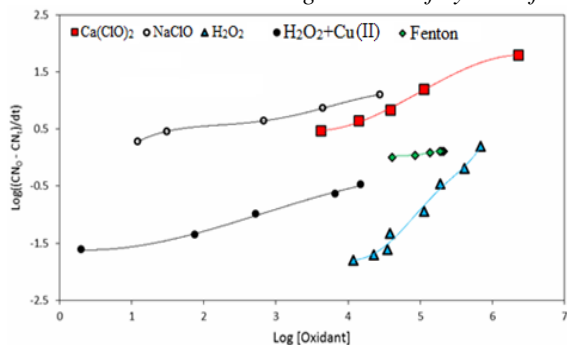


Fig. 4. Kinetic plots of cyanide degradation by various oxidations.

The results of non-linear kinetic modeling show the reverse status. For Ca(ClO)₂ and NaClO oxidants comparison is necessary to explain that in the gold processing plant flow sheet a portion of NaClO that was used in the elution stage to separate gold and silver and the reaction velocity is affected by the residual oxidizing agent.

The removal efficiency of the cyanide, calculated by the concentration differences between the initial and final values, was the criterion for process efficiency evaluation. Meanwhile, the absolute rate constant method was employed to evaluate the effect of various parameters on cyanide removal under the condition of constant H₂O₂ concentration, which refers to a pseudo-first-order kinetic equation. For each experiment, the apparent kinetic rate constant (K_{app}) for cyanide removal was derived from the linear representation of $\ln([C_0]/[C_t])$ versus time, where, $[C_0]$ and $[C_t]$ are the cyanide initial concentration and at t time, respectively. Figure 5 shows the relationship between Fe(II) and Cu(II) feeding time and the apparent kinetic rate constants for the second step. In the initial step, Fe(II) and Cu(II) dosage was fixed at 150 mg L⁻¹. The feeding time of Fe(II) and Cu(II) had a direct influence on the apparent kinetic rate constant. Firstly, up to 10 min, the corresponding k_{app} slightly increased, but was still somewhat lower than that of the first step, which might be attributed to the free radical scavenging. The further feeding time of Fe(II) and Cu(II) greatly increased the apparent kinetic rate constant and consequently achieved the highest value of 0.40 and 1.14 min⁻¹ at 40 and 60 min, respectively. Whereas for Fe(II) the value declined to 0.25 min⁻¹ when the feeding time was postponed to 50 min. Thus, the optimum feeding time is 30-40 min for

Fe(II) and 50 min for Cu(II).

Temperature increase leads to an increase in the reaction rate constant and the fraction of molecules that have energy equal to or higher than the activation energy.

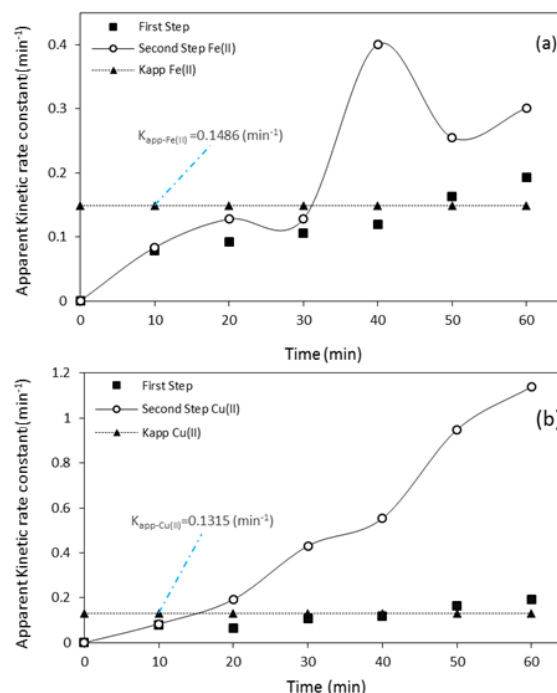


Fig. 5. The relationship between Fe(II) (a) and Cu(II) (b) feeding time and kinetic rate constants.

Figure 6 shows the relationship between $\ln(k)$ and $1/T$, where k is the rate constant and T is the reaction temperature. A reaction that has large activation energy is slow because only a small fraction of the molecules collide with sufficient energy to reach the transition state. The rate of the reaction increases when the temperature increases as more molecular collisions occur with energy equal to or greater than the activation energy. Also, the more molecules present, the greater is the probability of collision and the faster is the rate. Thus reaction rate increases with the increase in the concentration of reactant molecules. So, the results in Table 3 show that the activation energy of the reaction H₂O₂ was about 13.09 kJ/mol, the activation energy of the reactions where Cu(II) was added was about 8.56 kJ/mol, and the activation energy of the Fenton process was about 10.62 kJ/mol.

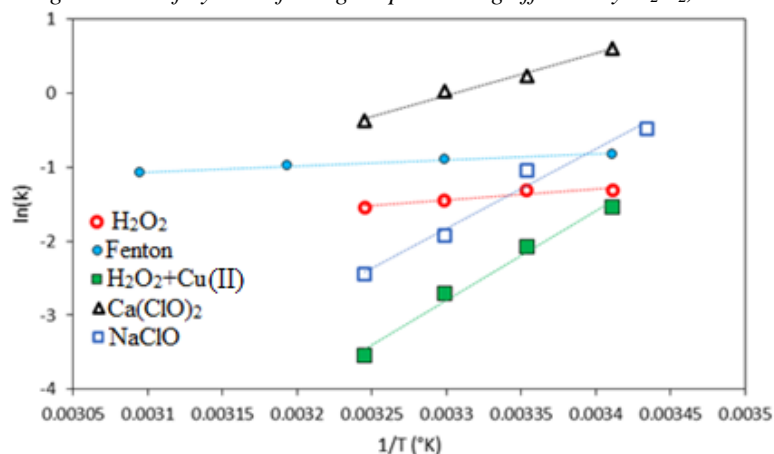


Fig. 6. Kinetic rate *versus* temperature for calculation of oxidation process activation energy.

Table 3. The values of activation energy, kinetic constant rate and correlation coefficient.

Oxidant	Activation energy (kJ/mol)	K (min ⁻¹)×10 ⁻³	R ²
H ₂ O ₂	13.09	0.0918	0.9848
Fenton	10.62	16.9295	0.9542
H ₂ O ₂ +Cu(II)	8.56	3.6600	0.9865
Ca(ClO) ₂	47.32	0.8202	0.9865
NaClO	94.96	24.4700	0.9824

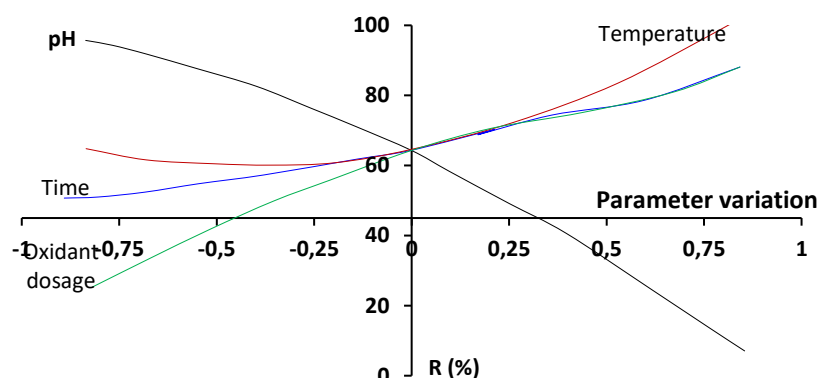


Fig. 7. The effect of influential parameters (pH, temperature, amount of oxidant, time and catalyst dosage) on the removal of cyanide at optimum conditions.

Modeling by response surface method

Response surface method (RSM) is one of the useful designs to fit the empirical models to the investigational data obtained from experimental design [60-63]. RSM contains many types of design two of which are extensively utilized in chemical methods such as advanced oxidation process [62, 64-66]. Design Expert 11 software was employed to obtain the experimental design for determining the interaction between operational independent parameters consisting of pH, time, temperature, catalyst dosage and amount of oxidant. The variation of operational parameters values was based on Table 1. According to the experimental studies, among the five processes, Ca(ClO)₂ process was selected as the optimal process and modeled. The effect of the five operational parameters

obtained by RSM is illustrated in Fig. 7. The obtained results show that cyanide degradation has a direct relation with temperature, amount of oxidant and time parameters and has an inverse relation with pH parameter. For calcium hypochlorite oxidant, the optimum conditions are: pH 11.5, time 20-25 min, temperature 35 °C and amount of oxidant 0.4 g/L which resulted in maximum cyanide degradation of 99.5% experimentally which was near to the RSM predicted cyanide degradation of 99.15%.

CONCLUSIONS

In this work, cyanide degradation was done by three oxidants in five processes. Sodium hypochlorite, calcium hypochlorite and hydrogen peroxide without and with Fe(II) and Cu(II) catalyst

were utilized for cyanide removal from gold processing wastewater. Major parameters that may affect the cyanide degradation such as pH, temperature, oxidants dosage and the reaction time were investigated. The maximum cyanide degradation happened at alkaline pH. All of the processes were considered at 20-30 °C. The dosage of different oxidants for the five processes was varied between 0.9-4.87 g/L. Also, non-linear kinetic modeling was done and each process was modeled as a mathematical equation that is flexible to calculate the required oxidant for any cyanide concentration. So, the comparison of kinetic rate constants (k) is as follows: NaClO > Fenton > H₂O₂+Cu(II) > Ca(ClO)₂ > H₂O₂. In addition, reaction activation energies for all five oxidants were calculated and the order is: NaClO > Ca(ClO)₂ > H₂O₂ > Fenton > H₂O₂+Cu(II). The cyanide release is an inevitable phenomenon in gold mines and given the environmental regulations and the obligation to reduce the amount of cyanide toxicity before entering the tailing dam, such studies can help in the selection of an oxidizing agent with higher efficiency and lower cost.

Conflict of interest: On behalf of all authors, the corresponding author states that there is no conflict of interest.

REFERENCES

1. S. M. Seyed Arabi, R. S. Lalehloo, M. R. T. B. Olyai, G. A. M. Ali, H. Sadegh, *Physica E*, **106**, 150 (2019).
2. G. A. M. Ali, A. Barhoum, V. K. Gupta, A. A. Nada, H. El-Maghrabi, K. Ramesh, E. R. Shaaban, H. Algarni, K. F. Chong, *Curr. Nanosci.*, **15**, DOI: 10.2174/1573413715666181205122307 (2019).
3. H. Sadegh, G. A. M. Ali, A. S. H. Makhlof, K. F. Chong, N. S. Alharbi, S. Agarwal, V. K. Gupta, *J. Mol. Liq.*, **258**, 345 (2018).
4. S. P. Lee, G. A. M. Ali, H. Algarni, K. F. Chong, *J. Mol. Liq.*, **277**, 175 (2018).
5. P. K. Papegowda, A. A. Syed, *Int. J. Environ. Res.*, **11**, 91 (2017).
6. N. Dwivedi, C. Balomajumder, P. Mondal, *Water Resour. Ind.*, **15**, 28 (2016).
7. P. Gupta, S. Ahammad, T. Sreekrishnan, *J. Hazard. Mater.*, **315**, 52 (2016).
8. S. M. S. M. Zain, R. Shaharudin, M. A. Kamaluddin, S. F. Daud, *Atmos. Pollut. Res.*, **8**, 678 (2017).
9. R. Mudliar, S. Umare, D. Ramteke, S. Wate, *J. Hazard. Mater.*, **164**, 1474 (2009).
10. S. Tian, Y. Li, H. Zeng, W. Guan, Y. Wang, X. Zhao, *J. Colloid Interface Sci.*, **482**, 205 (2016).
11. A. Akcil, *Miner. Eng.*, **15**, 695 (2002).
12. I. J. Kim, M. Ramalingam, Y.-A. Son, *Sens. Actuators, B*, **246**, 319 (2017).
13. J. Azamat, A. Khataee, *Comput. Mater. Sci.*, **128**, 8 (2017).
14. J. Hisham, K. M. Elsouisy, K. A. Hartany, *Arabian J. Chem.*, **9**, S198 (2016).
15. D. Donato, D. Madden-Hallett, G. Smith, W. Gursansky, *Ecotoxicol. Environ. Saf.*, **140**, 271 (2017).
16. D. Donato, O. Nichols, H. Possingham, M. Moore, P. Ricci, B. Noller, *Environ. Int.*, **33**, 974 (2007).
17. M. Kobya, E. Demirbas, F. Ozyonar, G. Sirtbas, E. Gengec, *Process Saf. Environ. Prot.*, **105**, 373 (2017).
18. E. Oraby, J. Eksteen, B. Tanda, *Hydrometallurgy*, **169**, 339 (2017).
19. Y. Zheng, Z. Li, X. Wang, X. Gao, C. Gao, *Electrochim. Acta*, **169**, 150 (2015).
20. N. Sinbuathong, B. Kongseri, P. Plungklang, R. Khun-anake, *Kasetsart J.*, **34**, 74 (2000).
21. M. Belykh, S. Petrov, A. Y. Chikin, R. Adeshin, N. Belkova, *Appl. Biochem. Microbiol.*, **53**, 331 (2017).
22. N. Pueyo, N. Miguel, J. Ovelleiro, M. Ormad, *Water Sci. Technol.*, **74**, 482 (2016).
23. L. Chu, J. Wang, J. Dong, H. Liu, X. Sun, *Chemosphere*, **86**, 409 (2012).
24. T. I. Mudder, M. M. Botz, A. Smith, Treatment and Recovery of Cyanide, in Chemistry and Treatment of Cyanidation Wastes, Mining Journal Books LTD London, 2001.
25. M. Sarla, M. Pandit, D. Tyagi, J. Kapoor, *J. Hazard. Mater.*, **116**, 49 (2004).
26. S.-H. Joo, S. Hong, N.-J. Kim, *J. Loss Prev. Process Ind.*, **44**, 143 (2016).
27. L. A. C. Teixeira, J. P. M. Andia, L. Yokoyama, F. V. da Fonseca Araújo, C. M. Sarmiento, *Miner. Eng.*, **45**, 81 (2013).
28. T. O. Nunan, I. L. Viana, G. C. Peixoto, H. Ernesto, D. M. Verster, J. H. Pereira, J. M. Bonfatti, L. A. C. Teixeira, *Miner. Eng.*, **108**, 67 (2017).
29. N. Pueyo, N. Miguel, R. Mosteo, J. L. Ovelleiro, M. P. Ormad, *J. Environ. Sci. Health*, **52**, 182 (2017).
30. O. Eletta, O. Ajayi, O. Ogunleye, I. Akpan, *J. Environ. Chem. Eng.*, **4**, 1367 (2016).
31. N. Singh, C. Balomajumder, *Water Conserv. Sci. Engin.*, **2**, 1 (2017).
32. L. Martínková, M. Chmátal, *Water Res.*, **102**, 90 (2016).
33. Z. Feketeová, V. H. Sládkovičová, B. Mangová, A. Pogányová, I. Šimkovic, M. Krumpál, *Ecotoxicology*, **25**, 202 (2016).
34. X. Yu, R. Xu, C. Wei, H. Wu, *J. Hazard. Mater.*, **302**, 468 (2016).
35. S. Chergui, A. R. Yeddou, A. Chergui, F. Halet, H. Amaouche, B. Nadjemi, A. Ould-Dris, *Toxicol. Environ. Chem.*, **97**, 1289 (2015).
36. C. A. Johnson, *Appl. Geochem.*, **57**, 194 (2015).
37. E. Neyens, J. Baeyens, *J. Hazard. Mater.*, **98**, 33 (2003).
38. M. Kitis, E. Karakaya, N. O. Yigit, G. Civelekoglu, A. Akcil, *Water Res.*, **39**, 1652 (2005).
39. S. Golbaz, A. J. Jafari, R. R. Kalantari, *Desalin. Water Treat.*, **51**, 5761 (2013).
40. A. Babuponnusami, K. Muthukumar, *J. Environ.*

- M.-S. Kamrani et al.: Degradation of cyanide from gold processing effluent by H_2O_2 , $NaClO$ and $Ca(ClO)_2$...
Chem. Eng., **2**, 557 (2014).
41. Z. Zhao, W. Dong, H. Wang, G. Chen, W. Wang, Z. Liu, Y. Gao, B. Zhou, *Chemosphere*, **180**, 48 (2017).
 42. G. Moussavi, M. Pourakbar, E. Aghayani, M. Mahdavianpour, S. Shekoohyian, *Chem. Eng. J.*, **294**, 273 (2016).
 43. G. Drochioiu, K. Popa, D. Humelnicu, M. Murariu, I. Sandu, A. Cecal, *Toxicol. Environ. Chem.*, **90**, 221 (2008).
 44. A. Khodadad, P. Teimoury, M. Abdolahi, A. Samiee, *Mine Water Environ.*, **27**, 52 (2008).
 45. N. Kuyucak, A. Akcil, *Miner. Eng.*, **50**, 13 (2013).
 46. M. Huertas, L. Sáez, M. Roldán, V. Luque-Almagro, M. Martínez-Luque, R. Blasco, F. Castillo, C. Moreno-Vivián, I. García-García, *J. Hazard. Mater.*, **179**, 72 (2010).
 47. M. D. Adams, *Miner. Eng.*, **53**, 241 (2013).
 48. A. R. Yeddou, S. Chergui, A. Chergui, F. Halet, A. Hamza, B. Nadjemi, A. Ould-Driss, J. Belkouch, *Miner. Eng.*, **24**, 788 (2011).
 49. R. R. Dash, A. Gaur, C. Balomajumder, *J. Hazard. Mater.*, **163**, 1 (2009).
 50. E. Yazıcı, H. Deveci, I. Alp, *J. Hazard. Mater.*, **166**, 1362 (2009).
 51. S. Tian, Y. Li, X. Zhao, *Electrochim. Acta*, **180**, 746 (2015).
 52. H. Ijadpanah-Saravi, S. Dehestaniathar, A. Khodadadi-Darban, M. Zolfaghari, S. Saeedzadeh, *Desalin. Water Treat.*, **57**, 20503 (2016).
 53. A. H. Hall, J. Saiers, F. Baud, *Crit. Rev. Toxicol.*, **39**, 541 (2009).
 54. N. Pueyo, J. Rodríguez-Chueca, J. Ovelleiro, M. Ormad, *Water Air Soil Pollut.*, **227**, 222 (2016).
 55. A. Mehrdad, B. Massoumi, R. Hashemzadeh, *Chem. Eng. J.*, **168**, 1073 (2011).
 56. F. Carrillo-Pedroza, F. Nava-Alonso, A. Uribe-Salas, *Miner. Eng.*, **13**, 541 (2000).
 57. D. Murzin, T. Salmi, *Catalytic Kinetics: Chemistry and Engineering*, Amsterdam, Elsevier, 2016.
 58. R. J. Ouellette, J. D. Rawn, *Organic Chemistry: Structure, Mechanism, and Synthesis*, Elsevier, 2014.
 59. G. Job, R. Rüffler, *Physical Chemistry from a Different Angle: Introducing Chemical Equilibrium, Kinetics and Electrochemistry by Numerous Experiments*, Job Foundation, Hamburg, Germany, Springer International Publishing, 2016.
 60. P. Naderi, M. Shirani, A. Semnani, A. Goli, *Ecotoxicol. Environ. Saf.*, **163**, 372 (2018).
 61. O. A. Habeeb, K. Ramesh, G. A. M. Ali, R. M. Yunus, *J. Wuhan Univ. Technol.-Mater. Sci. Ed.*, **32**, 305 (2017).
 62. O. A. Habeeb, K. Ramesh, G. A. M. Ali, R. M. Yunus, *J. Teknol.*, **79**, 1 (2017).
 63. Manohari, J. Singh, Y. Kadapakkam Nandabalan, *Int. J. Environ. Res.*, **11**, 63 (2017).
 64. A. Arslan, E. Topkaya, D. Bingöl, S. Veli, *Sustainable Environ. Res.*, **28**, 65 (2018).
 65. O. A. Habeeb, K. Ramesh, G. A. M. Ali, R. M. Yunus, *J. Chem. Engin. Ind. Biotechnol.*, **1**, 1 (2017).
 66. O. A. Habeeb, K. Ramesh, G. A. M. Ali, R. M. Yunus, T. K. Thanusha, O. A. Olalere, *Aust. J. Basic Appl. Sci.*, **10**, 136 (2016).

Characterization of raw and chemically activated natural zeolite as a potential sorbent for heavy metal ions from waste water

N. S. Krstić^{1*}, M. N. Stanković¹, D. M. Đorđević¹, V. D. Dimitrijević¹, M. Marinković¹, M. G. Đorđević^{1,2}, A. Lj. Bojić¹

¹University of Niš, Faculty of Science and Mathematics, Department of Chemistry, Višegradska 33, 18000 Niš, Serbia

²PUC for water supply and sewerage "Naissus", Knežinje Ljubice 1/1, 18000 Niš, Serbia

Received February 1, 2019; Accepted February 25, 2019

In this study, raw and chemically activated natural zeolite from Zlatokop deposit (Serbia) were investigated by FTIR, XRD, SEM-EDX, TGA and BET in order to define their properties as further potential sorption materials. Obtained results indicate porous (meso-pore range) and defined crystal aluminosilicate structure of these materials, with Na⁺, K⁺, such as Ca²⁺ and Mg²⁺ as dominating exchangeable cations. Content of clinoptilolite (*ca.* 90%) indicates the high quality of the zeolite samples. Preliminary sorption analyses of these materials toward copper(II) ion from aqueous solution showed good removal efficiency for base activated zeolite (zVBB) compared to raw natural (zVBN) and acid activated (zVBA) zeolite. Since these were preliminary sorption tests, the investigated zeolites will be further examined under different experimental conditions.

Key words: Zlatokop zeolite, activation, FTIR, XRD, SEM-EDX, TGA, BET, heavy metal sorption.

INTRODUCTION

Zeolites are crystalline aluminosilicate minerals with structures built of SiO₄ and AlO₄ tetrahedra which are linked by their corners. Natural zeolites are widely used: for purification of water, soil improvement, animal food production, food supplements and additives, radioprotection, etc. [1]. The possibilities of using zeolites for pollutants removal from wastewaters have been extensively studied. Their use is also stimulated by the availability and low cost, in addition to excellent physicochemical properties, like selective sorption of different metals and non-toxic nature [2, 3]. Also, zeolites have a high surface area due to their porous and rigid structure [4]. Clinoptilolite, a member of the heulandite group (HEU type zeolite), is the most abundant natural zeolite. Its tabular morphology shows an open reticular structure of easy access exhibited by (eight- and ten-membered ring) channels [5, 6].

The protection and improvement of water resources have received increased attention in the world. Over the years, various materials in native form or chemically modified, have been studied for their ability to remove pollutants from wastewaters. Studied materials should be low cost, widely available and environmentally friendly. [7]

In this study characterization of raw natural zeolite and chemically activated natural zeolite from Zlatokop deposit (Serbia) was done using FTIR, XRD, SEM-EDX, TGA and BET. These zeolites were investigated as a further potential

sorbent for inorganic (heavy metal ions, anions) and/or organic (industrial colours, pesticides, drugs) pollutants from water systems. Also, preliminary sorption analyses were done (waste water model system with Cu²⁺ ion). Raw natural nonactivated zeolite was designated further in the manuscript as „zVBN“, while activated zeolites were designated as „zVBA“ (acid activation – HCl) and „zVBB“ (base activation – NaOH).

Zeolite deposit

Zlatokop deposit is located in south-east Serbia near Vranjska Banja and represents one of the largest zeolite deposits in Serbia (Figure 1a). This zeolite deposit is related to Miocene volcanic activity and classified as high-quality zeolite deposit in Serbia (more than 70% of clinoptilolite) [8] This deposit is related to volcanic and volcanic-clastic rocks of lake sediments, with estimated reserves of zeolite of *ca.* 0.59 Mt [9].

EXPERIMENTAL

Sample preparation and activation

Natural zeolite sample (Figure 1b) was crushed in an agate mortar and sieved in order to obtain fractions of different particle size. The fraction of 0.8 – 1.25 mm was washed with distilled water to remove surface dust and then dried in the oven at 100-105 °C. Prepared material was activated with 2M NaOH and 2M NaCl. The mixtures were stirred for 12 h using a magnetic stirrer at room temperature, separated by centrifugation, thoroughly washed with deionized water. The zeolite samples were dried in the oven at 100-105 °C.

* To whom all correspondence should be sent.

E-mail: nenad.krstic84@yahoo.com

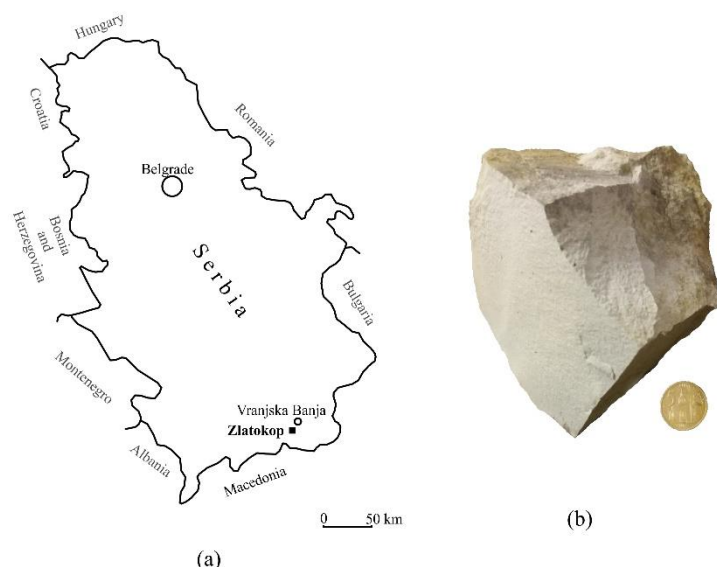


Figure 1. Geographical location of Zlatokop zeolite deposit (a) and zeolite sample (b)

Fourier transform infrared (FTIR) spectrometry

The FTIR spectra of samples were obtained by using KBr pellets with Fourier transform infrared spectrometer Bomem Hartmann & Braun MB-100 in the wavelength range $4000 - 400 \text{ cm}^{-1}$.

Scanning electron microscopy with energy dispersive X-ray spectroscopy (SEM-EDX)

The morphology of the zeolite samples surface was analyzed by SEM (Hitachi SU8030). EDS analysis (Thermo Scientific NORAN System 7, USA) provided elemental information *via* the analysis of X-ray emissions from the sorbent surface. For SEM-EDX analysis samples were attached to aluminum stubs using Leit-C carbon cement. Samples were imaged uncoated.

Surface area analysis using the Brunauer-Emmett-Teller (BET) method

The specific surface area was measured by nitrogen adsorption using the Micromeritics Gemini 5 surface area analyzer, USA.

Thermogravimetric (TG) analysis

TG analysis was performed using TGA Q5000 (TA Instruments, USA).

X-ray diffraction (XRD) analysis

Zeolite samples were finely ground using a mortar and pestle and placed into standard sample holders. Data were collected with a Bruker D8 Advance X-ray Diffractometer (Bruker, Germany) in theta-theta geometry in reflection mode with $\text{Cu K}\alpha$ radiation. Data collection was between $5-70^\circ 2\theta$, step size of 0.02° and a counting time of 1 sec per step.

Preliminary sorption experiment

Preliminary sorption abilities of raw and chemically modified zeolites were investigated in a model system with copper(II) ion as we have done in our previous investigations. The concentrations of Cu(II) ions in the solution before and after adsorption were determined by using an atomic absorption spectrophotometer (AAAnalyst 300, Perkin Elmer, USA) [7, 10].

RESULTS AND DISCUSSION

FTIR. The FTIR spectra of zeolite samples recorded in the wavelength region between 400 and 4000 cm^{-1} are shown in Figure 2.

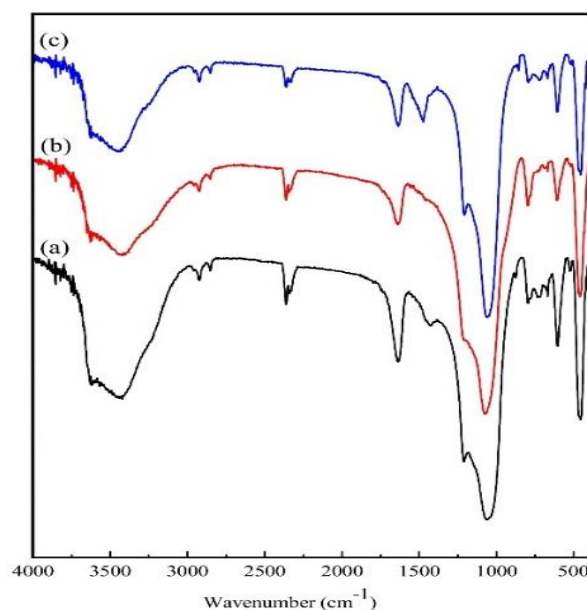


Figure 2. FTIR spectra of zVB_N (a), zVB_A (b) and zVB_B (c).

Characteristic bands for natural zeolite can be identified. Wide band between 2900 and 3750 cm^{-1}

is attributed to the existence of OH group stretching vibrations (from Al-OH or present water). Deformation vibration of molecularly bound water in the zeolite structure is characterized by bands in the spectra in the region 1600-1650 cm^{-1} . The bands in the range 950-1250 cm^{-1} correspond to asymmetric stretching vibration of structural tetrahedra units of the aluminosilicate lattice Si(Al)-O of the zeolite. The bands in the range 455-790 cm^{-1} correspond to stretching vibration of O-Si(Al)-O groups and bending vibrations of Si(Al)-O bonds. According to the obtained data there are no significant changes in the FTIR spectra after chemical modification of natural zeolite, but it was confirmed that these are aluminosilicate materials with defined crystal structure [11, 12].

SEM-EDX. SEM micrographs of the investigated zeolite samples are presented on Figure 3. These micrographs show the porous and well-defined crystal structure of natural and modified zeolite samples.

EDX analysis was done by measuring different parts of the sample (seven points) in order to get more precise elemental compositions of the investigated samples (Figure 4).

Data from Figure 4 indicate the aluminosilicate structure of zeolite with Na^+ , K^+ , such as Mg^{2+} and Ca^{2+} as dominating exchangeable cations. Average values of these ions are decreasing after zeolite

activation with hydrochloric acid for Na^+ and K^+ by ca. 90%, while for Ca^{2+} and Mg^{2+} ions by ca. 55%. After base activation Na^+ value increases (ca. six times), K^+ and Ca^{2+} decrease (by ca. 20% and 10%, respectively), while there are no changes for Mg^{2+} value. All these changes are the result of ion exchange processes after acid and base modifications (H^+ or Na^+ or OH^- ions). These results are in accordance with literature data for zeolites from the Balkan region [13, 14].

XRD. XRD diffractograms of zVB_N , zVB_A and zVB_B samples are shown on Figure 5. According to the data from Figure 5 the dominant zeolite's mineral is clinoptilolite (ca. 90%), which confirms the appearance of an intense peak at the 2θ angle of 22° [15]. XRD data also showed that the investigated natural zeolite contains other minerals quartz, mordenite, albite and calcite in minority. Comparing XRD diffractograms of zVB_N , zVB_A and zVB_B it can be noticed that there are no significant differences between natural and chemically modified zeolites, except the disappearance of the calcite peak at the 2θ angle of around 29.5° [16] in the sample zVB_A , due to dissolving calcite in hydrochloric acid, which is in accordance with the EDX results where a decrease of carbon value by ca. 45% after acid and by ca. 20% after base activation can be noticed (Figure 4).

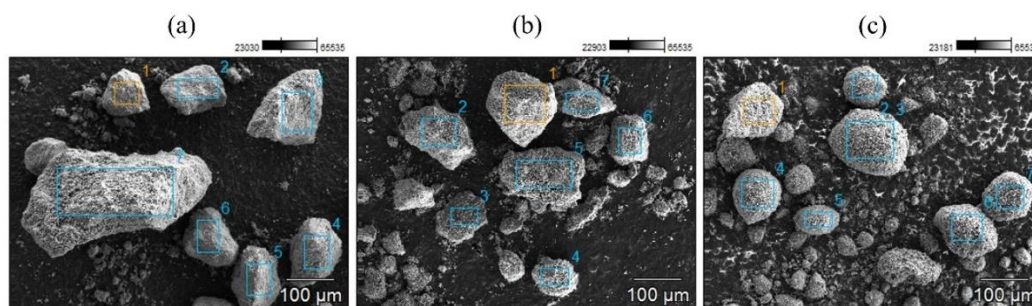


Figure 3. SEM micrographs of zVB_N (a), zVB_A (b) and zVB_B (c).

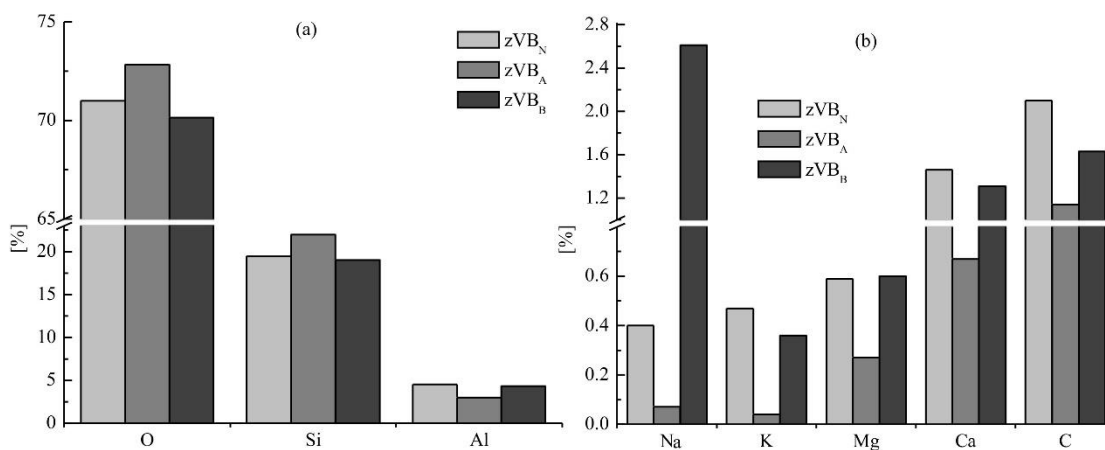


Figure 4. EDX analysis of average elements in zeolite samples [atom %, error ± 2 sigma; total 100%]

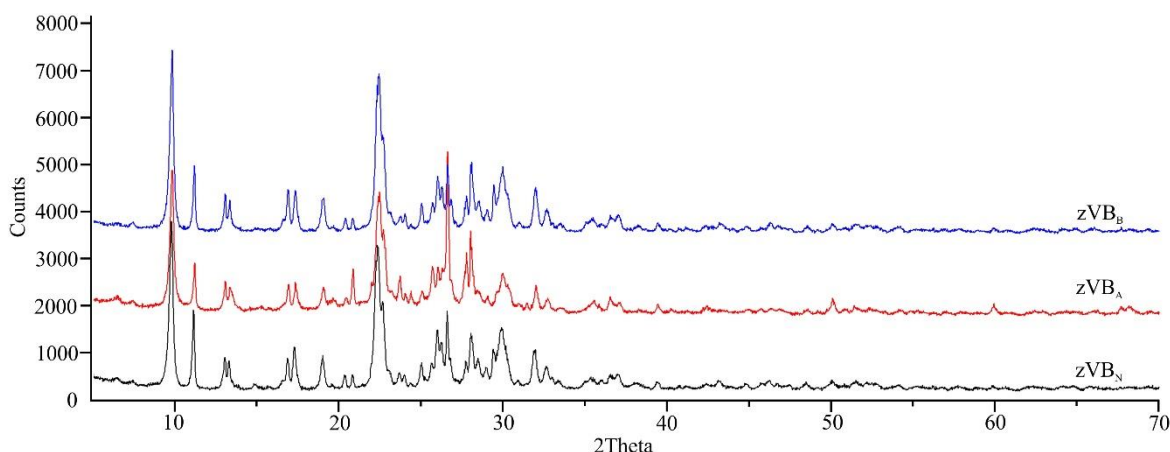


Figure 5. XRD diffractograms of zeolite samples

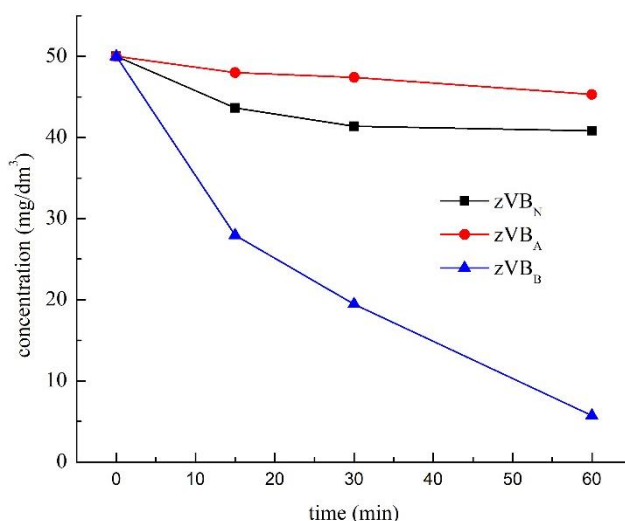


Figure 6. Effect of contact time on the removal of Cu(II) by zeolite materials

Table 1. Textural properties of the zeolite samples

Sample	BET surface area $S_{BET}(m^2g^{-1})$	Average pore diameter (nm)	BJH cumulative desorption pore volume (cm^3g^{-1})
zVB _N	22.87	15.42	0.0863
zVB _A	21.47	15.17	0.0746
zVB _B	31.79	15.39	0.1316

Preliminary sorption results. The preliminary results of the sorption abilities of the obtained zeolite (particle size 0.8-1.25 mm) materials toward copper(II) ions in aqueous solution are shown in Figure 6. These results indicate that raw unmodified natural zeolite (zVB_N) and zeolite modified with hydrochloric acid (zVB_A) show similar, but not significantly efficient sorption properties. Copper removal efficiency, RE (%) is *ca.* 19% for zVB_N and *ca.* 10% for zVB_A. By treatment with sodium hydroxide (zVB_B) better sorption properties (RE, *ca.* 90%) than zVB_N and zVB_A for removal of Cu(II) ions from wastewater were achieved. The concentration of copper declined sharply with contact time in the first 15

minutes and continued this trend in the range of investigated contact time.

Clinoptilolite is a porous crystal material, which adsorption properties are strongly related to the framework structure, which has performance for physical adsorption and ion exchange [17]. According to the ion exchange mechanism, ions present in the pores of zeolite crystalline lattices are substituted by toxic metal ions from the solution. The ion exchange process is reversible, and the zeolite may be recovered for further use [14].

Surface area analysis. Table 1 summarizes the results of the textural properties of the tested zeolite samples. In comparison with the results of other authors, very similar values of specific surface area,

mean pore diameter and pore volume were determined for (unmodified) raw zeolite (zVB_N) and the acid treated zeolite (zVB_A) [18]. A sample of zeolite treated with NaOH (zVB_B) shows a significant increase in the BET specific surface area and BJH cumulative desorption pore volume. Increase in the specific surface area of the sample (zVB_B) can be possibly related with the phenomenon of presence of cations or minerals which block the pore channels, so the limited extent of zeolite crystalline structure reduces its sorption activity [19], but treatment with NaOH produces an improved adsorbent which is confirmed by the results of the adsorption. The increase in the mesopore volume of the NaOH-treated clinoptilolite is probably caused by unblocking of the channels of the aluminosilicate framework structure of the zeolite through dealumination and decationation during base leaching, and possibly also by dissolution of any amorphous silica

blocking the channels of the clinoptilolite structure [20]. All of the above leads to the improvement of the adsorption activity of the mentioned (zVB_B) zeolite sample.

The N_2 adsorption/desorption isotherms of the zeolite samples showed a typical *s*-shape behavior of IV-type with a type-H3 of hysteresis loop that indicated the existence of mesopores (Figure 7a). The clinoptilolite samples have characteristic presence of this type of hysteresis loop, which can be attributed to multilayer adsorption followed by capillary condensation either in mesopores of impurities (feldspars, quartz, etc.) or in the space developed between the zeolite crystallites [21]. The pore system of all tested zeolite samples is in the meso-pore range between bimodal distributed pores characterized with maxima in pore size between 2–5 nm and 10–50 nm with an average pore diameter around 15 nm in size according to the BJH desorption isotherms (Figure 7b).

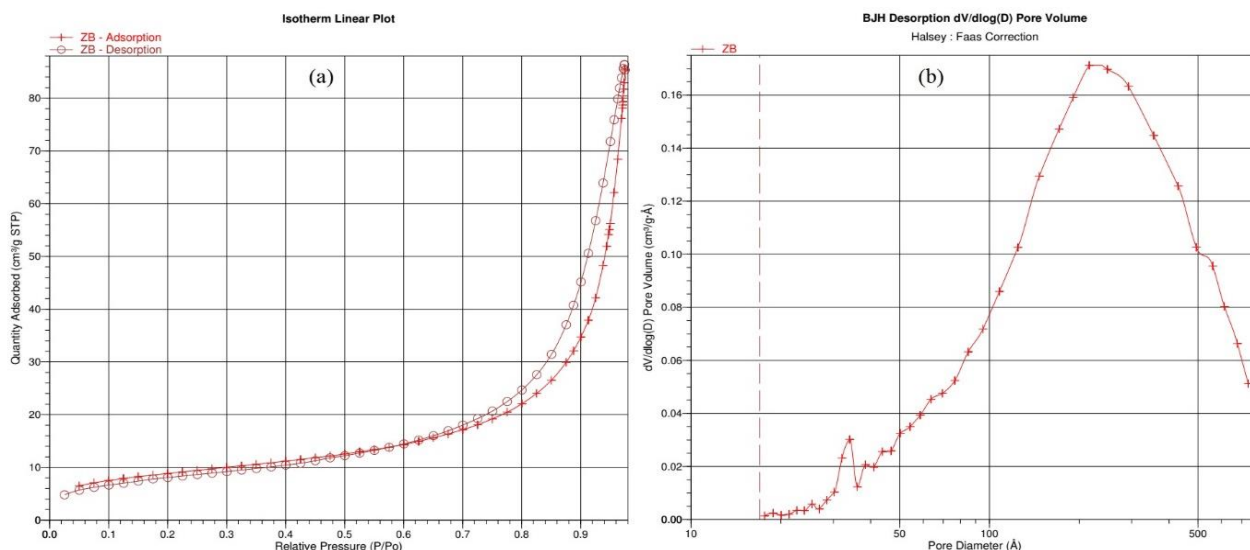


Figure 7. N_2 adsorption/desorption isotherm of zVB_B sample (a) and pore size distribution for zVB_B sample (b)

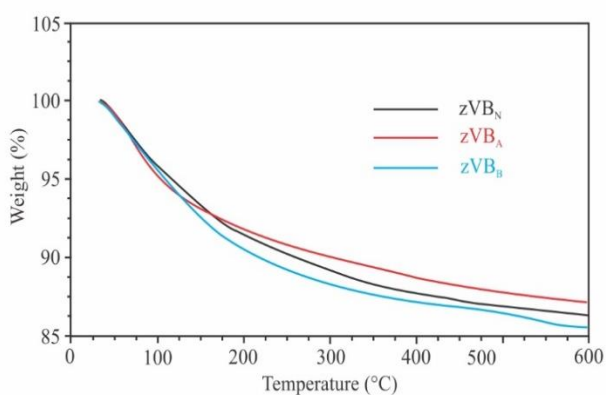


Figure 8. TG curves of the zeolite samples

TG analysis. The results of thermogravimetric analysis of the tested zeolite samples are summarized in Figure 8. Thermal treatment of the

zeolite samples leads to a loss of mass in the range 20–600 °C, because of surface dehydration and dehydroxylation.

The process of zeolitic water elimination is held in a few stages. At temperatures below 100 °C physically adsorbed water is mainly eliminated, further increase of temperature in the range 100–300 °C or higher, leads to removal of hydroxyls through the associative desorption mechanism. At temperatures in the range 200–600 °C almost all hydroxyl groups leave the surface, moreover the isolated OH groups are eliminated at higher temperatures. Changes in temperature of zeolitic water elimination can be a consequence of the presence of different exchangeable cations in zeolites [22]. Based on the results of the

thermogravimetric analysis of the tested zeolite samples presented in Figure 8 it can be noticed that the elimination of intact water is observed up to 120 °C. The most essential loss of mass is observed at 120-400 °C because of associative desorption of hydroxy species and desorption of intact water. A sample of zeolite (zVB_B) treated with NaOH shows the largest loss of mass (ca. 14.50 %), unlike the samples zVB_K and zVB_N with mass loss (ca. 12.90% and ca. 13.70 %, respectively), which can be possibly related to the increase in the specific surface area of the sample (zVB_B). Moreover, differences in TG curves presented in Figure 8 can be related to differences in complex connectivity of pores and variation in their sizes as a result of exchangeable cation replacement with protons.

CONCLUSION

According to the obtained results based on FTIR, XRD, SEM-EDX, TGA and BET analyses, the investigated zeolite from Zlatokop deposit (Serbia) is aluminosilicate material with defined crystal structure and high quality (ca. 90% clinoptilolite) with a pore system in the meso-pore range. Preliminary results of the investigated zeolite materials zVB_N, zVB_A and zVB_B toward removing copper(II) ions from aqueous solution showed good sorption characteristics of zVB_B zeolite (particle size 0.8 – 1.25 mm), which is in accordance with the data obtained by BET and TGA analyses. Since these were preliminary sorption tests, zeolites (raw and activated) will be further examined with the aim to improve their sorption properties, both for inorganic and organic water pollutants, under different experimental conditions (longer contact time, different particle size of zeolite – using natural zeolite with much smaller particle size (zeolite powder), temperature, dose of sorbent, etc.).

Acknowledgement: This work was supported by the Ministry of Education, Science and Technological Development of the Republic of Serbia under the Project TR34008.

REFERENCES

1. M. Tomasevic-Canovic, *J. Serb. Chem. Soc.*, **70**, 1335 (2005).
2. H. Cui, L. Y. Li., J. R. Grace, *Water Res.*, **40**, 3359 (2006).
3. G. Yuan, H. Seyama, M. Soma, B. K. G. Theng, A. Tanaka, *J. Environ. Sci. Health*, **34**, 625 (1999).
4. E. Alvarez-Ayuso, A. Garcia-Sanchez, X. Querol, *Water Res.*, **37**, 4855 (2003).
5. N. Rajic, Dj. Stojakovic, S. Jevtic, N. Zabukovec Logar, J. Kovac, V. Kaucic, *J. Hazard. Mater.*, (172), 1450 (2009).
6. A. Radosavljevic Mihajlović, A. Došen, J. Stojanović, V. Kašić, V. Simić, *Proceedings of the 5th Serbian-Croatian-Slovenian Symposium on Zeolites*, Zlatibor, Serbia, 116 (2013).
7. M. N. Stankovic, N. S. Krstic, J. Z. Mitrovic, S. M. Najdanovic, M. M. Petrovic, D. V. Bojic, V. D. Dimitrijevic, A. Lj. Bojic, *New J. Chem.*, **40**, 2126 (2016).
8. V. Simić, D. Životić, N. Andrić, A. Radosavljević-Mihajlović, V. Kašić, 9th International Conference on the Occurrence, Properties and Utilization of Natural Zeolites, Belgrade, Serbia, 217 (2014).
9. R. Jelenković, A. Kostić, D. Životić, M. Ercegovac, *Geol. Carpath.*, **59(4)**, 345 (2008).
10. M. N. Stanković, N. S. Krstić, I. J. Slipper, J. Z. Mitrović, M. D. Radović, D. V. Bojić, A. Lj. Bojić, *Aust. J. Chem.*, **66(2)**, 227 (2012).
11. W. Mozgawa, M. Krol, K. Barczyk, *Chemik.*, **65(7)**, 667 (2011).
12. K. Byrappa, B.V. Suresh Kumar, *Asian J. Chem.*, **19(6)**, 4933 (2007).
13. N. Popov, T. Popova, J. Rubio, S. R. Taffarel, *Geochem. Mineral. Petrol.* **49**, 83 (2012).
14. S. Cerjan Stefanovic, N. Zabukovec Logar, K. Margeta, N. Novak Tusar, I. Arcon, K. Maver, J. Kovac, V. Kaucic, *Micropor. Mesopor. Mat.*, **105**, 251 (2007).
15. M. M. J. Treacy, J. B. Higgins, Collection of simulated XRD powder patterns for zeolites, Elsevier, 2001.
16. <http://rruff.info/Calcite/R050128>
17. X. Li, C. Lin, Y. Wang, M. Zhao, Y. Hou, Clinoptilolite Adsorption Capability of Ammonia in a Pig Farm, *Procedia Environ. Sci.*, **2**, 1598 (2010).
18. D. A. Kennedy, M. Mujčin, C. Abou-Zeid, F. H. Tezel, *Micropor. Mesopor. Mat.*, **274**, 327 (2019).
19. M. A. Hernandez, F. Rojas, V. H. Lara, *J. Porous Mater.*, **7**, 443 (2000).
20. O. Korkuna, R. Lebeda, J. Skubiszewska-Ziamba, T. Vrublevska, V. M. Gunko, J. Ryczkowski, *Micropor. Mesopor. Mater.*, **87**, 243 (2006).
21. E. Kouvelos, K. Kesore, T. Steriotis, H. Grigoropoulou, D. Bouloubasi, N. Theophilou, S. Tzintzos, N. Kanelopoulos, *Micropor. Mesopor. Mater.*, **99**, 106 (2007).
22. M.W. Kasture, P.N. Joshi, H.S. Soni, V.V. Joshi, A.L. Choudhari, V.P. Shiralkar, *Adsorp. Sci. Technol.*, **16**, 135 (1998).

Effect of tomato juice storage on vitamin C and phenolic compounds and their stability over one-year period

N. V. Pavlović¹, J. D. Mladenović², N. M. Zdravković³, Đ. Z. Moravčević⁴, D. Ž. Poštić⁵, J. M. Zdravković^{1*}

¹Institute for Vegetable Crops, 11420 Smed. Palanka, Karadjordjeva 71, Serbia

²University of Kragujevac, Agronomski Fakultet, 32000 Čačak, Cara Dušana 34, Serbia

³Institute of Veterinary Medicine of Serbia, Vojvode Toze 14, 11000 Belgrade, Serbia

⁴University of Belgrade, Faculty of Agriculture, Nemanjina 6, 11080 Beograd-Zemun, Serbia

⁵Institute for Plant Protection and Environment, T. Drajzera 9, 11000 Belgrade, Serbia

Received February 20, 2019; Accepted February 26, 2019

The stability of bioactive components: vitamin C and phenols in thermally processed tomato juice for 12 months in three different storage conditions was studied. The experiment was carried out on thermally treated tomato juice made from a selected line of industrial tomatoes (SPO-109). Mashed tomato juice without skin and seeds was cooked for 7 min at 100°C. The samples were stored in the light at +20°C; in the dark at +20°C; and in the dark at +4°C. The measurement of the changes of the bioactive components parameters during 12 months of storage was performed at 2 month-intervals. Degradation of phenols was not significant for 12 months of storage. Different ambient conditions caused significant changes and loss of nutrients. Vitamin C was lost when stored in the light for the first two months of storage (30.35%), and after one year from 41.56% for storage in the dark at +20°C (24.58%), and 25.51% at +4°C. There was no difference in vitamin C content when stored in dark conditions at different temperatures, while significantly important differences were found between storing in the light and storing in the dark at + 20°C and + 4°C, respectively.

Key words: storage, different conditions, tomato juice, vitamin C, phenols

INTRODUCTION

Tomato (*Lycopersicon esculentum* Mill.) is a vegetable that is consumed fresh (in a salad) and also processed: dried, in sauces, juices, etc. Industrial processing usually includes thermal treatment and/or homogenization and both ways disrupt the cell matrix of tomato fruit [1]. Disruption of the cell wall structure during thermal processing directly affects the availability of different nutrients. Tomato fruits are a major part of human diet since they are an important source of substances with positive effects on health with its vitamins, minerals and antioxidants [2]. Tomato is a plant with antioxidative impact against wide spectra of biotic and abiotic stresses people are exposed to [3]. Furthermore, processed fruits when stored in an adequate way can represent a significant source of bioactive nutrients.

The level of ascorbic acid (vitamin C) in tomato fruit varies from 10 to 88 mg/100 g of fresh weight. Ascorbic acid has an important role in human diet and its intake prevents different diseases [4]. This range of variation appears as a consequence of diversified tomato breeds, and differences among cultivation procedures [5]. Vitamin C belongs to a group of thermally labile and its degradation starts

at 70°C. Significant losses of ascorbic acid can appear in fruits after picking, during storage, however the highest losses appear during processing, when exposed to high temperatures. This degradation appears as a consequence of oxidation and impact of high temperatures [6]. Cold treatment i.e. low temperatures better preserve vitamin C during processing than high temperatures [7]. Besides the climatic conditions the content of vitamin C depends on genotype impact, crop management, fertilizers, fruit development, maturation, and senescence [8,9], which interacting with one another give more or less quality raw material (tomato fruit) used for processing. Maintenance of vitamin C in processed products mainly depends on the length of storage time. In long-term storage conditions, maintenance depends primarily on the influence of climate factors in the warehouse [10]. Increasing the nutritive quality of processed tomato fruit by increasing / preserving the high content of ascorbic acid is always a desirable goal [11].

There are only a few studies regarding the research of phenol preservation in finished tomato products during storage longer than 6 months. Additional research is needed to determine the nutritional quality and its changes during storage, with an emphasis on the phenol changes in ketchup and tomato juice [12]. The storage of tomato juice

* To whom all correspondence should be sent:

E-mail: jasna.zdravkovic@gmail.com

and ketchup results in a mild decrease of polyphenols over time. Degradation of phenolic compounds during storage is attributed to the residual peroxidase activity involved in the oxidative degradation of phenolic compounds. Ketchup had greater stability during storage of tomato juices after 9 months at +4°C [13]. However, Pérez-Vicente *et al.* [14] found slight changes in the content of total phenolic compounds in juices stored less than 6 months at room temperature. Maintenance of total phenolic compounds during storage could be due to the inactivation of the enzymes responsible for their degradation. Degradation of phenolic compounds during storage was determined at +40°C and higher [15]. Storage time has a significant effect on the preservation of the phenol content and antioxidant activity [16]. Temperature conditions and length of storage are the basic factors of preservation of phenolic compounds in products from thermally processed tomatoes.

This experiment aimed to analyze and determine the level of change of certain bioactive components (vitamin C and total phenols) during long storage (12 months) in thermally processed tomato juice. During the long storage the experimental groups were exposed to different temperatures in light and in dark (which realistically reflects the conditions of storage of tomato juices in markets) in order to find the optimal conditions and length of storage that could benefit human health.

MATERIALS AND METHODS

The experiment was conducted on thermally processed tomato juice of a selected line of industrial tomatoes (SPO). Juice from mashed tomatoes without skin and seeds was cooked for 7 min at 100°C. Hot juice was poured in glass bottles and hermetically sealed. The samples were stored in glass packaging, in the light at +20°C; in the dark at +20°C and in the dark at +4°C. The measurement of changes of parameters of bioactive components (vitamin C, total phenols and) during the year of storage was performed every 2 months (totally 7 measurements during the experiment: 0-made juice, 2, 4, 6, 8, 10, 12 months storage).

Determination of vitamin C

Pale tomato juice was obtained by pressing 100 cm³ of tomato juice and mixed with equal quantity (100 cm³) of a mixture of HPO₃ and glacial CH₃COOH. Then, the mixture was filtered through creased filter paper. The first 5-10 cm³ of filtered mixture were thrown away and the aliquot part was taken from the rest of the mixture for the further investigation. If necessary, the investigated sample

was diluted with cooled boiled distilled water, so the aliquot part contained about 2 mg of ascorbic acid. The process of determining ascorbic acid in the sample: 10 cm³ of filtered sample (containing 5 cm³ of juice and 5 cm³ of a mixture of HPO₃ and glacial CH₃COOH) was applied to three Erlenmeyer flasks using a pipette. Each sample was titrated with Tillmans reagent (TR) solution until pale pink, for about 5 sec. At the same time, the solution of TR was titrated and blind tested until pale pink [18].

The content of ascorbic acid (mg/cm³) = $(V - V_1) \times T \times 100/g$

where: V – cm³ of TR solution used for titration in trial testing; V₁ – cm³ of TR solution used in blind testing; T– titer solution TR (mg C₆H₈O₆ / 1 cm³ TR solution); g – juice volume in cm³ in the aliquot part of sample.

Total phenols content

Total phenols in the tomato ethanol extracts of 20 g tomato juice, 100 cm³ in ethanol were estimated according to the Folin–Ciocalteu method [27]. The extract was diluted to a concentration of 1 mg/mL, and aliquots of 0.5 mL were mixed with 2.5 mL of Folin–Ciocalteu reagent (previously 10-fold diluted with distilled water) and 2 mL of NaHCO₃ (7.5%). Aliquots were left for 15 min at 45°C, and then the absorbance was measured at 765 nm on a spectrophotometer against a blank sample. Gallic acid (GA) was used to calculate the standard curve. The assays were carried out in triplicate; the results were the mean values ± standard deviations expressed as mg of gallic acid equivalents per gram of dry extract (mg of GA/g).

Data analysis

Genotype differences were determined according to ANOVA model for random block system. Differences between the levels of bioactive components in fresh fruits and products, ratio juice storage: light, 20°C, dark, 20°C and dark, 4°C, were shown according to significant differences by the Tukey's test.

Storage in three ambient conditions was followed by a trend line. This line represents the average state of the observed phenomena through time. Model of linear trend [19]) applied was:

$$y^{\wedge}=a+ bx,$$

$$\text{where: } b = \frac{\sum x_i y_i - n \cdot \bar{x} \cdot \bar{y}}{\sum x_i^2 - n \cdot \bar{x}^2},$$

$$a = \bar{y} - \bar{x} \cdot b$$

Multiple correlation and regression represents an extended dependence of one parameter (storage in conditions of light at +20°C) on impact of several independent variables (storage in the dark at +20°C

N. V. Pavlović et al.: Effect of tomato juice storage on vitamin C and phenolic compounds and their stability... and +4°C, respectively) on individual maintenance of bioactive components during long-term storage [20].

RESULTS AND DISCUSSION

According to the results of storing tomato juice for 12 months in different conditions, the loss of vitamin C was determined. The highest loss in this experiment was at storage in light at +20°C, where the degradation process was the fastest. Trend of vitamin C loss was in linear shape in all followed parameters in the experiment; the determination coefficient at storage at +20°C in light had the lowest value $R^2=0.66$, while for storage in the dark at +20°C this coefficient was $R^2=0.9759$ and $R^2=0.974$ at +4°C, which confirms the linear shape of vitamin C loss (Fig. 1).

There were significant differences between storage conditions in the dark at both temperatures (+20°C and +4°C) and storage in light, proven by Tukey's test, with 95% accuracy. There were no

significant differences among storage in the dark at both temperatures (Table 1). Similar results can be confirmed based on correlation coefficients. All three storage conditions showed high correlation between each other (Table 2).

Percentage of loss of vitamin C in the first two months was 30.35% and after one year 48.79%, when stored at light at +20°C. However, when stored in the dark the situation was clearly different: in the first two months the loss was 7.08% (at +20°C), and when stored in a chilled room at +4°C there were no losses during this period (Table 3).

There were no statistically significant differences in vitamin C content between tomato juice containers kept in dark (20°C and 4°C) while significant differences were found among containers stored in the light and in the dark (20°C and 4°C, respectively), Table 1.

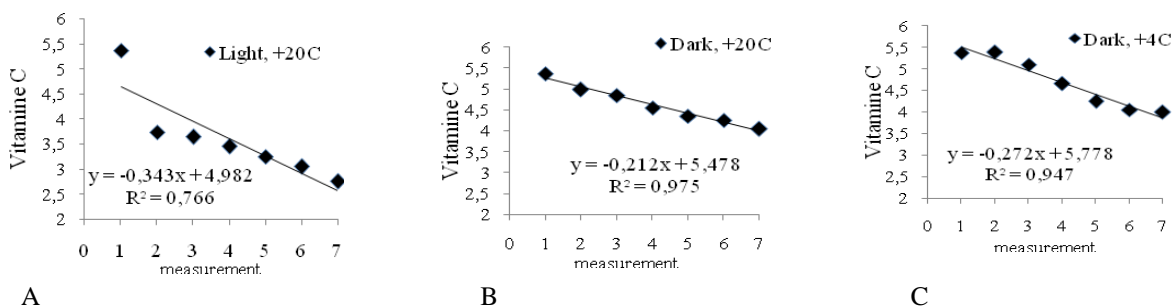


Figure 1. The average values and tendency of vitamin C depletion during storage for 12 months in different conditions (A- light +20°C, B- dark +20°C, C- dark +4°C)

Table 1. Tukey's multiple comparison test for differences in vitamin C content during storage time in different conditions

Tukey's Multiple Comparison Test	Mean difference	q	Summary	p=95%
Light, +20°C : Dark, +20°C	-1.023	4.107	*	-1.922 to -0.124
Light, +20°C : Dark, +4°C	-1.080	4.336	*	-1.979 to -0.181
Dark, +20°C : Dark, +4°C	-0.057	0.229	ns	-0.956 to 0.842

* $p \leq 0.05$; ns not significant

Table 2. Partial correlation coefficient of vitamin C content in different storage conditions

	Dark, +20°C	Dark, +4°C
Light, +20°C	0.923**	0.783 **
Dark, +20°C		0.958**
Dark, +4°C		

* $p \leq 0.05$; ** $p \leq 0.01$; ns not significant

Table 3. Percentage of vitamin C depletion during 12 months of storage of pasteurized tomato juice

Storage time (months)	Light, +20°C	% loss	Dark, +20°C	% loss	Dark, +4°C	% loss
0m	5.37		5.37		5.37	
2m	3.74	30.35	4.99	7.08	5.37	0.00
4m	3.64	32.22	4.85	9.68	5.1	5.03
6m	3.45	35.75	4.55	15.27	4.65	13.41
8m	3.25	39.48	4.35	18.99	4.25	20.86
10m	3.05	43.20	4.25	20.86	4.05	24.58
12m	2.75	48.79	4.05	24.58	4.00	25.51

Temperature and type of processing affect the vitamin C loss during storage. During thermal treatment vitamin C is destroyed usually by reactions of oxidation at high temperatures in presence of air [21]. The losses of vitamin C were higher than 50% in juices pasteurized at high temperatures during 21 days of storage, and there was 50% decrease of vitamin C in the tomato juice sample in the first 30 days of storage [22]. Significant decrease of vitamin C during the first month of storage was due to oxygen presence in the package and it is probably responsible for most of the loss during long-time storage, according to Min and Zhang [22].

Odriozola-Serrano *et al.* [17] found significantly higher level of vitamin C in tomato juice obtained by pasteurization at low temperatures compared to high temperatures. In their research they proved that during the first week of storage the concentration of vitamin C was higher in tomato juice treated by light pasteurization. They also found no significant difference in vitamin C content between the 7th and 21st day of storage, although this time of storage is considered to be short, which cannot be projected at maximal length of tomato juice storage (one year). The level of phenols in tomato juice during 12 months varied depending on storage conditions (Fig. 2). When stored in the light

at +20°C losses were slow, while after 10 and 12 months the loss of phenols in tomato juice was fast (Fig. 2 A), unlike vitamin C which was lost the most in the first months of storage and later had a slow trend (Fig. 1 A).

Losses in phenol content during storage in the dark on both experimental temperatures had similar dynamic and line tendency, which was proved by the high values of determination coefficient (R^2) close to 1 (Fig. 1 B and C). Loss of phenol content at light at +20°C was 80.49% while in dark it was 33.90 and 29.79%, in dark at +20°C and +4°C respectively (Table 4). It is interesting that the level of phenols did not differ in dynamics of loss in the first eight months of storage regardless of different experimental conditions. A critical point is particularly noticeable, where the percentage of loss after 8 months was 25.62%, while after 10 months it increased to 77.14% when stored in the light at +20°C (Table 4). There were no statistically significant differences of loss of phenol at different storage conditions, as shown in Table 5.

Generally, thermal treatment of tomato fruits causes loss of total phenol content [23]. Thermally treated tomato products displayed a significant loss of phenol components (chlorogenic acid) from 4.4 to 3.5- 3.8 mg/100 ml FV after 56 days at 4°C [16].

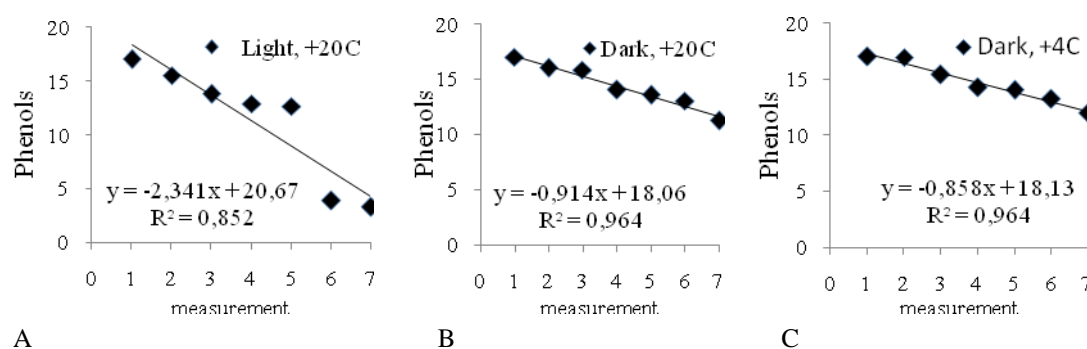
**Figure 2.** The average value and tendency of phenols loss during 12 months of storage in different conditions A) light +20°C, B) dark +20°C, C) dark +4°C

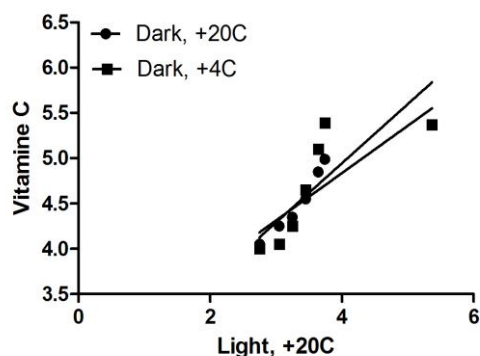
Table 4. Percentage of phenol loss in pasteurized tomato juice during 12 months of storage

Storage time (months)	Light, +20°C	% loss	Dark, +20°C	% loss	Dark, +4°C	% loss
0m	17.02		17.02		17.02	
2m	15.55	8.64	16.05	5.70	16.98	0.24
4m	13.80	18.92	15.85	6.87	15.41	9.46
6m	12.89	24.27	14.05	17.45	14.25	16.27
8m	12.66	25.62	13.55	20.39	14.05	17.45
10m	3.89	77.14	13.05	23.33	13.25	22.15
12m	3.32	80.49	11.25	33.90	11.95	29.79

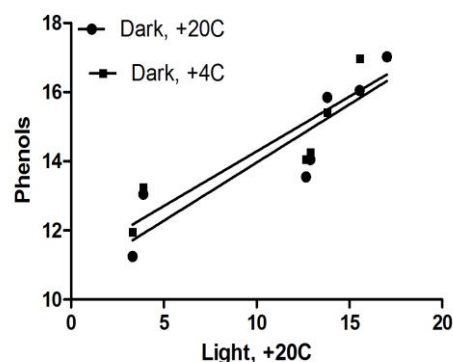
Table 5. Tukey's multiple comparison test of differences in phenols content during storage time at different conditions

Tukey's multiple comparison test	Mean difference	q	Summary	95%
Light 20°C : Dark, +20°C	-3.099	2.315	ns	-7.928 to 1.731
Light 20°C : Dark, +4°C	-3.397	2.544	ns	-8.227 to 1.433
Dark, 20°C : Dark, +4°C	-0.299	0.224	ns	-5.128 to 4.531

ns not significant



A) $x=0.143+0.844x^2-0.09x^3$
 $p=0.003^{**}$, $p=0.0372^{**}$



B) $x=1.369+2.695x^2-1.953x^3$
 $p=0.0067^{**}$, $p=0.0058^{**}$

Figure 3. Regression dependence of tomato juice storage at +20°C and storage in the dark at +20°C and +4°C, respectively.

The highest significant loss of phenols was found by Klimczak *et al.* [24] in storage from 0-6 months, while the loss of phenol was stable and in linear tendency when stored for 4 months at +4 and +20°C [25,26]. Parallel analysis of polyphenols degradation and decrease of hydrophile antioxidative capacity proved the significant loss of polyphenols during storage from 0-6 months (7-12%), while the antioxidative capacity dropped after 9 months of storage (10-12%) [12]. Although, differently from these studies of phenol content during the storage period, Pérez-Vicente *et al.* [14] found slight changes in total phenolic compounds in tomato juices stored for 4 months at +18 °C.

The analysis of the regression dependence between the investigated methods of storage (storage in light as a dependent variable compared to independent variables related to storage in dark conditions and at different temperatures), and

partial regression coefficient, proved the statistical significance of storage conditions in which tomato juice was kept (Fig. 3 A, B). Regardless to comparison tests performed for the whole storage stream (Tukey's Multiple Comparison Test) partial coefficients of regression determined more specifically the changes after 12 months of storage in function of dynamics of loss of certain bioactive nutrients. This analysis of degradation during storage explains that the best way of storage was storage in the dark. The significance was in dynamics of degradation which was in function of way storage of tomato juice (Fig. 3 A, B). Degradation according to a simple comparison test (Tukey's test) for phenol content was not significant for long-time storage for 12 months.

However, ambient conditions caused a significant loss of these components, especially when stored in light, compared to storage in the

dark (partial coefficient of multiple regression, Fig. 3) since dynamics of degradation in the first months was slower.

CONCLUSION

The increase in people's awareness of the need to nutrient value with added value as health improvement substance has put tomato and its products on an important position in human diet. Tomato juice is its very popular product, consumed quite a lot.

This experiment proved that degradation of total phenols from tomato juice during 12 months of storage was not significant. Also, the experiment proved that the conditions of storage of tomato juice significantly impact on its nutritive compounds. Degradation was caused by storage at light compared to dark. Total content of vitamin C in processed tomato juice was found after the first two months of storage at light (30.35%). The obtained experimental data could be very useful for choice of adequate warehouse for long-term storage of tomato juice in the perspective of preserving vitamin C and total phenols as health-valuable nutrients.

Acknowledgement: *This study was supported by the Serbian Ministry of Education, Science and Technological Development: Projects No. TR31059 (Integrating biotechnology approach in breeding vegetable crops for sustainable agricultural systems).*

REFERENCES:

1. K. H. Van het Hof, B.C. De Boer, L. B. Tijburg, B. R. Lucius, I. Zijp, C. E. West, J. G. Hautvast, J.A. Weststrate, *J. Nutr.*, **130**, 1189 (2000).
2. L. Frusciante, P. Carli, M. R. Ercolano, *Mol. Nutr. Food Res.*, **51**, 609 (2007).
3. R. D. Gallie, *Scientifica*, **1**, 24 (2013).
4. A. K. Schlueter, C. S. Johnston, *J. Evid. Based Complement. Altern. Med.*, **16**, 49 (2011).
5. V. Locato, S. Cimini, L. D. Gara, *Front. Plant Sci.*, **4**, 152 (2013).
6. B. A. Fox, A. G. Cameron, Food science, nutrition & health, 6th edn., (Chapter 13: Vitamins). J.W. Arrowsmith Ltd., Bristol, UK, 1995, p. 236.
7. W. Davey, D. Van Montaguinze, M. Sanmartin, A. Kanellis, N. Smirnoff, J. Benzie, J. Strain, D. Favell, J. Fletcher, *J. Sci. Food Agr.*, **80**, 825 (2000).
8. R. K. Toor, G. B. Savage, A. Heeb, *J. Food Comp. Anal.* **19**, 20 (2006).
9. G. R. Borguini, D. H. Markowicz, J. M. Moita-Neto, F. S. Capasso, E. A. Torres, *Braz. Arch. Biol. Technol.*, **56**, 521 (2013).
10. A. Raiola, M. M. Rigano, R. Calafiore, L. Frusciante, A. Barone, Mediators of Inflammation, ID 139873, 2014, p. 16.
11. V. Ruggieri, B. B. Hamed Amalia, L. Frusciante, M. L. Chiusano, *Plant Mol. Biol.*, **91**, 397 (2016).
12. A. Vallverdu-Queralt, S. Arranz, A. Medina-Remon, I. M. Casals-Ribes, R. Lamuela-Raventos, *J. Agric. Food Chem.*, **59**, 9358 (2011).
13. A. Vallverdu-Queralt, A. Medina-Remón, I. Casals-Ribes, C. Andres-Lacueva, A. L. Waterhouse, R.M. Lamuela-Raventos, *LWT - Food Sci. Tech.*, **47**, 154 (2012).
14. A. Pérez-Vicente, P. Serrano, P. Abellán, C. García-Viguera, *J. Sci. Food Agr.*, **84** (7), 639 (2004).
15. V. Lavelli, G. Giovanelli, G., *J. Sci. Food Agr.*, **83**, 966 (2003).
16. I. Odriozola-Serrano, R. Soliva-Fortuny, V. Gimeno-Ano, O. Martin-Belloso, *J. Food Eng.*, **89**, 210 (2008).
17. I. Odriozola-Serrano, R. Soliva-Fortuny, O. Martín-Belloso, *Food Sci. Emerg. Technol.*, **9**, 272 (2008a).
18. Praktikum iz Biohemije, M. Cvijović, G. Aćamović-Đoković (eds.), Agronomski Fakultet, Čačak (srb), 2005, p. 250.
19. Osnovi statističke analize, R. Njegić, M. Žižić, M. Lovrić, D. Pavličić (eds.), Savremena administracija, Beograd, 1991, p. 498.
20. R. A. Hoshmand, Statistical methods for environmental & agricultural sciences, 2nd edn., CRC Press, Boca Raton, New York, USA, 1998, p. 439.
21. C. Leoni, Improving the nutritional quality of processed fruits and vegetables: the case of tomatoes, in fruit and vegetable processing: Improving quality. W. Jongen (ed.), Woodhead Publishing Ltd and CRC Press, LLC, Cambridge, 2002, p. 83.
22. S. Min, Q. H. Zhang, *Food Chem. Toxicol.*, **68**, 1600 (2003).
23. R. Pavlović, J. Mladenović, N. Pavlović, N., M. Zdravković, D. Jošić, J. Zdravković, *Acta Sci. Pol. Hort. Cult.*, **16**(3), 119 (2017).
24. I. Klimczak, M. Malecka, M. Szlachta, A. Gliszczynska-Swiglo, *J. Food Compos. Anal.*, **20**, 313 (2007).
25. G. Giovanelli, A. Paradiso, Stability of dried and intermediate moisture tomato pulp during storage. *J. Agric. Food Chem.*, **50**, 7277 (2002).
26. A. Gliszczynska-Swiglo, B. Tyrakowska, *J. Food Sci.*, **68**, 1844 (2003).
27. V. L. Singleton, R. Orthofer, R. M. Lamuela-Raventós, *Methods Enzymol.*, **299**, 152 (1999).

Photocatalytic degradation of the pharmaceuticals *Paracetamol* and *Chloramphenicol* by Ln–modified ZnO photocatalysts

N. Kaneva, A. Bojinova*, K. Papazova, D. Dimitrov

Laboratory of Nanoparticle Science and Technology, Department of General and Inorganic Chemistry, Faculty of Chemistry and Pharmacy, University of Sofia, 1164 Sofia, Bulgaria

Received January 5, 2019; Revised June 19, 2019

Ln-modified (Ln = La, Ce, Eu) zinc oxide powders are synthesized by green thermal method. The materials are characterized by various techniques such as XRD, BET, TEM, SEM, EDX and UV-visible spectroscopy. The photocatalytic activity of the nanostructured ZnO modified with different rare earths is tested in the photodegradation of the commonly used drugs *Paracetamol* and *Chloramphenicol* in aqueous solution under UV light illumination. Highest degradation efficiencies are encountered for the materials modified with La³⁺, degradation efficiencies values of 95.88% (*Paracetamol*) and 80.74% (*Chloramphenicol*) are achieved after 240 min of photocatalytic treatment. The photodegradation efficiency of doped ZnO powders follows the order La>Eu>Ce. This trend is observed in the course of degradation of both drugs (*Paracetamol* and *Chloramphenicol*). a_bojinova@hotmail.com

Keywords: rare earth, zinc oxide, *Paracetamol*, *Chloramphenicol*, photocatalytic degradation

INTRODUCTION

Pharmaceuticals and personal care products are a group of emerging environmental contaminants, which induce physicochemical and physiological effects in humans at low doses [1,2]. The latter distinguish them as unique group of contaminants from other contaminants like the persistent organic pollutants. Active pharmaceutical ingredients were detected in environment since 1970, when the first studies on drug contaminated domestic wastewaters were published [3,4]. An increasing number of investigations confirmed the presence of various pharmaceuticals and personal care products (PPCPs) in different environmental compartments worldwide [5] at low concentrations (ng L⁻¹ to µg L⁻¹), but their input into the environment is continuous. Despite that most of the data, reported in literature, concern the occurrence of drugs of each therapeutic class in the aquatic environment, several reviews [6-8] mainly concern their attention on therapeutic classes detected in environment, presenting data collected from 134 articles published between 1997 and 2009 (Fig. 1). The data is useful to find out the most appropriate active substances for ecotoxicity tests. According to data present in literature, scientific community has mainly concerned their attention on therapeutic classes such as, non-steroidal anti-inflammatory drugs, blood lipid lowering agents, antibiotics and sex hormones. By these reasons, this paper will focus in drugs belonging to those therapeutic classes. Non-steroidal anti-inflammatory drugs sold in high quantities without a prescription, are used

as pain killers in veterinary and human medicine. The antibiotic substances consumption worldwide is in hundreds of thousands of tons annually. In veterinary medicine, more than 70% of all consumed pharmaceuticals are antibiotics, and ~6% in human medicine.

Pharmaceuticals are structurally designed to maximize their biological activity at low concentrations and developed to produce a prolonged action and have continuous everyday release to the environment [9]. These properties highlight the risks associated with the inadvertent presence of PPCPs in the environment. It has become a major concern because PPCPs are extensively and increasingly used in modern life, human and veterinary medicine and have continuous everyday release to the environment [9]. Therefore a priority pollutant lists have been developed by the European Union and by the United States Environmental Protection Agency, pointing a variety of contaminants present in wastewaters, storm water runoff and surface water. There is a lack of data on the toxicological implications in both target and non-target organisms after chronic exposure to complex mixtures of PPCPs at sub-therapeutic levels [9]. Much research is needed to characterize the influence of such exposure also on the public health status in the contaminated geographic areas. Further investigation is needed to provide more detailed definition of seasonal variations of PPCPs and their bioaccumulation in aquatic organisms [11].

* To whom all correspondence should be sent:
E-mail: a_bojinova@hotmail.com

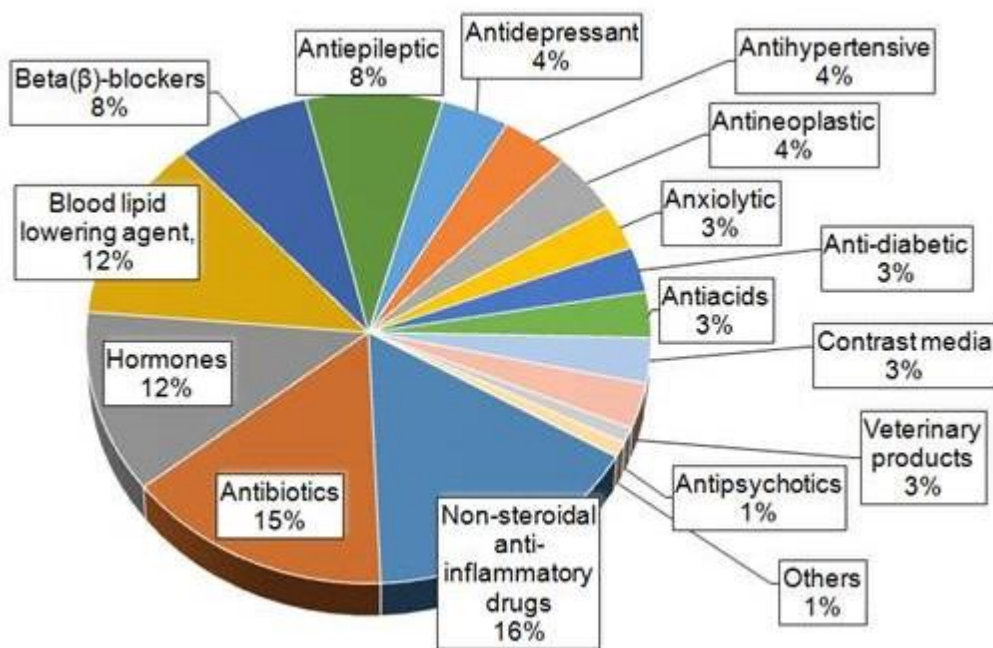


Fig. 1. Relative percentage of the most detected in the surface and groundwater therapeutic classes.

Some researchers [12-14] initially highlight the importance and further study on possible bioaccumulation by aquatic biota, including its implications for human exposure via consumption of contaminated fish or shellfish.

For this study, we selected commonly used pharmaceuticals with high volumes of production that have already been detected in the aquatic environment and in wild animals - anti-inflammatory antipyretic *paracetamol* (PCA) and antibiotic *chloramphenicol* (CA).

Photocatalysis, as advanced oxidation process, seems an efficient approach for purification of drugs contaminated waters using UV-irradiated inorganic oxides [15-19]. Zinc oxide and titania are the metal oxides, most widely used as photocatalysts. In comparison to TiO₂, in case of ZnO the lifetime of photogenerated electrons is significantly higher and the rate of recombination is lower, making ZnO an attractive material for photocatalytic applications [20]. Therefore this work is focused on photocatalysis with doped ZnO powders.

This study is a part of our greater investigation on lanthanide doped ZnO photocatalysts. The previous parts refer to: degradation of Malachite Green and Reactive Black 5 (at dye concentrations of 3, 5, 7 and 10 ppm) by doped with 0.5 and 1 % La ZnO nanoparticles, prepared by sol-gel method [21]; photocatalytic mineralization of 20 ppm Reactive Black 5 in natural Black Sea water [22]; photo-oxidation of ethylene in air as gas-phase

model pollutant with Ln-doped (Ln = La, Ce, Eu) ZnO powders [23].

EXPERIMENTAL

Reagents and materials

The commercial oxide powders: ZnO (>99.0 %) and ethanol absolute grade (99.5%) were supplied from ACROS Organics; La₂O₃ (>99.0 %), Eu₂O₃ (>99.0 %) and Ce(NO₃)₃·6H₂O (>99.0 %) were purchased from Fluka. All the solutions, used in the experiments, were prepared with distilled water.

The commercially available drugs *Paracetamol* (λ_{\max} = 243 nm, \geq 99.0% purity) and *Chloramphenicol* (λ_{\max} = 278 nm, \geq 99.0% purity) from Actavis were chosen as model contaminants for the photocatalytic water purification tests. A brief description of the investigated commonly used pharmaceuticals is given below.

Paracetamol is classified as a mild analgesic. It is commonly used for the relief of headaches and other minor aches and pains and is a major ingredient in large number cold and influenza remedies. In comparison to other over the counter pain relievers, *Paracetamol* is significantly more toxic in case of overdose [24,25]. Some of its side effects are pointed in Table 1.

Chloramphenicol is broad-spectrum antibiotic. It is active against both Gram-positive and Gram-negative bacteria and against numerous groups of microorganisms as well. CA acts through inhibition of the microorganism protein synthesis and therefore is effective for treatment of number of

infectious diseases. The latter and its low cost and availability, made *Chloramphenicol* extensively used for most eye and ear infections cure and for treatment of domestic animals [26. However, the

drug is associated with serious toxic effects in humans [27,28] (Table 1). This is the reason why *Chloramphenicol* usage in food-producing animals is banned in lots of countries and EU [29].

Table 1. Side effects of paracetamol and chloramphenicol

Pharmaceutical	Side effects	
	High doses	Prolonged use
<i>Paracetamol</i> C ₈ H ₉ NO ₂	Hepatotoxicity, skin, liver and kidney damage,	Change the effect of other pharmaceutical drugs (rifampicin, cimetidine, chloramphenicol, busulfan)
<i>Chloramphenicol</i> C ₁₁ H ₁₂ Cl ₂ N ₂ O ₅	Violations of blood-forming apparatus; haemolytic anemia leukemia, nausea, vomiting, diarrhea, stomatitis (gastrointestinal) reactions, headache, depression (neurotoxic effects), rash, itching, burning, redness, swelling, fever (allergic).	The development of fungal infections and resistance of microorganisms to the product

Catalysts modification and characterization

Three series of Ln- modified ZnO powders were prepared by simple and green thermal method (using simple preparation conditions and reduced synthesis time, with stable natural and nontoxic reagents, without any chemical residue after preparation of the samples). In our previous investigation it was experimentally found out that 2 mol% Ln content in the modified ZnO was optimal is for the mineralization of organic dye Reactive Black 5 [22]. Therefore, here we applied the same composition for photopurification of water from drugs contamination. For preparation of Ln-ZnO photocatalysts, calculated amounts of La₂O₃ (respectively Eu₂O₃ or Ce(NO₃)₃·6H₂O) and ZnO, corresponding to 2 mol% Ln content, were mixed thoroughly. Then small quantity of ethanol (~1-1.5 ml per g sample) was added as medium for more complete mixing to ensure intimal contact between the particles of both oxides. The initial charge was mixed for 10 min, then treated for 30 min by ultrasound (ultrasonic bath IKEDA RIKA 100 V 50/60Hz) and dried finally for 1 h at 100°C in order to obtain fine Ln-ZnO powders for photocatalysis. Each series of powder photocatalysts – La, Eu and Ce modified ZnO were prepared by repetition of the same procedure at the same dopants concentration - 2 mol%.

The surface area of pure and Ln-modified ZnO powders was estimated with BET analysis (N₂ adsorption). Prior the BET analysis, the samples were degassed for 4 h at 150°C before the N₂ adsorption. Pure ZnO and Ln-modified ZnO surfaces morphology was investigated by SEM (JSM-5510 JEOL operated at acceleration voltage of 10 kV). The elemental analysis and chemical characterization of the samples surface were

performed by energy-dispersive X-ray spectroscopy via Quantax200 EDX detector, Bruker Resolution 126 eV. The crystallinity and phase composition of the catalysts were analyzed by X-ray diffraction (diffractometer Siemens D500 with Cu K α radiation within 2 θ range 25–40° at a step of 0.05°2 θ and counting time 2 s/step). The average crystallite sizes were calculated by Scherrer's equation:

$$d_{hkl} = k \cdot \lambda / \beta \cdot \cos(2\theta) \quad (1)$$

where d_{hkl} is the average crystallite size (nm), λ is the wavelength of CuK α radiation ($\lambda = 0.154056$ nm), θ is the Bragg's diffraction angle, β is the full-width at half maximum intensity of the main characteristic peak (at 2 θ converted to radians) and k is a constant ~0.9.

Photocatalytic experiments

The photocatalytic experiments were performed in a cylindrical glass reactor [22, 30, 31]. The volume of the aqueous suspensions was 250 ml. The catalyst concentration was 1 g dm⁻³. The initial drugs concentration was 50 ppm for *Paracetamol* and 25 ppm for *Cloramphenicol*. The suspensions were first stirred in complete darkness for 30 min to reach sorption-desorption equilibrium of the drugs molecules onto the catalysts surface. After that the illumination was started to carry out the photocatalysis. The source of irradiation was 18 Watt fluorescent BLB UV-A lamp emitting mainly in the region of 340-360 nm. The lamp was fixed at 9 cm above the solution and the UV-light enters the suspension across its interface with the air. The intensity of irradiation at the suspensions surface was 0.014 W/cm². Aliquot samples of 5 ml were taken at determined time intervals (UV lamp switched off), centrifuged and then filtered through 0.22 μ m membrane filters for complete removal of

the catalyst particles. The drugs concentration in each aliquot was determined at the maximum of pharmaceutical drugs absorbance (243 nm for *Paracetamol* and 278 nm for *Cloramphenicol*) by spectrophotometer Evolution 300 Thermo Scientific (range 200 - 500 nm). After measurement each aliquot, together with the photocatalyst particles, was returned to the treated suspension. All photocatalytic tests were performed at room temperature $23\pm 2^\circ\text{C}$. Stirring (350 rpm) was kept constant along the experiments to assure oxygen saturation, uniform access of UV light and constant transfer rate of the contaminants to the catalyst surface. The pH of the investigated suspensions,

determined by pH meter Hanna instruments, was found to be in the range of 5.7–6.4.

RESULTS AND DISCUSSION

The surface morphology of pure and Ln-modified ZnO powders, observed by SEM, is presented in Figure 2. The micrographs indicate that the modified (La, Ce and Eu) ZnO catalysts are similar, flower-like in shape. The average particle size of 0.4–0.45 μm for modified ZnO, determined from the SEM images, is greater than that of pure ZnO – about 0.25 μm .

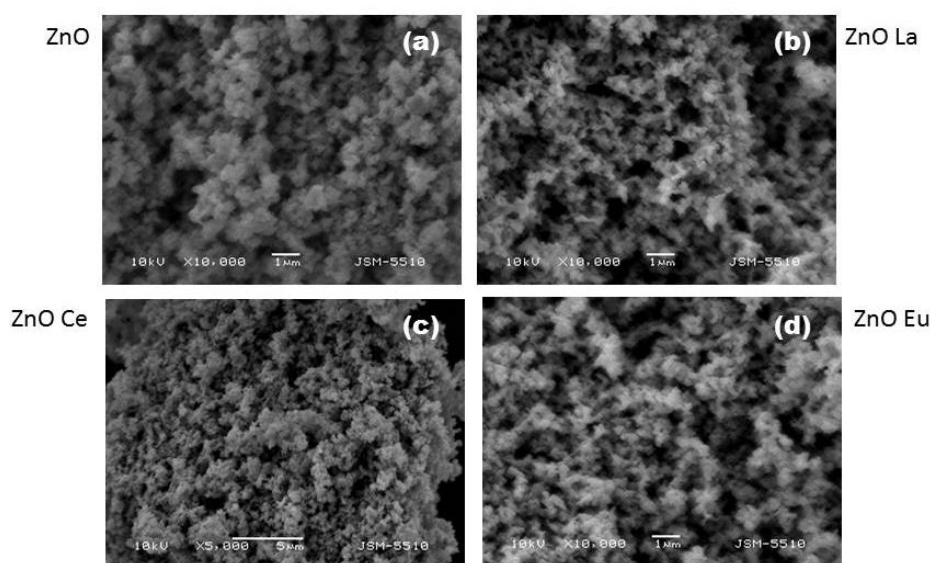


Fig. 2. SEM images of pure ZnO (a) and 2 mol% Ln-modified: La-ZnO (b); Eu-ZnO (c); Ce-ZnO (d) powders.

Fig. 3a, b and c represent EDX analysis of Ln-modified ZnO powder samples and their corresponding X-ray diffraction spectra (Fig. 3d-f). The obtained results from EDX confirm the presence of the dopants La, Ce and Eu onto the surface of catalysts particles. The absence of extra peaks, except the expected ones in the EDX spectrum, shows that the prepared modified (La, Ce and Eu) ZnO catalysts have no impurities. The JCPDS database (Powder Diffraction Files, Joint Committee on Powder Diffraction Standards, Philadelphia PA, USA, 1997) was used to identify the crystal phase composition of the powder samples. The main diffraction peaks (100), (002) and (101) of the samples indicate that ZnO is present as hexagonal wurtzite crystalline phase (PDF # 80-0075). No characteristic peaks of impurity phases like $\text{Zn}(\text{OH})_2$ are observed. There are very low peaks corresponding to formation of

La_2O_3 (PDF # 83-1350), Eu_2O_3 (PDF # 74-1988) and yellowish CeO_2 (PDF # 81-0792), due to the low dopants concentration - 2 mol%. The XRD patterns of all the modified (La, Ce and Eu) ZnO catalysts are similar, which shows that there is no change in the crystal structure. The average crystallite size, calculated from the most intensive peak (101) is $d_{\text{hkl}} = 36$ nm for pure ZnO and $d_{\text{hkl}} = 43$ nm for modified (La, Ce and Eu) ZnO catalysts.

The increase in crystallite and particle size upon La, Ce and Eu doping can be attributed to formation of Ln–O–Zn bonds on the surface of the Ln-modified samples, which affects the size of crystallites [32]. The latter is favored by the higher electronegativity and the larger ionic radius of RE cations (103 pm for La^{3+} cations, 108 pm for Eu^{3+} cations and Ce^{4+} cations - ionic radius of 100 pm) than 74 pm for Zn^{2+} cations. The incorporation of Ln cations in ZnO expands its lattice [33, 34].

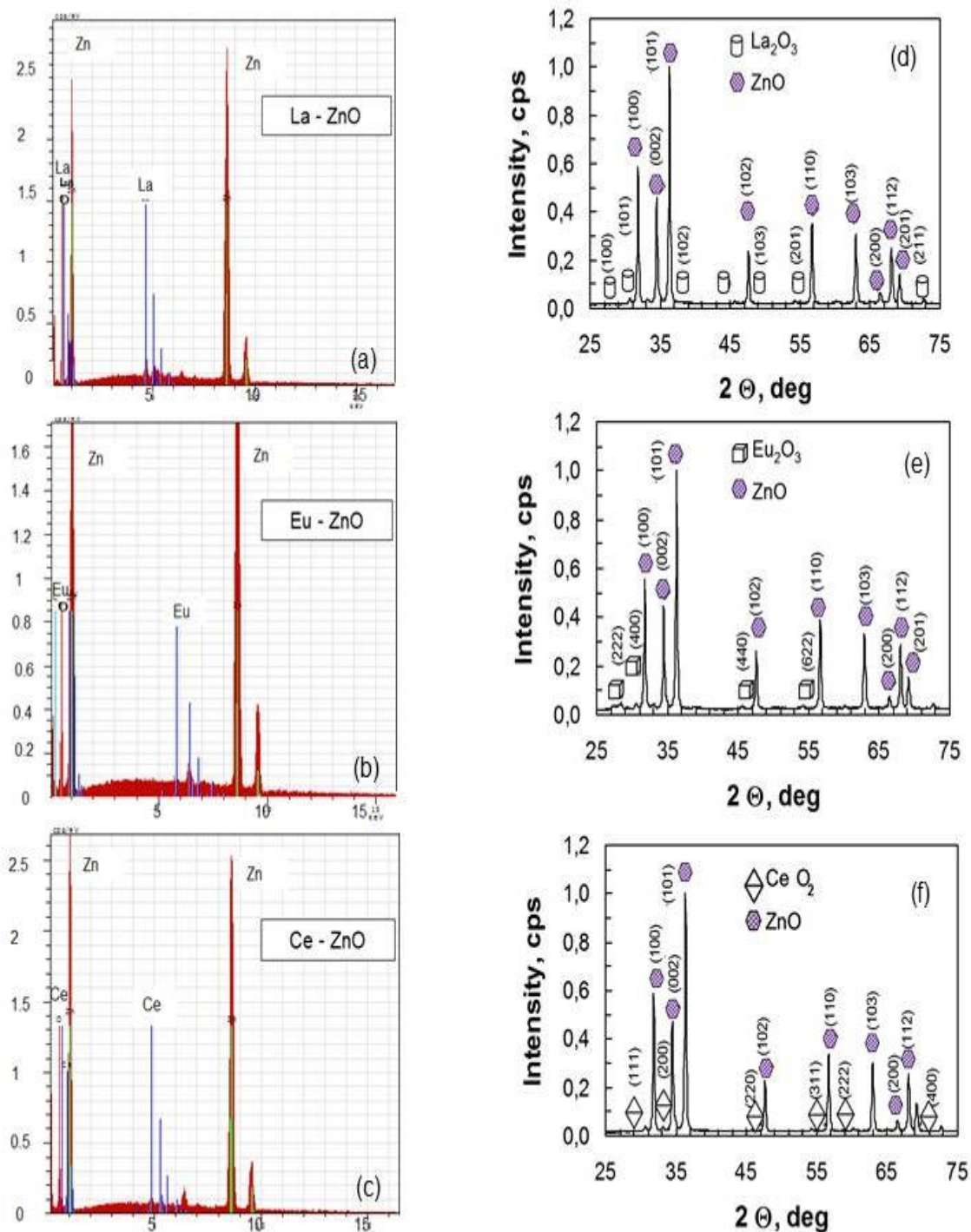


Fig. 3. EDX spectra of ZnO powders modified with La³⁺ (a), Eu³⁺ (b), Ce³⁺ (c) and XRD patterns of La-ZnO (d), Eu-ZnO (e), Ce-ZnO (f) powder photocatalysts.

The surface area of Ln modified powder samples, determined by BET analyses, using N₂ adsorption is found to be 32.34 m²/g for La, 31.43 m²/g for Ce and 31.74 m²/g for Eu modified catalyst. The surface area of modified catalysts is greater in comparison to that of pure ZnO - 10.30 m²/g.

The photocatalytic activity of Ln (2 mol %) modified ZnO powders towards decomposition of the model pharmaceutical contaminants, *Paracetamol* and *Chloramphenicol*, under UV light

irradiation is compared in Figure 4 and 5. The heterogeneous photocatalytic process is commonly approximated to pseudo-first-order reaction with respect to the contaminant and can be described following the equation:

$$\ln(C_i/C_{in}) = -kt \quad (2)$$

Here C_{in} is the initial concentration of drugs solution, C_i is the drugs concentration at irradiation time t , and k is the rate constant of photocatalysis.

The solid lines in Fig. 4 are linear fits of the experimental data points by Eq. 2. The slope of logarithmic scale linear fits represents the rate constant of photocatalysis k . The corresponding rate constants values k of photocatalysis for all samples are also presented in Fig. 4. As seen from the presented data the Ln modified catalysts faster degrade paracetamol (Fig. 4a) than chloramphenicol (Fig. 4b), despite to its higher initial concentration - 50 ppm for PCA and 25 ppm for CA. In both drugs photodestruction the best result is achieved with the doped with La sample:

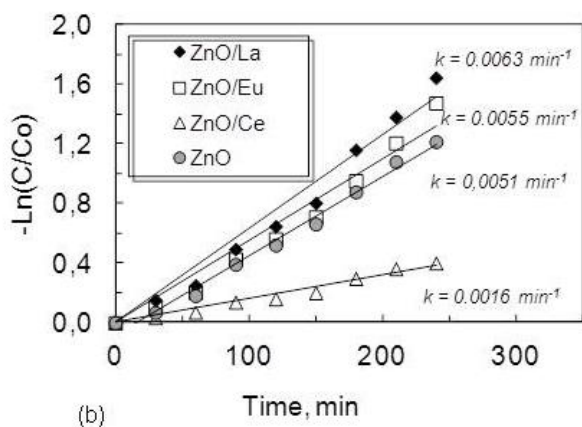
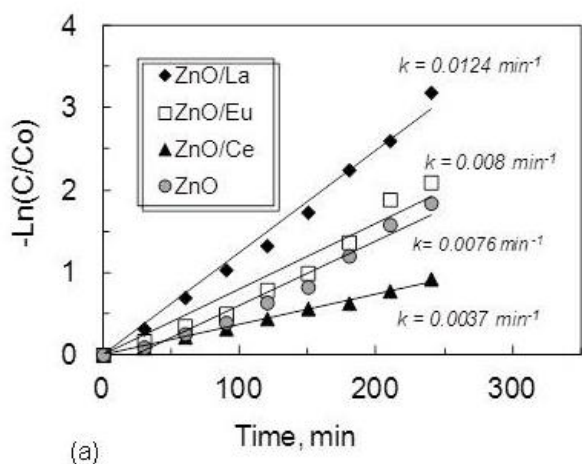


Fig. 4. Kinetics of the photocatalytic degradation of Paracetamol (a) and Chloramphenicol (b) from aqueous solutions under UV illumination in the presence of pure ZnO and different Ln-modified ZnO powder catalysts.

The data in Fig. 5 correspond to 240 min UV light irradiation time. The ZnO powders, doped with La show highest degradation degree of pharmaceuticals ($D_{PCA} = 95.88\%$ and $D_{CA} = 80.74\%$). The samples prepared by Eu doping have higher ($D_{PCA} = 87.72\%$ and $D_{CA} = 60.34\%$) photocatalytic efficiency in comparison to these, modified with Ce ($D_{PCA} = 77.17\%$ and $D_{CA} = 33.06\%$

$k_{PCA} = 0.01264\text{ min}^{-1}$ and $k_{CA} = 0.0063\text{ min}^{-1}$. The lowest photocatalytic activity shows Ce – modified ZnO sample. These experimental results are confirmed by the degree of photocatalytic mineralization of the drugs ($D\%$) (Fig. 5), calculated by the equation:

$$D\% = (C_{in} - C_t) / C_{in} \times 100 \quad (3)$$

Where C_{in} is the initial drugs concentration and C_t is the concentration of pharmaceutical pollutant after selected moment of illumination time t .

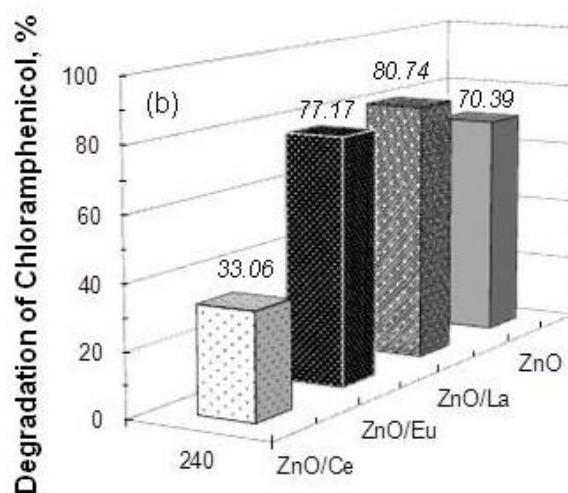
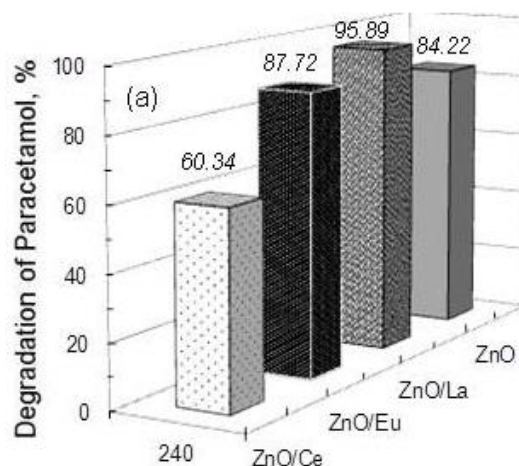


Fig. 5. Photomineralization degree of Paracetamol (a) and Chloramphenicol (b) by Ln-modified ZnO powders. The data correspond to 240 min UV light illumination time.

$\%$). In accordance to the experimental data, the photodegradation efficiency of doped ZnO powders follows the order La>Eu>Ce. This trend is observed in the course of degradation of both drugs (PCA and CA).

The expected mechanism of photocatalysis with Ln modified ZnO is connected to the possibility for energy transfer between the introduced rare earth

ion energy levels and the conduction/valence band of host ZnO photocatalyst. The 4f-shells of an Ln ion can accept or donate e^- from or to the energy bands of the host with the reactions of valence change such as: $\text{Ln}^{3+} + e^- \rightarrow \text{Ln}^{2+}$ (for La and Eu) or $\text{Ln}^{4+} + e^- \rightarrow \text{Ln}^{3+}$ (in case of Ce).

The high efficiency of La and Eu modified ZnO samples can be explained with successful charge separation and production of free radicals. La modified ZnO manifests highest efficiency, which can be attributed to highest number of oxygen vacancies in this case (reasoned by the different charge and electronegativity of La and Zn ions) and as a result – stronger adsorption of OH^- ions onto the catalysts surface. The latter favors the formation of $\bullet\text{OH}$ by reaction of h^+ and OH^- . The $\bullet\text{OH}$ radicals are extremely strong non-selective oxidants, which degrade the organic molecules at the surface of La modified ZnO. In case of Eu modified ZnO the introduced Eu energy levels are close, but lower to the energy of ZnO conduction band, which favors formation of $\bullet\text{O}_2^-$ radicals by reaction of photogenerated e^- and O_2 . In case of Ce modified ZnO the reverse process (transferring of e^-) is forbidden, which leads to deep e^- trapping and the observed low photocatalytic efficiency of Ce-modified ZnO sample.

The prepared Ln modified ZnO photocatalysts seem promising for the purification of drugs contaminated wastewaters.

CONCLUSIONS

Ln modified (2 mol %) ZnO powders are prepared by thermal method. Their structural and photocatalytic properties have been established. It's experimentally found that Ln-ZnO powders achieve faster degradation of PCA, compared to that of CA under UV-light irradiation. Higher degradation efficiencies are encountered for the modified with La ZnO powders, degradation efficiency values of 95.88% (PCA) and 80.74% (CA) are observed after 240 min of photocatalytic treatment. With Eu^{3+} the following removal efficiencies are obtained: 87.72% (PCA) and 77.17% (CA). The modified powders with Ce^{3+} have the lowest photocatalytic efficiency. The high efficiency of La and Eu modified ZnO samples can be explained with successful charge separation and production of free radicals.

Acknowledgements. Authors are grateful to Operational program "Science and Education for Smart Growth", project BG05M2OP001-2.009-0028, DFNI-T02/16, Russian Presidential Program of Engineer Advanced Trading and Horizon 2020

REFERENCES

1. A.J. Ebele, M A-E Abdallah, S Harrad, *Emerging Contaminants*, **3**, 1 (2017).
2. A. Sangion, P. Gramatica, *Environ. Int.*, **95**, 131 (2016).
3. A.W. Garrison, J.D. Pope, F. Allen, Identification and Analysis of Organic Pollutants in Water. In: Ann Arbor Science Publishers, Keith, L.H. (Ed.), Ann Arbor Science, 1976, 517–556.
4. C. Hignite, D.L. Azarnoff. *Life Sci.*, **20**, 337 (1977).
5. M. Ezechias, J. Janochova, A. Filipova, Z. Kresinova, T. Cajthaml, *Chemosphere*, **152**, 284 (2016).
6. L.H.M.L.M. Santos, A.N. Araújo, Adriano Fachini, A. Pena, C. Delerue-Matos, M.C.B.S.M. Montenegro, *J. Hazardous Mater.*, **175**, 45 (2010).
7. H.-J. Son, Seong, S.H, Jang, *J. Korean Soc. Environ. Engrs*, Review Paper 453 (2011). DOI: 10.4491/KSEE.2011.33.6.453
8. M.G. Lusk, G.S. Toor, Y.-Y. Yang, S. Mechtensimer, M. De, T.A. Obreza, *Critical Rev. Environ. Sci. Technol.*, **47**, 455 (2017). DOI: 10.1080/10643389.2017.1327787
9. A. Nikolaou, S. Meric, D. Fatta, *Anal. Bioanal. Chem.*, **387**, 1225 (2007).
10. N. Abedi, A. Nabi, E. Mangoli, A.R. Talebi, *Middle East Fertility Soc. J.*, **22**, 323 (2017).
11. A. Puckowski, K. Mioduszewska, P. Łukaszewicz, M. Borecka, M. Caban, J. Maszkowska, P. Stepnowski, *J. Pharm. Biomed. Analysis*, **127**, 232 (2016).
12. L. Connolly, E. Ropstad, S. Verhaegen, *Trends Anal. Chem.*, **30**, 227 (2011).
13. Z. Wei, N.W. Kelsey, H. Nancy, A.D. Nathan, R.S. Clinton, Uptake, Translocation, and Accumulation of Pharmaceutical and Hormone Contaminants in Vegetables. Retention, Uptake, and Translocation of Agrochemicals in Plants, American Chemical Society, 2014.
14. E. Wielogorska, C.T. Elliott, M. Danaher, O. Chevallier, L. Connolly, *Food Control.*, **48**, 48 (2015).
15. D. Kanakaraju, Beverley D. Glass, Michael Oelgemoller, *J. Environ. Manag.*, **219**, 189 (2018).
16. S. Carbonaro, M.N. Sugihara, T.J. Strathmann, *Appl. Catal. B Environ.*, **129**, 1 (2013).
17. O.K. Dalrymple, D.H. Yeh, M.A. Trotz, *J. Chem. Technol. Biotechnol.*, **82**, 121 (2007).
18. P. Calza, V.A. Sakkas, C. Medana, C. Baiocchi, A. Dimou, E. Pelizzetti, T. Albanis, *Appl. Catal. B Environ.*, **67**, 197 (2006).
19. J.P. Candido, S.J. Andrade, A.L. Fonseca, F.S. Silva, M.R.A. Silva, M.M. Kondo, *Environ. Sci. Pollut. Res.*, **23**, 1991 (2016).
20. M.A. Hernández-Carrillo, R. Torres-Ricárdez, M.F. García-Mendoza, E. Ramírez-Morales, G. Pérez-Hernández, *Catalysis Today* in press. <https://doi.org/10.1016/j.cattod.2018.04.060>

21. N. Kaneva, A. Bojinova, K. Papazova, *J. Phys. Conf. Ser.*, **682**, 012022 pdf (2016) doi:10.1088/1742-6596/682/1/012022.
22. N. Kaneva, A. Bojinova, K. Papazova, D. Dimitrov, *Catalysis Today*, **252** 113 (2015).
23. N. Kaneva, A. Bojinova, K. Papazova, D. Dimitrov, A. Eliyas, *Bulg. Chem. Commun.*, **49**, 172 (2017).
24. S. Vitols, *J. Intern. Med.*, **253**, 95 (2003).
25. J. Kurtovic, S.M. Riordan, *J. Intern. Med.*, **253**, 240 (2003).
26. K. Ajit, A. Sarmah, M. Meyer, A. Boxall, *Chemosphere*, **65**, 725 (2006).
27. I. Liphshitz, A. Loewenstein, *Br. J. Ophthalmol.*, **75**, 64 (1991).
28. C. Diskin, *Mayo. Clin. Proc.*, **80**, 1392 (2005).
29. K. Woodward (2004) In: Watson, D.H. (Ed.) *Pesticide, Veterinary and Other Residues in Food*. Woodward Publisher Limited, Cambridge, 176 (Chapter 8).
30. S. Siuleiman, N. Kaneva, A. Bojinova, D. Dimitrov, K. Papazova, *Bulg. Chem. Commun.*, **49** (G), 199 (2017).
31. S.A. Syuleiman, N.D. Yakushova, I.A. Pronin, N.V. Kaneva, A.S. Bojinova, K.I. Papazova, M.N. Gancheva, D.Tz. Dimitrov, I.A. Averin, E.I. Terukov, V.A. Moshnikov, *Technical Physics*, **62**, 1709 (2017).
32. J. Lin, J.C. Yu, D. Lo, S.K. Lam, *J. Catal.* **183**, 368 (1999).
33. A.F. Wells, "Structural Inorganic Chemistry," 5th ed., Clarendon Press, Oxford, 1984, p. 1288.
34. C.L. Muhich, *J. Phys. Chem. C*, **121**, 8052 (2017).

On the role of texture and physicochemical characteristics on adsorption capacity of granular activated carbon

N. Pasupulety*, H. Driss, A. A. Al-Zahrani, M. A. Daous and L. A. Petrov

Chemical & Materials Engineering Department, College of Engineering, King Abdulaziz University, P.O. Box 80204 Jeddah 21589, Saudi Arabia

Received February 5, 2019; Accepted June 1, 2019

Granular activated carbons (GACs) obtained from date's stones were used as adsorbents for the adsorption of phenol, dibenzothiophene (DBT) and 4,6-dimethyl dibenzothiophene (4,6-DMDBT) in solution. The equilibrium adsorption results were correlated with textural and chemical characteristics of GACs. The amount of micropores with pore diameter about 1.289 nm was found high in GAC samples prepared at lower $ZnCl_2$ ratio ($R=0.5$). These are favorable for phenol and DBT adsorption in solution. SEM analysis revealed pores of elliptical shape for GACs prepared at $R=0.5$. GACs with slit-shaped mesopores are beneficial for the adsorption of 4,6-DMDBT in solution. The estimated critical pore diameter was about 0.87 nm for phenol adsorption on GACs. Whereas, the critical pore diameter for adsorption of DBT and 4,6-DBT was about 0.71 and 0.97 nm, respectively, on the studied GACs. GAC samples produced at a lower R value showed greater amount of total surface functional groups compared to GAC samples prepared at a higher R value. Hence, the removal performance of phenol was found high on GACs prepared at $R=0.5$. However, under identical adsorption conditions, slight hindrance in adsorption of DBT and 4,6-DMDBT was observed on GACs due to the bulkiness of the molecules.

Keywords: Granular activated carbon, adsorbent, phenol, dibenzothiophene, 4,6-dimethyl dibenzothiophene

INTRODUCTION

Activated carbon (AC) is successfully prepared from different agricultural wastes such as apricot stones, date fruit stones, nutshells, plum kernels, and rice husks [1-9]. It is also produced from various municipal wastes such as PET waste, sewage sludge and discarded tires [10-14]. It is well known that porous materials like AC have high adsorption capacity for a variety of liquid and gas adsorbates [15]. AC is also widely used in catalysis [16,17], food, beverage and pharmaceutical industries [18,19]. The surface chemistry of AC plays a key role in adsorption mechanisms and behaviors [20,21].

Dry date's stones contain 5-10% moisture, 6-7% proteins, 7-10% oil, 1-2% ash, 10-20% crude fibers and 55-65% carbohydrates [22]. They have the lowest lignin content, the highest cellulose and hemicellulose contents compared with almond shells, pecan shells and walnut shells [4]. The surface chemistry of GAC depends on pretreatment conditions such as acid concentration (HCl), activation temperature, and activation time [23]. Therefore, the physicochemical characteristics of GAC samples prepared under different conditions were investigated in this study. GAC samples produced with different chemical activator-to-date's stones weight ratio (R), carbonization temperature (T_c) and carbonization time (t_c) were employed in phenol, DBT and DMDBT adsorption

experiments. Date's stones impregnation with $ZnCl_2$ causes degradation of the cellulosic material upon carbonization. The dehydration and degradation of the cellulosic material result in charring, aromatization of the carbon skeleton and creation of the pore structure [24]. $ZnCl_2$ selectively strips H and O away from date's stones as H_2O and H_2 rather than hydrocarbons, CO or CO_2 [25].

In this paper, BET surface area and SEM analysis was used to determine the textural parameters of lab prepared GAC samples. Surface functional groups were determined by using Boehm titrations and XPS. The equilibrium adsorption data of phenol, DBT and DMDBT were fitted to Langmuir isotherm equation. The possible correlation between the textural properties and phenol, DBT and DMDBT removal performance of the GAC samples are discussed.

EXPERIMENTAL

The detailed preparation of GACs and the carbonization process are reported elsewhere [26]. The carbonization process was done at two different temperatures $T_c = 600$ or 700 °C with duration of 1 and 3 h (t_c). The samples prepared at $T_c = 600$ °C, $R=0.5$ and $t_c = 1$ and 3 h are labeled as GAC 1 and 2, respectively. The samples prepared at $T_c = 700$ °C, $R=0.5$ and $t_c = 1$ and 3 h are labeled as GAC 3 and 4, respectively. The samples prepared at $T_c = 600$ °C, $R=2$ and $t_c = 1$ and 3 h are labeled as GAC 5 and 6, respectively. The samples

* To whom all correspondence should be sent:

E-mail: pasupulety@gmail.com;
nsampathra@kau.edu.sa

N. Pasupulety et al.: On the role of texture and physicochemical characteristics on adsorption capacity of granular ...
 prepared at $T_c = 700\text{ }^\circ\text{C}$, $R=2$, $t_c = 1$ and 3 h are labeled as GAC 7 and 8, respectively.

Adsorption measurements

Characterization

BET surface area and pore size measurements were performed on a NOVA 2200e instrument (Quntachrome). Multipoint BET surface area, pore size and total pore volume measurements were done using NOVAVIN software provided with the equipment. Sample morphology was determined by using FE-SEM, equipped with ETD and VC detectors. XPS results of GAC samples were collected on a SPECS GmbH system equipped with Mg $K\alpha$ 1253.6 eV X-ray source. The reported binding energy values are based on C 1s 285.0 eV. The surface acid-base groups of the produced GAC samples were determined by the Boehm titration method [15, 16]. One gram of GAC sample each was placed in 50 cm^3 of 0.1 N solutions of the following reagents: sodium hydroxide, sodium carbonate, sodium bicarbonate and hydrochloric acid. The vials were sealed and shaken for 24 h at room temperature ($25\text{ }^\circ\text{C}$). Later, each of these solutions was filtered and 5 cm^3 of filtrate was titrated with HCl (0.1 N) or NaOH (0.1 N), respectively. The number of acidic sites was determined under the assumption that NaOH neutralizes carboxylic, lactonic and phenolic groups; sodium carbonate neutralizes carboxylic and phenolic groups and sodium bicarbonate neutralizes only carboxylic acid groups. The number of the basic sites was calculated from the amount of hydrochloric acid that reacted with the carbon surface.

Equilibrium adsorption studies of phenol were conducted by using 25 cm^3 of phenol-water solutions with concentrations between 10 and 150 mg/l using 0.1 g of GAC sample with an average particle size of 1.50 mm. The adsorption measurements of the control sample were carried out at temperature of $25\text{ }^\circ\text{C}$ under continuous shaking for 24 and 48 h. The initial and final concentration of phenol was determined using a Genysis10 UV/Vis spectrophotometer calibrated at $\lambda_{\text{max}}=268\text{ nm}$.

DBT and 4,6-DMDBT decane solutions with concentration between 10 and 200 mg/l were used for equilibrium adsorption studies. Each, 0.4 g of GAC sample with an average particle size of 1.0 mm was charged into a conical flask containing the above solutions and adsorption studies were conducted at room temperature of $25\text{ }^\circ\text{C}$ under continuous stirring. The concentrations of DBT and 4,6-DMDBT before and after the adsorption were determined by using Shimadzu GC equipped with Rxi-5ms capillary column fitted to FID. The collected adsorption data were fitted to a Langmuir isotherm described by the equation below:

$$q_e = q_m \frac{K_L C_e}{1 + K_L C_e}$$

where, q_m is the amount of solute (phenol, DBT and DMDBT) adsorbed in mg g^{-1} of dry GAC, C_e is the equilibrium concentration of the phenol, DBT and 4,6-DMDBT in solution in mg l^{-1} . K_L is Langmuir constant [27].

RESULTS AND DISCUSSIONS

Nitrogen adsorption isotherms

Nitrogen adsorption isotherms of GAC samples are shown in Fig. 1.

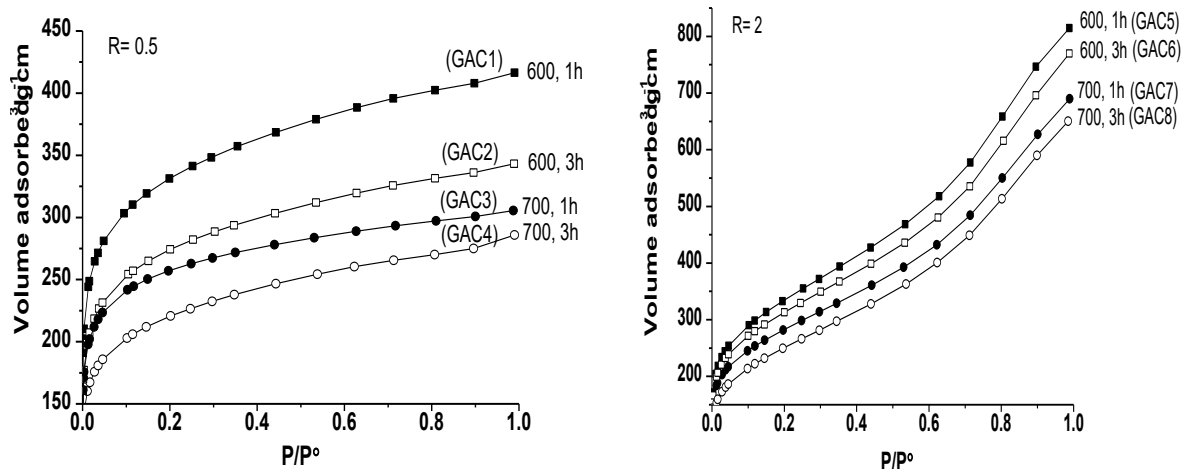


Fig. 1. Nitrogen adsorption isotherms of GAC samples prepared at $R=0.5$ and 2 .

Table 1. Nitrogen adsorption parameters of GAC samples.

Sample	BET surface area $\text{m}^2 \text{g}^{-1}$	* Total SA $\text{m}^2 \text{g}^{-1}$	* Micropore area $\text{m}^2 \text{g}^{-1}$ ($\text{dp} < 2 \text{nm}$)	* V_t $\text{cm}^3 \text{g}^{-1}$	* V_{meso} $\text{cm}^3 \text{g}^{-1}$	* V_{micro} $\text{cm}^3 \text{g}^{-1}$	* dp MAX nm	* dp nm
GAC1	1212.4	1505	1210	0.619	0.200	0.419	1.289	1.289
GAC2	998.5	1279	1049	0.510	0.164	0.346	1.328	1.289
GAC3	802.0	1030	835	0.421	0.149	0.272	1.289	1.289
GAC4	951.0	1300	1143	0.456	0.101	0.355	1.276	1.289
GAC5	1172.0	1207	482	1.171	0.972	0.199	1.646	1.686
GAC6	1106.8	1159	486	1.095	0.894	0.201	1.7	1.487
GAC7	990.8	1081	492	0.984	0.806	0.178	1.6	1.646
GAC8	984.9	1075	472	0.971	0.797	0.174	1.48	1.567

V_t = total pore volume; V_{mic} = micropores ($< 2 \text{ nm}$); V_{mes} = mesopores ($2\text{-}50 \text{ nm}$); dp MAX = pore diameter maxima in nm; dp = pore diameter; * = NLDFT cylindrical pore model.

Pore size distribution data were obtained by using nonlinear density function theory (NLDFT) adopting the cylindrical pore model and are presented in Table 1. Predominant micropores were observed over mesopores in GAC samples produced at $R=0.5$, whereas systematic development of mesoporosity was observed in GAC samples prepared at $R=2$. Further, an increase in the activation temperature (T_c) decreased the micropore volume in the studied GAC samples. The total pore volume and pore diameter (dp) were increased with the increase in R value (Table 1). The BET surface area was found to be high in 600°C -activated samples, whereas the BET surface area of GAC samples activated at 700°C was lower at a given R value. This decrease in the surface area is associated with pore collapse most probably caused by the heat treatment [29]. The surface area and pore size distribution results suggest that pores were developed with different sizes during the activation of the prepared GAC samples.

SEM studies

Textural properties of synthesized GAC samples were studied through SEM analysis. The micrographs at $R=0.5$ and 2 for $T_c = 600$ or 700°C , respectively, are presented in Fig. 2. At $R=0.5$, the influence of T_c and t_c on the textural properties of GAC samples is shown in Fig. 2a to c. Formation of pores with elliptical shape with pore diameter about $2 \mu\text{m}$ was observed for $T_c = 600$ or 700°C (Fig. 2a, b) at $t_c = 1 \text{ h}$, whereas, the elliptical-shaped pores with larger size ($4 \mu\text{m}$) were observed at $t_c = 3$

h and $T_c = 700^\circ\text{C}$ (Fig. 2c, GAC4). The results suggest that pore-widening process took place with the increase in T_c from 600 to 700°C and with increase in t_c from 1 h to 3 h .

Slit-like pores with the size of opening between 10 and $13 \mu\text{m}$ and width between 3 and $7 \mu\text{m}$ were observed at $R=2$ (Fig. 4, GAC8). Further, the widening process transformed elliptical-shaped pores to slit-shaped pores for the GAC samples produced at $R=2$ and $T_c = 700^\circ\text{C}$. Pores development in the GAC samples was associated with the removal of ZnCl_2 residues and other impurities such as ZnO during the washing and activation process. In addition, only 16% of ZnCl_2 was recovered after the activation and washing process for GAC4 sample which suggests that the removal of ZnCl_2 is intensified by means of evaporation at heat treatment of 700°C for 3 h at $R=0.5$ [26].

At $R=2$, smooth melt structure was observed in the images and the presence of this melt would reduce the surface pores area of the GAC samples. Under identical T_c and t_c the removal of ZnCl_2 and ZnO impurities was intensified in samples produced at $R=0.5$ compared to samples prepared at $R=2$ [26]. Activation of GACs above 700°C resulted in caking and agglomeration on the char structure and thus produced chars with an intact external surface [30]. The SEM images are in agreement with pore size distribution studies, wherein slit-like mesopores were observed for GAC samples produced at $R=2$.

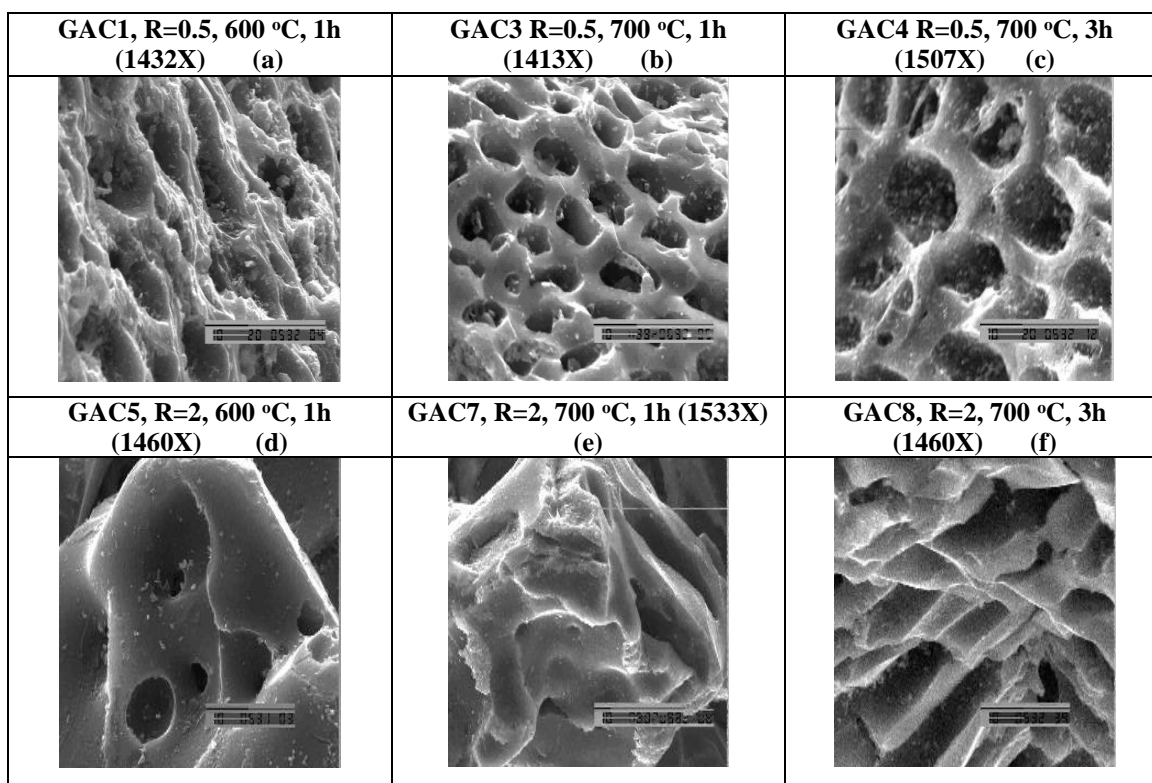


Fig. 2. SEM micrographs of the GAC samples prepared by different activation processes

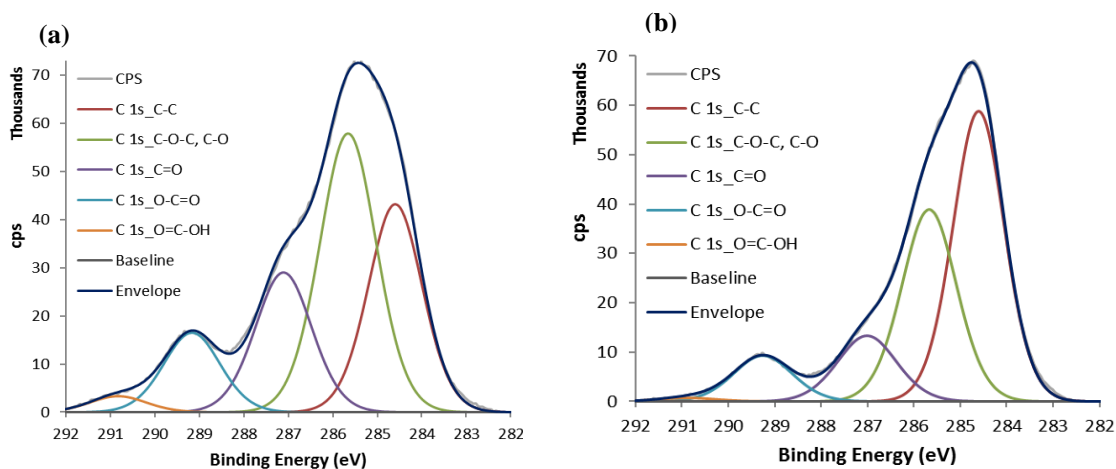


Fig. 3. XPS analysis of (a) GAC4 and (b) GAC8 samples.

Boehm titration results

Acid and base surface functional groups of the prepared GAC samples were accessed through Boehm titrations and the data are presented in Table 2. Principally, three types of acid functional groups are known in activated carbons such as carboxylic, lactonic and phenolic groups. Similar acid functional groups were observed in the studied GAC samples after different activation processes. Nevertheless, GAC samples produced at lower R values showed a greater amount of total surface functional groups per microporous surface area

compared to GAC samples prepared at higher R values. Further, acid groups were predominant over base groups in the studied GAC samples. The result suggests that all the GAC samples are acidic in character.

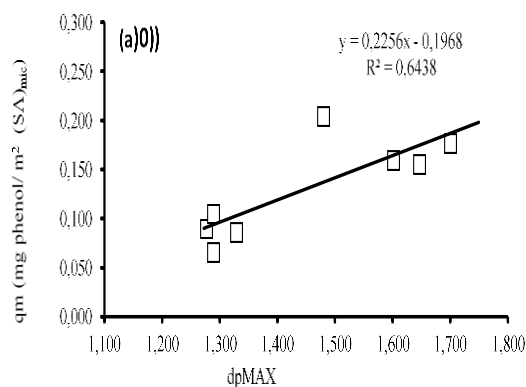
XPS results

C1s XPS results of GAC4 and GAC8 samples are presented in Fig. 3.

These samples show a broad pattern in the binding energy region of 282-292 eV. The Shirley deconvolution yielded five chemically-shifted signals centered at 284.6, 285.8, 287.1, 289.3 and

N. Pasupulety et al.: On the role of texture and physicochemical characteristics on adsorption capacity of granular ...
 290.9 eV, respectively. The signal at 284.6 eV was ascribed to sp^3 carbon present in GAC.

Four more carbon-related components at 285.8, 287.1, 289.3 and 290.9 eV were assigned to -C-O, carbonyl (-C=O), carboxylate (-O-C=O) and carboxyl (-COOH) functionalities, respectively. Presence of sp^3 carbon suggests the existence of unoxidized domains in the prepared samples. These results were in agreement with Boehm titrations wherein acid-base functional groups were detected. It is clear from the XPS results that transformation of unoxidized domains to oxidized functional groups was intensified at a lower R value ($R=0.5$) compared to the higher R value ($R=2.0$) during the activation at 700 °C for 3 h. It is associated with



removal of $ZnCl_2$ and other zinc impurities from the samples during the activation process.

Phenol removal by GAC samples

GACs used for phenol adsorption measurements had an average grain size of 1.50 mm. Surface diffusivity and faster adsorption rate can be attributed to the lower internal mass transfer resistance of the adsorbent due to its large pore size [31]. Phenol molecule size was reported between 0.46 and 0.55 nm [32]. Critical pore diameter (dp critical) for phenol adsorption on GACs was estimated by plotting the graph between dp MAX and Langmuir adsorption capacity (q_m) per micropore surface area.

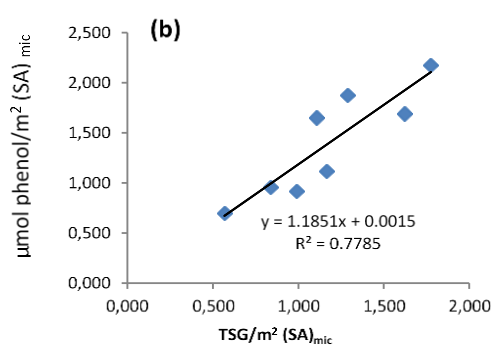


Fig. 4 (a) Critical pore diameter of GACs in phenol adsorption; (b) TSG *versus* phenol adsorption capacity of GACs.

Solving the linear equation in Fig. 4a led to the dp critical value of 0.87 nm. The estimated dp critical value is much higher than the phenol molecule size. In addition, the micropore volume was found to be high in GACs prepared at $R=0.5$ compared to $R=2$ (Table 1). For GAC1 to 4, the pore diameter was about 1.289 nm and the amount of these pores were found high in these samples compared to GAC5 to 8. Hence, greater adsorption capacity for phenol was observed.

Fig. 4b shows the correlation between phenol adsorption capacity and total surface functional groups. Linear regression was used to calculate the correlation coefficient (R^2). The obtained R^2 value was about 0.778, which suggests that adsorbent surface functional groups are vital for the adsorption of phenol in solution. The Boehm titration results in Table 2 clearly demonstrate that development of surface function groups was facile at $R=0.5$ compared to $R=2.0$. Moreover, phenol is a weak acid and the surface with a greater number of basic functional groups can adsorb a greater amount of phenol than other surfaces with a

smaller number of basic functional groups. Hence, GAC2 and GAC4 samples with adequate surface basicity with greater total surface functional groups (TSG) have exhibited greater phenol adsorption capacity.

DBT and 4,6-DMDBT removal by GAC samples

GACs used for sulfur adsorption measurements had an average grain size of 1.0 mm. DBT and 4,6-DMDBT molecule size was reported approximately in the range of 0.70 to 0.80 nm [33].

The estimated critical pore diameter for DBT and 4,6-DMDBT was about 0.71 and 0.97 nm, respectively, from the linear regression equations in Fig. 5a. It is clear from Tables 1 and 2 data that DBT adsorption is high on GAC1 to 4 samples which have a greater amount of micropores with pore diameter of 1.289 nm. Further, the graph between TSG of GACs *versus* sulfur adsorption data in Fig. 5b yielded R^2 value of 0.70 which is less than phenol R^2 value. The result reveals that there is a hindrance for DBT adsorption on GACs due to its bulkiness. Further, the dp critical value for DBT adsorption on GACs (0.71 nm) is close to

N. Pasupulety et al.: On the role of texture and physicochemical characteristics on adsorption capacity of granular ... the molecular size of DBT which also indicates strain in its adsorption. Hence, the adsorption tendency for DBT is less than for phenol on GACs under identical adsorption conditions. In case of 4,6-DMDBT the estimated critical pore diameter was about 0.97 nm (Fig. 5a, triangles). The plot between TSG of GACs *versus* sulfur adsorption capacity in Fig. 5c produced R² value of 0.69, which is slightly less than DBT R² value. It is obvious from the results that the methyl groups

present on DMDBT slightly increased the adsorption resistance on GACs (Table 2).

Therefore, samples with a greater number of mesopores (GAC5 to 8) showed greater adsorption tendency for 4,6-DMDBT. Furthermore, SEM analysis revealed ordered elliptical-shaped pores for GACs prepared at R=0.5 which are favorable for phenol and DBT adsorption. On the other hand, at R=2.0 slit-shaped pores developed in samples GAC5 to 8 seem to be advantageous for 4,6-DMDBT adsorption in solution.

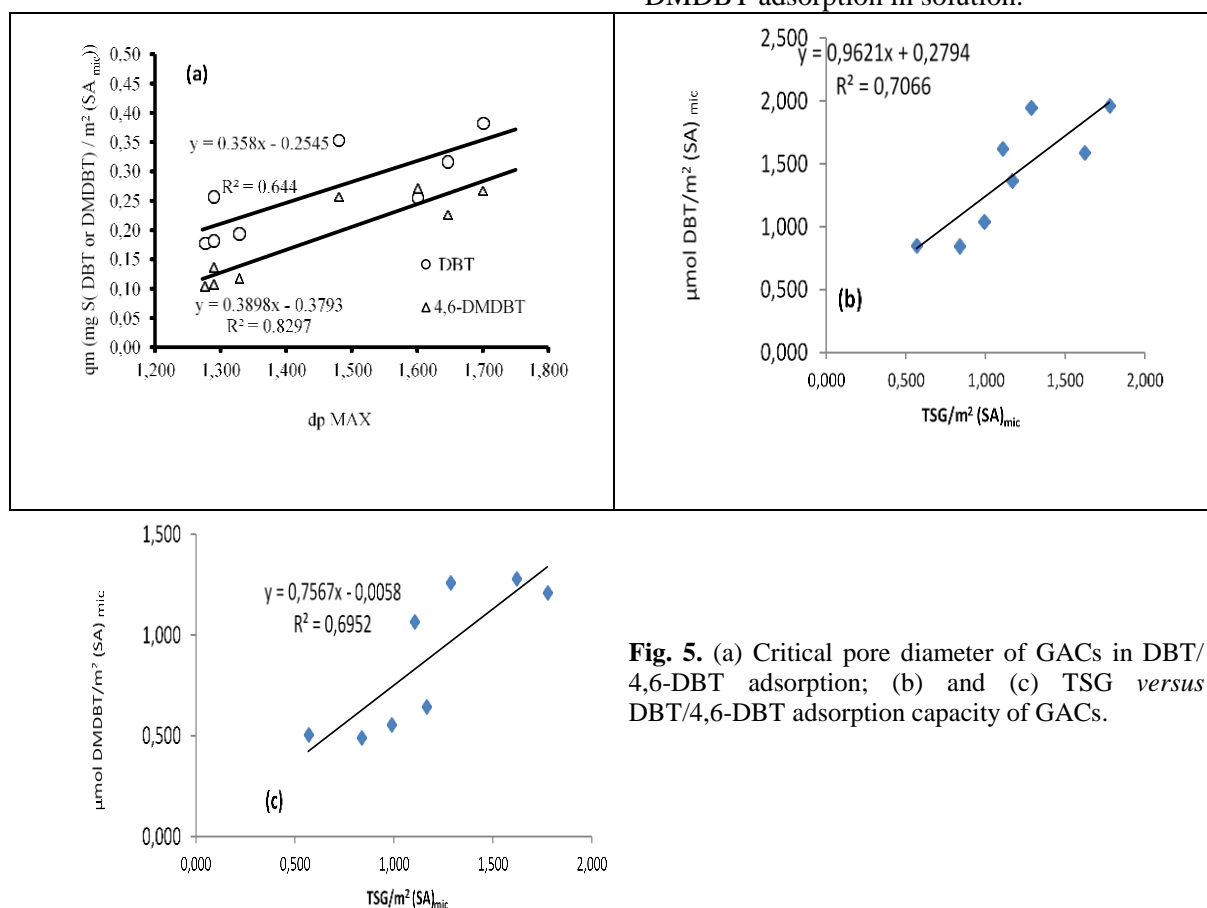


Fig. 5. (a) Critical pore diameter of GACs in DBT/4,6-DBT adsorption; (b) and (c) TSG *versus* DBT/4,6-DBT adsorption capacity of GACs.

CONCLUSIONS

Elliptical-shaped pores were developed in GACs prepared at R=0.5. GACs prepared at R=0.5 have a greater amount of micropores favorable for adsorption of phenol and DBT in solution. Slit-shaped pores were developed in GACs obtained at R=2.0. These samples were rich in mesopores beneficial for 4,6-DMDBT adsorption in solution. GAC samples produced at a lower R value showed a greater amount of total surface functional groups compared to GAC samples prepared at a higher R value. Hence, the removal performance of phenol

was found high on GACs prepared at R=0.5. However, slight hindrance in adsorption of DBT and 4,6-DMDBT was observed on GACs due to the bulkiness of the molecules.

Acknowledgements: This work was supported by the Deanship of Scientific Research (DSR), King Abdulaziz University, Jeddah, under grant no.(D-090-135-1439). The authors, therefore, gratefully acknowledge the DSR technical and financial support.

Table 2. Boehm titration results and Langmuir adsorption capacity of GAC samples.

Sample	Carboxylic mM g ⁻¹	Lactonic mM g ⁻¹	Phenolic mM g ⁻¹	Base mM g ⁻¹	Total surface groups (TSG)	q _m (mg g ⁻¹) phenol	q _m (mg g ⁻¹) DBT	q _m (mg g ⁻¹) 4,6- DMDBT
GAC1	0.327	0.283	0.083	0.099	0.792	79.72	38.01	19.59
GAC2	0.407	0.284	0.110	0.253	1.054	104.80	35.01	18.64
GAC3	0.219	0.273	0.233	0.234	0.959	87.88	36.56	17.32
GAC4	0.357	0.271	0.048	0.299	0.975	103.00	35.00	18.06
GAC5	0.179	0.282	0.195	0.066	0.722	74.93	26.87	16.48
GAC6	0.260	0.298	0.013	0.208	0.779	85.99	33.31	19.61
GAC7	0.356	0.282	0.022	0.199	0.859	78.35	21.89	20.19
GAC8	0.289	0.252	0.151	0.219	0.911	96.57	29.63	18.32

REFERENCES

1. K. Gergova, S. Eser, *Carbon*, **34**, 879 (1996).
2. C.A. Philip, B.S. Girgis, *J. Chem. Technol. Biotechnol.*, **67**, 248 (1996).
3. A.A.M. Daifullah, B.S. Girgis, *Water Res.*, **32**, 1169 (1998).
4. C.A. Toles, W.E. Marshall, M.M. Johns, *J. Chem. Technol. Biotechnol.*, **72**, 255 (1998).
5. C.A. Toles, W.E. Marshall, M.M. Johns, *Carbon*, **37**, 1207 (1999).
6. M. Ahmedna, W.E. Marshall, R.M. Rao, *Bioresour. Technol.*, **71**, 113 (2000).
7. R.S. Juang, F.C. Wu, R.L. Tseng, *J. Colloid Interface Sci.*, **227**, 437 (2000).
8. Y.L. Diao, W.P. Walawender, L.T. Fan, *Bioresour. Technol.*, **81**, 45 (2002).
9. L.J. Kennedy, J.J. Vijaya, G. Sekaran, *Ind. Eng. Chem. Res.* **43**, 1832 (2004).
10. S. Nagano, H. T. Tamon, T. Adzumi, K. Nakagawa, T. Suzuki, *Carbon*, **38**, 915 (2000).
11. K. Nakagawa, T. Sugiyama, S.R. Mukai, H. Tamon, Y. Shira, W. Tanthapanichakoon, *J. Chem. Eng. Jpn.*, **37**, 889 (2004).
12. F. Rozada, M. Otero, A. Moran, A.I. Garcia, *J. Hazard. Mater.* **124**, 181(2005).
13. V. Boonamnuyvitaya, S. Sae-ung, W. Tanthapanichakoon, *Sep. Purif. Technol.*, **42**, 159 (2005).
14. F.S. Zhang, J.O. Nriagu, H. Itoh, *Water Res.*, **39**, 389 (2005).
15. B.S. Girgis, A.A. Attia, N.A. Fathy, *Colloids Surf. A.*, **299**, 79 (2007).
16. J.D. Webb, S. MacQuarrie, K. McEleney, C.M. Crudden, *J. Catal.*, **252**, 97 (2007).
17. X.L. Tang, J.M. Hao, H.H. Yi, J.H. Li, *Catal. Today*, **126**, 406 (2007).
18. H. Marsh, in: Activated Carbon Compendium: A collection of papers from the journal Carbon 1996–2000. Elsevier, Amsterdam, 2001.
19. C. Moreno-Castilla, M.A. Alvarez-Merino, M.V. Lopez-Ramon, J. Rivera-Utrilla, *Langmuir*, **20**, 8142 (2004).
20. M. F. R. Pereira, S. F. Soares, J. J. M. Orfao, J. L. Figueiredo, *Carbon*, **41**, 811 (2003).
21. C. Moreno-Castilla, *Carbon*, **42**, 83 (2004).
22. B.S. Girgis, A.N.A. El-Hendawy, *Microporous Mesoporous Mater.*, **52**, 105 (2002).
23. Y. A. Alhamed, *J. Hazard. Mater.*, **170**, 763 (2009).
24. M. Smisek, S. Cerny, in: Active Carbon: Manufacture, Properties and Applications, Elsevier, Amsterdam, 1970.
25. Q.R. Qian, M. Machida, H. Tatsumoto, *Bioresource Technol.*, **98**, 353 (2007).
26. Y. A. Alhamed, *Bulg. Chem. Commun.*, **40**, 26 (2008).
27. R. C. Bansal, M. Goyal, in: Activated Carbon Adsorption, Taylor & Francis Group, London, 2005.
28. A.M. Warhurst, G.D. Fowler, G.L. McConnachie, S.J.T. Pollard, *Carbon*, **35**, 1039 (1997).
29. M.A. Al-Omair, E.A. El-Sharkawy, *Environ. Technol.*, **28**, 443 (2007).
30. A. Ahmadpour, D.D. Do, *Carbon*, **35**, 1723 (1997).
31. S. Haji, C. Erkey, *Ind. Eng. Chem. Res.*, **42**, 6933 (2003).
32. L.- G. Ewa, *Adsorption*, **22**, 599 (2016).
33. Z. Wenwu, L. Meifang, Z. Yasong, W. Qiang, Z. Qing, *Energy & Fuels*, **31**, 7445 (2017).

Study of degradation phenomenon for transmission lubricants

I. Radulescu*, A. V. Radulescu

University Politehnica Bucharest, 313 Spl. Independentei, Sector 6, 060042 Bucharest, Romania

Received December 9, 2018; Revised March 14, 2019

Lubricants degradation process is quantified by the changes in physical characteristics and chemical composition of oils, which are caused by internal and external factors and the severity of operating conditions. Experimental methods for determining the degree of lubricants wear and their durability led to the development of a methodology for the assessment and the quantification of lubricants life cycle.

The degradation phenomenon of two transmission lubricants was investigated using physico-chemical, rheological and microscopic methods. For comparison, the lubricants were tested in fresh state and used state.

The rheological measurements were performed on a Brookfield viscometer CAP2000+ equipped with cone-and-plate geometry, for a temperature range between 20 ... 70°C, using the viscometer Peltier system. For the microscopic tests a transmission electron microscope JEOL Japan - JEM - 200 CX was used, in order to obtain information on the wear particles shape and concentration.

The experiments have shown that the wear degree of the lubricant influences the rheological behavior of the tested samples over the whole range of temperatures and determines the presence of specific wear particles in used lubricants.

Keywords: Lubricant, Degradation, Rheology, Microscopy

INTRODUCTION

The lubricants degradation is a quantified process, by using physical characteristics and changes in chemical composition of oils; these are caused by internal and external factors and by the severity of operating conditions. The degradation of lubricants during time is due to the mechanical loads, to the operating temperature and contamination; the result is the lubrication deterioration and the worsening of other functions (providing cooling parts, their corrosion protection, etc.). The degradation process is progressive and it is more intense if the service conditions are more severe. There is a variety of external factors involved in determining of the lubricants degradation and their disuse [1–3]:

- the contamination with different impurities or chemical agents during the usage, transport or storage;
- the mechanics of thermal overstressing;
- the possibility of increased aeration and water penetration into the oil in bigger quantity.

The consequence of reported changes is the shortened lubricant use, which is associated, in some cases, with endangering the safety of the equipment. The problem of a long use of industrial lubricants is transposed over the existence of a life cycle, which is economically satisfactory. The lubricants choice affects the longer use of the production equipment and life cycle costs [4].

The basic physical and chemical characteristics of the lubricant quality do not always reach the limit values at the oil drain interval and the

transmission oil is still suitable for future use. Knowing the chemical characteristics and intensity of the wear products on lubricant, it is possible to evaluate the transmission performance parameters to determine the optimized oil change intervals [5, 6].

One of the most important factors for lubricant degradation is the modification of the rheological properties at different temperatures [7]. Rheological modeling of lubricants has always been a subject of great importance when working with oil from different fields of interest. The need for predicting the rheological behavior of lubricants when experiencing conditions outside the available measuring range for the equipment designed in accordance with API specifications has always been present [8, 9]. Another indicator for the deterioration of operational characteristics of the transmission oils is the occurrence of the oxidation phenomenon, which takes place through the formation of oxidized aliphatics. The increase in acidity changes the structure and lubricating properties of the oil, even in the presence of commercial additives [10, 11].

During the operation of the mechanical transmission, the wear particles of organic (hydrocarbon) and inorganic (wear debris) products represent one of the main types of oil contamination [12, 13]. In order to monitor the presence of such particles in the lubricant, the transmission electron microscopy (TEM) and selected area electron diffraction (SAED) methods can be used [14–16].

The purpose of this paper is to investigate the rheological properties of two transmission

* To whom all correspondence should be sent:
E-mail: irena_sandu@yahoo.com

lubricants for motorcycle gearboxes (75W90 and 75W140), in fresh and used state, correlated with the oxidation phenomenon and the presence of the contaminated particles in the oils.

THEORY

The rheological model proposed for the prediction of the lubricant behaviour is based on Cross equation [17–20], which can be found on virtually every research rheometer software package and it can be used to extract some meaningful numbers from the “full” viscosity *versus* shear rate profile:

$$\eta = \eta_{\infty} + \frac{\eta_0 - \eta_{\infty}}{1 + (\lambda\dot{\gamma})^m}$$

where:

- $\dot{\gamma}$ – shear rate;
- η – viscosity at any given shear rate $\dot{\gamma}$;
- η_0 – zero shear viscosity representing the magnitude of the viscosity at the lower Newtonian plateau;
- η_{∞} – infinite shear viscosity;
- λ – Cross time constant which has dimensions of time;
- m – dimensionless rate constant indicating the degree of dependence of the viscosity on shear rate in the shear-thinning region.

Concerning the thermal model assumed for the variation of the rheological parameters of the studied lubricants, three possibilities have been considered [21]:

Jarchov and Theissen model:

$$\eta = \eta_{50} e^{B \frac{50-t}{95+t}}$$

where:

- η – lubricant apparent viscosity;
- η_{50} – lubricant apparent viscosity at 50 °C;
- B – non-dimensional parameter;
- t – temperature.

Cameron model:

$$\eta = K e^{\frac{b}{95+t}}$$

where:

- η – lubricant apparent viscosity;
- K – viscosity parameter;
- b – temperature parameter;
- t – temperature.

Reynolds model:

$$\eta = \eta_{50} e^{m(t-50)}$$

where:

- η – lubricant apparent viscosity;
- η_{50} – lubricant apparent viscosity at 50 °C;
- m – temperature parameter;
- t – temperature.

In order to obtain the main values of the characteristic parameters specific for Cross model (Eqn. 1) and for all three thermal models (Eqns. 2, 3 and 4), the experimental data were numerically treated using the regression analysis method [22–25].

EXPERIMENTAL

The rheological measurements were performed on a Brookfield viscometer CAP2000+ equipped with cone-plate geometry and using a Peltier system for controlling the temperature. The CAP 2000+ Series viscometers are medium to high shear rate instruments with integrated temperature control of the test sample material. Concerning the technical parameters of the viscometer, rotational speed selection ranges from 5 to 1000 rpm. Temperature control of sample is possible between either 5°C (or 15°C below ambient, whichever is higher) and 75°C. The viscometer uses a Capcalc32 software for complete control and data analysis. A “velocity imposed gradient” test was used at the room temperature of 20°C. The experimental test consists of a load from the 10 s⁻¹ to 13333 s⁻¹ shear rate gradient, followed by an unload in order to highlight the thixotropy of the lubricant - “shear memory”.

For the microscopic tests a transmission electron microscope JEOL Japan - JEM - 200 CX was used, in order to obtain information on the wear particles shape and concentration. The main characteristic parameters of the microscope are: 2),

- lattice resolution [Å]: 1.4;
- point-to-point resolution [Å]: 2.6;
- acceleration voltage [kV]: 80, 100, 120, 160, 200;
- magnification: ×1000 to ×300000.

Oil samples were allowed to decant by sampling the densest part. The extracted sample was dropped in a small size crucible and washed several times with heptane to remove the fatty portion. The heptane treatment (washing) was done until the traces of oil had completely disappeared, so that the useful sample could be inserted into the electron microscope without danger for the high vacuum in the column. Remaining part: additions, impurities, deposits from wear representing the sample of interest was prepared for electronic microscopy.

The main steps to sample preparation for TEM + SAED were:

- the non-fat part was mixed with ethyl alcohol and deposited on special microscope grids, 3 mm in diameter, of Cu or Ni covered with C;
- some of the grids were covered/overshadowed with a very thin layer of C in a JEOL vacuum evaporation installation for fastening in the beam and for increasing the contrast.

The method is used for particle systems less than 10 μm. Particle studies also involve the determination of the existing phase, which can be highlighted by electron diffraction on a selected area (SAED). The advantage, compared to X-ray diffraction, is the possibility of showing particles found in the sample in extremely small quantities (<<0.1% or even a single group of particles).

Table 1. Physicochemical properties of fresh lubricants

Parameter	Lubricant	75W 90	75W 140
Density at 15°C (59°F) ASTM D1298		900 kg/m ³	906 kg/m ³
Kinematic viscosity at 40°C (104°F) ASTM D445		72.6 mm ² /s	170 mm ² /s
Kinematic viscosity at 100°C (212°F) ASTM D445		15.2 mm ² /s	24.7 mm ² /s
Viscosity index VIE ASTM D2270		222	178
Flash point ASTM D92		200°C	212°C
Pour point ASTM D97		-60°C	-36°C

The lubricants used for testing are two transmission lubricants (75W90 and 75W140), in fresh and used state (2000 km). These are 100%

synthetic extreme pressure lubricants, characterised by an efficient antiwear protection, with a better resistance at high temperature and a longer life time. The lubricants are specially designed for racing vehicle gearboxes, synchronised or not synchronised gearboxes, gearbox/differential, transfer gearboxes and hypoid differentials. The physical and chemical properties of the lubricants in fresh state, offered by the manufacturer, are presented in Table 1.

RESULTS AND DISCUSSION

The first stage of the experiment was focused on the influence of the wear degree of the lubricant on its rheological properties. The rheograms (Figure 1) are obtained by plotting viscosity as a function of the shear rate, as an average of three points, using the Capcalc32 software specific for the viscometer. Analysing the rheograms from Figure 1, it can be seen that all the lubricants, in fresh or used state, do not exhibit any thixotropic behaviour. For lubricant 75W90, there is almost no difference between fresh state and used state, both of them having the same viscosity for the whole range of the investigated shear rates. Regarding the lubricant 75W140, there is a significant difference between the two states, observing that the viscosity of used lubricant is always smaller than of the fresh one, for any shear rate in the considered field.

The corresponding rheological parameters for both the lubricants in fresh and used state, according to the Cross model (Eqn. 1), are presented in Table 2.

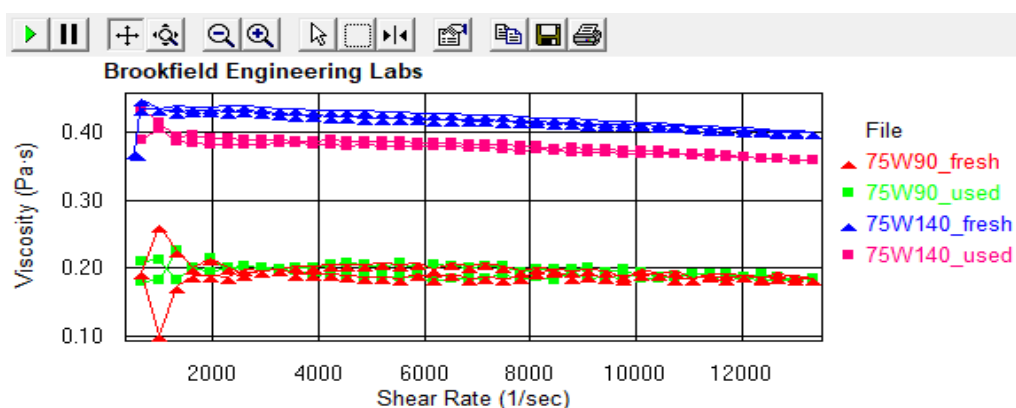


Figure 1. Rheograms for 75W90 and 75W140 oils in fresh and used state

Table 2. Parameters of the Cross model for the transmission lubricants in fresh and used state

Type of oil	Wear degree	Cross model			
		η_{∞} , Pa·s	η_0 , Pa·s	λ , s	m
75W90	fresh	0.153	0.229	$7.595 \cdot 10^{-4}$	0.065
	used	0.118	0.307	$3.057 \cdot 10^{-3}$	0.175
75W140	fresh	0.257	0.628	$1.725 \cdot 10^{-3}$	0.104
	used	0.220	0.574	$1.753 \cdot 10^{-3}$	0.095

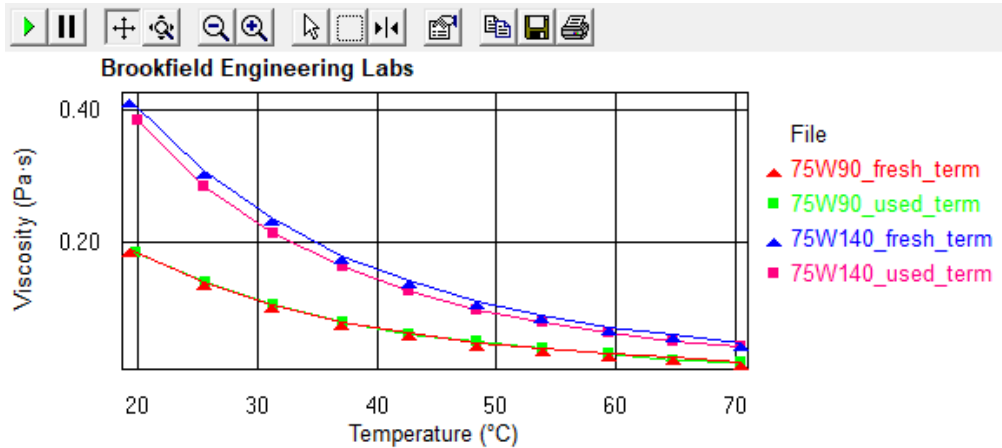


Figure 2. Variation of the apparent viscosity with temperature for 75W90 and 75W140 oils, in fresh and used state

Table 3. Variation of the rheological parameters of lubricants with temperature

Parameter		Jarchov and Theissen model			Cameron model			Reynolds model		
		η_{50} , Pa·s	B	Corr. coeff.	K , Pa·s	b , °C	Corr. coeff.	η_{50} , Pa·s	m , °C ⁻¹	Corr. coeff.
75W90	Fresh	0.0446	5.419	0.998	$1.979 \cdot 10^{-4}$	785.75	0.998	0.0435	-0.0473	0.999
	Used	0.0446	5.517	0.997	$1.776 \cdot 10^{-4}$	799.97	0.997	0.0432	-0.0478	0.999
75W140	Fresh	0.1043	5.232	0.998	$5.572 \cdot 10^{-4}$	758.58	0.998	0.1021	-0.0454	0.999
	Used	0.0919	5.520	0.999	$3.678 \cdot 10^{-4}$	800.46	0.999	0.0899	-0.0477	0.998

Table 4. Chemical properties of tested oils

Type of oil	Wear degree	Acidity value, mg KOH/g	Total Base Number, mg KOH/g
75W90	fresh	1.62	11.30
	used	1.64	11.38
75W140	fresh	1.71	11.54
	used	1.79	12.01

In order to investigate the influence of the lubricant wear degree on the apparent viscosity, a supplementary thermal test was performed. Figure 2 presents the variation of the apparent viscosity with the temperature, for both lubricants in fresh and used state, at a constant shear rate of 13333 s^{-1} . It can be seen that for 75W90 oil, there are almost no differences between fresh and used lubricant, while the oil 75W140 presents significant changes in used state comparative to fresh state.

Table 3 shows the values of the thermal rheological parameters of the studied lubricants, according to Jarchov and Theissen, Cameron and Reynolds models (Eqns. 2, 3 and 4). Analysis of the data from this table reveals that all three proposed models are appropriate to approximate the variation of the apparent viscosity with temperature, having values of the correlation coefficient almost equal to 1.

The explanation for the changes of the rheological properties of 75W90 and 75W140 oils

I. Radulescu, A. V. Radulescu: Study of degradation phenomenon for transmission lubricants

during the working period can be found by analyzing two of the most important chemical properties of the oils (see Table 4): Acidity value (ASTM D664) and Total Base Number (ASTM D2896).

It can be seen that for the oil 75W90 there is almost no change in acidity number and total base number during the entire operating period. This observation is directly correlated with the rheological and thermal behavior of the oil, in fresh and used state, for the whole range of shear rates and temperatures investigated.

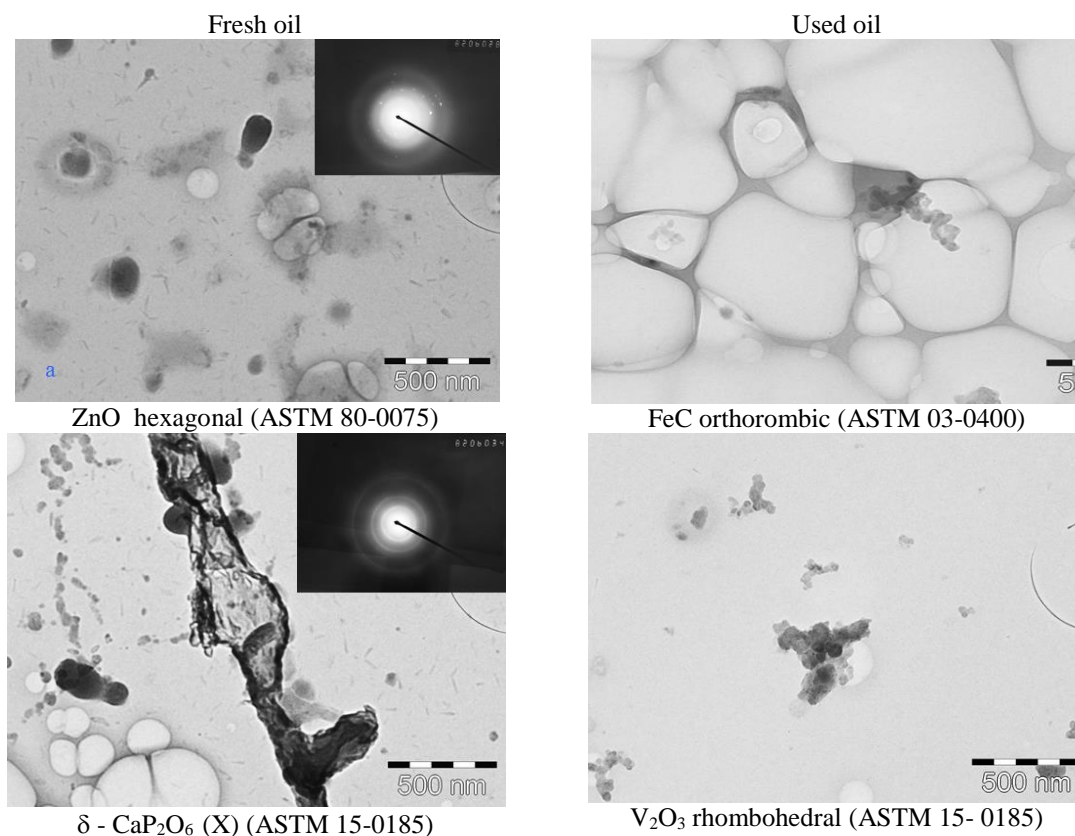
For the oil 75W140, which clearly showed differences for thermal and rheological properties between fresh and used state, this presents an increasing trend in acidity and alkalinity (total base number).

Regarding the wear particles' shape and concentration identified in fresh and used oil,

electronic microscopy was used. For both oils, 75W90 and 75W140, in fresh and used state, the same type of particles was identified:

- type of solid particles identified in fresh lubricant: ZnO hexagonal (ASTM 80-0075), δ -CaP₂O₆ (X) (ASTM 15-0185) and amorphous phase (Table 5);
- type of solid particles identified in used lubricant: FeC orthorhombic (ASTM 03-0400), V₂O₃ rhombohedral (ASTM 15-0185), Fe_{0.11}V₂O_{5.15} orthorhombic (ASTM 82-1871), SiO₂ hexagonal (ASTM 83-2187) and amorphous phase (Fig. 3).

Based on this microscopic analysis, it can be concluded that the presence of the solid particles in lubricants does not affect their rheological properties.



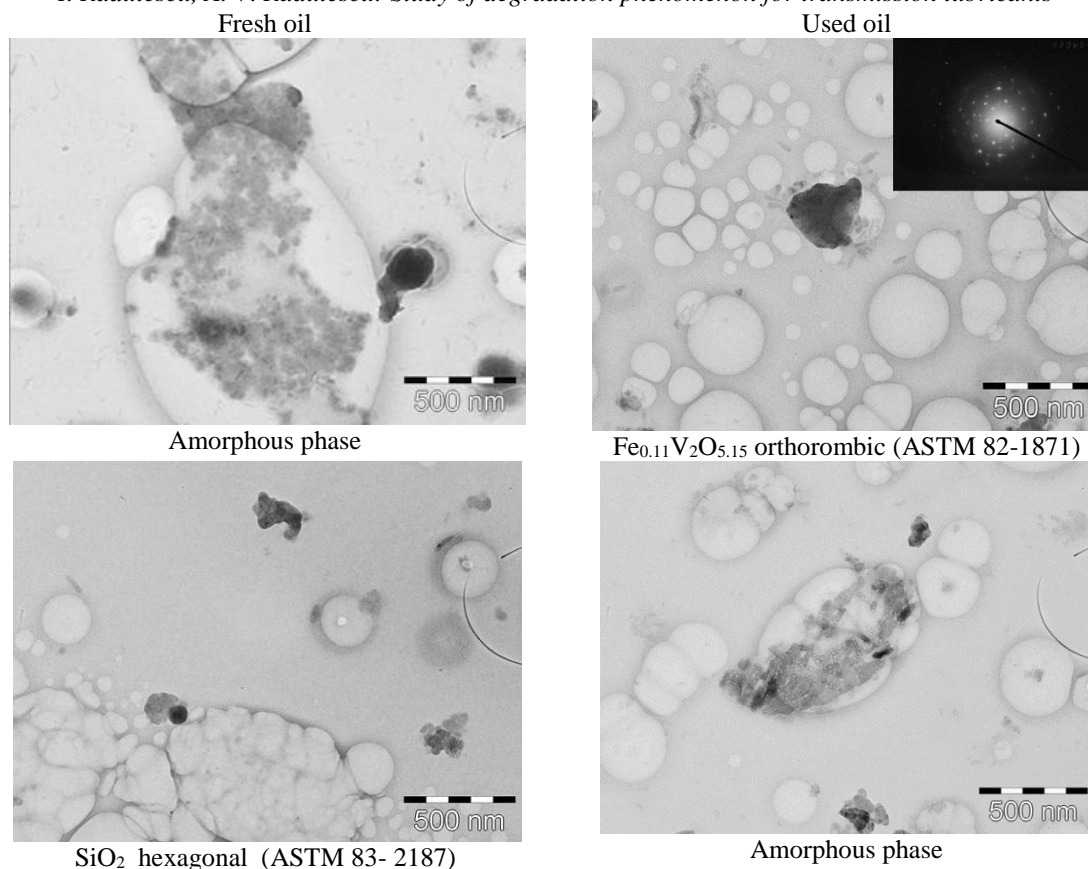


Fig. 3. Structural composition of fresh and used transmission oils.

CONCLUSIONS

The present paper investigated the rheological and chemical properties of two transmission lubricants for motorcycle gearboxes (75W90 and 75W140), in fresh and used state, correlated with the identification of the contaminated particles in the oils.

It was found that the lubricants do not exhibit a yield stress and thixotropy and that, above a critical shear rate, they exhibit shear-thinning behaviour, well described by the Cross model.

For lubricant 75W90, there is almost no difference between fresh state and used state, both of them having the same viscosity for the whole range of the investigated shear rates and the same thermal rheological parameters.

Regarding the lubricant 75W140, there is a significant difference between the two states, observing that the viscosity of the used lubricant is always lower than for the fresh one, for any shear rate in the considered field. The same conclusion is valid also for its thermal rheological parameters.

All three proposed models, which approximate the variation of the apparent viscosity with temperature (Jarchov and Theissen, Cameron and Reynolds), are appropriate for both lubricants, in fresh and used state.

The determination of the parameters for the rheological Cross model and also their variation with temperature is very useful to model the functioning of different friction couples, using the thermo-hydrodynamic theory of lubrication based on Reynolds equations.

There is a direct connection between the modification of the rheological properties of the lubricants in fresh and used state and the changes of their chemical properties (Acidity value and Total Base Number).

The presence of the solid particles in lubricants does not affect their rheological properties, but they are a clear indicator of the wear degree of lubricants. It is necessary to perform supplementary investigations in this direction, in order to connect the existence of the wear particles with the tribological properties of lubricants.

REFERENCES

1. G. E. Totten, S. R. Westbrook, R. J. Shah, Fuels and Lubricants Handbook: Technology, Properties, Performance, and Testing, ASTM International, 2003.
2. T. Mang, W. Dresel, Lubricants and lubrication, Wiley-VCH Verlag GmbH, Weinheim, 2007.
3. Z. Pawlak, Tribochemistry of lubricating oils, vol. 45, Elsevier, 2003.
4. J. D. Summers-Smith, A Tribology Casebook – A Lifetime in Tribology, Mechanical Engineering &

- Bury St. Edmunds Publications, London, Great Britain, 1997.
5. L. R. Rudnick, Synthetics, mineral oils and bio-based lubricants: chemistry and technology. CRC press, 2005.
 6. A. Wolak, G. Zajac, *Measurement*, **113**, 53 (2018).
 7. A. V. Radulescu, I. Radulescu, C. Georgescu, L. Deleanu, *Bulg. Chem. Commun.*, **48** (E2), 333, 2016.
 8. D. Levi, Z. Stoynov, D. Vladikova, *Bulg. Chem. Commun.*, **49** (C), 254, 2017.
 9. ***, Specification for Materials and Testing for Well Cements, 5th edn., API Spec., vol. 10, American Petroleum Institute, Dallas, TX, USA, 1990.
 10. S. Q. Rizvi, Lubricant Chemistry, Technology, Selection, and Design, West Conshohocken, ASTM International, 2009.
 11. R. Hadjikinova, M. Marudova, *Bulg. Chem. Commun.*, **48** (E2), 446, 2016.
 12. T. L. Krantz, A. Kahraman, *Tribol. T.*, **47**, 138 (2004).
 13. S. R. Perić, B. P. Nedić, D. R. Trifković, M. M. Vuruna, *Stroj. Vestn. J. Mech. E.*, **59**, 443 (2013).
 14. R. D. Evans, L. M. Karren, V. D. Craig, P. N. Harvey, *Tribol. T.*, **48**, 299 (2005).
 15. M. Patel, L. A. R. Cristy, S. Paolo, B. A. Pranesh, *Tribol. Int.*, **52**, 29 (2012).
 16. J. Ayache, L. Beaunier, J. Boumendil, G. Ehret, D. Laub, Sample preparation handbook for transmission electron microscopy: Techniques, vol. 2, Springer Science & Business Media, 2010.
 17. M. M. Cross, *J. Colloid. Interface Sci.*, **20**, 417 (1965).
 18. N. Yokoi, H. Yamada, K. Maruyama, Y. Mizukusa, A. J. Bron, J. M. Tiffany, S. Kinoshita, *Invest. Ophthalmol. Visual Sci.*, **48**, 438 (2007).
 19. C. Martinez, F. Miralles-Wilhelm, R. Garcia-Martinez, *WIT Trans. Eng. Sci.*, **60**, 61 (2008).
 20. M. Tazi, F. Erchiqui, F. Godard, H. Kaddami, A. Ajji, *J. Appl. Polym. Sci.*, **131**, 13 (2014).
 21. C. Balan, The rheology of lubricating grease, Amsterdam, The Netherlands, 2000.
 22. D. C. Crocker, How to use regression analysis in quality control, American Society for Quality Control, vol. IX, 1983.
 23. N. R. Draper, H. Smith, Applied regression analysis, vol. 326, John Wiley & Sons, 2014.
 24. J. Fox, Applied regression analysis, linear models, and related methods, Sage Publications, Inc., 1997.
 25. T. Amanzholov, B. Akhmetov, A. G. Georgiev, A. Kaltayev, R. K. Popov, D. B. Dzhonova-Atanasova, M. S. Tungatarova, *Bulg. Chem. Commun.*, **48** (E2), 109, 2016.

Analysis of the changes in the main characteristics and antioxidant properties in raspberries of "Rubin" variety depending on the altitude

S. I. Papanov^{1*}, Ek. G. Petkova², I. G. Ivanov³, St. D. Ivanova¹, D. I. Popov⁴

¹Medical University Plovdiv, Faculty of Pharmacy, 15A V. Aprilov Blvd., 4000 Plovdiv, Bulgaria

²Medical University Plovdiv, Medical College, 120 Br. Bakston Str., 4004 Plovdiv, Bulgaria

³University of food technologies Plovdiv, Technological Faculty, 26 Maritza Blvd., 4002 Plovdiv, Bulgaria

⁴Medical University Plovdiv, Faculty of Medicine, 15A V. Aprilov Blvd., 4000 Plovdiv, Bulgaria

Received December 17, 2018; Revised March 21, 2019

The study aimed at determination and analysis of total acidity (pH), titratable acidity, total polyphenols content, total anthocyanins content and DPPH antioxidant activity (radical scavenging activity) of *Rubus idaeus L. cv. Rubin* juice obtained from fruits of a variety grown in different geographical areas and altitudes in Bulgaria. Systematic approach and critical analysis of the available scientific periodicals was applied; DPPH method was used for determining the antioxidant activity (radical trapping activity). The value of pH index ranges from 2.99±0.03 to 2.75±0.03. The lowest level of common phenols 251.73 ± 0.20 mg GAE/100 mL was observed in raspberry from Banya town. Total anthocyanins were within the range of 13.79 ± 0.13 mg/100 mL (Dolna Banya town-643 m.) to 86.89 ± 0.06 mg/100 mL (Dobrihuta-1804 m.). Antioxidant activity (DPPH) has values from 37287 ± 030 mmol TE/100 ml (Uzundjovo village) to 2240.20 ± 19.10 mmol TE/100 ml (Dobrihuta-1804 m.). The antioxidant activity of raspberry juice obtained from *R. idaeus cv. Rubin* mainly depends on total anthocyanins content ($r^2 = 0.71$). The antioxidant activity significantly increases with the increase in altitude, i.e. they have a significant correlation ($r^2 = 0.81$).

Keywords: raspberry, antioxidant activity, phenols, anthocyanins.

INTRODUCTION

Rubus idaeus L. (raspberry) is a wild or cultural perennial bushy plant from *Rosaceae*, growing to a height of up to 2 meters. It is cultivated in areas with moderate climates, mainly in Europe and the USA. In the wild, raspberries grow in Europe, Asia, South America in temperate, tropical and subtropical climates [1,2]. The international tendency for cultivation and production of small edible fruits shows a permanent increase. Edible berry fruits, wild or cultivated, are proved as a traditional and rich source of bioactive compounds [3]. Many *Rubus* fruits are consumed fresh or as processed products such as juice, jams, jellies, syrups and wines [4]. The leaves and roots have been used in various medicinal applications. Recent studies have revealed that different parts of raspberry have essential positive effects on the human diet and health, which could be mainly ascribed to the presence of several health-related compounds such as organic acids, polyphenolics, tannins and sugars [2]. Fruits contain mainly 4.5 - 4.7% sugars, 1.1-2.0% organic acids (citric and malic acid), vitamin C (up to 45 mg/100 g), carotene and others compounds. In the raspberry fruits several classes of polyphenols have been identified, e.g., hydroxybenzoic acids, hydroxycinnamic acids, anthocyanins, pro-

anthocyanindins, flavonols, flavones, flavanols, flavanones, isoflavones, stilbenes and lignans. Particularly, identified polyphenols contribute substantially to the antioxidant complement of raspberry fruits, having potential health effects [5].

Raspberry (*Rubus idaeus L.*) is an important berry crop for both the fresh and the processing market. In addition to vitamins and minerals, a range of diverse polyphenols are present in the berries, including flavonoids such as anthocyanins, flavonols and flavanols, ellagitannins and ellagic acid derivatives [6]. Although genetic predisposition is the major factor influencing fruit quality, different agricultural practices, fruit maturity and environmental conditions can also affect berry metabolite amounts and composition [6]. As the harvest season progresses, climatic conditions can significantly impact on fruit quality [7]. Climatic factors such as light conditions (intensity, quality, photoperiod), temperature and precipitation can significantly affect growth and fruit quality, although there are also other abiotic and biotic stress factors [1,6,8].

The aim of the current study was the determination and analysis of total acidity (pH), titratable acidity, total polyphenols content, total anthocyanins content and DPPH antioxidant activity (radical scavenging activity) of *Rubus idaeus L. cv. Rubin* juice obtained from fruits variety grown in different geographical areas and altitudes in Bulgaria.

* To whom all correspondence should be sent:

E-mail: stoyan.papanov@abv.bg

METHODS AND MATERIALS

Raspberry samples

The present study was carried out on fruits of a set of 7 different areas collected at maturity from the main regions of raspberry cultivation (*Rubus idaeus* L cv. *Rubin* and wild type) in Bulgaria. They are grown in the following regions of Bulgaria with different altitudes: Pazardzhik, Plovdiv, Sofia and Haskovo. Fruits from Pazardzhik region were raised at an altitude of 1273 m - village of Nova Mahala, 196 m; - village of Kurtovo Konare, 295 m; - town of Banya, 1300 m - Byala cherkva (wild type raspberry); town of Sopot (hut Dobrila - 1804 m, wild type raspberry); Sofia district 643 m; - town of Dolna Banya, Haskovo region 171 m - village of Uzundjovo.

Juice extraction, pH and titratable acidity analysis

To obtain the juice, raspberry fruits were liquefied using a Phillips food processor. The obtained juice was prefiltered and then centrifuged at 3000 rpm for 15 min. pH was measured potentiometrically with a pH meter (WTWinoLab pH 7110, Germany). Titratable acidity, expressed as percentage of malic acid, was determined by titrating 10 mL of raspberry juice with 0.1 M NaOH to a pH point of 8.2. The results were expressed in g malic acid per 100 g juice.

Total phenolics content (TPC)

The total phenolic contents were measured using a Folin-Ciocalteu assay. Folin-Ciocalteu reagent (1 mL) (Sigma) diluted five times was mixed with 0.2 mL of sample and 0.8 mL of 7.5% Na₂CO₃. The reaction was performed for 20 min at room temperature in darkness. Then the absorbance of the sample was measured at 765 nm against blank sample, developed in the same way but without extract. The results were expressed in mg equivalent of gallic acid (GAE) per 100 g juice, according to calibration curve, built in the range of 0.02 - 0.10 mg gallic acid (Sigma) used as a standard.

Total monomeric anthocyanins analysis

The total monomeric anthocyanins content was determined using the pH differential method described by Lee *et al.* 2005 [9]. 2 g of juice were extracted with 8 mL of ethanol in a ultrasound bath for 15 min. The pH of juice samples was brought to 1.0 with potassium chloride and 4.5 with sodium acetate buffers. The dilutions were then allowed to equilibrate for 5 min at room temperature. The absorbance of the equilibrated solutions at 520 nm

for anthocyanins content and at 700 nm for haze correction was measured on a VIS spectrophotometer (Camspec M107, UK) with 1 cm path length disposable cuvettes. All absorbance measurements were carried out at room temperature against distilled water as a blank. Pigment content was calculated as cyanidin-3-glucoside equivalents with a molecular weight of 449.2 and an extinction coefficient of 26 900 L/(cm × mol).

Antioxidant activity (DPPH assay)

Each analyzed extract (0.15 mL) was mixed with 2.85 mL of freshly prepared 0.1 mmol solution of 1,1-diphenyl-2-picrylhydrazyl radical (DPPH, Sigma) in methanol (Merck). The reaction was performed at 37 °C in darkness and the absorptions at 517 nm were recorded after 15 min against methanol. The antioxidant activity was expressed as mmol Trolox equivalents (TE) per 100 g juice by using a calibration curve, built with 0.05, 0.1, 0.2, 0.3, 0.4 and 0.5 mmol of 6-hydroxy-2,5,7,8-tetramethylchroman-2-carboxylic acid (Trolox®, Fluka) dissolved in methanol (Sigma).

RESULTS AND DISCUSSION

Currently there is great interest to phytochemicals as bioactive components of food. The roles of fruits, vegetables, and red wine in disease prevention have been attributed, in part, to the antioxidant properties of their constituent polyphenols (vitamins E and C, and carotenoids) [10,11]. A special place in this prevention have fruits and leaves of raspberries.

Raspberries besides red can be black or gold. They are best developed in hilly and mountainous locations and areas with a cool and humid climate. In Bulgaria, two harvests of raspberries are common. They contain easily digestible carbohydrates, rich in dietary fibers, minerals and vitamins. Raspberries quench thirst and improve digestion, so they are used in dietary nutrition, especially for children. Thanks to the salicylic acid found in fruits, raspberries are also used to lower the body temperature.

Consumption of raspberries is associated with broad health benefits - reduced risk for heart disease, diabetes and cancer. The phenolic compounds contained in the raspberries such as flavonoids, phenolic acids, stilbens and procyanidins act synergistically [12].

To analyze *in vitro* the antioxidant activity of samples we used the DPPH method [13]. The antioxidant activity is in the range of 372 mmol TE /100 ml of juice to 2240.20 mmol TE /100 ml of juice (Table 1).

The results for titratable acidity (TA), and pH of raspberry juice obtained from different cultivars grown at different altitudes are presented in Table 1. There are no significant differences found between the obtained juices for the investigated parameters (titratable acidity and total acidity). The pH values ranged between 2.4 and 3.0 with an average value of 2.8 (Table 1). The titratable acidity values ranged between 2.1 and 2.7% with an average value of 2.4%. Citric and malic acids are the main organic acids in raspberry fruit responsible for titratable acidity [3]. Riaz and Bushway (1996) [14] reported a similar result for the mean values of the content of acids for raspberry reported as citric acid, in the range from 1.5 % to 2.6 % (Table 1). The differences between the maximal and minimal content amounted from 10% to 20% of the mean value. The mean contents of acids in the raspberry grown over 1000 m were lower than for those grown under 1000 m altitude. The results of this study showed considerable variation in the content of acids in the fruits of the same cultivar at different altitudes. The possible reason for the variation in the same cultivar could be rainfall and percentage of sunshine during the growing season, which could cause an increase in sugar and a decrease in acid content.

Main phenolic compounds of raspberry fruit were presented as anthocyanins and ellagitannins [15]. It is evident from Table 2 that the highest content of total phenols has the juice obtained from raspberry fruit collect from Banya town area (251.73 ± 0.20 mg GAE/100 mL), followed by Nova Mahala village, Uzundjovo village and Kurtovo Konare village. Additionally, many investigators reported that in raspberry fruit high

amounts of sanguin H-10, casuarictin/potentilin, castalagin/vescalagin, pedunculagin, and corilagin were identified (about 30 mg/100 g fresh weight) [16-18]. In accordance with Mikulic-Petkovsek *et al.* (2012) [3] it was established that the total polyphenol content of the investigated raspberry juice was from 250 to 180 mg GAE/100 mL. Additionally, the anthocyanins are other bioactive compounds with vital significance for human health. The cyanidin and pelargonidin glycosides: 3-sophoroside, 3-glucoside, 3-rutinoside and 3-glucosyl-rutinoside are dominating in raspberry fruit [1,15]. On this base we investigated the influence of altitude on the biosynthesis of anthocyanins. The results are presented in Table 2. The highest content of total anthocyanins has the juice obtained from raspberry fruit collected from Dobrila hut area with the highest altitude (Table 1) (86.89 ± 0.06 mg/100 mL juice), followed by Byala cherkva village and Uzundjovo village.

The obtained total anthocyanins (Table 2) were in lower concentrations in all samples compared to other cultivars which have about 104–198 mg/100 g fw of total anthocyanins [19]. But our results for total anthocyanins are in accordance with other cultivars cv. Amira and cv. Polka which are similar or higher (35-45 mg/100 g fw) [6].

With greater antioxidant activity are samples that have lower titratable acidity, i.e. these indicators are inversely proportional ($r^2 = -0.75$) (Table 3).

Similar results have been reported by other researchers. Pantelidis *et al.* (2007) reported a high correlation between total polyphenol and anthocyan content and total antioxidant capacity in different raspberry juices [19].

Table 1. Total acidity (pH) and titratable acidity of different samples of rasperry juice obtained from *R. idaeus* cv. *Rubin* and wild types.

Raspberry juice samples	Altitude (m)	Total acidity (pH)	Titratable acidity (%)
Uzundjovo village	171	2.99 ± 0.03	2.30 ± 0.01
Kurtovo Konare village	196	3.03 ± 0.03	2.43 ± 0.01
Banya town	295	2.37 ± 0.03	2.51 ± 0.01
Dolna Banya town	643	2.75 ± 0.03	2.70 ± 0.01
Byala cherkva village	1300	2.95 ± 0.03	2.45 ± 0.01
Nova Mahala village	1273	3.00 ± 0.03	2.23 ± 0.01
Dobrila hut (Balkan mountain)	1804	2.75 ± 0.03	2.13 ± 0.01

Table 2. Total polyphenol content, total anthocyanins content and antioxidant activity of investigated raspberry juice obtain from *R. idaeus* cv. *Rubin* and wild types.

Raspberry juice samples	Total polyphenols content, (g GAE/100 mL)	Total anthocyanins (mg /100 ml)	Antioxidant activity (DPPH method) (mmol TE/100 mL)
Uzundjovo village	219.88 ± 0.22	24.69 ± 0.12	372.87 ± 0.30
Kurtovo Konare village	219.88 ± 0.10	18.84 ± 0.01	402.92 ± 0.28
Banya town	251.73 ± 0.20	15.04 ± 0.11	457.38 ± 0.30
Dolna Banya town	179.26 ± 0.26	13.79 ± 0.13	481.79 ± 0.26
Byala Cherkva village	167.86 ± 0.10	27.95 ± 0.04	513.72 ± 0.21
Nova Mahala village	221.47 ± 0.25	19.56 ± 0.10	1988.52 ± 10.28
Dobrila hut (Balkan mountain)	183.41 ± 0.20	86.89 ± 0.06	2240.20 ± 19.10

Table 3. Correlation (r^2) between antioxidant activity and investigated parameters: altitude, total polyphenols content, total anthocyanins content, titratable acidity and total acidity

Parameters	Total polyphenols content	Total anthocyanins	Antioxidant activity	pH	Titratable acidity
Antioxidant activity	- 0.16	0.69	-	0.07	- 0.75
Altitude	- 0.61	0.71	0.81	0.09	- 0.52
Total polyphenols content	-	-0.40	- 0.16	-0.33	- 0.06
pH	-0.33	-0.03	0.07	-	-0.32
Titratable acidity	-0.06	-0.68	-0.75	-0.31	-

CONCLUSIONS

1. The total polyphenols content depends moderately to significantly decreasing (inverse) by the linear relationship ($r^2 = -0.33$ and $r^2 = -0.61$) with total acidity and altitude, respectively. With an increase in pH and altitude, the amounts of polyphenols decrease.

2. The total anthocyanins content depends on altitude with high direct (increasing) linear relationship $r^2 = 0.71$.

3. The antioxidant activity in raspberry juice obtained from *R. idaeus* cv. *Rubin* mainly depends on total anthocyanins content ($r^2 = 0.71$). The titratable acidity decreases when the content of total anthocyanins increases ($r^2 = -0.68$). The antioxidant activity significantly increases when altitude increases, i.e. they have significant correlation ($r^2 = 0.81$).

REFERENCES

1. A. Kassim, J Poette, A. Paterson, D. Zait, S. McCallum, M .Woodhead, K. Smith, C. Hackett, J. Graham, *Mol. Nutr. Food Res.*, **53**, 625 (2009).
2. I. Badjakov, M. Nikolova, R. Gevrenova, V. Kondakova, E. Todorovska, A. Atanassov. *Biotechnol. Biotec.*, **22**, 581 (2008).
3. M. Mikulic-Petkovsek, V. Schmitzer, A. Slatnar, F. Stampar, R. Veberic, *Journal of Food Science*, **77**, C1-C7 (2012).
4. S. Bowen-Forbes, Y. Zhang, M. G. Nair, *Journal of Food Composition and Analysis*, **23**, 554 (2010).
5. M. Heinonen, S. Meyer, N. Frankel, *Journal of Agricultural and Food Chemistry*, **46**, 4107 (1998).
6. Z. Zorenc, R. Veberic, D. Koron, M. Mikulic-Petkovsek, *Not Bot Horti Agrobo*, **45**(2), 417 (2017).
7. N. Miletić, A. Leposavić, B. Popović, O Mitrović, K. Kandić, *Acta Horticulturae*, **1099**, 211 (2015).
8. A. Sønsteby, O. M. Heide, *European Journal of Horticultural Science*, **77**(3), 97 (2012).
9. J. Lee, R. Durst, R. Wrolstad, *Journal of AOAC International*, **88**, 5, 1269 (2005).
10. K. Meyers, C. Watkins, M. Pritts, R. Liu, *J. Agric. Food Chem.*, **51**, 6887 (2003).
11. C. Rice-Evans, N. Miller, G. Paganga, *Trends in Plant Science*, **2**(4), 152 (1997).
12. A.L. Zhang, J. Li, S. Hogan, H. Chung, G.E. Welbaum, K. Zhou, *Food Chem.*, **119**, 592 (2010).

S. I. Papanov et al.: Analysis of the changes in the main characteristics and antioxidant properties in raspberries ...

13. I. Gülçin, F. Topal, R. Çakmakçi, A. C. Goren, M. Bilsel, U. Erdogan, *Journal of Food Science*, **76**, 585 (2011)
14. N. Riaz, A. Bushway, *Journal of Food Quality*, **19**, 457 (1996).
15. B. Burton-Freeman, A. Sandhu, I. Edirisinghe, Cardiometabolic and Neuronal Health Links, *Adv. Nutr.*, **7**, 44 (2016).
16. W. Mullen, T. Yokota, M. Lean, A. Crozier, *Phytochemistry*, **64**, 617 (2003).
17. M. Gasperotti, D. Masuero, U. Vrhovsek, G. Guella, F. Mattivi, *J. Agric. Food Chem.*, **58**, 4602 (2010).
18. I. Dincheva, I. Badjakov, V. Kondakova, P. Dobson, G. Mc Dougall, D. Stewart, *Int. J. Agric. Sci. Res.*, **3**, 127 (2013).
19. G. Pantelidis, M. Vasilakakis, G. Manganaris, G. Diamantidis, *Food Chemistry*, **102**, 777 (2007).

Mechanochemically synthesized N-doped ZnO for photodegradation of ciprofloxacin

N.G. Kostova^{1*}, M. Fabian², E. Dutkova²

¹ Institute of Catalysis, Bulgarian Academy of Sciences, Acad. G. Bonchev St., Bldg. 11, 1113 Sofia, Bulgaria

² Institute of Geotechnics, Slovak Academy of Science, 04001 Kosice, Slovakia

Received: February 5, 2019; Revised: June 14, 2019

N-doped ZnO photocatalyst was prepared using mechanochemical method with ammonium hydroxide as nitrogen source (ZnO-am). The mechanical activated ZnO sample was also prepared for comparison (ZnO-MA). As-milled samples were calcined at 673 K. The so prepared samples have been characterized by X-ray diffraction (XRD), diffuse reflectance (DRS) and photoluminescence (PL) spectroscopy. The XRD analysis shows wurtzite crystal structure of synthesized samples. The positions of diffraction peaks of mechanochemically synthesized nanostructured sample were shifted to slightly higher angles. The crystallite size decreased from 168 to 35 nm. Only a strong absorption band was registered in the UV region in the DRS spectrum of initial ZnO, while in the spectrum of N-doped ZnO-am sample absorption in the visible light region was also observed. All the samples were tested as photocatalytic materials in the model reaction of ciprofloxacin (CIP) photodegradation. The lower PL intensity of ZnO-am indicates a lower recombination rate of photoexcited electrons and holes. Doping nitrogen a new electron energy level is created inside the band gap of ZnO. The ZnO-am nanostructured sample has higher photocatalytic activity under visible light irradiation.

Keywords: mechanochemistry, ZnO, doping, photoluminescence, photocatalysis, visible light

INTRODUCTION

During the past several decades aqueous organic contaminants such as antibiotics discharged from industrial activities and hospitals have become increasingly harmful to human health and environment. Ciprofloxacin (CIP), a broad spectrum second generation fluoroquinolone class of antibiotic drug, has been widely used to fight against variety diseases [1]. CIP exists in different water resources such as wastewater, surface water or ground water. The drug could not be easily biodegraded during biological wastewater treatment process. Recently, the removal of environmental pollutants based on solar energy-driven semiconductor photocatalysis has been developed [2]. Zinc oxide, known as multifunctional materials, was subject of extensive studies as a photocatalysts due to its low price, non-toxicity and wide band gap [3]. Disadvantage of ZnO is its low photocatalytic activity under illumination with visible light. Diminishing the band gap of ZnO by non-metal doping is considered as one of the most effective strategies to improve the photocatalytic activity. Nitrogen is the best choice as it has nontoxicity, lower electronegativity and ionization energy than the oxygen atom. Various methods have been applied for

doping nitrogen to ZnO – e.g. precipitation [4], microwave irradiation [5], sol-gel [6], thermal decomposition [7], microwave-assisted hydrothermal method [8], microemulsion method [9], combustion method [10] and mechanochemical synthesis [11]. The latter method enables obtaining considerable quantities of materials in an economic way [12]. During the last years the mechanochemistry is being applied successfully for the preparation of catalysts [13], sulphides [14], perovskites [15], mixed oxides [16], as well as for doping oxides with metals and non-metals [17]. The mechanical grinding or milling often leads to the formation of defects in the materials. Their transformation into stable phases was induced by means of additional calcination, which cannot be achieved by most of the conventional methods [18]. In contrast to the most often applied sol-gel method for the synthesis of nitrogen-doped zinc oxide photocatalysts, the mechanochemical synthesis is an environment friendly method, which does not use toxic organic solvents [19].

In the present paper we provide a detailed analysis of the majority of properties of mechano-chemically treated ZnO-am and a proof of its photocatalytic activity in photodegradation of pollutants in waste water under visible light irradiation.

* To whom all correspondence should be sent
E-mail: nkostova@ic.bas.bg

EXPERIMENTAL

Materials

ZnO (Chimsnab Bulgaria AD), ammonia solution (NH₄OH, 28%, density 0.918 g/mL) (Neochim AD, Bulgaria) and ciprofloxacin (Sigma Aldrich, Germany) were used without further purification.

Preparation and characterization of N-doped photocatalyst

N-doped ZnO sample was prepared by mechanochemical synthesis from ZnO, and ammonia solution using a high-energy planetary ball mill Pulverisette 6 (Fritsch, Germany). The precursors were milled for 30 min at 550 rpm in ambient atmosphere using a chamber of 250 cm³ with 21 balls of 10 mm in diameter all made of zirconia. The ball-to-powder mass ratio was 40:1. After milling, the powdered mixture was calcined 2 h at 673 K. The sample was referred to as ZnO-am. The sample prepared by ball milling of zinc oxide without nitrogen source was named ZnO-MA.

The X-ray diffraction (XRD) patterns were recorded on a D8 Advance diffractometer (Bruker, Germany) using CuK_α radiation. The diffraction data were collected in the range of 20° < 2θ < 65°, with steps of 0.02° and a counting time of 9 s/step. The crystallite sizes were calculated applying Scherrer's equation.

UV-Vis spectra for evaluation of photophysical properties were recorded in diffuse reflectance mode (DRS) and transformed into absorption spectra through the Kubelka-Munk function [20]. A Thermo Evolution 300 UV-Vis Spectrophotometer, equipped with a Praying Mantis device with Spectralon as the reference was used.

The photoluminescence (PL) spectra at room temperature were acquired on a photon counting spectrofluorometer PC1 (ISS) with a photoexcitation wavelength of 325 nm. A 300 W xenon lamp was used as the excitation source. For measuring the PL intensity, the powders were suspended in absolute ethanol.

Photocatalytic procedure

Photodegradation of ciprofloxacin was carried out in a semi-batch slurry reactor containing 0.1 g catalyst and 100 mL of 10 mg·L⁻¹ CIP solution at 298 K under visible light. Prior to illumination, the suspensions were continuously stirred in dark for 30 min to ensure the adsorption/desorption equilibrium of the CIP on the photocatalyst powders. The suspension was then irradiated by visible light LED lamp (10 W) with distance 7 cm from the surface of

the slurry. At regular time interval, aliquot samples were taken and centrifuged to eliminate the photocatalyst. The concentration of CIP during the photocatalytic reaction was estimated using Spekol 11 (Carl Zeiss, Germany) spectrophotometer at 277 nm at room temperature. Each sample was turned back to the reaction mixture after the spectrophotometric measurement. All photocatalytic tests were performed at constant stirring rate of 400 rpm in presence of air flow and at room temperature.

RESULTS AND DISCUSSION

X-ray diffraction (XRD) was used to identify the crystalline phase structure of the samples. Fig. 1 represents the diffraction patterns of the initial ZnO and mechanochemically synthesized samples. The diffraction pattern of the initial ZnO displays sharp intensive peaks, identified as due to (100), (002), (101), (102) and (110) planes. The observed diffraction lines in the patterns of the mechanochemically treated samples are in accordance with those of hexagonal ZnO having wurtzite structure (JCPDS card 89-7102). No peaks of other phases have been registered.

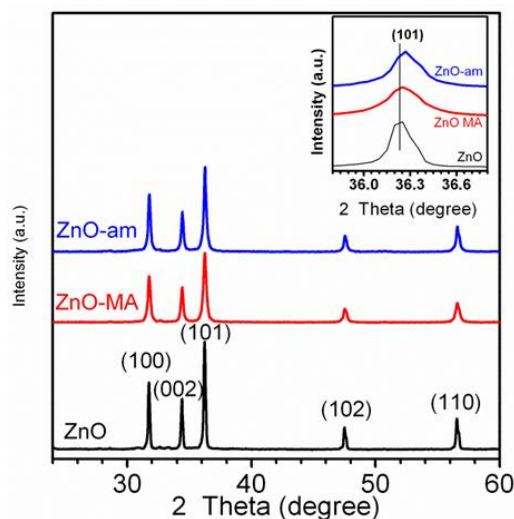


Fig. 1. XRD patterns of initial ZnO, ZnO-MA and ZnO-am samples.

After 30 minutes of mechanical treatment small differences were registered in the relative intensities of the diffraction lines. The decrease in intensity of the diffraction lines is larger in the diffraction pattern of ZnO-MA, while that of the nitrogen doped sample is not so distinctly expressed. The crystallites size was calculated based on the full width at half maximum (FWHM) of the peak (101) applying the equation of Scherrer. The average crystallites sizes are listed in Table 1.

Table 1. Lattice parameters, crystallites size and energy band gap of ZnO, ZnO-MA and ZnO-am samples

Sample	Lattice parameter (Å)		Crystallites size (nm)	Energy band gap (eV)	rate constant k (min^{-1})
	a = b	c			
ZnO	3.251(6)	5.209(4)	168	3.19	0.0007
ZnO-MA	3.252(1)	5.210(2)	32	2.54	0.0035
ZnO-am	3.249(2)	5.205(3)	35	1.74	0.0062

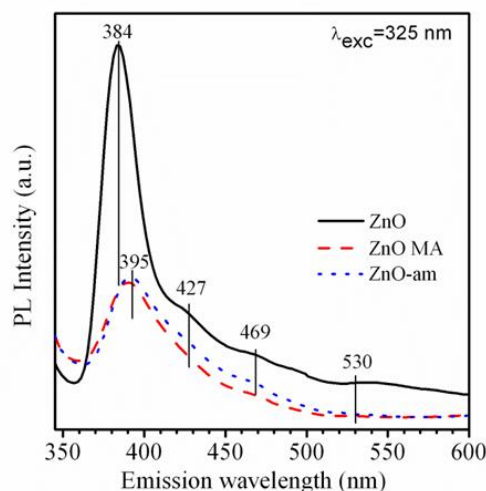
The lattice parameters of ZnO-MA sample increased after mechanical treatment which is consistent with the literature [21]. Nitrogen doping of ZnO led to reduction of the lattice parameters of ZnO-am sample (Table 1). The registered widening of the diffraction peaks in the XRD patterns of the mechanochemically synthesized samples witnesses decrease in the crystallites size from 168 nm for the initial ZnO down to 32 (35) nm for the other samples. A slight shift of the diffraction peaks to larger angle positions was observed in the dif-fraction patterns of the mechanochemically treated samples in comparison with the pure ZnO (inset of Fig. 1). On the other hand, our results differ from those of Dai *et al.* [22], where diffraction peak shifts toward lower angles was reported. The shift to the larger angle positions is within 0.015° for the sample ZnO-MA and 0.03° for the sample ZnO-am and, that is evidence for the formation of oxygen defects. The registered changes in the diffraction patterns could be explained with local modification of the structure occurring during the ball milling and stabilized in the consecutive thermal treatment [23].

The optical properties of the samples were investigated by means of PL and DRS. PL spectra supply information about the recombination of the photogenerated charges [24]. The photoluminescence spectra of the initial ZnO and those of the mechanochemically synthesized samples, dispersed in ethanol, are represented in Fig. 2.

The PL spectra of all samples contain a high intensity peak at 384 nm and low intensive bands at about 425, 467 and 530 nm. The strong UV emission can be assigned to a near-band-edge (NBE) emission originating from recombination of excited electrons in a localized level below the conduction band with holes in the valence band. In addition a slight shift of the UV peak is registered towards higher wavelength region in the PL spectra of ZnO-am and mechanically activated ZnO sample.

The registered significant widening of the band gives evidence for super-positioning of violet emission upon the UV emission, which can be assigned to electrons from the shallow neutral donor level to the upper level of the valence band [25-26]. The sharp decrease in intensity of the bands in the photoluminescence spectra of the mechanochemi-

cally synthesized samples indicates a lower recombination rate of electron-hole pairs. It has been generally accepted that the highly intensive photoluminescence means high degree of recombination of the photogenerated charge carriers (e^- and h^+), implying low photocatalytic activity [27] and vice versa - the low intensity of the emission bands in the photoluminescence spectrum means lower rate of recombination, which is assumption for high photocatalytic activity.

**Fig. 2.** Photoluminescence spectra of the initial ZnO, ZnO-MA and ZnO-am samples

UV-Vis diffuse reflectance spectra of the initial ZnO, the mechanically activated zinc oxide, as well as the mechanochemically treated samples, doped with nitrogen are shown in Fig. 3. In the ultraviolet region (200–360 nm) all the samples showed similar in intensity reflections. The optical spectrum of the initial sample is dominated by transition from the valence band to the conduction band, occurring at about 400 nm. Within the visible range of the spectra one can observe substantial differences in the spectra of the initial zinc oxide and the mechanochemically synthesized samples (Fig. 3). It is observable in the spectra of the mechano-chemically synthesized samples less intensive reflectance (more intensive absorbance) in the visible region from 400 up to 700 nm. In the reflectance spectra of ZnO-am sample was registered red shifting towards larger wavelengths in comparison with the initial ZnO. The more intensive absorbance in the visible region in the spectra of the

nitrogen-doped TiO₂ and ZnO is usually attributed to formation of oxygen vacancies, whereupon an additional electron energy level appears inside the band gap. Similar results have also been obtained by some other authors [28-29].

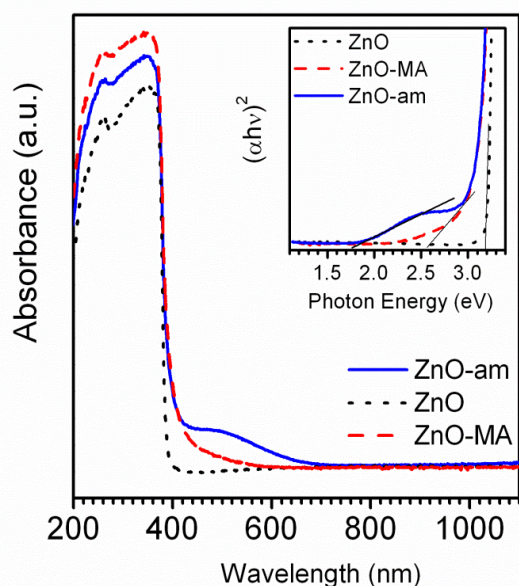


Fig. 3. Diffuse reflectance spectra (inset Tauc's plots) of the initial ZnO, ZnO-MA and ZnO-am samples.

The Tauc's method was applied for determining the band gap energy of the samples. The band gap of oxide semiconductors can be determined on the basis of the equation: $ahv = A(hv - E_g)^n$, where a is absorption coefficient, $h\nu$ is the incident photon energy, A is a constant, n value is $\frac{1}{2}$ for direct semiconductor [30]. The calculated values of the band gap energy are represented in Table 1. The band gap value obtained for the pristine ZnO sample (3.19 eV) is similar to other samples, synthesized by different methods [31]. After the doping the value of the band gap width is decreased down to 1.74 eV. It is obvious that the light-absorption edges of the mechanochemically treated samples exhibit a red-shift towards the visible region with respect to that of the initial ZnO sample. The initial ZnO sample is colored in white, while the mechanochemically synthesized samples doped with nitrogen are yellow, which is in accordance with their narrow band gap. This change in their color is connected with the presence of a second absorption band and it is the evidence for the creation of mid-gap state, located on the N 2p orbitals [32]. Nakamura et al. [33] supposed that the nitrogen doping is accompanied by a growing number of generated oxygen vacancies. As a result of this narrowing of the band gap of the doped titanium dioxide is manifested by shifting of the edge of the valence band due to mixing of N 2p and O 2p electron states and shifting of the lower edge of

conduction band in positive direction due to oxygen vacancies (see the scheme in Fig. 5).

The photocatalytic activity of all samples was tested in oxidative degradation of the ciprofloxacin. The CIP concentration after irradiation for a definite time was measured by UV-Vis spectrophotometer at $\lambda_{max} = 277$ nm. Negligible change in CIP concentration was registered in absence of photocatalyst, indicating CIP itself is stable and barely degraded under visible illumination (Fig. 4). The initial ZnO showed very low activity in the photodegradation of the dye, which is due to its low absorbance of visible light (proved by DRS in Fig. 3). ZnO-am nanostructured sample manifested the highest photocatalytic activity under irradiation with visible light among all studied photocatalysts. The value of CIP degradation efficiency over ZnO, ZnO-MA and ZnO-am was calculated at 4.25, 19, and 31% respectively.

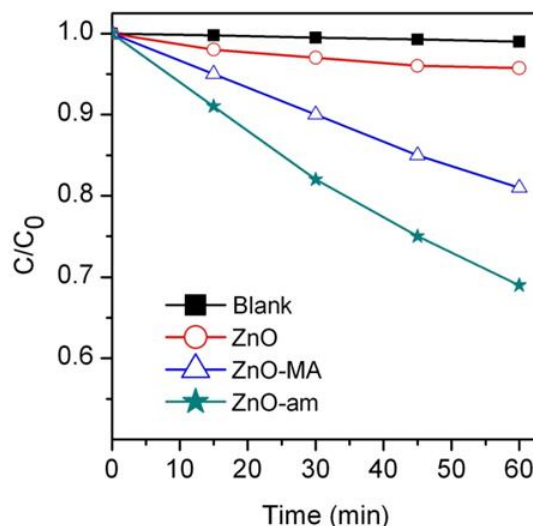


Fig. 4. Photodegradation of ciprofloxacin as a function of irradiation time of blank experiment without photocatalyst (■), initial ZnO (○), ZnO-MA (Δ) and ZnO-am (*) under visible light irradiation.

Pseudo-first-order kinetics of photodegradation was supposed from the linear plot of $-\ln(C_0/C)$ versus irradiation time t and the rate constants are listed in Table 1. The results show that ZnO-am sample has the highest apparent rate constant indicating an obvious enhancement of catalytic activity for the mechanochemically synthesized sample.

There are several reasons for the observed higher photocatalytic activity of the nitrogen doped mechanochemically synthesized sample. The smaller size of the crystallites is important factor, which leads to enhance mobility of the charge to the surface and assistance in efficient participation in the photocatalytic process. The initial ZnO showed 5 x larger size of the crystallites (see Table 1) and very low

photocatalytic activity. Other factors exerting influence on the photocatalytic activity are the composition and the electronic structure of the samples. Nitrogen doping of the zinc oxide results in a new internal electron level formed by N 2p electrons inside the band gap of the semiconductor. CIP degradation is very complex. The scheme of possible reaction mechanism of photocatalytic degradation of CIP with of ZnO-am is represented in Fig. 5.

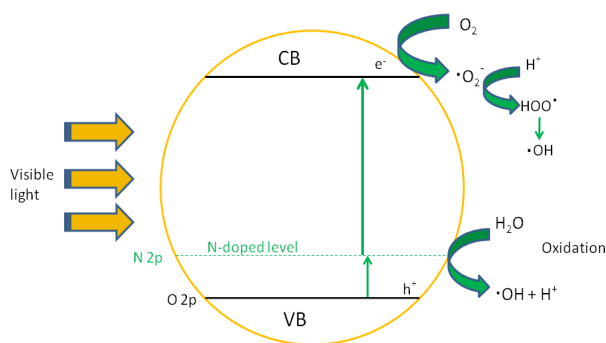


Fig. 5. Scheme of the possible reaction mechanism for the photocatalytic degradation of ciprofloxacin by ZnO-am under visible light irradiation.

The electrons removed from the valence band (VB) of ZnO upon irradiating with visible light are firstly excited to the newly formed electron energy level by visible light photons. Further, absorbing new photons they are transferred to the conduction band (CB) of ZnO. This means that the transfer of electron from VB to the CB in the ZnO-am sample can be realized through a two-stage transition even under irradiation by the lower energy visible light photons passing through the intermediate level N 2p. During the photocatalytic process the photo-generated electrons within the conduction band are migrating towards the surface and upon reacting with the oxygen molecules, adsorbed on the surface they form $\bullet\text{O}_2^-$ super oxide anion-radicals (Fig. 5). Further, they undergoes protonation forming $\text{HOO}\bullet$ hydroperoxide radicals. Mean-while the positively charged holes in the valence band migrate towards the surface and react with adsorbed H_2O molecules yielding the highly reactive hydroxyl radicals $\bullet\text{OH}$. Both types of active particles ($\text{HOO}\bullet$ and $\bullet\text{OH}$) initiate radical chain reaction mechanism leading to degradation of ciprofloxacin.

CONCLUSIONS

Nitrogen doped-ZnO nanostructured photocatalyst has been synthesized by the mechanochemical method applying ammonium hydroxide as nitrogen supplying precursor. Using photoluminescence

spectroscopy it was found out that in the mechanochemically synthesized N-doped ZnO-am nanostructured sample the rate of recombination of the charge carriers is considerably lower. DRS results revealed that the absorption edge of the mechanochemically synthesized ZnO-am photocatalyst presents red shift compared to ZnO indicating an enhanced visible light absorption, which enables the utilization of these materials as photocatalysts for the purification of wastewaters operating under visible light irradiation.

Acknowledgements: The authors are grateful to the Bulgarian Science Fund for financial support by project DNTS/Slovakia 01/2.

REFERENCES

1. C. Bojer, J. Schbel, T. Martin, M. Ertl, H. Schmalz, *Appl. Catal, B: Environ.*, **204**, 561 (2017).
2. N. Kaneva, A. Bojinova, K. Papazova, D. Dimitrov, *Bulg. Chem. Commun.*, **50**, Special issue H, 116 (2018).
3. A. di Mauro, M. E. Frgala, V. Privitera, G. Impellizzeri, *Mater. Sci. Semicond. Processing*, **69**, 44 (2017).
4. R. Kumari, A. Sahai, N. Goswami, *Progress in Natural Science: Materials International*, **25**, 300 (2015).
5. N. P. Herring, L. S. Panchakarla, M. Samy el-Shall, *Langmuir*, **30**, 2230 (2014).
6. J. J. Macias-Sanchez, L. Hinojosa-Reyes, A. Caballero-Quintero, W. de la Cruz, E. Ruiz-Ruiz, J. L. Hernandez-Ramirez, A. Guzman-Mar, *Photochim. Photobiol. Sci.*, **14**, 536 (2015).
7. H. Sudrajat, S. Babel, *Environ. Sci. Pollution Res.*, **23**, 10177 (2016).
8. G. Byzinski, C. Melo, D.P. Volanti, M. M. Ferrer, A. F. Gouveia, C. Ribeiro C, J. Andres, E. Longo, *Materials & Design*, **120**, 363 (2017).
9. A. B. Lavang, Y. S. Malghe, *J. Asian Ceram. Soc.*, **3**, 305 (2015).
10. G. Kale, S. Arbuj, U. Kawade, S. Rane, J. Ambekar, B. Kale, *Materials Chemistry Frontiers*, **2**, 163 (2018).
11. D. Chen, Z. Wang, T. Re, H. Ding, *J. Phys. Chem. C*, **118**, 15300 (2014).
12. A. F. Fuentes, L. Takacs, *J. Mater. Sci.*, **48**, 598 (2013).
13. K. Ralphs, C. Hardacre, S. L. James, L. Stuart, *Chem. Soc. Rev.*, **42**, 7701 (2013).
14. P. Balaz, M. Balaz, M. Achimovicova, Z. Bujnakova, E. Dutkova, *J. Mater. Sci.*, **52**, 11851 (2017).
15. Q. Zhang, F. Saito, *Adv. Powder Technol.*, **23**, 523 (2012).
16. M. Senna, P. Billik, A. Y. Yermakov, M. Skratek, M. Majerova, *J. Alloys Comp.*, **695**, 2314 (2017).
17. S. Livraghi, M. R. Chierotti, E. Giamello, G. Magnacca, M. C. Paganini, G. Cappelletti, C. L. Bianchi, *J. Phys. Chem. C*, **112**, 17244 (2008).
18. M. L. Sanjuan, C. Guglieri, S. Diaz-Moreno, G.

- Aquilanti, A. F. Fuentes, L. Olivi, J. Chaboy, *Phys. Rev. B*, **84**, 104207 (2011).
19. M. Balaz, A. Zorkovska, F. Urakaev, P. Balaz, J. Briancin, Z. Bujnakova, M. Achmovicova, E. Gock, *RSC Adv.*, **6**, 87836 (2016).
20. T. B. Ivetic, M. R. Dimitrievska, N. L. Fincur, L. R. Dacanin, I. O. Guth, B. F. Abramovic, S. R. Lukic-Petrovic, *Ceram. Inter.*, **40**, 1545 (2014).
21. J. Wang, Y. Xia, Y. Dong, R. Chen, L. Xiang, S. Komarneni, *Appl. Catal. B: Environ.*, **192**, 8 (2016).
22. J. Dai, M-H. Yuan, J-H. Zeng, Q-F. Dai, S. Lan, C. Xiao, S-L. Tie, *Optical Express*, **23**, 29231 (2015).
23. Z. Petrovic, M. Ristic, S. Music, M. Fabian, *Croat. Chem. Acta*, **90**, 135 (2017).
24. S. K. Mishra, R. K. Srivastava, S. G. Prakash, R. S. Yadav, A. C. Pandey, *Optoelectron Rev.*, **18**, 467 (2010).
25. A. B. Lavand, Y. S. Malghe, J. King Saud University – Science, **30**, 65 (2018).
26. X. Feng, H. Guo, K. Patel, H. Zhou, X. Lou, *Chem. Eng. J.*, **244**, 3227 (2014).
27. N. D. Abrazovic, M. Montone, L. Mirengi, I. A. Jankovic, M. I. Comor, *J. Nanosci. Nanotechnol.*, **8**, 613 (2008).
28. W. R. Lambrecht, A. Boonchum, *Phys. Rev. B*, **87**, 195 (2013).
29. M. Mapa, C. S. Gopinath, *Chem. Mater.*, **21**, 351 (2009).
30. D. Chen, L. Gao, A. Yasumori, K. Kuroda, Y. Sugahara, *Small*, **4**, 1813 (2008).
31. B. Chavillon, L. Cario, A. Renaud, *F. J. Amer. Chem. Soc.*, **134**, 464 (2012).
32. O. Game, U. Singh, A. A. Gupta, A. Suryawanshi, A. Anpurkar, S. Ogale, *J. Mater. Chem.*, **22**, 17302 (2012).
33. R. Nakamura, T. Tanaka, Y. Nakato, *J. Phys. Chem. B*, **108**, 10617 (2004).

Photocatalytic behavior of ZnSe-TiO₂ composite for degradation of methyl orange dye under visible light irradiation

N. G. Kostova*¹, M. Achimovicova², M. Fabian²

¹ Institute of Catalysis, Bulgarian Academy of Sciences, Acad. G. Bonchev St., Bldg. 11, 1113 Sofia, Bulgaria

² Institute of Geotechnics, Slovak Academy of Science, 04001 Kosice, Slovakia

Received April 22 2019; Revised June 14, 2019

In the present study we report the preparation of ZnSe-TiO₂ composite *via* a two-step mechanochemical synthesis. ZnSe with 10 nm crystallite size was mechanochemically synthesized in industrial mill using zinc and selenium as precursors. The composite material was synthesized in laboratory high-energy ball mill. The synthesized material was characterized by means of various techniques including X-ray powder diffraction (XRD) and UV-vis diffuse reflectance spectra (DRS). The results revealed a composite formation. The calculated band gap was 2.3 eV. The prepared structured materials were employed as photocatalysts for the degradation of methyl orange (MO) under visible light illumination. The results exhibited higher photocatalytic efficiency over ZnSe-TiO₂ composite material in comparison with those of pure ZnSe and TiO₂, which might be attributed to the high surface area and the synergetic effect between zinc selenide and titania. It was established that the reaction was of pseudo-first order. A possible mechanism was proposed. The mechanochemically synthesized ZnSe-TiO₂ composite material exhibited stability in photocatalytic activity after four cycles.

Keywords: mechanochemistry, photocatalysis, ZnSe, methyl orange, dye

INTRODUCTION

Heterogeneous photocatalysis using semiconductors has received attention because of its potential in solving environmental problems [1]. This method is based on the production of electron-hole pairs by illumination with suitable energy light of semiconductor materials. Nanosized particles have unique physical and chemical properties that make them applicable in the photocatalytic process [2, 3]. The photocatalytic degradation of toxic compounds (dyes, pesticides, etc.) using the photo-catalytic materials in an aqueous medium depends on the band gap, surface area, amount of catalyst, etc. Different metal oxides [4] and sulfides [5] have been employed as photocatalysts for dyes photodegradation. TiO₂ is one of the best photo-catalysts for environmental applications because of its strong oxidizing and reducing ability, low cost and availability. However, TiO₂ only responds to UV light due to its wide band gap, which restricts its applications [6]. Many attempts have been devoted to improving the visible-light photocatalytic activity of TiO₂. Recently, studies have reported various methods of coupling TiO₂ to a narrow-band gap semiconductor to enhance the photocatalytic efficiency under visible light irradiation. Coupling semiconductors with different band gap structures could enhance the electron-hole separation and increase the charge carrier lifetime,

which consequently enhances the photodegradation efficiency [7].

Metal chalcogenides semiconductors have narrow band gap and show good photocatalytic activity under visible light illumination [8, 9]. ZnSe is a type of II-VI semiconductor with a band gap of 2.67 eV at room temperature, which can be excited by visible light [10]. The chalcogenide semiconductors have been fabricated by different methods. Mechanochemical method is one of the powerful techniques for synthesis of sulfides. Mechanochemical synthesis of various chalcogenide semiconductors has been described in several works [11-15]. This preparation route concerns the solid state reactions induced by mechanical energy [16]. Gock and co-authors have described the industrial production of nanoscale metal sulfides by means of reactive grinding [17]. Recently, our research group reported the mechanochemically synthesized CdS-TiO₂ and ZnS-TiO₂ nanocomposites for use in photocatalytic applications [18, 19]. The coupling of CdS to TiO₂ may reduce the band gap of CdS-TiO₂ nanocomposites, thus facilitating the absorption of visible light [18].

The main aim of present research is to investigate photocatalytic properties of the ZnSe-TiO₂ composite prepared by mechanochemical synthesis. We chose the toxic and mutagenic methyl orange dye as a target pollutant because it is stable under visible light irradiation [20]. The photo-catalytic performance was evaluated by the removal efficiency of methyl orange (MO), involving the degradation.

* To whom all correspondence should be sent
E-mail: nkostova@ic.bas.bg

Moreover, the photocatalytic degradation kinetics and mechanism, so as the reusability of ZnSe-TiO₂ photocatalyst were studied.

EXPERIMENTAL

Materials

Chemicals used for the synthesis were zinc (97% mean particle size 39 μm , Iteq, Slovakia) and selenium powders (99.5%, mean particle size 46 μm , Aldrich, Germany) and commercial TiO₂ P 25 (Degussa, Holland). They were applied as received without further purification. Methyl orange was used in this study as a representative azo dye for the assessment of photocatalyst dye degradation ability. Methyl orange is an anionic azo dye which also works as a pH indicator (chemical formula C₁₄H₁₄N₃NaO₃S; chemical name 4-[4-(Dimethylamino)phenylazo]benzenesulfonic acid sodium salt; M 327.33; orange colour; pH 4.4).

Powder preparation

The ZnSe-TiO₂ composite was prepared by a two-step method. Firstly, the mechanochemical synthesis of ZnSe nanoparticles was performed by milling of the mixture of zinc and selenium powders in an industrial eccentric vibratory mill ESM 656-0.5 ks (Siebtechnik, Germany), according to the reaction: $\text{Zn} + \text{Se} = \text{ZnSe}$. The reaction is thermo-dynamically possible because of the negative value of enthalpy change $\Delta H_{298}^0 = -159 \text{ kJ mol}^{-1}$.

The following conditions were used for mechanochemical synthesis in the industrial eccentric vibratory mill: chamber and balls – tungsten carbide, balls diameter 30 mm with a total mass of 17 000 g; rotation speed of motor – 960 rpm, the amplitude of the inhomogeneous vibrations – 20 mm and milling time 15 min; loading of the mill – material of 5 L, milling mass of Zn – 45.3 g, mass of Se – 54.7 g, milling atmosphere – Argon. After that as prepared ZnSe powder was milled together with TiO₂ P 25 Degussa at a ratio of 1:4 for 30 min in a high-energy planetary ball mill at 500 rpm.

Characterization methods

X-ray diffraction measurements were carried out using a X'Pert diffractometer (Philips, Netherlands), working in the geometry with CuK α radiation. The JCPDS PDF database was utilized for phase identification. The crystallite size values of the products were calculated from (111) reflection using Scherrer's equation [21].

The specific surface area was determined by the low-temperature nitrogen adsorption method using a

Gemini 2360 sorption apparatus (Micromeritics, USA).

The diffuse reflectance UV-vis spectra for evaluation of photophysical properties were recorded in the diffuse reflectance mode and transformed to absorption spectra through the Kubelka-Munk function. A Thermo Evolution 300 UV-vis Spectrophotometer (ThermoScientific, USA), equipped with a Praying Mantis device was used. The reflectance data were obtained as a relative percentage of reflectance to a non-absorbing material (spectralon) which can optically diffuse light.

The photocatalytic activity of all samples was measured by means of methyl orange (MO) photo-degradation. The concentration of MO in reaction solution was 10 mg L⁻¹. In a typical measurement, 100 mL of aqueous suspension of MO and 100 mg of the photocatalyst were placed in the semi-batch suspension photocatalytic reactor under constant air flow. The obtained suspension was subjected to stirring in the dark for 30 min to obtain the adsorption-desorption equilibrium between the photocatalysts and organic pollutant. Then, the mixed suspension was kept under visible light illumination by halogen lamp (illumination intensity 8.9 mW·cm⁻²). All experiments were performed at a constant stirring rate of 400 rpm at room temperature. At a given time interval the illumination was stopped, 6 mL of suspension was sampled and centrifuged to remove the photo-catalyst. The temporal concentration of MO was estimated at 463 nm using a SPEKOL 11 (Carl Zeiss Jenna, Germany) spectrophotometer. Each analyzed aliquot sample was returned to the reaction mixture after the spectrophotometric measurement for further operation under constant volume. The illumination was switched on again.

RESULTS AND DISCUSSION

Fig. 1 shows the X-ray powder diffraction pattern of the mechanochemically synthesized product formed after 15 min of milling in the industrial vibratory mill. The XRD peaks at $2\theta = 27.3, 45.2, \text{ and } 53.6^\circ$ were indexed as the (111), (220), and (331) planes of cubic ZnSe. It is worth to note that the traces of the un-reacted Zn phase were also detected. The XRD analysis of the mechano-chemically synthesized ZnSe product confirmed its nanocrystalline nature. Calculated crystallite size using the reflection of ZnSe (111) plane was 10 nm.

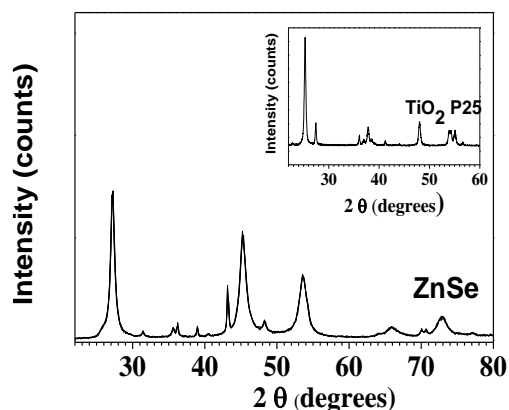


Fig. 1. XRD patterns of mechanochemically synthesized ZnSe, ZnSe-TiO₂, and commercial TiO₂ P25 (inset).

The specific surface area of mechanochemically synthesized ZnSe was 2.33 m²g⁻¹ and that of the commercial TiO₂ P25 was 52 m²g⁻¹. The mechanochemically synthesized ZnSe-TiO₂ composite possessed lower specific surface area ($S_{\text{BET}} = 40 \text{ m}^2\text{g}^{-1}$) indicating that milling resulted in deterioration of the porous structure. The reduction of S_{BET} value of TiO₂ upon milling was also reported in [22].

The optical properties of semiconductors were investigated by UV-visible diffuse reflectance spectroscopy. The absorbance data were obtained from diffuse reflectance data by the Kubelka-Munk method and the results are shown in Fig. 2. The absorption edge of TiO₂ P25 is located only in the UV region.

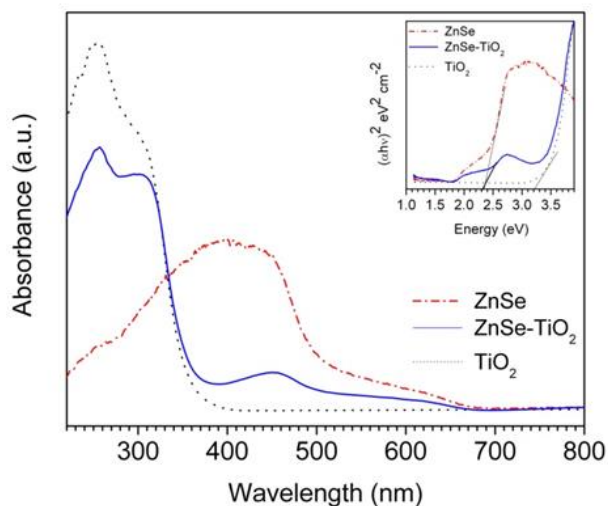


Fig. 2. UV-vis DRS of the TiO₂, ZnSe and ZnSe-TiO₂ samples. The inset shows plot of $(\alpha h\nu)^2$ vs. photon energy for the band gap energy.

The experimental result indicated that the mechanochemically synthesized ZnSe powder possessed good visible light absorption. This result is in accordance with the brownish colour of the

sample. It can be seen from Fig. 2 that after the coupling of mechanochemically synthesized ZnSe with TiO₂ P25, a well defined absorbance in the visible light region was observed in the optical properties of the ZnSe-TiO₂ composite and it was significantly enhanced compared to pure TiO₂.

The band gap energy (E_g) was calculated by a modified Kubelka-Munk function, $F(R)$ [23]. $F(R) = (1-R)^2/2R = K/S$, where K and S are the absorption and scattering coefficients, respectively. The absorption coefficient α is related to the incident photon energy by means of the Tauc's equation [24] $\alpha h\nu = C(h\nu - E_g)^{1/2}$, where C is a proportionality constant and $h\nu$ is the photon energy. The band gap of mechanochemically synthesized ZnSe was estimated by plotting $(\alpha h\nu)^2$ vs. $h\nu$ as shown in inset of Fig. 2 and extrapolating the linear portion near the onset of absorption edge to the energy axis. The band gap of mechanochemically synthesized ZnSe is 2.33 eV, which is narrower than that of bulk ZnSe (2.67 eV). Compared to TiO₂ P25, the band gap value of ZnSe-TiO₂ is smaller, indicating that the absorption ability of ZnSe-TiO₂ can be extended by coupling ZnSe to TiO₂.

The photocatalytic performance of the samples was evaluated under visible light irradiation using methyl orange azo dye as a model contaminant. Fig. 3a shows MO adsorption on the ZnSe, ZnSe-TiO₂ and TiO₂ samples measured at regular time intervals in the course of the dark period. The adsorption on the surface of the particles is fast during the initial 5 minutes. After that, there is a slight increase in adsorption until equilibrium is reached after 30 min of contact time. The adsorption capacities are determined using the equation: $Q = (C_0 - C) \cdot V/m$, where C_0 and C are the initial and current concentrations, respectively, V is the volume of the solution; m is the mass of the catalyst. The adsorption capacity of the photocatalysts in respect of MO dye after 30 min contact time without irradiation follows the line $\text{ZnSe} < \text{ZnSe-TiO}_2 < \text{TiO}_2$. The results show that the MO adsorption capacity of mechanochemically synthesized ZnSe is very small.

Fig. 3a inset indicates the absorption spectra of MO solution with the sample ZnSe-TiO₂ during visible light illumination. MO has an important peak at 463 nm that was monitored for investigating the MO degradation. Increasing illumination time, the absorption peak intensity decreased indicating photodecolourization of MO. Change in the solution colour also indicates and confirms the photodegradation of MO dye by ZnSe-TiO₂. The loss of absorbance was due to the destruction of the dye - N=N- chromophore group.

As shown in Fig. 3b, almost no MO degradation could be observed under visible light irradiation in the absence of a photocatalyst, suggesting that degradation by direct photolysis could be ignored. TiO₂ P25 exhibits only 4% photocatalytic efficiency under visible light irradiation which can be attributed

to its wide 3.2 eV band gap. Among the mechanochemically prepared samples, ZnSe-TiO₂ composite shows the highest photocatalytic activity with 80% MO degradation in 120 min (Fig. 4). The photocatalytic activities decreased in the order, ZnSe-TiO₂ > ZnSe > TiO₂.

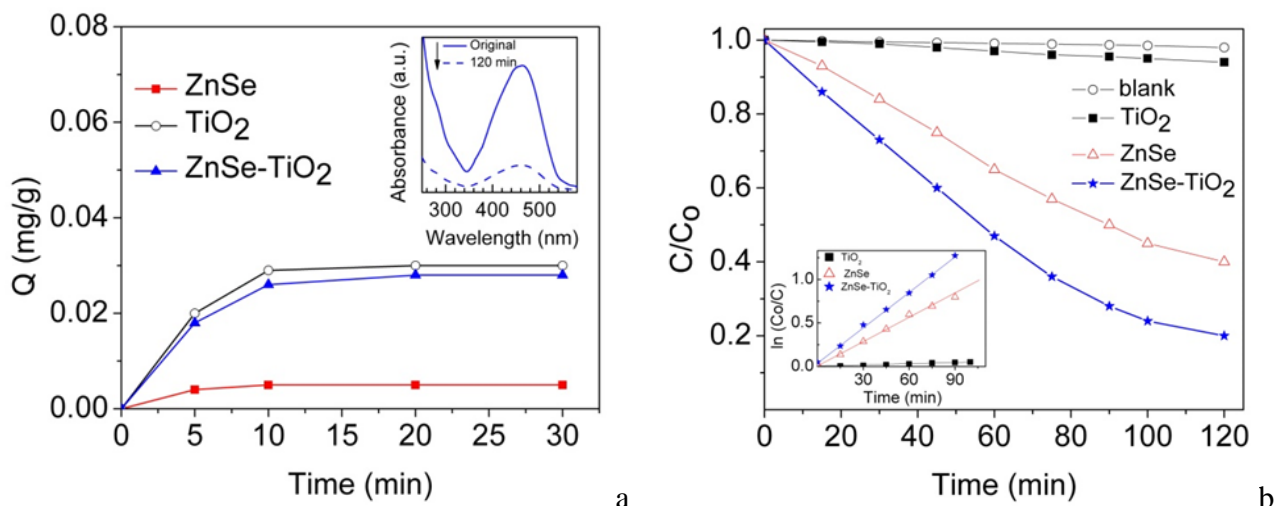


Fig. 3. a – Comparison of MO adsorption in dark on TiO₂, ZnSe, and ZnSe-TiO₂ samples and absorption spectra of original MO and after irradiation for 120 min in presence of ZnSe-TiO₂ composite (inset).; b – Degree of MO degradation as a function of irradiation time of blank experiment (without photocatalyst), TiO₂, ZnSe, and ZnSe-TiO₂ samples; kinetic curves of photocatalytic degradation of MO under visible light irradiation (inset).

The photocatalytic degradation process involving MO in aqueous solution can be interpreted through a modified Langmuir-Hinshelwood kinetic model. The reaction kinetics can be expressed as $\ln(C_0/C) = kt$, where C_0 and C are the initial and actual concentration of MO, respectively, and k is the apparent rate constant of the degradation. The photodegradation of MO under visible light irradiation, catalyzed by the mechanochemically synthesized ZnSe and ZnSe-TiO₂ fits pseudo-first order reaction (Fig. 3b inset). The rate constant of MO photocatalytic degradation over suspended semiconductor materials irradiated with visible light decreases in the following order: ZnSe-TiO₂ > ZnSe > TiO₂ (Fig. 3b inset). Compared with mechanochemically synthesized ZnSe the ZnSe-TiO₂ composite showed a 1.61-fold increase in the rate constant of MO degradation under visible light irradiation. The higher value of the rate constant of MO degradation with ZnSe-TiO₂ can be explained in terms of an increased rate of charge carriers (h^+ and e^-) separation in the photoexcited composite as a dominating kinetic factor.

The reusability of the ZnSe was also studied. Recycling experiments of ZnS-TiO₂ and ZnSe for MO photocatalytic degradation under visible light irradiation were carried out and the results are presented in Fig. 5. After each examination, the ZnSe was immersed into fresh MO azo dye solution of the

same concentration for another cycle. This process was repeated 4 times. There was no significant change in the efficiency of ZnSe photocatalyst even after four runs. This shows the reusability and stability of the mechanochemically prepared ZnSe photocatalyst.

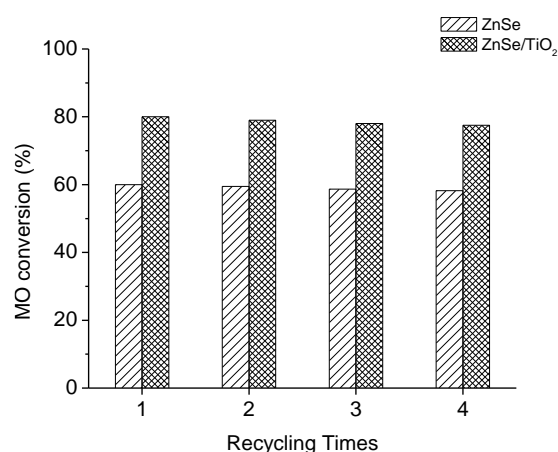


Fig. 4. The reusability diagrams of mechanochemically synthesized ZnSe and ZnSe-TiO₂ for 4 runs.

Methyl orange azo dye is characterized by nitrogen double bond ($-N=N-$) that is usually attached to radicals of aromatic groups. The azo bond is the most active bond in the azo dye molecules and can be oxidized by a positive hole or hydroxyl

radical or reduced by an electron in the conduction band. The cleavage of -N=N- bond leads to the decolorization of dye. The energy of the band gap of the mechanochemically synthesized ZnSe-TiO₂ estimated from the DRS is 2.33 eV. It is helpful to generate higher electron and hole pairs. When the ZnSe-TiO₂ composite is irradiated with visible light, it results in the excitation of electrons (e⁻) into the conduction bands (CB) of both TiO₂ as well as ZnSe semiconductors thereby leaving the holes (h⁺) behind in their valence bands (VB). Owing the suitable positions of conduction band and valence band, the electrons from the CB of ZnSe are transferred to conduction band of TiO₂, whereas the holes from TiO₂ valence band are thereby transferred to the VB of ZnSe (Fig. 5). The holes are subsequently trapped by absorbed H₂O on the surface of ZnSe to generate highly reactive hydroxyl radicals (•OH). The conduction band electrons may react with dissolved oxygen to form a superoxide anion radical (•O₂⁻). The radicals including •OH and •O₂⁻ present strong oxidizing properties and are able to cause deprecation of MO [8].

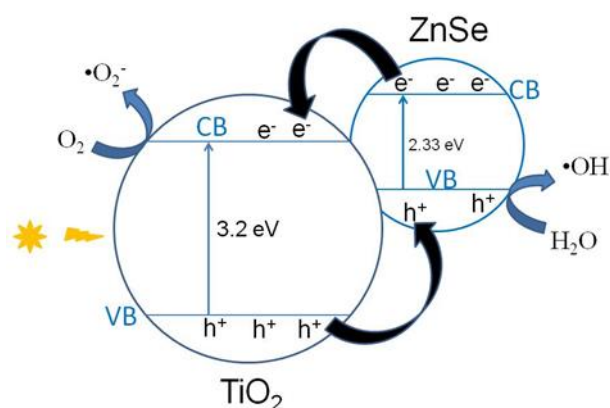


Fig. 5. The suggested mechanism for charge transfer of the photogenerated electrons and holes on mechanochemically synthesized ZnSe-TiO₂ under visible light irradiation.

To understand the mechanism of MO degradation on ZnSe-TiO₂ composite, it is necessary to detect which reactive species play a major role in the photocatalytic degradation process. During photodegradation of MO over ZnSe-TiO₂ composite, the h⁺, •OH, and •O₂⁻ are eliminated by adding EDTA (h⁺ scavenger), TBA - *tert*-butyl-alcohol (•OH scavenger) and BQ - *p*-benzoquinone (•O₂⁻ scavenger) into the reaction solution, respectively. Fig. 6 shows the MO photodegradation over ZnSe-TiO₂ composite in the absence and

presence of scavengers. The decrease of the removal rate in the presence of scavengers presents the following trend: BQ > EDTA > TBA. Hence, the superoxide radical is the main reactive species during photocatalytic degradation of MO. Thus, it was reasonable to conclude that •O₂⁻, h⁺, and •OH as oxidation species were indeed photogenerated on catalyst surface and responsible for the photocatalytic degradation of MO over mechanochemically synthesized ZnSe-TiO₂ composite.

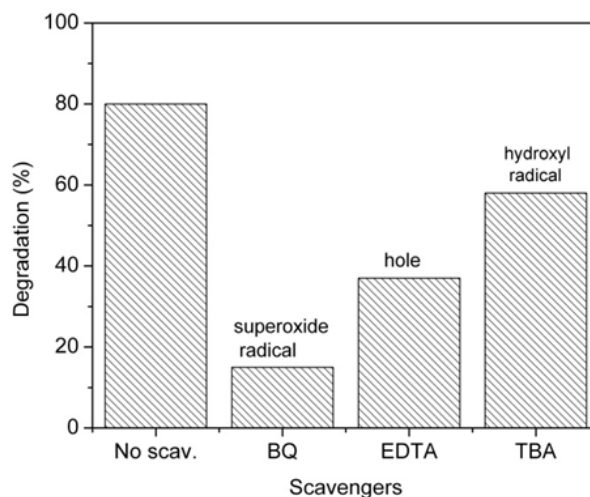


Fig. 6. Effect of different scavengers on MO photodegradation under visible light over the mechanochemically synthesized ZnSe-TiO₂ composite.

The mechanochemically synthesized ZnSe was demonstrated as an effective, environmentally safe and recyclable photocatalyst under visible light. The good photocatalytic properties of ZnSe open a new region of possible applications. The main advantage of the mechanochemically synthesized sample is that their band gaps is about 2.33 eV in comparison to TiO₂ (3.2 eV), which leads to the observed higher photocatalytic activity of ZnSe and ZnSe-TiO₂ composite under visible irradiation.

CONCLUSIONS

The industrial vibratory mill has been proved as an effective reactor for solid state synthesis of ZnSe nanoparticles starting from zinc and selenium as reaction precursors. The final ZnSe material possesses the cubic crystal structure. ZnSe-TiO₂ composite has been successfully synthesized by mechanochemical route. The photocatalytic results exhibit higher efficiency of the composite in comparison with pure ZnSe and TiO₂ under visible light. The reaction is pseudo-first order. The mechanochemically synthesized ZnSe-TiO₂ composite was demonstrated as an effective, environmentally safe and recyclable photocatalyst.

Acknowledgements: The present work was supported by the Bulgarian National Science Fund by project DNTS/Slovakia 01/2, Slovak Research and Development Agency APVV-18-0357 and „Research Centre of Advanced Materials and Technologies for Recent and Future Applications „PROMATECH“, ITMS 26220220186, of the Operational Program “Research and Development” financed through European Regional Development Fund.

REFERENCES

1. K. Daghrir, P. Drpgui, D. Robert, *Ind. Eng. Chem. Res.*, **52**, 3581 (2013).
2. L. Pan, X. Liu, Z. Sun, C. Q. Sun, *J. Mater. Chem. A*, **1**, 8299 (2013).
3. M. N. Gancheva, P. M. Konova, G. M. Ivanov, L. I. Aleksandrov, R.I. Iordanova, A.I. Naydenov, *Bulg. Chem. Commun.*, **50** Special issue, H 93 (2018).
4. V. Iliev D. Tomova, A. Eliyas, S. Rakovsky, M. Anachkov, L. Petrov, *Bulg. Chem. Commun.*, **47**, Special Issue C, 5 (2015).
5. M. Balaz, E. Dutkova, Z. Bujnakova, E. Tothova, N.G. Kostova, Y. Karakirova, J. Briancin, M. Kanuchova, *J. Alloys Comp.* **746**, 576 (2018).
6. O. Carp, C.L. Huisman, A. Reller, *Prog. Solid State Chem.*, **32**, 33 (2004).
7. N. G. Kostova, M. Fabian, E. Dutkova, N. Velinov, Y. Karakirova, M. Balaz, *Bulg. Chem. Commun.*, **50**, Special Issue H, 109 (2018).
8. K. Liu, L. Zhang, N. J. Ji, H. Liu, *Optoelectronics Adv. Mater. Rapid Commun.*, **8**, 873 (2014).
9. C. Sun, Y. Gue, W. Wen, L. Zhao, *Optical Mater.*, **81**, 12 (2018).
10. D. Ayodhya, G. Veerabhadram, *Mater. Today Energy*, **9**, 83 (2018).
11. P. Balaz, M. Balaz, E. Dutkova, A. Zorkovska, J. Kovac, P. Hronec, J. Kovac Jr., M. Chaplovicova, J. Mojzis, G.Mojzisoava, A. Eliyas, N. G. Kostova, *Mater. Sci. Eng. C*, **58**, 1016 (2016).
12. P. Balaz, M. Balaz, M. Achimovicova, Z. Bujnakova, E. Dutkova, *J. Mater. Sci.*, **52**, 11851 (2017).
13. M. Achimovicova, N. Daneu, E. Dutkova, A. Zorkovska, *Appl. Phys. A – Mater. Sci. & Process.*, **123** (3) Article Number 154 (2017).
14. M. Achimovicova, P. Balaz, Nanocrystalline metal selenides: Mechanochemical synthesis and utilizable properties, in: *Milling Fundamentals, Processes and Technologies* (M. Ramirez Ed.) pp. 71-122 (Book Chapter) ISBN-13, 978-1634830225, Nova Science Publishers, Inc. New York, 2015.
15. E. Dutkova, M. Caplovicova, I. Skorvanek, M. Balaz, A. Zorkovska, P. Balaz, L. Caplovic, *J. Alloys Comp.*, **745**, 863 (2018).
16. K. Assaker, B. Lebeau, L. Michelin, P. Gaudin, C. Carteret, L. Vidal, M. Bonne, J. L. Blin, *J. Alloys Comp.*, **649**, 1 (2015).
17. M. Achimovicova, P. Balaz, J. Durisin, N. Daneu, J. Kovac, A. Satka, A. Feldhoff, E. Goch, *Intern. J. Mater. Res.*, **102**, 441 (2011).
18. N.G. Kostova, E. Dutkova, A. Eliyas, E. Stoyanova-Eliyas, M. Fabian, P. Balaz, *Bulg. Chem. Commun.*, **47**, Special issue C pp.87 (2015).
19. N.G. Kostova, E. Dutkova, *Bulg. Chem. Commun.*, **48**, Special Issues G, 161 (2016).
20. K. T. Chung, C. E. Cerniglia, *Mutat. Res.*, **277**, 201 (1992).
21. H. P. Kligg, L. E. Alexander, *X-Ray Diffraction Procedures*, Wiley, New York, 1954; P. Scherrer, Bestimmung der Größe und der inneren Struktur von Kolloidteilchen mittels Röntgenstrahlen, *Nachr Ges Wiss Göttingen*, **26**, 98–100 (1918).
22. P. Dulian, M. Buras, W. Zukovski, *Polish J. Chem. Technol.* **18**, 68 (2016).
23. S. Valencia, J. M. Marin, G. Resrepo, *Open Mater. Sci. J.*, **4**, 9 (2010).
24. J. Tauc, R. Grigorovic, A. Vancu, *Phys. Status Solidi*, **15**, 627 (1966).

Toxicity prediction of organophosphorus compounds by QSAR

A. Hatipoglu*, S. Aydogdu, H. Dedeoglu, D. Civan

Yıldız Technical University, Chemistry Department, 34220, İstanbul, Turkey

Received April 6, 2019; Accepted February 12, 2018

Organophosphorus compounds are often used as pesticides and they are known as major environmentally hazardous chemicals. Conformational analysis and geometry optimizations of all organophosphorus compounds were carried out to determine the most stable structures. Modeling of the molecules was performed with DFT at B3LYP/6-31G* level. The solvation effects were computed using CPCM as the solvation model. A quantitative structure-activity relationship (QSAR) study was performed to correlate the toxicity of the organophosphorus compounds with calculated molecular descriptors by multilinear regression. The QSAR equations were validated internally and externally. The correlation coefficient (R^2) and cross-validation correlation coefficient (R^2_{cv}) were 0.9422 and 0.9192, respectively. These results show that the QSAR equations have both favourable estimation stability and good prediction power.

Keywords: DFT, toxicity, molecular descriptors, solvent effect.

INTRODUCTION

Organophosphorus compounds (OPs) are often used as pesticides, as insecticides and as warfare agents [1,2]. Organophosphorus compounds are known as major environmentally hazardous chemicals. It is estimated that only 5% of the consumed pesticides reach the target pest, the rest is dispersed into the environment. The increasing use over time is significantly enhancing the risks of environmental contamination of groundwater, food, plants, water resources and human beings [1,3-5]. Organophosphorus compounds are highly toxic and show their acute toxic effects by inhibiting the enzyme acetylcholinesterase (AChE). This inhibition leads to paralysis and even death. Different studies have shown that pesticide exposure is associated to adverse health effects such as depression, memory disorders, respiratory problems, dermal damage, neurological deficit, miscarriages, birth deformities and cancer [4,6,7].

There is a need for evaluating the potential hazard of these pesticides but traditional experimental investigations are often extremely time-consuming and expensive. One practical alternative would be to predict these toxic effects by using quantitative structure-activity relationships (QSARs) or quantitative structure-toxicity relationships (QSTRs) [8,9]. QSAR studies have been developed to assess the amount of toxicity for different chemicals from their molecular structure point of view. In development of QSAR, the descriptors fall into three classes: (i) physical or physicochemical properties (ii) quantum chemical descriptors and (iii) topological descriptors. These

descriptors are found to be useful because they help to characterize the electronic environment of a molecule [10,11].

Quantum-chemical descriptors have become quite popular recently and are widely used due to the reliability and accuracy, as well as capability to characterize the electronic properties of the molecule. Among the variety of computational approaches, density functional theory (DFT) is one of the most commonly used. The conceptual density functional theory has been exploited in various occasions to understand the chemical reactivity and site selectivity [1,12]. Several studies have been performed for the toxicity of organophosphates and organothiophosphates against different aquatic organisms. Many models have been derived for OPs with topological indices [1,2,5,13] and some of them derived with the logarithm of the octanol-water partition coefficient or some other physical properties [9, 13-18]. The models mentioned can be used to explain the toxicity of organophosphate and organothiophosphate pesticides.

However, the toxicity studies of OPs need to be improved because these molecules are hazardous for the environment. The aim of this work was to develop QSAR models to find suitable molecular descriptors to predict the toxicity of OPs. For this purpose various molecular descriptors such as hardness (η), energy of the highest occupied molecular orbital (E_{HOMO}), dipole moment (D) and charge of phosphorus atom (P_{ch}) were calculated. The relationships between the experimental rat oral lethal dose (LD_{50}) of the molecules and the calculated descriptors were examined through multilinear regression in order to determine the best

* To whom all correspondence should be sent:
E-mail: hatiparzu@yahoo.com

descriptor of the toxicity of the molecule. In order to determine both the stability and predictive power of QSAR models, leave-one-out cross-validation and external validation were performed on the developed models.

The general chemical structure of OPs is shown in Fig. 1 where R are methyl or ethyl groups and X - leaving groups such as alkyl, heterocyclic, etc. The optimized geometries of the OP molecules in this study are given in Figs. 2 and 3.

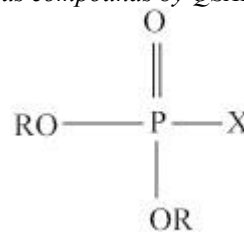


Figure 1. General structure of OPs.

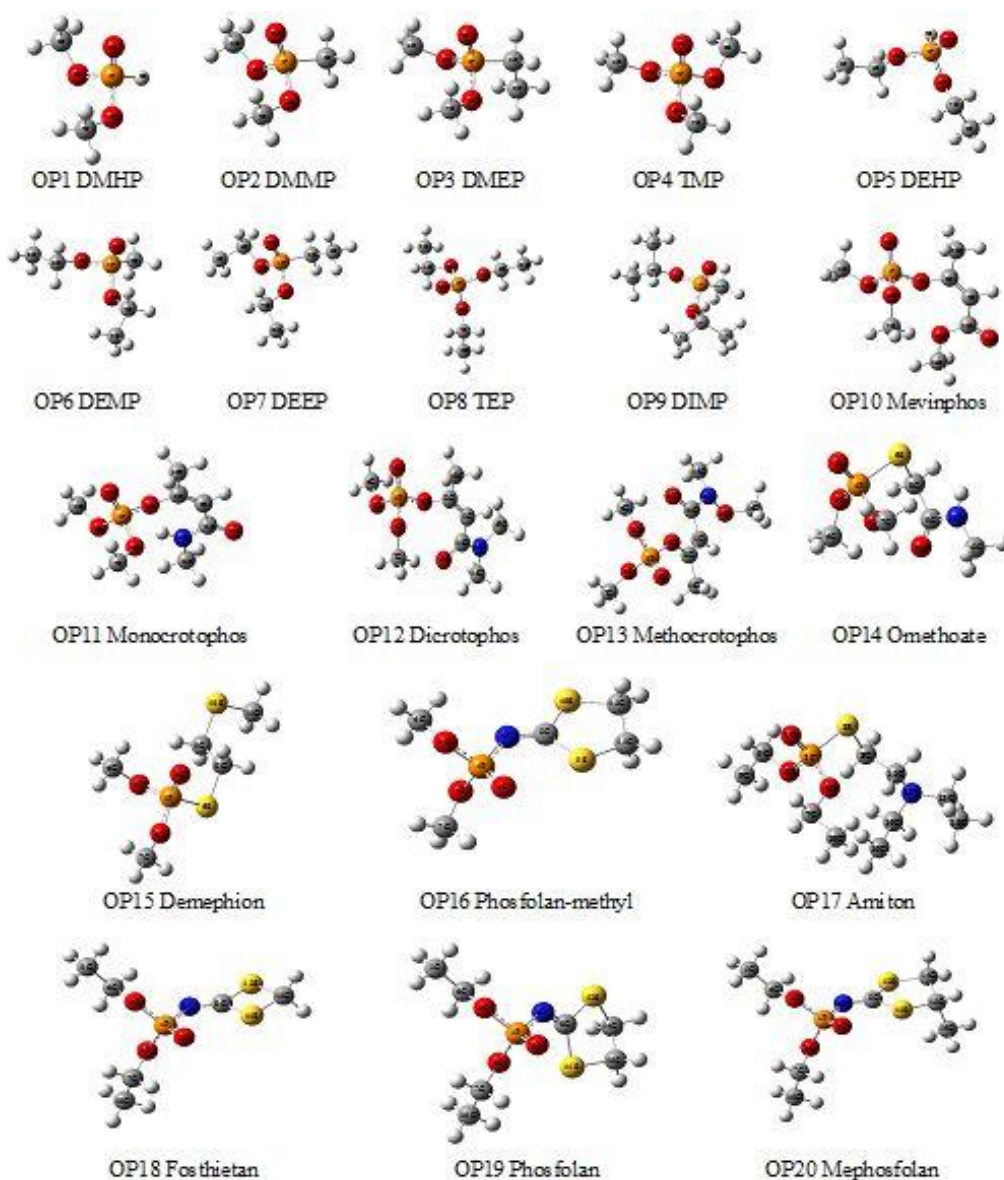


Figure 2. Optimized structure of training set (gray, carbon; red, oxygen; blue, nitrogen; orange, phosphorus; yellow, sulphur; blue, nitrogen; green, chlorine; white, hydrogen)

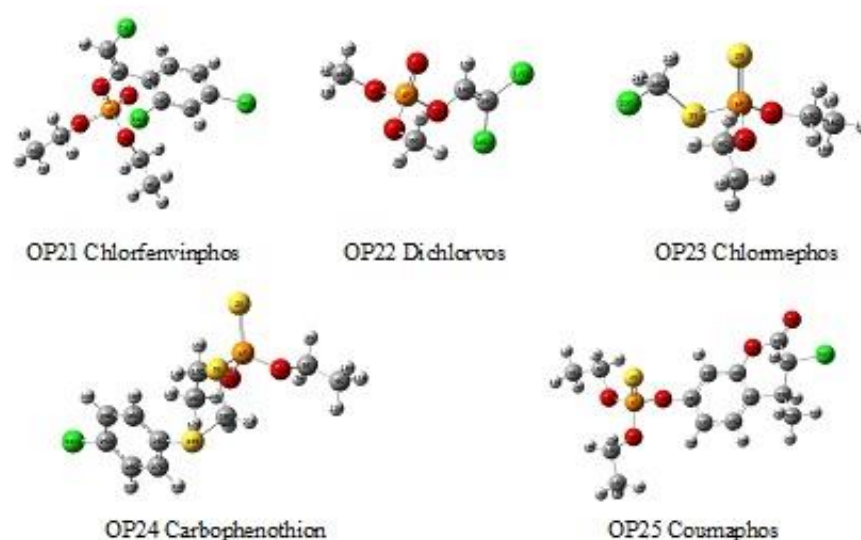


Figure 3. Optimized structure of the test set.

Table 1. Calculated molecular descriptors, η (au), E_{HOMO} (au), D (Debye), P_{charge} and experimental LD_{50} (mg/kg) for OP compounds.

	η	E_{HOMO}	D	P_{charge}	LD_{50}
OP 1	0.1827	-0.3010	2.7848	1.0072	3283
OP 2	0.1801	-0.2963	2.6548	1.1150	8210
OP 3	0.1752	-0.2885	2.5056	1.1482	1900
OP 4	0.1753	-0.3031	0.9631	1.1951	1095
OP 5	0.1807	-0.2987	5.2988	1.0235	4350
OP 6	0.1809	-0.2936	2.8593	1.1134	800
OP 7	0.1789	-0.2899	2.7453	1.1263	2330
OP 8	0.1757	-0.2984	4.7914	1.2348	1600
OP 9	0.1735	-0.2852	2.8630	1.1304	984
OP 10	0.1082	-0.2619	3.7891	1.2534	6.3
OP 11	0.1088	-0.2512	5.9621	1.2434	18.3
OP 12	0.1063	-0.2389	6.2476	1.2504	18.8
OP 13	0.1018	-0.2449	4.6495	1.2618	2
OP 14	0.1229	-0.2539	5.3691	1.0833	22
OP 15	0.1142	-0.2346	4.9309	1.0799	20
OP 16	0.1073	-0.2582	4.8449	1.1762	51
OP 17	0.1022	-0.1999	5.4711	1.0635	3.3
OP 18	0.1047	-0.2647	2.9489	1.1851	4.7
OP 19	0.1059	-0.2585	8.2244	1.1866	8.9
OP 20	0.1074	-0.2568	4.7903	1.1761	8.9
OP21	0.1055	-0.2494	3.7317	1.2874	10
OP22	0.1209	-0.2495	3.4911	1.2067	17
OP23	0.1123	-0.2603	2.9430	0.7863	7
OP24	0.1043	-0.2464	5.9263	0.7924	6.8
OP25	0.1052	-0.2467	7.8190	1.0026	13

Table 2. Statistical parameters for model equations

No	Equations	R	R^2	R_{adj}^2	SD	F
1	$\log LD_{50} = -2.70314 + 0.20416 P_{ch} + 32.53254 \eta$	0.9696	0.9402	0.9327	0.3106	125.7278
2	$\log LD_{50} = -3.13745 - 3.1370 E_{HOMO} + 31.08450 \eta$	0.9688	0.9386	0.9314	0.3237	129.9486
3	$\log LD_{50} = -3.13491 + 0.06483 D + 35.14140 \eta$	0.9707	0.9422	0.9354	0.3141	138.4956

Computational method

Computational studies were carried out using the Gaussian 03 software suite [19]. The molecular structures of 25 OPs were optimized using Density Functional Theory (DFT) with the three-parameter Becke–Lee–Yang–Parr (B3LYP) exchange–correlation functional at 6-31G (d) level. The force constants and vibrational frequencies of the molecules were determined after optimizing their geometries to ensure that they are minimal on the potential energy surface. The molecular descriptors were calculated from the orbital energies of the optimized geometries. The conductor-like polarizable continuum model (CPCM) was used to model solvent effects. The solvent was water at 25°C, with dielectric constant $\epsilon = 78.39$ [20].

Density functional theory was used extensively to calculate molecular properties of environmental organic pollutants [21]. In this study we calculated the global descriptor, namely hardness (η), for the toxicity predicting of OPs. According to the DFT, hardness, η , is defined as [22]:

$$\eta = \frac{1}{2} \left(\frac{\partial^2 E}{\partial N^2} \right)_{V(r)} \quad (1)$$

where E is the total energy of the system, N is the number of electrons in the system, and $v(r)$ is the external potential.

Hardness is calculated by using Koopmans' theorem [22]:

$$\eta = \frac{E_{LUMO} - E_{HOMO}}{2} \quad (2)$$

where E_{LUMO} is the energy of the lowest unoccupied molecular orbital and E_{HOMO} is the energy of the highest occupied molecular orbital.

All calculated descriptors such as hardness, energy of the highest occupied molecular orbital, dipole moment and charge of phosphorus atom, are listed in Table 1 for aqueous medium.

Data sources

The QSAR models presented in this paper were developed on 25 OP compounds. These compounds were divided into two groups: 20 OPs for the training set (OP1-OP20) given in Fig. 2 and 5 OPs for the test set (OP21-OP25) given in Fig. 3.

The toxicity of each compound was qualified in terms of LD_{50} (mg/kg). LD stands for "Lethal Dose". The value of LD_{50} for a substance is the dose required to kill half the members of a tested population after a specified test duration. LD_{50} is frequently used as a general indicator for acute toxicity. The experimental rat oral LD_{50} values

obtained from the literature are presented in Table 1 [23].

Statistical analysis

A QSAR model is a mathematical relationship between the chemical's quantitative molecular descriptors and its toxicological, biological, and physicochemical activities [24]. Multilinear regression is a common method used in QSAR studies. The multilinear regression is a statistical method used to find a relation between one dependent variable and several independent variables. This relation can be expressed as:

$$Y = A x_j + B y_j + C z_j + \dots + D$$

where A, B, C are regression coefficients and D is the intercept obtained through regression analysis, where x_j , y_j and z_j are the quantum chemical descriptors for the molecule J as independent variables. Y , as dependent variable, represents the expected values by the regression model.

The statistical qualities of the regression equations were judged by parameters such as R^2 (correlation coefficient), R^2_{adj} (adjusted correlation coefficient), F value (Fischer statistics) and SD value (standard deviation). Testing the stability, predictive power and generalization ability of the models is a very important step in QSAR study. As for the validation of predictive power of a QSAR model, two basic principles (internal validation and external validation) are available. The cross-validation is one of the most popular methods for internal validation. In this paper, the stability and prediction ability of models were examined by using leave-one-out (LOO) cross-validation. Cross-validation provides the values of PRESS (Predictive Residual Error Sum of Squares), SSY (Sum of squares of deviation of the experimental values from their mean) and R^2_{CV} coefficient (Cross-validation correlation coefficient) which can test the predictive power of the proposed model [25].

RESULTS AND DISCUSSION

QSAR analysis

This study was carried out for some 25 OP compounds in order to determine a quantitative structure–activity relationship between the molecular descriptors and the rat oral LD_{50} toxicity values. Regression analyses were performed using the experimental toxicity $\log LD_{50}$ as the dependent variable and the DFT-based descriptors, namely hardness (η), highest occupied molecular orbital energy (E_{HOMO}), dipole moment (D) and charge of phosphorus atom (P_{ch}) as the independent variables.

Twenty training compounds (OP1-OP20) were used for all model equations.

Table 3. Cross-validation parameters for the model equations.

	PRESS	$\frac{PRESS}{SSY}$	R^2_{CV}
Equation 1	2.0466	0.0835	0.9165
Equation 2	2.4796	0.0855	0.9145
Equation 3	2.3441	0.0808	0.9192

With the intention of finding certain molecular descriptors in order to determine the toxicity of OPs, we derived model equations by forward stepwise regression analysis. Among the several models generated, the three best two-parameter models were selected and they are listed in Table 2. The selection was based on the following mentioned statistically parameters. Generally, the higher R^2 and the higher F value indicate that the model is reliable. It is commonly assumed that a robust and reliable correlation is indicated by $R^2 \geq 0.75$ and $SD \leq 0.5$ [26]. As seen in Table 2, the derived model equations are statistically reliable, the correlation coefficients were found to be good (0.9386 – 0.9422) and the standard deviations were below 0.33. According to the model equations, dipole moment, charge of phosphorus atom and hardness positively affected toxicity; in contrast, the energy of the highest occupied molecular orbital had a negative correlation. In the derived model equations, the greatest value of regression coefficient was for hardness, it played a dominant role in the toxicity of OPs.

Validation of the QSAR models

In order to confirm that the models with excellent statistics have excellent predictive power too, we evaluated cross-validation parameters for model equations. Calculated cross-validation results are presented in Table 3 and results indicate that all models proposed were significant. The cross-validation was performed using the leave-one-out method (LOO) in which one compound is removed from the training set and the toxicity is correlated using the rest of the training set. Cross-validation provides the values of PRESS, SSY, PRESS/SSY and R^2_{CV} which we can use to test the prediction power of the model equation. PRESS is a good estimate of the real prediction error of the model equations. If PRESS is smaller than the SSY the model is considered to be statistically significant. In a reasonable QSAR model PRESS/SSY should be smaller than 0.4 and R^2_{CV} should be bigger than 0.5 [25]. In our results, good cross-validation R^2_{CV} was obtained for the models. As seen in Table 3, cross-

validation correlation coefficient R^2_{CV} values range from 0.9145 to 0.9192. The ratio PRESS/SSY ranges between 0.0808 – 0.0855 indicating that all proposed models are reliable.

Finally, in order to confirm our findings, the toxicity of the OPs predicted log LD₅₀ by model equations was compared with corresponding observed log LD₅₀ values. These comparisons are shown in Table 4. As is seen in the table, the predicted toxicity values agree with the experimental ones. The residual is the difference between observed and predicted log LD₅₀. The two numeric values are close enough to each other. The plot between the predicted and the observed toxicity values of OP compounds is shown in Fig. 4. The predictive ability of the QSAR models was also evaluated by external validation. The external validation results are given in Table 4. As seen in the table, the two numeric values (observed and predicted) are close to each other. This shows that the equations have excellent determining capability of the OP compounds toxicity.

Toxicity interpretation by QSAR analysis

Based on the QSAR equations, the main descriptors that could impact the toxicity of OPs were η , E_{HOMO} , D and P_{ch} . Hardness is a measure of the stability of the molecule. According to the maximum hardness principle (MHP) molecules arrange themselves so as to be as hard as possible [22]. Therefore, stable molecules are likely to be harder than less stable molecules and thus they have low reactivities. Hardness is the most important descriptor for the toxicity of OPs, as mentioned above. The positive coefficient of hardness demonstrated that the toxicity increases with hardness. E_{HOMO} was negatively correlated with the toxicity which could be seen in equation 2. E_{HOMO} is the electronic energy identical to the corresponding negative value of the ionization potential which can be used to measure the donating electron ability [22]. E_{HOMO} models the nucleophilic nature of the OPs which is important for their reaction with the active site of AChE [14]. Atomic charges are often used as an important concept and describe electronic aspects both of the whole molecule and of particular regions or fragments. They are often used in QSAR studies as descriptors [1,5]. In this study, the charge on the phosphorus atom is particularly important, because it is related with the toxicity of the OPs. The Mulliken charge analysis of the OP compounds shows that the increase in the positive charge on the phosphorus atom in a molecule leads to an increase in toxicity in most of the OP compounds. Fig. 5 shows the molecular electrostatic potential (MEP)

plot for OP12, OP14 and OP19. In the MEP plot, blue and green colors show positive electrostatic potential whereas red color shows negative electrostatic potential. As can be seen in Fig. 5, positive electrostatic charge regions belong to phosphorus and hydrogen atoms. Negative electrostatic charge regions represent oxygen atoms. In the electrostatic potential map, the phosphorus atom is in the centre of negative and positive charge separation. So inhibition reaction

occurs at this center and X is the leaving group shown in Fig. 1. The inhibition is a nucleophilic substitution which replaces the X group with the hydroxyl group of serine in the active site of AChE [14,27]. Overall, the toxic effect of OPs is mostly related with electronic descriptors as η , E_{HOMO} , D and P_{ch} which show that electron exchange occurs between OPs and biological molecules.

Table 4. Predicted and observed log LD₅₀ of OPs from model equations

	log LD _{50exp}	Eq.1	Residual	Eq.2	Residual	Eq.3	Residual
OP 1	3.5163	3.4462	0.0701	3.4859	0.0304	3.4660	0.0503
OP 2	3.9143	3.3836	0.5307	3.3904	0.5239	3.3662	0.5481
OP 3	3.2788	3.2310	0.0478	3.2136	0.0652	3,1843	0.0945
OP 4	3.0394	3.2438	-0.2044	3.2625	-0.2231	3.0878	-0.0484
OP 5	3.6385	3.3844	0.2541	3.4165	0.2220	3.5587	0.0798
OP 6	2.9031	3.4093	-0.5062	3.4068	-0.5037	3.4075	-0.5044
OP 7	3.3674	3,3469	0.0205	3.3330	0.0344	3.3299	0.0375
OP 8	3.2041	3.2649	-0.0608	3.2602	-0.0561	3.3501	-0.1460
OP 9	2.9930	3.1720	-0.1790	3.1504	-0.1574	3,1477	-0.1547
OP 10	0.7993	1.0728	-0.2735	1.0475	-0.2482	0.9130	-0.1137
OP 11	1.2625	1.0903	0.1722	1.0326	0.2299	1.0750	0.1875
OP 12	1.2742	1.0104	0.2638	0.9163	0.3579	1.0057	0.2685
OP 13	0.3010	0.8663	-0.5653	0.7952	-0.4942	0.7439	-0.4429
OP 14	1.3424	1.5163	-0.1739	1.4793	-0.1369	1.5320	-0.1896
OP 15	1.3010	1.2325	0.0685	1.1483	0.1527	1.1979	0.1031
OP 16	1.7076	1.0277	0.6799	1.0079	0.6997	0.9499	0.7577
OP 17	0.5185	0.8388	-0.3203	0.6665	-0.1480	0.8112	-0.2927
OP 18	0.6721	0,9450	-0.2729	0.9475	-0.2754	0.7356	-0.0635
OP 19	0.9494	0.9843	-0.0349	0.9653	-0.0159	1.1198	-0.1704
OP 20	0.9494	1.0310	-0,0816	1.0066	-0,0572	0.9498	-0.0004
OP21	1.0000	0.9919	0.0081	0.9243	0,0757	0.8144	0.1856
OP22	1.2304	1.4764	-0.2460	1.4033	-0.1729	1.3400	-0.1096
OP23	0.8451	1.1108	-0.2657	1.1699	-0.3248	1.0023	-0.1572
OP24	0.8325	0.8518	-0.0193	0.8776	-0.0451	0.9145	-0.0820
OP25	1.1139	0.9240	0.1900	0.9065	0.2074	1.0689	0.0451

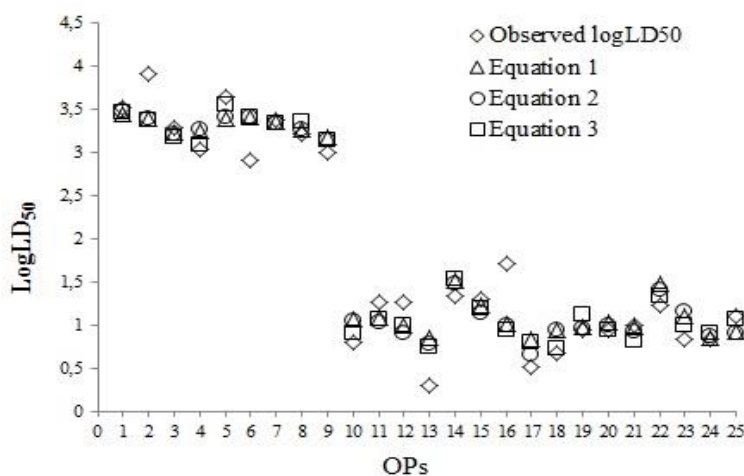


Figure 4. Comparison between the predicted and observed log LD₅₀ values of OPs

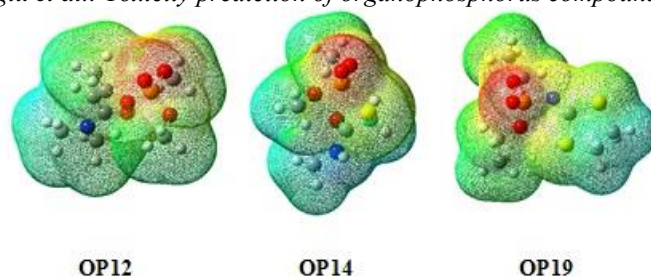


Figure 5. Molecular electrostatic potential representation of selected OPs

CONCLUSIONS

QSAR analysis was performed in this work for selected OPs on their oral toxicity to rats using quantum chemical descriptors. The usefulness of descriptors in the development of QSAR analysis was clarified by statistical analysis. The derived model equations were statistically significant and can be used for prediction purposes; they may be helpful for a better understanding of the toxicity of this class of compounds. It could be concluded that hardness, dipole moment, highest occupied molecular orbital energy and charge of phosphorus atom can be used as descriptors in the prediction of the toxicity of OPs. Due to the success of the developed regression model, it may be utilized to predict the toxicity of other OPs whose experimental toxicity data are not available.

Acknowledgement: The authors express their thanks to Yildiz Technical University Research Foundation (Project No: 2012-01-02-KAP02), for financial support.

REFERENCES

1. Y. Pauku, G. Hill, *Int. J. Quant. Chem.*, **112**, 1343 (2012).
2. R. Garcí'A-Domenech, P. Alarco N-Elbal, G. Bolas, R. Bueno-Mari, F. A. Chorda -Olmos, S. A. Delacour, M. C. Mourin Oz, A. Vidal, J. Ga' Lvez, *J. SAR QSAR Environ. Res.*, **18**, 745 (2007).
3. G. Davila-Vazquez, R. Tinoco, M.A. Pickard, R. Vazquez-Duhalt, *Enzyme Microb. Technol.*, **36**, 223 (2005).
4. C.T. Duarte, R. Roman, R. Tinoco, R.V. Duhalt, *Chemosphere*, **77**, 687 (2009).
5. S.A. Senior, M.D. Madbouly, A.M. El Massry, *Chemosphere*, **85**, 7 (2011).
6. M. B. Colovic, V. M. Vasic, N. S. Avramovic, M. M. Gajic, D. M. Djuric, D. Z. Krstic, *Toxicol. Lett.*, **233**, 29 (2015).
7. Y. Arima, H. Shiraishi, A. Saito, K. Yoshimoto, A. Namera, R. Makita, K. Murata, K. Imaizumi, M. Nagao, *J. Toxicol. Sci.*, **141**, 617 (2016).
8. S. Tao, X.H. Xi, F.L. Xu, B.G. Li, J. Cao, R. Dawson, *Environ. Pollut.*, **116**, 57 (2002).
9. D. Yan, X. Jiang, S. Xu, L. Wang, Y. Bian, G. Yu, *Chemosphere*, **71**, 1809 (2008).
10. A. Mohajeri, M.H. Dinpajoo, *J. Mol. Struct: THEOCHEM*, **855**, 1 (2008).
11. C. Hansch, D. Hoekman, A. Leo, D. Weininger, C.D. Selassie, *Chem. Rev.*, **102**, 783 (2002).
12. M. Elango, R. Parthasarathi, V. Subramanian, U. Sarkar, P.K. Chattaraj, *J. Mol. Struct: THEOCHEM*, **723**, 43 (2005).
13. F. Worrall, M. Thomsen, *Chemosphere*, **54**, 585 (2004).
14. E. Zvinavashe, T. Du, T. Griff, H.H.J. van den Berg, A.E.M.F. Soffers, J. Vervoort, A. J. Murk, I.M.C.M. Rietjens, *Chemosphere*, **75**, 1531 (2009).
15. D. Yan, X. Jiang, G. Yu, Z. Zhao, Y. Bian, F. Wang, *Chemosphere*, **63**, 744 (2006).
16. R. Todeschini, M. Vighi, R. Provenzani, A. Finizio, P. Gramatica, *Chemosphere*, **8**, 1527 (1996).
17. J. Devillers, *J. Toxicol. Methods*, **10**, 69 (2000).
18. J. Devillers, *J. SAR QSAR Environ. Res.*, **15**, 501 (2004).
19. Gaussian 03, Revision B.04. Gaussian, Inc., Pittsburgh, PA, 2003.
20. J. B. Foresman, A. Frisch, *Exploring Chemistry with Electronic Structure Methods*, Gaussian Inc., USA, 1996.
21. J. Shi, M. Feng, X. Zhang, Z. Wei, Z. Wang, *Environ. Sci. Pollut. Res.*, **20**, 6138 (2013).
22. R.G. Pearson, *J. Chem. Sci.*, **117**, 369 (2005).
23. <https://www.chem.nlm.nih.gov/chemidplus/> accessed 2017.
24. K. Roy, R. Narayan Das, P. Ambure, R. B. Aher, *Chemometr. Intell. Lab.*, **152**, 18 (2016).
25. H.V. Waterbeemd, *Chemometric Method in Molecular Design*, Wiley, N.Y., 2008.
26. A. Furuhashi, K. Hasunuma, Y. Aoki, *SAR QSAR in Environ. Res.*, **26**, 301 (2015).
27. M. Stoytcheva, *Pesticides - The Impacts of Pesticide Exposure*, InTech, India, 2011.

Study on fatigue properties of basic magnesium sulfate cement reinforced concrete beams based on response surface methodology

J. Zhang^{1*}, Y. Wen², L. Chen³

¹ Vocational and Technical College of Inner Mongolia Agricultural University, China

² Educational Center of Tumoteyou Banner, Baotou City, China

³ Chengdu Agricultural College, China

Received February 19, 2019; Accepted February 25, 2019

In order to study the fatigue properties of basic magnesium sulfate cement reinforced concrete beams, specimens of basic magnesium sulfate cement (BMSC) and ordinary Portland cement (PO·C) in strength grade of C40 and C50, respectively, were prepared. Response surface methodology was applied to this study. The results showed that under the fatigue load, the deflection value of the specimen decreases with the increase of the number of fatigue cycles. The fatigue cycle life of the BMSC specimens with higher strength grades is longer than that of the PO·C specimens, and the higher the strength grade, the more obvious the effect is. Under the fatigue load, the development of the mid-span deflection of the specimen showed an S-shaped trend, and the deflection in the BMSC specimen was smaller than that of the PO·C specimen. The spacing of the cracks in BMSC columns was smaller than that of PO·C columns because of the better bond performance between the reinforcing bars and the surrounding BMS concrete. But the crack widths of BMSC columns were close to the width of PO·C columns. It shows that the BMSC specimen has a high rigidity and good resistance to deformation.

Keywords: BMSC; reinforced concrete; fatigue property; Response surface methodology

INTRODUCTION

Basic magnesium sulfate cement (BMSC) is a new kind of sulfur magnesium oxychloride cement. The primary hydration product of BMS is the 5·1·7 phase [1-3]. Its chemical composition is $5\text{Mg}(\text{OH})_2 \cdot \text{MgSO}_4 \cdot 7\text{H}_2\text{O}$. The main advantages of BMS are low cost, early strength, high tensile strength, and corrosion resistance [2]. The chemical, physical, and mechanical properties of BMSC are close to those of Portland cement [4].

Energy conservation and environmental protection are the topics that are fully advocated in the development of modern society and the progress of human technology. It is well known that the technology of “twice grinding and once burning” is widely used in the calcium cement, which consumes a lot of energy. Magnesium oxide, which is one of the main raw materials of BMSC, needs only magnesite to be calcined at about 900 °C. In contrast, the clinker of Portland cement needs to be calcined at high temperature of 1,450 °C. In the process of producing Portland cement, raw materials and cement have to go twice through grinding. The raw materials and cement are difficult to grind and 10% of the total energy consumed is electricity. In contrast, magnesium oxide is ground after the decomposition of magnesium carbonate, which is liable to be ground and only needs to be ground once [5-8]. BMSC production has no other energy consumption. In

addition, Portland cement and its products are difficult to be recycled, while the hydration activity of BMS can be recovered at low temperature and then BMSC can be recycled. Above all, improvement of the performance of BMSC and expansion of its application in civil engineering not only can meet the requirements of energy conservation and environmental protection, but also coordinate for the sustainable economic development.

BMSC concrete is air-dried, magnesia-based concrete. Since the additives in BMSC can inhibit the hydration of MgO to weaken the crystallization stress and low solubility 5·1·7 phase, BMS concrete has better water resistance [5]. BMSC concrete has also advantages in corrosion resistance compared with Portland cement and sulfate aluminate cement [9-11]. It is therefore appropriate for high-performance, anti-corrosion concrete commonly used in salt-saturated, land environments [12-16].

In order to facilitate the large-scale application of basic magnesium sulfate cement concrete in structural engineering, a basic magnesium sulfate cement reinforced concrete beam member was prepared in this paper. Based on the static load and fatigue tests of basic magnesium sulfate cement reinforced concrete beams the fatigue properties of basic magnesium sulfate cement reinforced concrete beams were discussed by comparing with ordinary Portland cement reinforced concrete beams.

* To whom all correspondence should be sent:

E-mail: 245916447@qq.com

In this experiment, the primary material was BMSC with a specific surface area of 2,500 cm²/g, which was made of MgO, MgSO₄·7H₂O, fly ash, and admixture. A kind of locally available crushed gravel with a maximum size of 25 mm and specific density of 2,680 kg/m³ was used as the coarse aggregate. A locally available natural river sand with a fineness modulus of 2.44 and specific density of 2,700 kg/m³ was used as the fine aggregate.

Preparation of the reinforcement concrete columns

Six BMSC columns and two PC concrete columns were tested to investigate the different behavior of the two kinds of columns. The length of the reinforcement concrete columns was 1,500 mm. The thickness of concrete cover was 25 mm.

It can be seen from Fig. 1 that with the increase in the molar ratio, the flexural strength and compressive strength of the sheet first increase and then decrease. When the molar ratio is 6-8, the overall strength is the highest. When a-MgO/MgSO₄ is small, that is, when the content of a-MgO is low, the content of a-MgO hydration layer in the OH- and solid phase of the pore solution in the cement hydration process is small, resulting in strength. Phase 517 is slow to generate, resulting in lower early strength. When the a-MgO content is high, the remaining a-MgO after the formation of the 517 phase is hydrated to a lower strength Mg(OH)₂, that is, the 517 phase content per unit volume of the plate is lower, so the strength is also obviously reduced, therefore, it is recommended to choose a molar ratio of 6 to 8 when preparing the board.

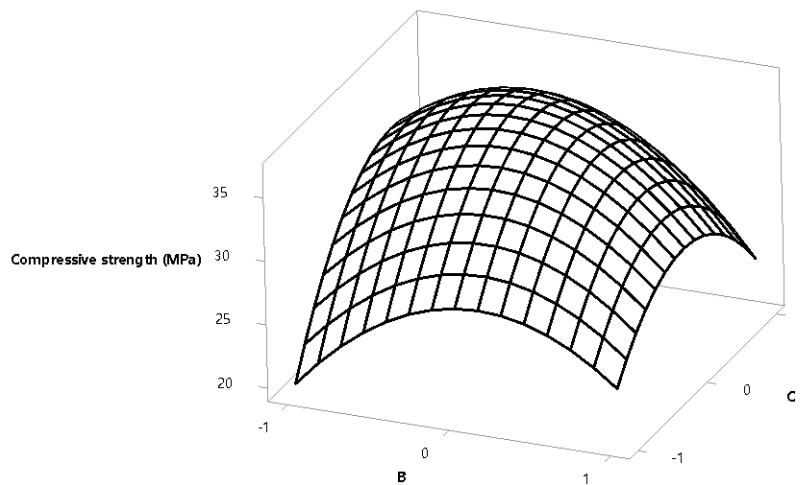


Figure 1. Surface plot of compressive strength (MPa) vs C, B

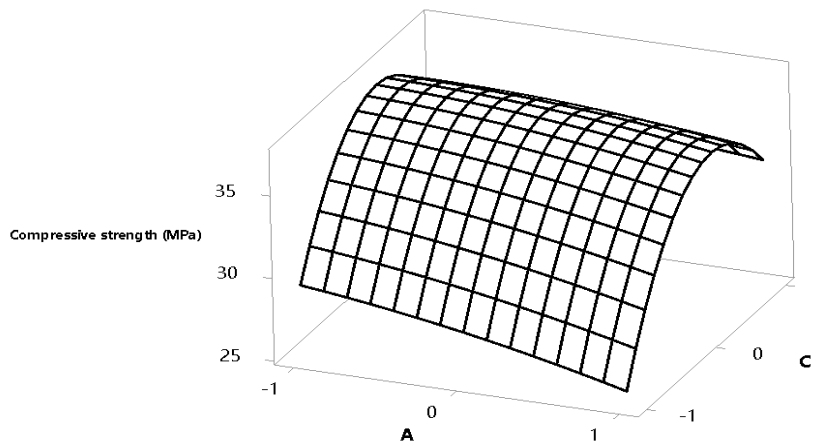


Figure 2. Surface plot of compressive strength (MPa) vs C, A

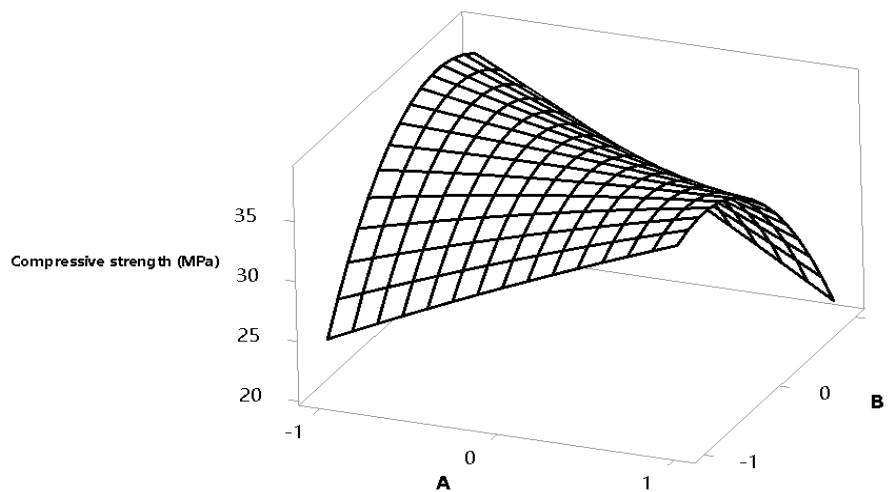


Figure 3. Surface plot of compressive strength (MPa) vs B, A

Figure 2 shows the effect of the amount of admixture on the strength of the composite sheet. It can be seen that the addition of the admixture has a great influence on the strength of the composite sheet. When no additives were added, the compressive strength was only 17.4 MPa, while when 0.4% of the admixture was added, the increase was 36.6 MPa, an increase of 110.3%.

In order to accelerate the production efficiency of the board, especially in winter production, sometimes manufacturers can adopt the method of early high temperature curing. Therefore, it is necessary to study the influence of temperature on the strength of the board and the mechanism of its influence. Figure 3 shows the effect of different early curing temperatures on the properties of the sheet. It can be seen that increasing the curing temperature can significantly increase its early strength. For example, after curing at 20°C for 1 d, after 50 h at 50°C and 80°C for 12 h, the compressive strength reached 17.6 MPa and 19.8 MPa, compared with 24°C at the same age. 0 MPa increased by 90% and 145%, respectively. After 7 days of curing at 50°C, the compressive strength was only reduced when it was maintained at 20°C for 28 days 7%. The early curing temperature was 80°C, and the compressive strength decreased by 14.6%.

The curing process has a great influence on the performance of the composite sheet. The use of early high-temperature curing can accelerate the production efficiency of the sheet, increase the

curing temperature, and increase its early strength. The late strength still has an increasing trend with the increase in age. Therefore, in the industrial production of composite sheets, the curing temperature is appropriately increased, and the production efficiency can be improved while the durability of the strength can be ensured. For Fig. 4, optimization of operating parameters is necessary to determine the optimum value of variables that yield the highest compressive strength. Optimization was done by a program based on the proposed quadratic model obtained for compressive strength. A desirable goal in the program was set for independent factors in the range with equal importance of 3 and for compressive strength at a maximum level with an importance factor of 5. Totally, 15 solutions were predicted by the software under the above-mentioned conditions. The optimum solution was selected based on economic considerations, availability and cost of reagents and energy. Based on these, curing temperature is 20°C, molar ratio is 7, additional dose is 0.6%.

Figure 5 shows the relationship between deflection and the number of fatigue cycles. It can be seen that under the fatigue load, the deflection value of the specimen decreases with the increase in the number of fatigue cycles. The fatigue cycle life of the BMSC specimen with high strength grade is longer than that of the PO·C specimen and the strength grade is higher. The high-strength BMSC specimens have a higher resistance to fatigue damage than the PO·C specimens.

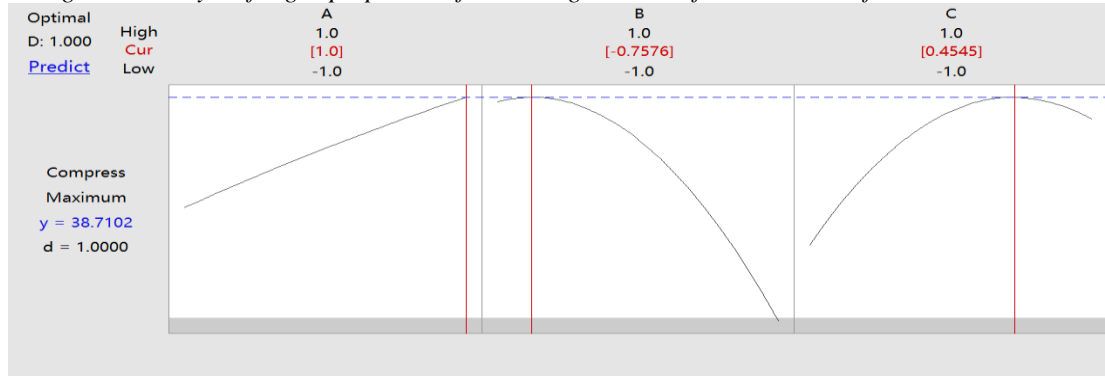


Figure 4. Multiple response prediction.

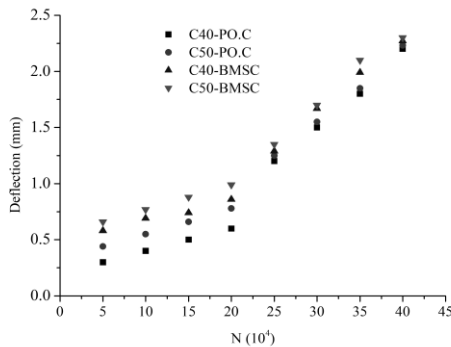
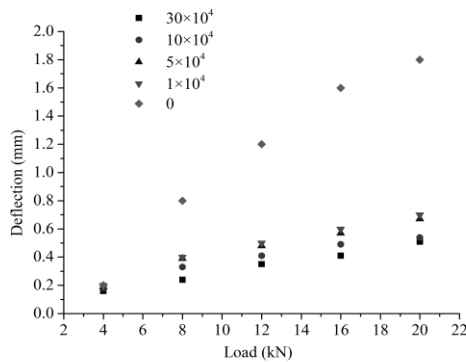
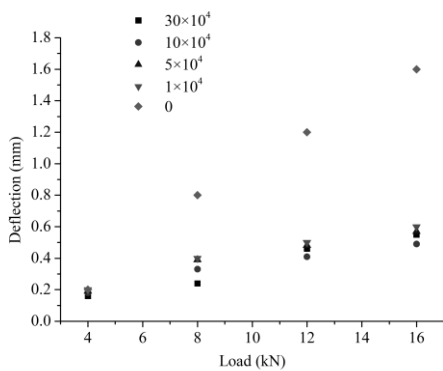


Figure 5. Relationship between deflection and fatigue cycles.



(a)



(b)

Figure 6. Deflection-load curves under fatigue load (a) BMSC specimen (b) PO·C specimen.

Figure 6 shows the cross-center deflection of the specimen *versus* the load at different fatigue cycles. It can be seen from the figure that the mid-span deflection of the specimen increases with the increase in the load. In the case of the same load, the mid-span deflection decreases with the increase in the number of fatigues. It can also be seen from the figure that the development of the mid-span deflection increment shows an S-shaped trend. At the initial stage of loading, and near fatigue failure, the deflection of the specimen during the mid-span will change greatly. Under the same conditions, the mid-span deflection of BMSC specimens is smaller than that of PO·C specimens. It shows that the BMSC specimen has high rigidity and good resistance to deformation.

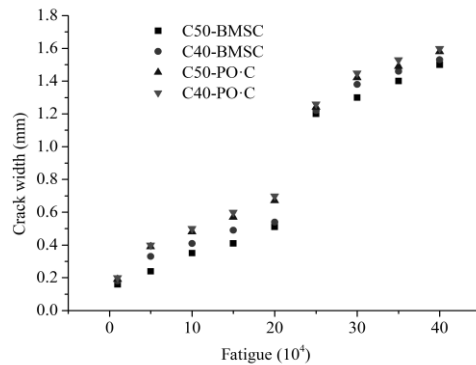


Figure 7. Relationship between fatigue and crack width.

The relationship between crack width and fatigue number of BMSC specimens is shown in Fig. 7. As the number of fatigues increases, the crack width of the test piece increases. Similar to the development of cracks in the static load test, new cracks are generated during the fatigue test, and the original cracks are continuously developed during the fatigue process. Under the same conditions, the crack width of the BMSC specimen is smaller than that of the PO·C specimen, and it can be seen that the BMSC specimen has high crack resistance.

CONCLUSIONS

Based on the results of this study, the following conclusions are drawn:

Under the fatigue load, the deflection value of the specimen decreases with the increase in the number of fatigue cycles. The fatigue cycle life of the BMSC specimens with higher strength grades is longer than that of the PO·C specimens, and the higher the strength grade, the more obvious the effect is. Under the fatigue load, the development of the mid-span deflection of the specimen showed an S-shaped trend, and the deflection in the BMSC specimen was smaller than that of the PO·C specimen. The spacing of the cracks in BMSC columns was smaller than that in PO·C columns because of the better bond performance between the reinforcing bars and the surrounding BMS concrete. But the crack widths of BMSC columns were close to the width of PO·C columns. It shows that the BMSC specimen has high rigidity and good resistance to deformation.

Acknowledgement: Fund of scientific Research Innovation Team construction of Vocational & Technical College of Inner Mongolia Agricultural University.

REFERENCES

1. X. Xu, Yu. Xu, L. Duan, *Construction and Building Materials*, **170**, 801 (2018).
2. J. Guo, B. Cao, C. I. Steefel, J. Chen, Ya. Hu, *Int. J. Greenhouse Gas Control*, **63**, 118 (2017).
3. M. N. Aziez, A. Bezzar, *J. Adhesion Sci. Technol.*, **32**, 272 (2018).
4. M. Maes,; N. De Belie, *Construction and Building Materials*, **155**, 630 (2017).
5. J. Chen, X.-P. Dong, Zh.-H. Liu, *Chinese J. Inorg. Chem.*, **32**, 935 (2016).
6. P.-J. Han, Sh. Wang, F. Y. Chen, *J. Central South Univ.*, **22**, 1869 (2015).
7. N. Saca, M. Georgescu, *Construction and Building Materials*, **71**, 246 (2014).
8. Zh.-g. Li, W.-j. Dong, J.-w. Liu, S.-w. Yu, J.-t. Guo, B. Liu, T.-y. Yan, *Bull. Chinese Ceramic Soc.*, **35**, 3101 (2016).
9. Zh.-g. Li, S.-w. Yu, J.-t. Guo, W.-j. Dong, J.-w. Liu, *Bull. Chinese Ceramic Soc.*, **35**, 4140 (2016).
10. N. Saca, M. Georgescu, *Revista Romana de Materiale-(Romanian Journal of Materials)*, **44**, 5 (2014).
11. Yu. Yang, G. Wang, S. Xie, *J. Testing .Eval.*, **40**, 1244 (2012).
12. W. Chen, Ch. Wu, H. Zhang, Sh. Zheng, F. Chen, *J. Qinghai Univ.y*, **35**, 48 (2017).
13. Zh. Wu, H. Yu, H. Ma, Y. Zhang, Q. Mei, B. Da, Y. Tan, Sh. Hua, *The Ocean Eng.*, **36**, 59 (2018).
14. X. Liu, X. Tang, J. Su, T. Zhang, A. Zhang, *J. Water Resour. Architect. Eng.*, **13**, 161 (2015).
15. Y. Xiao, H. Wu, *J. Material Civil Eng. ASCE*, **12**, 139 (2000).
16. V. M. Karbhari, Y. Gao, *J. Material Civil Eng.*, **9**, 185 (1997).

Copper leaching from chalcopyrite concentrate by sodium nitrate in sulphuric acid solution – chemometric approach

M. D. Sokić^{1*}, B. R. Marković¹, L. L. Pezo², S. B. Stanković¹, A. S. Patarić¹,
Z. V. Janjušević¹, B. Lj. Lončar³

¹*Institute for Technology of Nuclear and Other Mineral Raw Materials, Bulevar Franša d'Eperea 86, 11000 Belgrade, Serbia*

²*Institute of General and Physical Chemistry, University of Belgrade, Studentski trg 12-16, 11000 Belgrade, Serbia*

³*Faculty of Technology, University of Novi Sad, Bulevar Cara Lazara 1, 21000 Novi Sad, Serbia*

Received March 25, 2019, Revised May 25, 2019,

Hydrometallurgical processing of the copper concentrates is a promising alternative to the conventional pyrometallurgical production of copper due to significantly lower environmental impact, capital and operational costs. Development of the hydrometallurgical process for copper recovery from mineral concentrate requires extensive work in testing and optimization of operational parameters from laboratory to semi-industrial scale. Mathematical modelling of the copper leaching process can save human labour and time. Leaching of copper from chalcopyrite concentrate using sulphuric acid and sodium nitrate as an oxidant was tested, and the influence of temperature, particle size, stirring speed and concentrations of sulphuric acid and sodium nitrate were evaluated. Obtained results showed that increasing temperature and concentrations of sulphuric acid and sodium nitrate increase the leaching degree of copper, while increasing particle size and stirring speed reduce copper extraction. In this paper, second-order polynomial models (SOP) were applied to experimental data. Presented results show that mathematical models fit experimental data. The conclusion is that SOP models are a promising tool to be used for modelling leaching processes of metals.

Keywords: leaching, chalcopyrite, copper, influence of working parameters, mathematical modelling

INTRODUCTION

Although hydrometallurgy provides more environmentally friendly production of copper, and copper ores in the world's exploited deposits are being continually depleted, getting more complex, and grades of the valuable elements are constantly declining [1], approximately 80-85 % of the global annual copper production is still produced pyrometallurgically in smelters [2,3]. One of the main obstacles for wider application of hydrometallurgy are difficulties in copper leaching from the most abundant copper mineral, chalcopyrite, which accounts for approximately 70 % of the global copper reserves [3]. Chalcopyrite is one of the most reluctant copper minerals to leach and smelting it often provides better extraction of this metal from mineral concentrate [3,4]. Slow and incomplete leaching of chalcopyrite is a consequence of the formation of passivation layers on the mineral surface [3,5]. Passivation layers can be formed by sulphides, polysulphides, elemental sulphur [6,7], iron oxides, hydroxides, hydroxysulphates and jarosites [8,9]. Also, due to lower reaction temperatures, hydrometallurgical processes are significantly slower than pyrometallurgical ones. Effective leaching of chalcopyrite from mineral concentrate requires the application of oxidant, and/or high pressure [4,10].

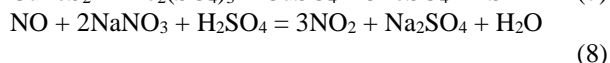
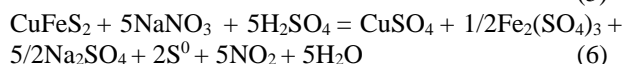
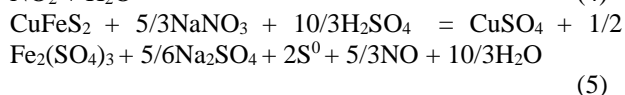
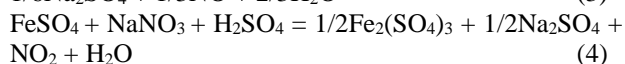
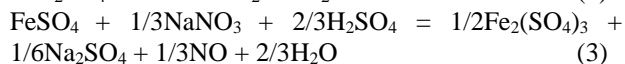
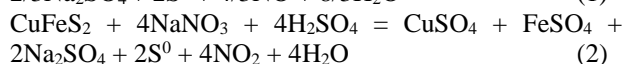
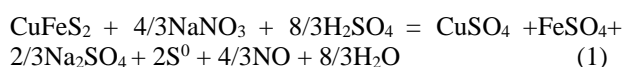
Also, acidophilic microorganisms (bacteria and archaea) can be applied to catalyse leaching of copper from chalcopyrite [11-13]. Numerous research papers were published describing the application of various oxidants in order to enhance leaching of copper from chalcopyrite [2,3,14-18]. Optimization of the leaching process for the selected raw mineral material requires extensive work on testing the influence of various parameters on the leaching degree of copper. Development of a mathematical model that can be used to predict the leaching degree based on input data acquired by laboratory experiments.

This could significantly accelerate the optimization and development of leaching technology on the industrial scale. Second-order polynomial models (SOP) have a wide application in different areas of science and industry. These models allow prediction of the system's behaviour based on the input data collected during laboratory experiments. In the presented research, leaching of copper from chalcopyrite concentrate using sodium nitrate as an oxidant was tested and experimental results were used as input data for the development of a mathematical model. Sodium nitrate was selected because of its good performance as a leaching agent for chalcopyrite [17]. The aim of this work is to develop second-order polynomial models (SOP) for copper leaching and to test if experimental data collected during leaching

* To whom all correspondence should be sent:
E-mail: m.sokic@itnms.ac.rs

experiments fits into the model. In a series of experiments the influence of leaching duration, temperature, stirring speed, sulphuric acid concentration and sodium nitrate concentration on the leaching degree of copper was measured. Obtained data fit into the SOP model, proving that this mathematical model can be applied for theoretical modelling of copper leaching from the chalcopyrite concentrate. Such models can significantly accelerate the development of industrial scale leaching technologies.

The main chemical reactions (1-9) for leaching of chalcopyrite using sodium nitrate in sulphuric acid were identified by computational thermodynamic analysis performed by HSC 6.1 software (Outotec Research Oy, Finland) and analysis of the reaction products [17]:



The change in Gibbs free energy for chemical reactions 1-9 was calculated for temperatures from 25 °C to 90 °C and atmospheric pressure. The calculated negative values of Gibbs free energy for reactions 1-8 indicate that these reactions are thermodynamically feasible at the given conditions.

EXPERIMENTAL

Materials and methods

Chalcopyrite concentrate was obtained from the flotation plant of the „Rudnik“ mine in Serbia. Four particle size fractions were obtained by wet sieving. Mineralogical analysis of the concentrate was performed by chemical and X-ray diffraction analysis and qualitative and quantitative light microscopy.

Leaching experiments were performed in a 2L glass reactor equipped with a teflon stirrer, thermometer, glass funnel for adding solid samples, sampling device and condenser. The samples were collected at regular time intervals for chemical analysis by AAS (Perkin Elmer Analyst 300

Norwalk, USA). The phase content was determined by X-ray analysis using diffractometer (PHILIPS PW- 1710) and qualitative and quantitative light microscopy (Carl Zeiss-Jena, JENAPOL-U).

Experiments were conducted by varying one of the parameters important for copper leaching: temperatures from 20 to 90 °C, particle class -75, -75 +50, -50 +37 and -37 µm, sulphuric acid concentration from 0.6 to 2.0 M, sodium nitrate concentration from 0.15 to 0.90 M and stirring speed 100-400 rpm.

Temperature

A first set of experiments was conducted under following conditions: 1.5 M H₂SO₄, 0.6 M NaNO₃, stirring speed 300 rpm, solids concentration 20 g of concentrate in 1.2 dm³ of the solution, duration of experiment 240 min. Temperature was set to 70 °C, 75 °C, 80 °C, 85 °C and 90 °C.

Particle size

Experimental conditions: T=80 °C, 1.5 M H₂SO₄, 0.6 M NaNO₃, stirring speed 300 rpm, solids concentration 20 g of concentrate in 1.2 dm³ of the solution, duration of experiment 240 min. Particle class: -75, -75 +50, -50 +37 and -37 µm.

Stirring speed

Experimental conditions: T=80 °C, 1.5 M H₂SO₄, 0.6 M NaNO₃, stirring speed 300 rpm, solids concentration 20 g of concentrate in 1.2 dm³ of the solution, duration of experiment 240 min. Stirring speed: 100, 200, 300 and 450 rpm.

Sulphuric acid concentration

Experimental conditions: T=80 °C, 0.6 M NaNO₃, stirring speed 300 rpm, solids concentration 20 g of concentrate in 1.2 dm³ of the solution, duration of experiment 240 min. Concentrations of H₂SO₄: 0.6, 1.0, 1.5 and 2M.

Sodium nitrate concentration

Experimental conditions: T=80 °C, 1.5 M H₂SO₄, stirring speed 300 rpm, solids concentration 20 g of concentrate in 1.2 dm³ of the solution, duration of experiment 240 min. Concentration of NaNO₃: 0.15, 0.20, 0.45, 0.60, 0.75 and 0.90 M.

Mathematical modelling and statistical analysis

The second-order polynomial (SOP) models were fitted to the observed experimental data. Five mathematical models of the following form were developed to relate leaching degree of copper (Y) and process variables [19,20]:

$$Y_k = \beta_{k0} + \sum_{i=1}^2 \beta_{ki} \cdot X_i + \sum_{i=1}^2 \beta_{kii} \cdot X_i^2 + \beta_{k12} \cdot X_1 \cdot X_2, \quad k=1-2, \quad (10)$$

where: β_{k0} , β_{ki} , β_{kii} , β_{k12} are constant regression coefficients; Y_k is leaching degree of Cu, while X_1 is the duration of the process (t) and X_2 is one of the following parameters: temperature (T), particle class (Class), stirring speed (v), concentrations of sulphuric acid ($C_{H_2SO_4}$) or sodium nitrate (C_{NaNO_3}). In this article, ANOVA was conducted to show the significant effects of independent variables on the responses, and to show which of the responses were significantly affected by the varying treatment combinations.

The adequacy of the developed models was tested using coefficient of determination (r^2), reduced chi-square (χ^2), mean bias error (MBE), root mean square error (RMSE), and mean percent error (MPE). These commonly used parameters can be calculated as follows [21]:

$$\chi^2 = \frac{\sum_{i=1}^N (y_{exp,i} - y_{pre,i})^2}{N - n},$$

$$RMSE = \left[\frac{1}{N} \times \sum_{i=1}^N (y_{pre,i} - y_{exp,i})^2 \right]^{1/2},$$

$$MBE = \frac{1}{N} \times \sum_{i=1}^N (y_{pre,i} - y_{exp,i}),$$

$$MPE = \frac{100}{N} \times \sum_{i=1}^N \left(\frac{|y_{pre,i} - y_{exp,i}|}{y_{exp,i}} \right) \quad (11)$$

where: $y_{exp,i}$ stands for the experimental values and $y_{pre,i}$ are the predicted values obtained by calculating from the model for these measurements. N and n are the numbers of observations and constants, respectively.

Characterization of chalcopyrite concentrate

The chalcopyrite concentrate was enriched during the flotation of a $CuFeS_2$ - PbS - ZnS polymetallic ore in the “Rudnik” flotation plant (Rudnik–Serbia). Granulometric composition of the tailings was determined by wet sieving (37 μm sieve). Grain size of the residual fraction was determined by dry sieving using 50 μm and 75 μm sieves. Granulometric and chemical compositions of the tailings are presented in Table 1 [17]. Results of the chemical analysis show that grain size does not significantly affect the chemical composition of the concentrate.

Qualitative and quantitative mineralogical analysis revealed that the most abundant copper mineral in the concentrate was chalcopyrite (78.22 %), followed by sphalerite (6.29 %), galenite (2.63 %) and pyrrhotite (1.16 %). Dominant gangue minerals were quartz, silicates and carbonates [22]. Microscopic image of the concentrate sample is presented in Figure 1, showing liberated grains of chalcopyrite and one galenite grain.

Influence of particle size on the leaching degree of copper, $Y_{Cu}(t, Class)$

Copper extraction increased with decreasing particle size. Maximal copper extraction reached 69 % using -37 μm fraction. Smaller particles provided a larger contact surface for the chemical reactions with the oxidant. Particle size of -37 μm was used in the following experiments.

Table 1. Grain sizing and chemical composition of the chalcopyrite concentrate [17].

Particle size (μm)	Mass %	Element (%)			
		Cu	Fe	Zn	Pb
+ 75	7.32	23.38	22.25	3.43	4.08
- 75 + 50	21.15	26.55	24.43	4.28	1.70
- 50 + 37	5.18	26.95	24.75	4.36	1.85
- 37	66.35	27.08	25.12	4.15	2.28

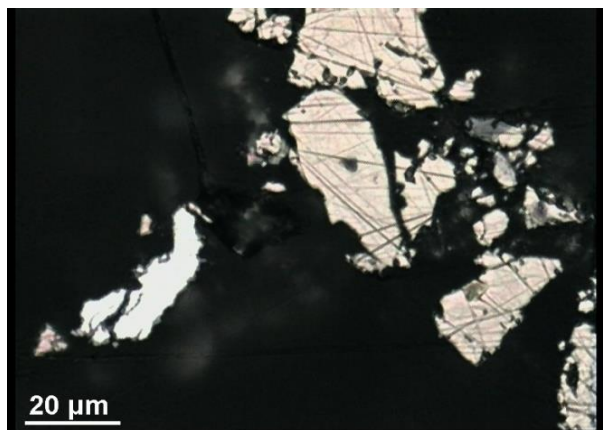


Figure 1. Liberated grain of chalcopyrite (yellow) and galenite (white). Reflected light, oil immersion, II N.

Influence of temperature on the leaching degree of copper, $Y_{Cu}(t, T)$

Copper extraction increased with increasing temperature. Maximal copper extraction was 75.5 % at 90 °C. The extraction of copper was rapid during the first 30 min of the experiment; after that period copper extraction was slower due to the formation of a sulphur passivation layer (chemical equations 3-5).

Influence of stirring speed on the leaching degree of copper, $Y_{Cu}(t, v)$

Stirring speed does not have a significant influence on copper extraction. Slight decrease in the leaching degree was observed at steering speeds higher than 100 rpm. Liquid turbulence created at higher steering speeds might interfere with the adsorption of oxidant on the surface of chalcopyrite.

Influence of sulphuric acid concentration on the leaching degree of copper, $Y_{Cu}(t, C_{H_2SO_4})$

Concentration of sulphuric acid has significant influence on copper extraction. The leaching degree increased from 47 % using 0.6 M H_2SO_4 to 75 % using 2.0 M H_2SO_4 . This observed effect is explained by the fact that the oxidizing potential of NO_3^- ions increases with the increase in solution acidity [23].

Influence of sodium nitrate concentration on the leaching degree of copper, $Y_{Cu}(t, C_{NaNO_3})$

As expected, increasing concentration of the oxidant $NaNO_3$ led to increased extraction of copper (Fig. 3e). Maximal copper extraction was 75 % after 240 min of leaching using 0.9M $NaNO_3$.

Experimental results were fitted to the SOP models ($Y_{Cu}(t, T)$; $Y_{Cu}(t, \text{Class})$; $Y_{Cu}(t, v)$; $Y_{Cu}(t, C_{H_2SO_4})$, $Y_{Cu}(t, C_{NaNO_3})$). As can be seen from the data in Figure 2, most of the terms in SOP models for prediction of the leaching degree of copper (Y_{Cu}) were statistically significant at $p < 0.01$ level. The quadratic term v was statistically significant at $p < 0.05$ level, while the quadratic term $C_{H_2SO_4}$ was found statistically insignificant. The linear term t was the most influential one, no matter which other parameter was changed.

In the cases where interaction between factors was statistically significant, complete information regarding the effect of the factors on the responses can be perceived on the basis of the three-dimensional contour plots. The three-dimensional response surface plots (Figure 3) were plotted for experimental data visualization (experimental data are presented as white dots) and for the purpose of observation of the fitting of regression models to experimental data. The observed three-dimensional contour plot of Y_{Cu} surface showed a 'rising ridge' pattern. These graphics show a good correlation between experimental data and model results, as suggested by Madamba [24], which was also confirmed by the calculated coefficients of determination: 0.979; 0.991; 0.998; 0.994 and 0.981 for models: $Y_{Cu}(t, T)$; $Y_{Cu}(t, \text{Class})$; $Y_{Cu}(t, v)$; $Y_{Cu}(t, C_{H_2SO_4})$ and $Y_{Cu}(t, C_{NaNO_3})$, respectively.

Experimental results have shown that temperature significantly affects copper extraction: the temperature increase is followed by an increase in the copper leaching degree [17]. Similar influence of temperature was obtained during leaching of chalcopyrite by potassium dichromate [25,26], and copper (I) sulphide by sodium nitrate and sulphuric acid [27]. At lower temperatures the molecules in the reaction system do not possess enough energy for chemical reactions. The dissolution of copper increased with increasing sulphuric acid and sodium nitrate concentrations, too. The oxidizing potential of NO_3^- ions increases with the increase of solution acidity, which contributes to the leaching of copper. Bredenmann and van Vuuren [28] and Vračar *et al.* [27] detected the same influence of $NaNO_3$ concentration during the leaching of nickel sulphide concentrate by sulphuric acid and sodium nitrate, while several other authors confirmed the similar effect of sulphuric acid concentration [25-27].

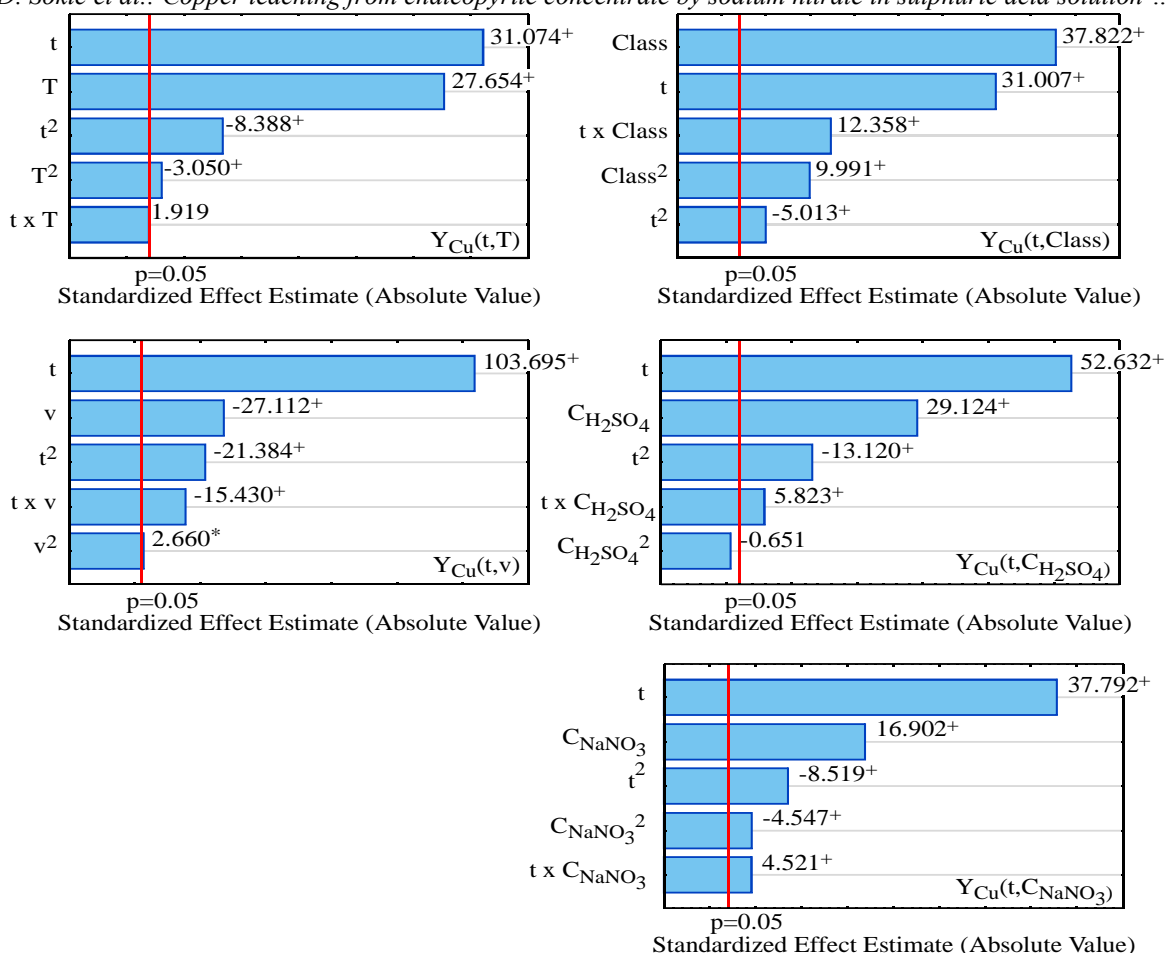


Figure 2. Pareto charts for $Y_{Cu}(t, T)$; $Y_{Cu}(t, \text{Class})$; $Y_{Cu}(t, v)$; $Y_{Cu}(t, \text{CH}_2\text{SO}_4)$ and $Y_{Cu}(t, \text{CNaNO}_3)$

On the other hand, the reaction rate decreased with increasing particle size [17]. Smaller particles provided a larger contact surface between chalcopyrite and the oxidant [25,26,29].

The stirring speed did not significantly influence the rate of the chalcopyrite dissolution, but a slight decrease was observed, probably due to the poor adsorption capacity of chalcopyrite surface for nitrate ions. The same results were obtained during the leaching of chalcopyrite by hydrogen peroxide in the presence of ethylene glycol by Mahajan *et al.* [30]. Antonijević *et al.* [31] noticed that the rate of pyrite dissolution increased as the stirring speed decreased due to better contact between pyrite particles and peroxide. During the chalcopyrite leaching in the $\text{H}_2\text{SO}_4 + \text{K}_2\text{Cr}_2\text{O}_7$ system, Aydogan *et al.* [26] noticed that chalcopyrite dissolution increased with increasing stirring speed up to 400 rpm, and thereafter the rate significantly declined.

Residual analysis

The quality of the model fit was tested in Table 1, the higher r^2 values, and the lower χ^2 , RMSE, MBE,

and MPE values show the better fit to the experimental results [21]. The residual analysis of the developed model was also performed. Skewness measures the deviation of the distribution from normal symmetry. If skewness is clearly different from 0, then the distribution is asymmetrical, while normal distributions are perfectly symmetrical. Kurtosis measures the 'peakedness' of a distribution. If kurtosis is clearly different from 0, then the distribution is either flatter or more peaked than normal; the kurtosis of the normal distribution is 0. The analysed mean values, standard deviations (SD), and the variance of the residuals are shown in Table 2. These results showed a good approximation to a normal distribution around zero with a probability of 95% ($2 \times \text{SD}$), which means a good generalization ability of the developed model for the range of observed experimental data. SOP models had an insignificant lack of fit tests, which means that all the models represented the data satisfactorily.

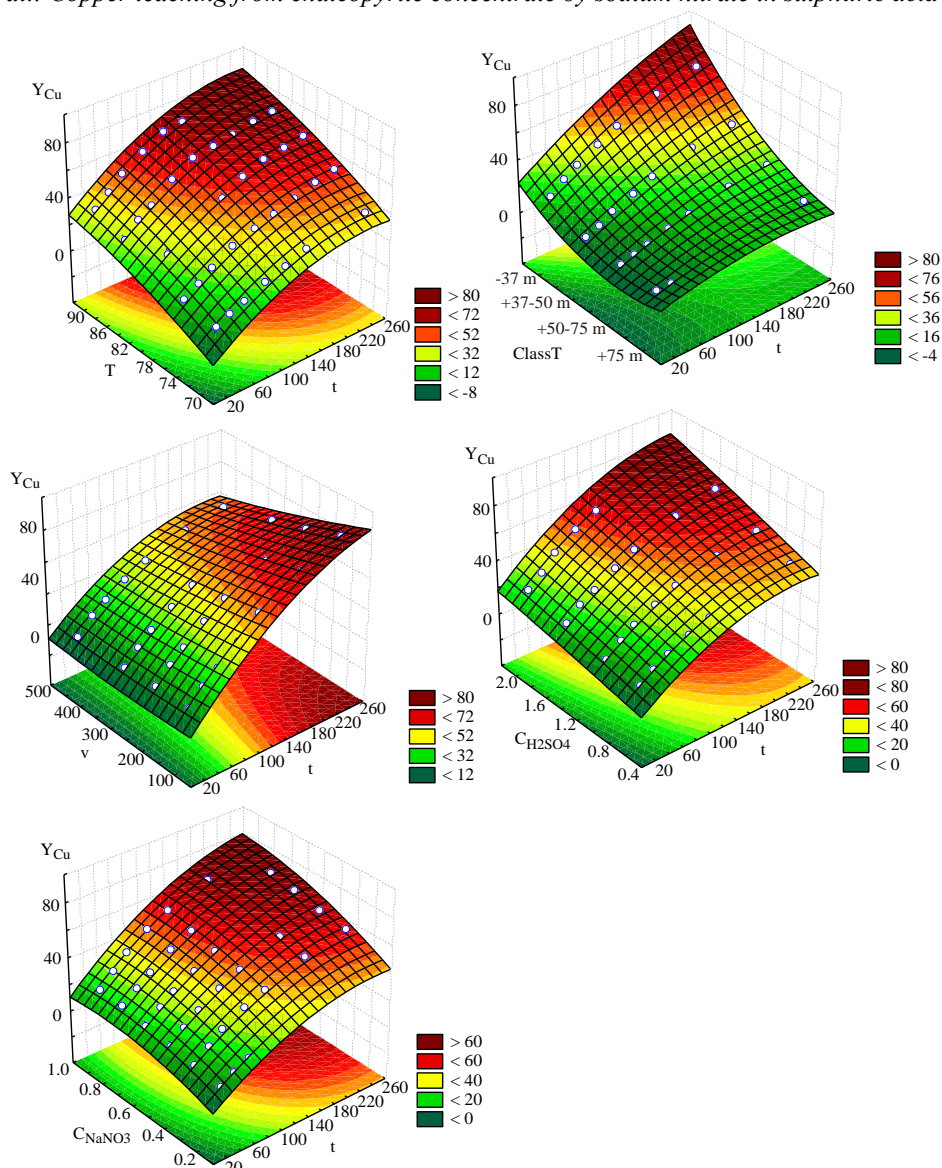


Figure 3. Three-dimensional contour plot of Y_{Cu} responses, affected by temperature (T), particle size (Class), steering speed (v), concentration of H_2SO_4 ($C_{H_2SO_4}$) and $NaNO_3$ (C_{NaNO_3}).

Table 2. The 'goodness of fit' tests of the developed mathematical models

	χ^2	RMSE	MBE	MPE	r^2	Skew.	Kurt.	Mean	SD	Var.
$Y_{Cu}(t, T)$	8.6	2.9	-7.7E-14	7.4	0.979	0.254	-0.627	0.000	2.897	8.39
$Y_{Cu}(t, Class)$	3.0	1.7	2.3E-11	19.0	0.991	0.017	-1.105	0.000	1.688	2.85
$Y_{Cu}(t, v)$	0.7	0.8	-9.4E-15	2.0	0.998	-0.503	0.032	0.000	0.802	0.64
$Y_{Cu}(t, C_{H_2SO_4})$	2.0	1.4	-4.4E-15	3.5	0.994	0.369	-0.492	0.000	1.392	1.94
$Y_{Cu}(t, C_{NaNO_3})$	6.7	2.5	-3.0E-15	6.0	0.981	0.259	0.434	0.000	2.560	6.55

CONCLUSION

The obtained relationship between the independent extrinsic factors (temperature, time, particle size, steering speed, concentration of H_2SO_4 and $NaNO_3$) and the dependent responses (targeted leaching degree of copper) could be a

useful tool to assess and manage the optimal production parameters.

Results of laboratory experiments revealed that the leaching degree of copper from chalcopyrite concentrate increases with the increase in temperature, concentrations of H_2SO_4 and $NaNO_3$ and reduction of particle size, while the increase of steering speed slightly decreases the leaching degree of copper.

The responses predicted by the proposed model are in good agreement with the experimental data. Regardless of all the other raw materials and processing parameters the proposed models performed the prediction accurately within the range of observed set of values. The models tend to be universal and higher r^2 values and lower χ^2 , MBE, RMSE and MPE values should be obtained. The developed SOP models were statistically significant as predicted and observed response variables correspond well.

The developed SOP models could be successfully implemented to optimize the copper leaching process from selected mineral raw materials.

Nomenclature:

T - temperature (°C)

t - time (min)

Class - particle class (μm)

v - stirring speed (rpm)

$C_{\text{H}_2\text{SO}_4}$ - sulphuric acid concentration (M)

C_{NaNO_3} - sodium nitrate concentration (M)

Y_{Cu} - copper leaching degree (%)

Acknowledgement: This work was funded by the Ministry of Education, Science and Technological Development of the Republic of Serbia (Grant number 34023).

REFERENCES

1. A. Mitovski, N. Štrbac, M. Sokić, M. Kragović, V. Grekulović, *Metall. Mater. Eng.*, **23**, 267 (2017).
2. Y. Li, N. Kawashima, J. Li, A. P. Chandra, A. R. Gerson, *Adv. Colloid. Interface. Sci.*, **197-198**, 1 (2013).
3. H. R. Watling, *Hydrometallurgy*, **140**, 163 (2013).
4. A. A. Baba, K. I. Ayinla, F. A. Adekola, M. K. Ghosh, O. S. Ayanda, R. B. Bale, A. R. Sheik, S. R. Pradhan, *International Journal of Mining Engineering and Mineral Processing*, **1**, 1 (2012).
5. C. Klauber, *Int. J. Miner. Process.*, **86**, 1 (2008).
6. K. B. Fu, H. Lin, H. Wang, H. W. Wen, Z. L. Wen, *Int. J. Miner. Metall. Mater.*, **19 (10)**, 886 (2012).
7. R. P. Hackl, D. B. Dresinger, E. Peters, J. A. King, *Hydrometallurgy*, **39**, 25 (1995).
8. E. M. Córdoba, J. A. Muñoz, M. L. Blázquez, F. González, A. Ballester, *Hydrometallurgy*, **93**, 81 (2008).
9. M. D. Sokić, V. L. Matković, B. R. Marković, N. D. Štrbac, D. T. Živković, *Hem. Ind.*, **64**, 343 (2010).
10. R. Padilla, D. Vega, M. C. Ruiz, *Hydrometallurgy*, **86**, 80 (2007).
11. J. D. Batty, G. V. Rorke, *Hydrometallurgy*, **83**, 83 (2006).
12. D. Dreisinger, *Hydrometallurgy*, **83**, 10 (2006).
13. T. J. Harvey, M. Bath, in: *Biomining*, D. E. Rawlings, D. B. Johnson (eds.), Springer-Verlag, Berlin-Heidelberg, 2007, p. 97.
14. T. Agacayak, A. Aras, S. Ayadogan, M. Erdemoglu, *Physicochem. Probl. Miner. Process.*, **50**, 657 (2014).
15. O. Gok, C. G. Anderson, *Hydrometallurgy*, **134-135**, 40 (2013).
16. G. Nazari, E. Asselin, *Hydrometallurgy*, **96**, 183 (2009).
17. M. D. Sokić, B. R. Marković, D. T. Živković, *Hydrometallurgy*, **95**, 273 (2009).
18. M. M. Antonijević, Z. D. Janković, M. D. Dimitrijević, *Hydrometallurgy*, **73**, 329 (2004).
19. G. E. P. Box, D. W. Behnken, *Technometrics*, **2**, 455 (1960).
20. A. I. Khuri, S. Mukhopadhyay, *Wiley Interdiscip. Rev. Comput. Stat.*, **2**, 128 (2010).
21. M. Arsenović, L. Pezo, S. Stanković, Z. Radojević, *Appl. Clay Sci.*, **115**, 108 (2015).
22. M. Sokić, S. Radosavljević, B. Marković, V. Matković, N. Štrbac, Ž. Kamberović, D. Živković, *Metall. Mater. Eng.*, **20**, 53 (2014).
23. N. V. Pacović, *Hydrometallurgy*, ŠRIF, Bor, Yugoslavia, 1980, p. 95 (in Serbian).
24. P. S. Madamba, *Food. Sci. Technol.*, **35**, 584 (2002).
25. M. M. Antonijević, Z. D. Janković, M. D. Dimitrijević, *Hydrometallurgy*, **35**, 187 (1994).
26. S. Aydogan, G. Ucar, M. Canbazoglu, *Hydrometallurgy*, **81**, 45 (2006).
27. R. Vračar, N. Vučković, Ž. Kamberović, *Hydrometallurgy*, **70**, 143 (2003).
28. R. Bredenhann, C. P. J. Van Vuuren, *Miner. Eng.*, **12**, 687 (1999).
29. D. J. Droppert, Y. Shang, *Hydrometallurgy*, **39**, 169 (1995).
30. V. Mahajan, M. Misra, K. Zhong, M. C. Fuerstenau, *Miner. Eng.*, **20**, 670 (2007).
31. M. M. Antonijević, M. D. Dimitrijević, Z. D. Janković, *Hydrometallurgy*, **46**, 71 (1997).

ERRATUM

The name of N. Vasilchina was omitted in the author list because of technical mistake in the paper entitled “High voltage cathode materials based on lithium cobaltate with nickel and manganese doping” published in BCC, Volume 50, Special Issue A (pp.171-176) 2018.

The title and the authors should be as follows:

K. Banov^{1,2}, H. Vasilchina¹, T. Petkov², R. Boukoureshtlieva¹, D. Ivanova²,
L. Fachikov², V. Kotev⁴ and B. Banov*^{1,3}

- ¹) Institute of Electrochemistry and Energy Systems, IEES, 1, Acad. G. Bonchev str., bl. 10, 1113 Sofia
- ²) University of Chemical Technology and Metallurgy – UCTM, bul. “Kl. Ohridski” N:8, 1756 Sofia
- ³) European Polytechnical University – EPU, 23, “St. St. Cyril and Methodius” str., 2300 Pernik
- ⁴) Institute of Mechanics, IM, 1, Acad. G. Bonchev str., bl. 4, 1113 Sofia

Instructions about Preparation of Manuscripts

General remarks: Manuscripts are submitted in English by e-mail. The text must be typed on A4 format paper using Times New Roman font size 11, normal character spacing. The manuscript should not exceed 15 pages (about 3500 words), including photographs, tables, drawings, formulae, etc. Authors are requested to use margins of 2 cm on all sides.

Manuscripts should be subdivided into labelled sections, e.g. **Introduction, Experimental, Results and Discussion**, etc. **The title page** comprises headline, author's names and affiliations, abstract and key words. Attention is drawn to the following:

a) **The title** of the manuscript should reflect concisely the purpose and findings of the work. Abbreviations, symbols, chemical formulas, references and footnotes should be avoided. If indispensable, abbreviations and formulas should be given in parentheses immediately after the respective full form.

b) **The author's** first and middle name initials and family name in full should be given, followed by the address (or addresses) of the contributing laboratory (laboratories). **The affiliation** of the author(s) should be listed in detail by numbers (no abbreviations!). The author to whom correspondence and/or inquiries should be sent should be indicated by asterisk (*) with e-mail address.

The abstract should be self-explanatory and intelligible without any references to the text and containing not more than 250 words. It should be followed by key words (not more than six).

References should be numbered sequentially in the order, in which they are cited in the text. The numbers in the text should be enclosed in brackets [2], [5, 6], [9–12], etc., set on the text line. References are to be listed in numerical order on a separate sheet. All references are to be given in Latin letters. The names of the authors are given without inversion. Titles of journals must be abbreviated according to Chemical Abstracts and given in italics, the volume is typed in bold, the initial page is given and the year in parentheses. Attention is drawn to the following conventions: a) The names of all authors of a certain publication should be given. The use of "et al." in the list of references is not acceptable. b) Only the initials of the first and middle names should be given. In the manuscripts, the reference to author(s) of cited works should be made without giving initials, e.g. "Bush and Smith [7] pioneered...". If the reference carries the names of three or more authors it should be quoted as "Bush et al. [7]", if Bush is the first author, or as "Bush and co-workers [7]", if Bush is the senior author.

Footnotes should be reduced to a minimum. Each footnote should be typed double-spaced at the bottom of the page, on which its subject is first mentioned. **Tables** are numbered with Arabic numerals on the left-hand top. Each table should be referred to in the text. Column headings should be as short as possible but they must define units unambiguously. The units are to be separated from the preceding symbols by a comma or brackets. Note: The following format should be used when figures, equations, etc. are referred to the text (followed by the respective numbers): Fig., Eqns., Table, Scheme.

Schemes and figures. Each manuscript should contain or be accompanied by the respective illustrative material as well as by the respective figure captions in a separate file (sheet). As far as presentation of units is concerned, SI units are to be used. However, some non-SI units are also acceptable, such as °C, ml, l, etc. The author(s) name(s), the title of the manuscript, the number of drawings, photographs, diagrams, etc., should be written in black pencil on the back of the illustrative material (hard copies) in accordance with the list enclosed. Avoid using more than 6 (12 for reviews, respectively) figures in the manuscript. Since most of the illustrative materials are to be presented as 8-cm wide pictures, attention should be paid that all axis titles, numerals, legend(s) and texts are legible.

The authors are required to submit the text with a list of three individuals and their e-mail addresses that can be considered by the Editors as potential reviewers. Please, note that the reviewers should be outside the authors' own institution or organization. The Editorial Board of the journal is not obliged to accept these proposals.

The authors are asked to submit **the final text** (after the manuscript has been accepted for publication) in electronic form by e-mail. The main text, list of references, tables and figure captions should be saved in separate files (as *.rtf or *.doc) with clearly identifiable file names. It is essential that the name and version of the word-processing program and the format of the text files is clearly indicated. It is recommended that the pictures are presented in *.tif, *.jpg, *.cdr or *.bmp format.

The equations are written using "Equation Editor" and chemical reaction schemes are written using ISIS Draw or ChemDraw programme.

EXAMPLES FOR PRESENTATION OF REFERENCES

REFERENCES

1. D. S. Newsome, *Catal. Rev.–Sci. Eng.*, **21**, 275 (1980).
2. C.-H. Lin, C.-Y. Hsu, *J. Chem. Soc. Chem. Commun.*, 1479 (1992).
3. R. G. Parr, W. Yang, *Density Functional Theory of Atoms and Molecules*, Oxford Univ. Press, New York, 1989.
4. V. Poncic, G. C. Bond, *Catalysis by Metals and Alloys (Stud. Surf. Sci. Catal., vol. 95)*, Elsevier, Amsterdam, 1995.
5. G. Kadinov, S. Todorova, A. Palazov, in: *New Frontiers in Catalysis (Proc. 10th Int. Congr. Catal., Budapest, (1992)*, L. Guzzi, F. Solymosi, P. Tetenyi (eds.), Akademiai Kiado, Budapest, 1993, Part C, p. 2817.
6. G. L. C. Maire, F. Garin, in: *Catalysis. Science and Technology*, J. R. Anderson, M. Boudart (eds), vol. 6, SpringerVerlag, Berlin, 1984, p. 161.
7. D. Pocknell, *GB Patent 2 207 355* (1949).
8. G. Angelov, PhD Thesis, UCTM, Sofia, 2001, pp. 121-126.
- 9 JCPDS International Center for Diffraction Data, Power Diffraction File, Swarthmore, PA, 1991.
10. CA **127**, 184 762q (1998).
11. P. Hou, H. Wise, *J. Catal.*, in press.
12. M. Sinev, private communication.
13. <http://www.chemweb.com/alchem/articles/1051611477211.html>.

Texts with references which do not match these requirements will not be considered for publication!!!

CONTENTS

In memoriam, for Prof. Lubomir Boyadzhiev.....	303
<i>M.F. Khanfar, E. S. M. Abu-Nameh, A. T. Afaneh, M. M. Saket, A. Ahmad, W. Faraj, M. Khalil H. Al Khotaba, M. Al Bujog</i> , Voltammetric detection of hydrochlorothiazide at molybdenum oxide modified screen printed electrodes.....	305
<i>M. Ashjari, S. Masoud Kandomal</i> , The effect of plastic waste and elemental sulfur additives on chemical and physical properties of bitumen.....	312
<i>S. Rennane, N. Bendjaballah-Lalaoui, M. Trari</i> , Comparative removal of naphthalene by adsorption on different sand/bentonite mixtures.....	315
<i>S. M. Pereva, Ts. P. Sarafska, V. Petrov, M. Spassova, S. Bogdanova, T. Spassov</i> , Ibuprofen/ β -CD complexation by controlled annealing of their mechanical mixture.....	326
<i>W. Uz-Zaman, R. Rehman, J. Anwar, J. Zafar</i> , A novel approach to analyze total amino acids contents of food samples by computational image scanning densitometry.....	332
<i>W. Uz-Zaman, R. Rehman, J. Anwar, J. Zafar</i> , Rapid photo-catalytic degradation of methylene blue, tartrazine and brilliant green dyes by high flux UV irradiation photolysis reactor.....	337
<i>V. R. Angelova, V. I. Akova, K. I. Ivanov</i> , Comparative study of the methods for the determination of organic carbon and organic matter in soils, compost and sludge.....	342
<i>Š. Komorsky-Lovrić, M. Lovrić</i> , Theory of staircase cyclic voltammetry of two electrode reactions coupled by a chemical reaction.....	348
<i>S.B. Dimitrijević, S.Č. Alagić, M.M. Rajčić-Vujasinović, S.P. Dimitrijević, A.T. Ivanović</i> , IR/Raman characterization of Au-mercaptotriazole crystals.....	358
<i>M. R. Franco Júnior, N. R. A. F. Rocha, W. A. Pereira, N. P. Merlo</i> , Removal of LAS from water by activated carbon and resins in a continuous process.....	365
<i>U. Stamenković, S. Ivanov, I. Marković</i> , The influence of isochronal aging on the mechanical and thermophysical properties of the EN AW-6060 aluminum alloy.....	372
<i>P. T. Q. Le</i> , Phytochemical screening and antimicrobial activity of extracts of <i>Cassia alata</i> L. leaves and seeds.....	378
<i>M.-S. Kamrani, K. Seifpanahi-Shabani, A. Seyed-Hakimi, G.A.M. Al, Sh. Agarwa, V. K. Gupta</i> , Degradation of cyanide from gold processing effluent by H_2O_2 , NaClO and $Ca(ClO)_2$ combined with sequential catalytic process.....	384
<i>N.S. Krstić, M.N. Stanković, D.M. Đorđević, V.D. Dimitrijević, M. Marinković, M.G. Đorđević, A. Lj. Bojić</i> , Characterization of raw and chemically activated natural zeolite as a potential sorbent for heavy metal ions from waste water.....	394
<i>N.V. Pavlović, J.D. Mladenović, N.M. Zdravković, Đ.Z. Moravčević, D.Ž. Poštić, J.M. Zdravković</i> , Effect of tomato juice storage on vitamin C and phenolic compounds and their stability over one-year period.....	400
<i>N. Kaneva, A. Bojinova, K. Papazova, D. Dimitrov</i> , Photocatalytic degradation of the pharmaceuticals <i>Paracetamol</i> and <i>Chloramphenicol</i> by Ln-modified ZnO photocatalysts.....	406
<i>N. Pasupulety, H. Driss, A.A. Al-Zahrani, M.A. Daous, L.A. Petrov</i> , On the role of texture and physicochemical characteristics on adsorption capacity of granular activated carbon.....	414
<i>I. Radulescu, A V. Radulescu</i> , Study of degradation phenomenon for transmission lubricants.....	421
<i>S. I. Papanov, Ek. G. Petkova, I. G. Ivanov, St. D. Ivanova, D. I. Popov</i> , Analysis of the changes in the main characteristics and antioxidant properties in raspberries of "Rubin" variety depending on the altitude.....	428
<i>N.G. Kostova, M. Fabian, E. Dutkova</i> , Mechanochemically synthesized N-doped ZnO for photodegradation of ciprofloxacin.....	433
<i>N.G. Kostova, M. Achimovicova, M. Fabian</i> , Photocatalytic behavior of ZnSe-TiO ₂ composite for degradation of methyl orange dye under visible light irradiation.....	439
<i>A. Hatipoglu, S. Aydogdu, H. Dedeoglu, D. Civan</i> , Toxicity prediction of organophosphorus compounds by QSAR.....	445
<i>J. Zhang, Y. Wen, L. Chen</i> , Study on fatigue properties of basic magnesium sulfate cement reinforced concrete beams based on response surface methodology.....	452
<i>M. D. Sokić, B.R. Marković, L.L. Pezo, S.B. Stanković, A.S. Patarić, Z.V. Janjušević, B.Lj. Lončar</i> , Copper leaching from chalcopyrite concentrate by sodium nitrate in sulphuric acid solution – chemometric approach.....	457
<i>Erratum</i>	464
<i>Instruction to authors</i>	465
	467